Fabrication of nanoelectronic devices for applications in flexible and wearable electronics

Parikshit Sahatiya

A Dissertation Submitted to

Indian Institute of Technology Hyderabad

In Partial Fulfillment of the Requirements for
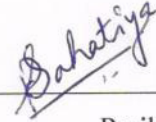
The Degree of Doctor of Philosophy

भारतीय प्रौद्योगिकी संस्थान हैदराबाद
Indian Institute of Technology Hyderabad

Department of Electrical Engineering

January, 2018

Declaration

I declare that this written submission represents my ideas in my own words, and where others' ideas or words have been included, I have adequately cited and referenced the original sources. I also declare that I have adhered to all principles of academic honesty and integrity and have not misrepresented or fabricated or falsified any idea/data/fact/source in my submission. I understand that any violation of the above will be a cause for disciplinary action by the Institute and can also evoke penal action from the sources that have thus not been properly cited, or from whom proper permission has not been taken when needed.
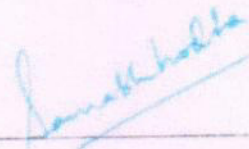
Parikshit Sahatiya

(ee14resch11016)

Approval Sheet

This thesis entitled "Fabrication of nanoelectronic devices for applications in flexible and wearable electronics" by Mr. Parikshit Sahatiya is approved for the degree of Doctor of Philosophy from IIT Hyderabad.

Dr. Saurabh Lodha

Associate Professor, Department of Electrical Engineering, IIT Bombay

Examiner 1
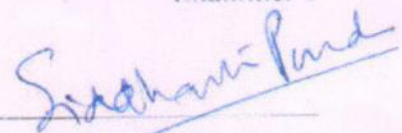
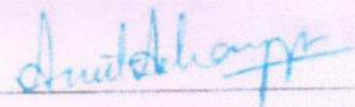Dr. Siddhartha Panda

Professor, Department of Chemical Engineering, IIT Kanpur

Examiner 2

Dr. Amit Acharayya

Associate Professor, Department of Electrical Engineering, IIT Hyderabad
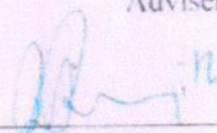
Internal Examiner

Dr. Sushmee Badhulika

Associate Professor, Department of Electrical Engineering, IIT Hyderabad

Adviser/Guide

Dr. Ranjith Ramadurai

Associate Professor, Department of MSME, IIT Hyderabad

Chairman

Acknowledgements

I would like to express my sincere gratitude and special appreciation to my advisor Dr. Sushmee Badhulika, Associate Professor, Department of Electrical Engineering, Indian Institute of Technology Hyderabad for the continuous support of my PhD study and related research, for her patience, motivation and immense knowledge. It has been my honor to be her first PhD student. Her contribution of time, ideas, and motivation has made my PhD experience more productive and stimulating. I could not have imagined having a better advisor and mentor for my PhD study.

Besides my advisor, I would like to thank my Doctoral Committee members: Dr. Kaushik Nayak, Dr. Amit Acharayya and Dr. Ranjith Ramadurai for their insightful comments and encouragement to widen my research and has helped me improve the quality of this thesis.

The company of my PhD colleagues Rinky Sha, Arthi Gopalakrishnan has contributed immensely to my personal and professional development at IIT Hyderabad. The group has been the source of friendship as well as sound advice and collaboration. The company of them has been very memorable and cherishing. I would like to acknowledge Solomon Jones, Thanga Gomathi who were at IIT Hyderabad as Junior Research Fellows. I express my obligations to them for their help during the experiments and providing me with critical data for my PhD research. Other past and present members that I had the pleasure to work with are Dr. Vishnu Nandimalla, post-doctoral researcher, graduate students Raja Sekhar, Akash Shinde and Madhava Chepuri, undergraduate student Anand Kadu, Junior Research Fellow Chandrasekhar Reddy and Santhosh Kannan and summer intern Harshit Gupta.

I would like to thank Indian Nanoelectronics User Program (INUP), IITB for the cleanroom fabrication facility for device fabrication and characterization facility. A special thanks to Dr. K. Nageswari for her kind support in characterization of devices under INUP, IITB. I would like to extend my thanks to Department of Chemistry and Material Science & Engineering, IITH for their help with

Last but not the least, I finally acknowledge the people who mean a lot to me, my mother Jaywanti Sahatiya and my brother Roshan Sahatiya who always believed in me and constantly inspired me to pursue my dreams. I thank you for all the patience, selfless love, care and pain you went through to shape my life. I have learnt so much from my brother that I cannot put them in words. I would never be able to pay back the love and affection showered upon me by you guys. Also, I express my heartfelt thanks to my sister in law Sanju Sahatiya for her support and love. I am thankful to me niece Nysha Sahatiya for giving me immense happiness during last 3 months.

Words cannot express how grateful I am to my wife Pranjali Sahatiya for all the sacrifices that she has made on my behalf before and after marriage. Her patience, love, support, encouragement has helped sustain me such far. I greatly value her contribution and deeply appreciate her belief in me. Without her help, I would not have been able to complete much of what I have done and become who I am. It would be ungrateful if I thank Pranjali in these few words. My heartfelt regard goes to my father in law Devidas Attarde, mother in law Jayshree Attarde and sister in law Deepali Attarde for their belief, love and moral support. This work of dissertation would not have been possible without the support and inspiration of all these special and amazing people in my life.

Dedicated to

To my Mother Jaywanti Sahatiya.

Abstract

Conventional electronic devices fabricated on rigid crystalline semiconductors wafers have evolved with the motivation to miniaturize thereby realizing faster, smaller and densely integrated devices. A parallel research that is rapidly evolving for future electronics is to integrate the property of flexibility and stretchablity to develop human friendly devices. There have been number of reports on fabricating sensors and electronic devices on stretchable, bendable and soft materials like polyimide, polyurethane sponge, natural rubber, cellulose paper, tissue paper etc. using various nanomaterials such as 2D materials, metal oxides, carbon nanomaterials and metal nanowires. These nanomaterials possess excellent electronic, thermal, mechanical and optical properties making them suitable for fabrication of broadband photodetectors, temperature, pressure and strain sensors which find applications in the field of optoelectronics, sensors, medical, security and surveillance.

While most reports on photodetectors focus on improving the responsivity in one region of electromagnetic spectrum by fabricating materials hybrids, the main issue still remains unaddressed which is the inability to absorb wide range of electromagnetic spectrum. Most photodetectors comprise of p-n heterojunction, where one of the material is responsible for absorbance, having metal contacts on p and n type allows for effective separation of photogenerated carriers. But for a broadband photodetector, both the materials of the heterojunction should participate in the absorbance. In such a case, metal contacts on p and n type will trap either the photogenerated electrons or hole which leads to the failure of the device. The first part of the thesis focus on the development of flexible broadband photodetectors based on MoS_2 hybrid.

Next chapter of the thesis deals with the improvement of responsivity by fabrication of solution processed heterojunction and piezotronic diode on flexible paper substrate for enhanced broadband photodetector and active analog frequency modulator by application of external mechanical strain. The fabricated MoS_2 based

heterojunctions was further utilized at circuit level for frequency modulation. The external applied strain not only modulates the transport properties at the junction which not only enhances the broadband photoresponse but also changes the depletion capacitance of junction under reverse bias thereby utilizing it for frequency modulation at circuit level.

The next part of thesis deals with fabrication of new type of electronic, skin-like pressure and strain sensor on flexible, bio-degradable pencil eraser substrate that can detect pressure variations and both tensile and compressive strain and has been fabricated by a solvent-free, low-cost and energy efficient process. Eraser, serves as a substrate for strain sensing as well as acts as a dielectric for capacitive pressure sensing, thereby eliminating the steps of dielectric deposition which is crucial in capacitive based pressure sensors. Detailed mechanism studies in terms of tunneling effect is presented to understand the proposed phenomena. As a proof of concept, an array of 6 x 8 devices were fabricated and pressure mapping of alphabets "I", "T" and "H" were plotted which were highly consistent with the shape and weight distribution of the object.

.

Nomenclature

DI – Deionized

MoS_2 – Molybdenum disulfide

SWCNTs – Single Walled Carbon Nanotubes

MWCNTs – Multi Walled Carbon Nanotubes

IoT – Internet of Things

a-Si – amorphous Silicon

ZnS – Zinc sulfide

V_2O_5 – Vanadium pentoxide

CuO – Copper oxide

NiO – Nickel oxide

SnO – Tin oxide

PEN - polyethylene naphthalene

PDMS – polydimethylsiloxane

PET - polyethylene terephthalate

PMMA – polymethylmethacrylate

PI - Polyimide

UV – Ultraviolet

NIR – Near Infrared

FET – Field Effect Transistor

PU – polyurethane

XRD – X-ray diffraction

XPS – X-ray photoelectron spectroscopy

PL - photoluminescence spectroscopy

FESEM – Field Emission Scanning Electron Microscopy

TEM – Transmission Electron Microscopy

FTIR – Fourier Transform Infrared Spectroscopy

IV – current-voltage

CV – capacitance- voltage

TMDs - Transition-Metal Dichalcogenide

RF – Radio frequency

ZIF – Zeolithic Imidazolate Framework

PCBs – Printed Circuit Boards

LO – Longitudinal optic

TO – Transverse optic

SO – surface optic

CH_4N_2S – Sodium molybdate

NH_3 – Ammonia

CO_2 – Carbon dioxide

H_2S – Hydrogen sulfide

EQE – External quantum efficiency

CB – Conduction Band

VB – Valence Band

PLD – Pulse laser deposition

CVD – Chemical Vapor Deposition

PVD – Physical Vapor Deposition

Al – Aluminum

DMF – Dimethylforamide

PAN – Polyacrylonitrile

CQD – Carbon Quantum Dot

FWHM – Full Width Half Maximum

LUMO – Lowest Unoccupied Molecular Orbital

HOMO – Highest Occupied Molecular Orbital

Rpm – rate per minute

ZnO – Zinc oxide

GaAs – Gallium Arsenide

CdS – Cadmium sulfide

Gr – Graphene

CMOS – Complementary Metal Oxide Semiconductor

PVC – Polyvinyl chloride

LPCVD – Low Pressure Chemical Vapor Deposition

HMTA – Hexamethylenetetramine

LC – Inductor capacitor

DSO – Digital Storage Oscilloscope

GF – Gauge Factor

E-skin – Electronic Skin

Contents

Chapter 1

Introduction

1.1 Introduction

Sensors are devices that detect or measure physical and chemical quantities such as temperature, pressure, sound, and concentration and are converted into an electrical signal. The main requirements of a good sensor are high sensitivity, high selectivity, fast response, low cost, and high reliability that can be operated on site and in situ. The emergence of nanotechnology has led to a strategic shift in sensor technology towards more sensitive recognition layers, increasingly complex architectures, and reduced size and more so because of the known fact that silicon-based semiconducting metal oxide technologies will reach its limit in the near future.

Rapid progress in the synthesis and fundamental understanding of surface phenomena of nanomaterials has enabled their incorporation into sensor architectures. Functional nanomaterials are strong candidates for sensors, because their reduced dimensions create an increase in environmental sensitivity. The reduced dimensionality also creates structures with exceptionally high surface area to volume ratio, and some materials, such as 2D MoS_2 [1], graphene [2], reduced graphene oxide [3] and single wall carbon nanotubes (SWNTs) [4] and metal oxides [5] are composed almost entirely of surface atoms. These two consequences of reduced size result in a class of materials that has the potential for unsurpassed sensitivity towards changes in its physical and chemical properties.

However, all established classes of high-performance electronics exploit single crystal inorganic materials, such as silicon or gallium arsenide, in forms that are fundamentally rigid and planar. The human body is, by contrast, soft and curvilinear. This mismatch in properties hinders the development of devices capable of intimate, conformal integration with humans, for applications ranging from human-machine interfaces, sensors, electronic skin and multifunctional sensors for Internet of Things (IoT). Hence there is heightened need for not only the flexible materials but also integrating them on flexible substrate which would be a step ahead in biointegrated devices. For developing flexible electronics devices there is need for material investigation which are flexible and stretchable. One envisioned solution involves the use of organic electronic materials, whose flexible properties have

generated interest in them for potential use in paper-like displays, solar cells, and other types of consumer electronic devices [6-7]. Such materials are not, however, stretchable or capable of wrapping curvilinear surfaces; they also offer only moderate performance, with uncertain reliability and capacity for integration into complex integrated circuits. Functional 2D nanomaterials such as MoS_2, graphene and 1D materials such as carbon nanotubes and metal oxides are promising candidate for the development of flexible electronic devices and sensors because of their high mobility, high thermal conductivity, high young's modulus etc.

1.2 Review of status in research and development in the subject

1.1.1 Material Review

For developing flexible electronic devices there is need for material investigation which are flexible and stretchable. There are reports on several materials such as a – Si [8], low temperature polycrystalline silicon [9], metal oxides [10], nanowires [11] and organic semiconductors [12] to be promising candidates for flexible electronics, but they have several problems associated with them. a – Si have poor mobility and less flexibity [13]. Low temperature polycrystalline have relativity good mobility but has uniformity and process ability problems associated with it [14]. Even the temperature has to be compatible with other process, as at high temperature the mobility of polycrystalline silicon decreases. Metal oxides are costly and have less environmental stability [15]. In search of functional materials for multisensory applications, 2D MoS_2 has gained significant interest among other 2D materials due to its exciting electronic and chemical properties. The ability to tune bandgap of MoS_2 by thickness modulation has opened up numerous opportunities for its use in electronic applications. Further, the compatibility of MoS_2 with different flexible substrates makes it a versatile material suitable for flexible and wearable sensors. Carbon nano materials such as one dimensional carbon nanotube (CNT) and two dimensional graphene have gained much attention for flexible electronics because of their attractive and motivating properties. The carrier mobility of CNT has been reported to be as high as ~ 80,000 cm^2V^{-1} s^{-1}, [16] and that of graphene on insulator substrate to be ~ 100,000 $cm2V-1$ $s-1$. [17] Such high mobility values motivates the use of both CNT and graphene in high speed electronics. The current capacity of both CNTs and graphene have been reported to be 109 cm^{-2} [18]. Thermal conductivity of SWCNTs and graphene at room temperature claimed to be is 3,500 $Wm-1K-1$ and 5,300 $Wm^{-1}K^{-1}$ [19] respectively with transmittance of nearly 97 %. Both CNTs and graphene have outstanding mechanical properties with

Young's modulus of 1 TPa and tensile strength of 130 GPa [20]. For the above stated reasons and properties, MoS_2, CNTs and graphene are considered to be most promising material for next-generation flexible electronics. To further expand the scope of applications that pristine nanomaterials offers, hybrids of MoS_2, CNTs and graphene with different metal oxides and metal chalcogenides have been synthesized and utilized in energy storage, electrochemical sensors, photodetectors etc. Nanostructured transition metal chalcogenides have gained interest due to their importance in field of sensing and electronic applications.16 Among metal chalcogenides, ZnS is a n type semiconductor with bandgap of ~ 3.7 eV and has been utilized for a variety of applications in the field of energy harvesting, sensors, electronic and optoelectronic applications. Since ZnS is a sulfur based metal chalcogenide and has lattice parameters close of MoS2, the synergistic effect allows for the growth of MoS_2/ZnS hybrids. Further, Transition metal oxides such as vanadium oxides family find wide applications in electronics due to their reversible phase transitions from metals to semiconductors. Particularly, Vanadium Pentaoxide (V_2O_5) from vanadium oxides family has gained a lot of attention because of its direct bandgap of 2.2 to 2.8eV which makes it potential candidate for optoelectronic and photoelectric applications. However synthesis of V_2O_5 is a challenging task because of its affinity to exist in different oxidation states. Combining 2D MoS_2 with 1D V_2O_5 would be a step forward in the fabrication of novel flexible electronic devices having potential applications in broadband photodetectors. Also, coupling MoS_2 with different semiconductors results in formation of heterojunction with efficient charge separation, high electron transfer rate and broadband absorption. There are reports on hybrids of MoS_2 with various metal oxides such as ZnO, CuO, NiO, SnO for applications ranging from electronics to energy storage metal oxides. Out of all the metal oxides, p type copper oxide (CuO) forms hybrid p-n junction with n type MoS_2 thereby expanding the scope of electronic applications of pristine MoS_2.

1.2.2. Substrate

Flexible substrates provide ideal platforms for exploring some of the unique characteristics that arise in metamaterials via mechanical deformation. The use of flexible substrates to demonstrate metamaterials with novel functionalities is gaining increasing attention worldwide. The most commonly used flexible substrates for metamaterials are PDMS and polyimide, due to their widespread use in flexible electronics. Other flexible substrates utilized for metamaterial devices include metaflex [21], polyethylene naphthalene (PEN) [22], polyethylene terephthalate (PET) [23], polymethylmethacrylate (PMMA) [24], and polystyrene [25]. Polyimide is an ideal choice as substrate for flexible electronics due to its strong adhesion to metal coatings, which provides a high degree of strain delocalization.

Polyimide provides operating range of -269° to 400° C with very high glass transition makes it ideal for deposition techniques such as sputtering and E beam evaporation. Its adhesion to photoresist and resistant to corrosive acids used while etching is another feature which allows direct patterning of structures onto it [26]. Moreover, it is biocompatible [27] which is of foremost importance for wearable electronics. Also, most of the above mention polymer substrates are microfabrication compatible and the devices can be fabricated using sophisticated cleanroom techniques which offers tremendous applications in the fabrication of reliable flexible electronic devices. Despite the advantages offered by plastic substrates, their inability to withstand high processing temperatures, poor recyclability, and non-biodegradability makes them unsuitable for the development of eco-friendly flexible electronics for IoT applications. However, all flexible substrates are not microfabrication compatible and hence there is an urgent need to develop lithography free solution phase processes for the fabrication of devices on flexible substrates such as cellulose paper and eraser substrate.

Sensing mechanism:

There are number of complementary and competing sensor technologies relying on different physical and chemical principles. Different detection principles can be used in various sensors. Our interest not only governs solid state sensors but also extends to flexible devices and sensors which can be integrated onto humans and environmental flora and fauna.

Conductance based sensors:

Conductance-based sensors come under the category of sensors where the sensing mechanism is based on monitoring the change in resistance when exposed to a particular compound or light (UV and IR). In conductance-based sensors, an active material, which may be a functional nanomaterial or hybrid nanomaterial, is deposited between two metal contacts. Binding of a target agent or absorption of photons with the sensing platform causes a change in resistance between the metal contacts. This change in resistance is proportional to the concentration of the absorbed photons, and thus the sensor provides an indication of both presence and quantity of the target agent.

Two different configurations (Chemiresistor and ChemFET) have been employed to develop nanosensors and nanodevices. In Chemiresistor configuration, the current passes through the sensing material bridging between the source and drain electrodes. The charge transfer or photogenerated electrons occurring at the surface sensing alters the current flow.

4

In FET configuration, the conductance on the nanostructure between source and drain is altered by a gate electrode capacitively coupled through a thin dielectric.

1.3. Research Objective

Based on the mentioned discussion regarding the materials and substrates utilized for flexible electronics, the overall aim of this thesis is to fabricate flexible and wearable electronic devices and its applications in broadband photodetector and artificial electronic skin with following specific objectives.

To fabricate flexible broadband photodetector covering entire range of electromagnetic spectrum from Ultraviolet to Near Infrared region

While most reports on photodetectors focus on improving the responsivity in one region of electromagnetic spectrum by fabricating materials hybrids, the main issue still remains unaddressed which is the inability to absorb wide range of electromagnetic spectrum. Most photodetectors comprise of p-n heterojunction, where one of the material is responsible for absorbance, having metal contacts on p and n type allows for effective separation of photogenerated carriers. But for a broadband photodetector, both the materials of the heterojunction should participate in the absorbance. In such a case, metal contacts on p and n type will trap either the photogenerated electrons or hole which leads to the failure of the device. Thus the goal is to grow combination of hybrid materials on flexible substrate by simple hydrothermal method such that both the materials are exposed to illumination and engineer the device fabrication to collect the photogenerated carriers in UV to NIR region of electromagnetic spectrum.

To increase the responsivity of the broadband photodetectors by external strain modulation

Semiconductor interfaces are vital components for fabricating electronic and optoelectronic devices. Properties of interfaces between two hetero-structured semiconductors play an important role in modulating the electronic structure and carrier behavior in modern nanoelectronics devices. Thus ability to precisely tailor the properties of the semiconductor interfaces provides lot of possibilities to enhance performance or add new functionalities altogether in devices. Semiconductor interface engineering is gaining interest in recent years to rationally design and fabricate novel nanoelectronics devices. There are different ways to modulate the electronic structure and carrier behavior in semiconductors which include

structure design, surface treatment, chemical doping etc. Strain modulation is considered as an effective means of tuning the electronic structure and carrier behavior in semiconductors. Moreover, at nanoscale, materials possess higher toughness and hence strain modulation effect could be more significant. The objective of this work is to utilize external strain modulation in heterojunctions to enhance the responsivity of broadband photodetectors by modulating the schottky barrier of the fabricated heterojunctions.

To fabricated pressure and strain sensors using solvent/lithography free method for electronic skin applications

Conventional electronic devices fabricated on rigid crystalline semiconductors wafers have evolved with the motivation to miniaturize thereby realizing faster, smaller and densely integrated devices. A parallel research that is rapidly evolving for future electronics is to integrate the property of flexibility and stretchablity to develop user friendly devices. There have been number of reports on strain and pressure sensors on stretchable, bendable and soft materials like polyimide, polyurethane sponge, natural rubber, cellulose paper, tissue paper etc. using various nanomaterials such as metal oxides, carbon nanomaterials and metal nanowires. Even though these devices are low cost, environmental friendly and involve low energy fabrication processes, they lack the multi-functionality of both pressure and strain sensing, which is essential for artificial electronic skin applications. PU sponge is highly flexible but possess less stretchablity which limits its use as strain sensor. Moreover, making the sponge conductive for pressure sensing applications involves processes like spin coating, dip coating and freeze drying which use toxic solvents and subsequently degrade the performance of the device. Fabricating devices on cellulose paper has the advantage of being eco-friendly and low-cost, but low tear resistance and poor stretchablity of cellulose paper restricts its use in robust applications. Natural rubber is an ideal choice for fabricating pressure and strain sensors as it possesses high tear resistance, stretchablity and is also bio-degradable. To achieve flexibility and stretchablity of the devices two common strategies have been used. First is to directly bond thin conductive materials having low young's moduli to rubber/elastic substrate. Second method is to fabricate the device using intrinsically stretchable conductors that are assembled by mixing conductive material into elastomeric matrix. But above methods make use of toxic solvents and acids for achieving proper dispersion which not only makes the whole process eco-unfriendly but also degrades the performance of the device. Moreover, conductive filler is functionalized for proper adhesion of conductive materials onto rubber/elastic substrate which not only reduces the

conductivity of the materials but also induces defects. The objective of this work is to fabricate pressure and strain sensors on eraser substrate using solvent/lithography free method which can then be utilized for electronic skin applications.

Study of the morphology and electrical characterization of these devices and then applying it for sensing applications

Chemical characterization in terms of X-ray diffraction (XRD), Raman spectroscopy, X-ray photoelectron spectroscopy (XPS), UV-vis-NIR spectroscopy, photoluminescence spectroscopy (PL) and structural characterization using Scanning electron microscopy (FESEM) and Transmission electron microscopy were performed to confirm the formation of functional nanomaterials and their hybrids. Further electrical characterization in terms of IV, CV were performed to understand the electrical properties of the fabricated devices. Finally, the fabricated devices were tested for various sensing applications such as broadband photodetector, pressure and strain.

1.4. Organization of Thesis

Chapter 2 discusses the fabrication of MoS_2/ZnS hybrid on paper substrate and its application in broadband photodetector

Chapter 3 discusses the fabrication of discrete 1D V_2O_5 nanowires on 2D MoS_2 and its application in flexible broadband photodetector

Chapter 4 discusses the fabrication of 0D carbon dot on 2D MoS_2 and its application in flexible broadband photodetector

Chapter 5 discusses the strain modulation concept for increasing the responsivity of broadband photodetector fabricated using 2D ZnO/Graphene heterojunction

Chapter 6 discusses the fabrication of MoS_2/CuO piezotronic diode for increasing the responsivity of broadband photodetector and active frequency modulation

Chapter 7 describes the solvent/lithography free fabrication of pressure and strain sensor on eraser substrate for artificial electronic skin application

Chapter 8 gives the summary of the work done and the conclusion

1.5. References

1. Li, T., & Galli, G. Electronic properties of MoS$_2$ nanoparticles. *The Journal of Physical Chemistry C*, **2007**, 111(44), 16192-16196.

2. Allen, M. J., Tung, V. C., & Kaner, R. B. Honeycomb carbon: a review of graphene. *Chemical reviews*, **2009**, 110(1), 132-145.

3. Zhu, Y., Murali, S., Cai, W., Li, X., Suk, J. W., Potts, J. R., & Ruoff, R. S. Graphene and graphene oxide: synthesis, properties, and applications. *Advanced Materials*, **2010**, 22(35), 3906-3924.

4. Dresselhaus, M. S., Dresselhaus, G., Eklund, P. C., & Rao, A. M. (2000). Carbon nanotubes. In The Physics of Fullerene-Based and Fullerene-Related Materials, **2000**, 331-379.

5. Sun, Y. F., Liu, S. B., Meng, F. L., Liu, J. Y., Jin, Z., Kong, L. T., & Liu, J. H. Metal oxide nanostructures and their gas sensing properties: a review. *Sensors*, **2012**, 12(3), 2610-2631.

6. Yin, Z., Li, H., Li, H., Jiang, L., Shi, Y., Sun, Y.,& Zhang, H. (2011). Single-layer MoS2 phototransistors. *ACS Nano*, **2011**, 6(1), 74-80.

7. Huang, C. K., Ou, Y., Bie, Y., Zhao, Q., & Yu, D. Well-aligned graphene arrays for field emission displays. *Applied Physics Letters*, **2011**, 98(26), 263104

8. Garnier, F., Horowitz, G., Peng, X., & Fichou, D. An all-organic" soft" thin film transistor with very high carrier mobility. *Advanced Materials*, **1990**, 2(12), 592-594.

9. Duan, X., Niu, C., Sahi, V., Chen, J., Parce, J. W., Empedocles, S., & Goldman, J. L. High-performance thin-film transistors using semiconductor nanowires and nanoribbons. *Nature*, **2006**, 425(6955), 274-278.

10. Nomura, K., Ohta, H., Takagi, A., Kamiya, T., Hirano, M., & Hosono, H. Room-temperature fabrication of transparent flexible thin-film transistors using amorphous oxide semiconductors. *Nature*, **2004**, 432(7016), 488-492.

11. SeobáLee, Seung, and Seung HwanáKo. "Very long Ag nanowire synthesis and its application in a highly transparent, conductive and flexible metal electrode touch panel." *Nanoscale*, **2012**, 6408-6414.

12. Loo, Y. L., Someya, T., Baldwin, K. W., Bao, Z., Ho, P., Dodabalapur, A., & Rogers, J. A. Soft, conformable electrical contacts for organic semiconductors: High-resolution plastic circuits by lamination. *Proceedings of the National Academy of Sciences*, **2002**, 99(16), 10252-10256.

13. Shah, A., Meier, J., Buechel, A., Kroll, U., Steinhauser, J., Meillaud, F., & Dominé, D. Towards very low-cost mass production of thin-film silicon photovoltaic (PV) solar modules on glass. *Thin solid Films*, **2006**, 502(1), 292-299.

14. Jacunski, Mark D., Michael S. Shur, and Michael Hack. "Threshold voltage, field effect mobility, and gate-to-channel capacitance in polysilicon TFTs." *IEEE Transactions on Electron Devices*, **1996**, 1433-1440.

15. Jiang, J., Li, Y., Liu, J., Huang, X., Yuan, C., & Lou, X. W. D. Recent advances in metal oxide-based electrode architecture design for electrochemical energy storage. *Advanced Materials,* **2012**, 24(38), 5166-5180.

16. Dürkop, T., Getty, S. A., Cobas, E., & Fuhrer, M. S. Extraordinary mobility in semiconducting carbon nanotubes. *Nano Letters*, **2004**, 4(1), 35-39.

17. Mayorov, A. S., Gorbachev, R. V., Morozov, S. V., Britnell, L., Jalil, R., Ponomarenko, L. A., & Geim, A. K. Micrometer-scale ballistic transport in encapsulated graphene at room temperature. *Nano Letters*, **2011**, 11(6), 2396-2399.

18. Yu, J., Liu, G., Sumant, A. V., Goyal, V., & Balandin, A. A. Graphene-on-diamond devices with increased current-carrying capacity: carbon sp2-on-sp3 technology. *Nano Letters*, **2012**, 12(3), 1603-1608.

19. Balandin, A. A., Ghosh, S., Bao, W., Calizo, I., Teweldebrhan, D., Miao, F., & Lau, C. N. Superior thermal conductivity of single-layer graphene. *Nano Letters*, **2008**, 8(3), 902-907.

20. Lee, C., Wei, X., Kysar, J. W., & Hone, J. Measurement of the elastic properties and intrinsic strength of monolayer graphene. *Science*, **2008**, 321(5887), 385-388.

21. X. Xu, B. Peng, D. Li, J. Zhang, L. M. Wong, Q. Zhang, S. Wang, and Q. Xiong, *Nano Letters*, **2011**, 11, 3232.

22. B. Ng, S. M. Hanham, V. Giannini, Z. C. Chen, M. Tang, Y. F. Liew, N.Klein, M. H. Hong, and S. A. Maier, *Optical Express*, **2011**, 19, 14653.

23. Y. Li, L. W. Tan, X. T. Hao, K. S. Ong, F. Zhu, and L. S. Hung, *Applied Physics Letters*, **2005**, 86, 153508.

24. T. Tumkur, G. Zhu, P. Black, Y. A. Barnakov, C. E. Bonner, and M. A. Noginov, *Applied Physics Letters*, **2011**, 99, 151115.

25. N. Gibbons, J. J. Baumberg, C. L. Bower, M. Kolle, and U. Steiner, *Advanced Materials*, **2009**, 21, 3933.

26. Briseno, A. L., Mannsfeld, S. C., Ling, M. M., Liu, S., Tseng, R. J., Reese, C., & Bao, Z. Patterning organic single-crystal transistor arrays. *Nature*, **2006**, 444(7121), 913-917.

27. Yang, J., Wei, D., Tang, L., Song, X., Luo, W., Chu, J., & Du, C*., RSC Advances*, **2015**, 5(32), 25609-25615.

Chapter 2

Large-area, flexible broadband photodetector based on ZnS-MoS$_2$ hybrid on paper substrate

Abstract

Flexible broadband photodetectors based on 2D MoS$_2$ have gained significant attention due to their superior light absorption and increased light sensitivity. However, pristine MoS2 have absorption only in visible and near IR spectrum. This paper reports a paper-based broadband photodetector having ZnS-MoS$_2$ hybrids as active sensing material fabricated using a simple, cost effective two step hydrothermal method wherein trilayer MoS$_2$ was grown on cellulose paper followed by the growth of ZnS on MoS$_2$. Optimization in terms of process parameters were done to yield uniform trilayer MoS$_2$ on cellulose paper. UV sensing property of ZnS and broadband absorption of MoS$_2$ in visible and IR, broadens the range from UV to near IR. ZnS played the dual role for absorption in UV and in the generation of local electric fields thereby increasing the sensitivity of the sensor. The fabricated photodetector exhibited a higher responsivity towards the visible light when compared to UV and IR light. Detailed studies in terms of energy band diagram is presented to understand the charge transport mechanism. This represents the first demonstration of a paper-based flexible broadband photodetector with excellent photoresponsivity and high bending capability that can be used for wearable electronics, flexible security and surveillance systems etc.

2.1. Introduction

High performance, flexible broadband photodetectors are essential components of optoelectronic systems and, find extensive applications in optical communication, environmental monitoring, image sensing, foldable displays and surveillance [1]. Recent studies on photodetectors have mainly focused on fabricating devices using various nanomaterials. But the major issue of these photodetectors is their inability to absorb wide ranges of the electromagnetic spectrum. There are several reports of photodetectors using

10

hybrid materials wherein the addition of transport material decreases the recombination rate thereby increasing the photocurrent [2, 3] but absorption in a wide range of electromagnetic spectrum still remains a challenge. To overcome this drawback, researchers have fabricated devices wherein the transport material itself acts as a photo absorber [4]. Synthesizing hybrid structures wherein the transport materials also acts as a photo absorber is an effective means to increase the range of electromagnetic spectrum.

Molybdenum disulfide (MoS_2), a widely used Transition-Metal Dichalcogenide (TMD), has unique properties such as variable bandgap (1.8 eV - 1.2 eV), reduced dimensionality, high carrier mobility, strong electron-hole confinement, light sensitivity and excellent light absorption extending from visible to NIR region [3, 5]. Coupling the tunable layer dependent behavior of MoS_2 with above-mentioned properties makes it suitable for a wide range of optoelectronic applications, especially photodetectors. Moreover, combining MoS_2 with other semiconductors results in the efficient charge separation [6]. high electron transfer rate and increases the solar light absorption [7].

Amongst several wide band gap semiconductors, Zinc sulfide (ZnS) has been a well-established material for UV photodetection [8] due to its wide band gap (3.77 eV), high exciton binding energy (40 meV) [9] and fast switching time on illumination with UV light [10]. To further enhance the properties and expand the range of applications and absorption range of electromagnetic spectrum, efforts have been made to synthesize hybrids of MoS_2 along with other metal oxides. Since wurtzite ZnS is also a sulfur based compound and has lattice parameters close to that of hexagonal MoS_2 [11], there exists a synergistic effect that facilitates the growth of ZnS-MoS_2 hybrids. ZnS-MoS_2 hybrids have been prepared using various methods such as sulfurization of Mo on RF magnetron sputtered ZnS thin film, [6] surfactant assisted exfoliation for MoS_2 followed by hydrothermal [11] and using MoS_2 with metal-organic framework ZIF-8 [12]. Among the various methods available, hydrothermal synthesis is the most versatile method as it provides the ability to synthesize hybrid nanostructures at low cost with distinct morphologies and high phase purity [13].

There are reports on broadband photodetectors, which use hybrid nanostructures either for enhanced sensitivity or for increasing the absorption range of electromagnetic spectrum [14, 15]. However, most of them do not cover the larger part of the electromagnetic spectrum and are fabricated on the rigid silicon substrate or flexible plastic substrates, which make use of sophisticated cleanroom processes that are expensive and energy inefficient [16]. As the basis of future sustainable technology, researchers of late are actively focusing on the

development of paper-based electronics due to its numerous advantageous such as low cost, light weight, mechanical flexibility and high performance compared to conventional electronic devices [17, 18]. Furthermore, paper-based electronic devices are known for their high biocompatibility, which allows for its easy integration with wearable electronic devices and biodegradability thereby addressing the problem of landfill. Till date, a wide array of paper-based electronic devices such as solar cells, supercapacitors, flexible displays, transistors, printed circuit boards (PCBs) has been reported [17].

Herein, we report the fabrication of a novel paper-based broadband photodetector using hybrids of ZnS-MoS$_2$. The photodetector was fabricated using a simple two-step hydrothermal method. The photodetector exhibited broad absorption covering UV, visible and IR region of the electromagnetic spectrum. ZnS contributed to the UV light detection and MoS$_2$ responded towards visible and IR. The fabricated photodetector shows increasing responsivity in the order of IR, UV and visible light, thereby indicating the high sensitivity of the device towards visible light. Discrete distribution of ZnS was observed on MoS$_2$ thereby not covering the entire MoS$_2$, which facilitated the absorption in UV, visible and IR region. The straddling type band alignment between ZnS and MoS$_2$, allows for efficient separation of photogenerated electron-hole pairs, thereby increasing the responsivity of the fabricated device. Moreover, the photodetector was fabricated on flexible cellulose paper, which makes the overall design of the sensor not only cost effective but also environmental friendly. To the best of our knowledge, this is the first report on paper based broadband photodetector with ZnS-MoS$_2$ hybrids as active sensing materials.

2.2.   Results and Discussion

The fabrication process is schematically shown in Figure 2.1. Detailed procedure of the fabrication process is explained in Experimental section. In brief, two step hydrothermal process was performed wherein MoS$_2$ was grown on cellulose paper followed by the growth of ZnS on MoS$_2$. Cellulose paper decomposes at 275°C [19] and hence was chosen for the growth of MoS$_2$ and ZnS which require hydrothermal temperature in the range of 200°C-220°C. Two-step hydrothermal method was performed over one pot synthesis of ZnS-MoS$_2$ hybrid as single step synthesis renders favorable for the growth of ZnS only rather than the formation of ZnS-MoS$_2$ hybrids. This is because ZnS precipitates are formed readily in the presence of Zn^{2+} and S^{2-} at room temperature [20] whereas formation of MoS2 requires heating at elevated temperatures [21]. It was observed that ZnS particles were formed during the preparation of nutrient solution thereby inhibiting the formation of MoS$_2$ crystals.

Optimization in terms of different hydrothermal temperatures was performed for the growth of MoS_2 and ZnS. At low temperatures of 180°C, crystallinity of MoS_2 was poor which is consistent with the report [22]. At elevated temperatures, cellulose paper substrate degrades and becomes fragile, which then adversely affects the flexibility nature of the substrate. Hence 200°C was optimized for the MoS_2 growth which had improved crystallinity over low temperatures and the substrate retained its flexibility properties. For ZnS growth, optimization was performed for hydrothermal temperature and time. As the hydrothermal time was increased for more than 1 hour, thick growth of ZnS was observed which did not adhere well to the substrate. Hence 200°C for 1 hour was optimized for discrete ZnS growth on MoS_2/cellulose paper. Also thick growth of ZnS would have led to complete coverage of MoS_2 by ZnS microspheres which would have hindered broadband absorption. Discrete growth is important in this case, as MoS_2 can be exposed to visible and NIR illumination.

The crystal structure of the as-grown MoS_2 and ZnS-MoS_2 were studied using XRD. Figure 2.2 a shows the XRD pattern of pristine MoS_2 and ZnS-MoS_2. The diffraction peaks of MoS_2 matches well with the JCPDS card no. 37-1492, which reveals the hexagonal phase of MoS_2. For pristine MoS_2, two broad peaks corresponding to (100) and (110) planes were observed. The peak broadening might be a consequence of the synthesis temperature (200°C) [22]. The (002) plane reflection cannot be noticed at $2\theta \sim 14°$, which might be due to the presence of few-layer (<5) MoS_2 or graphene-like MoS_2 [23]. The occurrence of low angle diffraction peak can be attributed to the increased interlayer spacing [24] and the diffraction of X-rays resulting from closely spaced few layered MoS_2 [25]. The interlayer spacing of as-grown MoS_2 was calculated to be 0.90 nm, whereas, bulk MoS_2 exhibits an interlayer spacing of 0.615 nm [23]. For ZnS-MoS_2 hybrids, the prominent peaks of MoS_2 are retained and additional diffraction peaks for ZnS were observed. The diffraction pattern of ZnS matches with the wurtzite (hexagonal) ZnS. (JCPDS card no. 36-1450) [26]. Also, prominent peaks at $2\theta \sim 16°$ and 22° were observed in both the pristine MoS2 and ZnS-MoS_2 hybrids which can be assigned to cellulose paper.[27] The presence of peaks for cellulose implies that the paper substrate was immune to degradation during the hydrothermal process.

To further confirm the formation of the hybrid and to investigate the details of the number of MoS_2 layers in the ZnS-MoS_2 hybrid, Raman analysis was performed as shown in Figure 2.2b which exhibits strong Longitudinal optic (LO), transverse optic (TO) and surface optic (SO) phonon modes. The peaks at ~282 cm^{-1}, ~336 cm^{-1} and ~668 cm^{-1} corresponds to E2 (TO), SO and 2LO modes of ZnS. The occurrence of SO mode in between the LO and TO

13

modes might be due to the activation of the symmetry breaking mechanism related to the surface of ZnS [28]. Peaks corresponding to LA (M) mode and A1g mode of MoS_2 are observed at ~230 cm^{-1} and 401 cm-1, respectively [29]. The peak signifying the E12g mode of MoS_2 might be suppressed due to the growth of ZnS on MoS_2 layer. Raman spectra of pristine MoS_2 is depicted in the inset of Figure 2.2b. Two characteristic peaks of MoS_2 were noticed at 383 cm^{-1} and 405 cm^{-1}, which are assigned to E12g and A1g phonon modes, respectively. E12g mode involves the in-plane vibrations of Mo atoms whereas A1g mode is due to the out of plane vibrations of the S atoms [30]. The peak position difference between the two modes was calculated to be ~22, corresponding to trilayer MoS_2 [31].

Figure 2.3a shows the FESEM images of cellulose paper after the growth of MoS_2 wherein the porous microfibers morphology of cellulose paper was clearly observed thereby indicating that growth of MoS_2 does not affect the morphology of cellulose paper. From the low magnification FESEM images shown in Figure 2.3a, the growth of 3D MoS_2 micro flowers on the entire surface of 3D hierarchically arranged cellulose fibers can be clearly observed. The average diameter of the 3D MoS_2 micro flowers formed was calculated to be ~1 μm, as shown in Figure 2.3b. High magnification FESEM images shown in Figure 2.3c of MoS_2 confirms the formation of micro flowers by the self-assembly of several MoS_2 nanosheets, with an average sheet thickness of 2-3 nm. Figure 2.3d shows the FESEM image of ZnS growth on MoS_2-cellulose paper wherein further growing of ZnS does not affect the microfibers morphology of cellulose paper. FESEM images shown in Figure 2.3e and 2.3f corresponds to ZnS-MoS_2, depicting the growth of ZnS sub-microspheres with an average diameter range of 320-520 nm on the surfaces of MoS_2 in a sporadic manner. From the FESEM images, it was clearly seen that ZnS microspheres have a high surface roughness and there seems to be a good interfacial contact between ZnS and MoS_2.

To further explore the possibility of utilizing the as fabricated ZnS-MoS_2 hybrid device as a broadband photodetector, optical absorption spectra was obtained from UV-Visible-NIR spectroscopy. Figure 2.4 shows the absorption spectra of the ZnS-MoS_2 hybrids, which revealed the growth of ZnS on MoS_2 extends the optical absorption in UV light region while retaining the absorption peaks of MoS_2. Two strong peaks around ~215 and 335 nm can be attributed to the absorption of light by ZnS microspheres. The absorption peaks in visible and NIR region are invisible due to the high-intensity absorption peaks of ZnS in UV light region, which are plotted separately by scaling down the intensity values as shown in the inset of Figure 4. This clearly suggests that the as-grown ZnS-MoS_2 hybrid offers a broad range of optical absorption, which can be potentially used as a broadband sensing material.

Optical bandgap was calculated for individual MoS_2 and ZnS which were found to be 1.53 eV and 3.7 eV respectively. Tauc plot for both MoS_2 and ZnS can be found in the Appendix A as Figure S1.

The growth of MoS_2 micro flowers was initiated by the formation of amorphous nanoparticles of MoS_2 during hydrothermal reaction. The nanoparticles formation at this phase is facilitated by the presence of sulfurization reagent (CH_4N_2S) which performs the dual role of acting as a sulfur donor and reducing agent. Aggregation of these nanoparticles under optimal conditions of temperature and time period results in the formation of spherical MoS_2 clusters which acts as the seed for the growth of MoS_2 nanosheets [32, 33]. The van der Waals interaction that exists between individual sheets of MoS_2 contributed to the evolution of MoS_2 nanosheets into 3D micro flowers [34]. The growth of ZnS begins with the dissolution of Zinc chloride and hydrolysis of thiourea in the solution. This hydrolysis results in byproducts such as ammonia (NH_3), carbon dioxide (CO_2) bubbles, and hydrogen sulfide (H_2S) in the reaction medium. Of those, H_2S in the hydrothermal vessel reacts with the solvent (water) liberating S^{2-} ions. The Zn^{2+} and S^{2-} ions in the solution could enter the CO_2 bubble due to the influx of ions resulting in the formation of ZnS nanoparticles [35]. But, ZnS nanoparticles are unstable owing to their high surface energy. Thus, to minimize the effect of surface energy, ZnS nanoparticles tend to aggregate resulting in the formation of microspheres [36].

The as-fabricated devices with ZnS-MoS_2 as channel and Ag paste as contacts were utilized for broadband photodetector covering UV, visible and IR range. UV lamp with 365 nm wavelength, IR lamp with wavelength 780 nm and visible light with wavelength 554 nm were used to conduct experiments. Prior to I-V measurements, the devices were kept in dark for 12 hours to stabilize them. The current-voltage (I-V) characteristics of the fabricated broadband photodetector under dark and illuminated conditions along with their temporal response under illumination are shown in Figure 2.5. From the linearity of the room temperature I-V curves, it is clear that the device exhibits ohmic behavior. Upon light illumination, increase in current was observed w.r.t the intensity of illuminated light, which can be attributed to the increased number of photogenerated electrons. As the illumination time was increased, an increase in the photocurrent was observed which is due to increase in the number of photogenerated electron-hole pairs. It should be noted that the photoelectron generation occurs only in ZnS during the illumination of UV light whereas for visible and IR illumination, generation of photoelectrons occurs in MoS_2. The highest photocurrent was observed for visible light illumination (having an intensity of 5.31 mW/cm^2). Figure 2.5 b,

15

d, and f shows the normalized resistance change ($\Delta R/R$) of the photodetector under UV, visible and IR illumination as a function of time, for three repeated cycles. On illumination with UV light (intensity-19.1 mW/cm^2), a normalized resistance change of 21.6 % was observed as seen in Figure 2.5b. Whereas, a resistance change of 33.5 % and 19.68 % was noticed for illumination with visible light (5.31 mW/cm^2) and IR light (82.9 mW/cm^2) as shown in Figure 2.5d and Figure 2.5f respectively. Maximum change in resistance was observed for visible light compared to UV and IR indicating that the fabricated photodetector is more sensitive to visible than UV and IR. It should be noted that even though the intensities used were different for measurements, responsivity was calculated using same intensities, which was highest for visible light, which further, confirms that the sensor, was more sensitive to visible light compared to UV and IR. The rise time of the device was calculated from 10% to 90% of maximum value and was found to be 22, 11 and 31 seconds for UV, visible and NIR light respectively. Low-rise time for visible light suggests that sensor exhibits quick response towards visible light compared to UV and IR illumination. Low response speed of the fabricated photodetector might be attributed to improper band alignment between the two semiconductors where the distribution of ZnS on MoS$_2$ is not continuous, but is discrete, which leads to improper band alignment. But discrete distribution is important as MoS$_2$ can be exposed to visible and NIR illumination. Covering entire MoS$_2$ with ZnS would led to development of only UV photodetectors with very less or no response towards visible and NIR light. Moreover, the growth of MoS$_2$ is on cellulose paper, which is a dielectric material and hence reduces the carrier mobility in MoS$_2$ thereby reducing the response time. [37] Also, due to the trapped charges at sulfur vacancies reduction in carrier mobility of MoS$_2$ is observed. Similar low response time has been reported for MoS$_2$ on plastic substrates. [38]

The important Figures of merit of a photodetector are responsivity and external quantum efficiency (EQE), a measure of photocurrent generated per unit power of incident light on sensing area. The equation (1) and (2) gives the formula of photoresponsivity (R_λ) and EQE respectively.

$$R_\lambda = \frac{I_\lambda}{P_\lambda \times A}$$
(1)

$$EQE = hc \times R_\lambda / e\lambda$$
(2)

Where I_λ is the photocurrent, P_λ is the power and A is the active sensing area of photodetector [39]. EQE calculated was 0.4×10^{-2} % for visible light. As shown in Figure

2.6a, the responsivity increases with the excitation power density of the illuminated light. A responsivity of 17.85 µA/W was observed for visible light illumination and 9.4 µA/W was found to be the responsivity under UV illumination. The responsivity for IR light, with a value of 4.52 µA/W was the least among the measured values. Therefore, it can be inferred that the fabricated photodetector is highly sensitive to visible light when compared to UV and IR. This can be attributed to the larger area exposed to MoS_2 as compared to ZnS, as evident from FESEM thereby resulting in an increased photogenerated electron-hole pairs in MoS_2 when compared to ZnS, which leads to the higher photocurrent. Comparing to the existing reports on MoS_2 based photodetectors on rigid silicon substrates which exhibits very high responsivity [40], the responsivity calculated for the as fabricated device is low. The reason for low EQE and low responsivity is the low crystallinity of the MoS_2 and also due to the fact the carrier mobility of MoS_2 is reduced by growing it on cellulose paper substrate. Even though the calculated EQE and responsivity is less it was found to be comparable to the reports available on broadband photodetector on other flexible plastic substrates [41, 42]. It should be noted that the area of MoS_2 lying underneath ZnS microspheres (ZnS-MoS_2 interface) was not exposed to visible light radiation. Despite, the lack of complete exposure of MoS_2 to visible light, the photodetector shows high sensitivity towards the visible light which could be attributed due to the local electric fields that are generated at the ZnS-MoS_2 interface. Even though ZnS blocks the visible and IR light to be exposed on MoS_2, they play an important role in achieving higher sensitivity than pristine MoS_2 as ZnS on MoS_2 generates local electric fields, which help in the electron transport towards the metal contacts. In the case of pristine MoS_2, electric fields are generated only at the metal-MoS_2 interface and are absent in the areas far away from the metal-MoS_2 interface. Hence, due to the absence of electric field away from metal/MoS_2 interface, the electron-hole pair does not separate efficiently and tend to recombine which decreases the electrons collected at the metal contacts and thereby decreases photocurrent. Therefore, in case of pristine MoS_2, the contribution is only due to the photogenerated electrons at the metal-MoS_2 interface, which decreases the sensitivity. I-V characteristics of pristine MoS_2 under visible and IR illumination can be found in Appendix A as Figure S2. In the case of ZnS on MoS_2 due to the difference in the work function between ZnS and MoS_2, local electric fields are created at the interface of ZnS-MoS_2, which helps in the separation of electron-hole pair at the area, which are away from the metal-MoS_2 interface thereby adding up more photogenerated electrons to be collected at the metal contacts. Hence, in case of ZnS-MoS_2, the separation of photogenerated electron-hole not only happens at metal-MoS2 interface but also at ZnS-MoS_2 interface thereby covering larger portion.

To demonstrate the robustness of the flexible paper substrate based ZnS-MoS$_2$ device and evaluate its performance after repeated bending cycles, the sensor was attached to double-sided tape and bending (both compressive and tensile) was performed manually. After specific amount of bending cycles, measurements for UV, visible and IR photodetection were performed at intensity of 19.1 mW/cm^2.

Figure 2.6b shows the graph of responsivity with bending cycles wherein very negligible change was observed in the values of responsivity thereby suggesting that the performance of the as fabricated device performance does not deteriorate with bending.

The optoelectronic behavior of the fabricated photodetector in dark and illuminated conditions can be better understood from the band diagrams of ZnS and MoS$_2$ and the charge transfer schematics, as shown in Figure 2.7a and 2.7b. The electron affinity reported for ZnS and few-layer MoS$_2$ are 3.9 [43] and 4.0 eV [44] respectively. At the ZnS and MoS$_2$ interface, the flow of electrons from ZnS to MoS$_2$ results in the alignment of fermi levels thereby reaching equilibrium condition.[6] Under UV light illumination, photogeneration of electron-hole pairs occurs in ZnS microspheres when the energy of the illumination is greater than or equal to the bandgap energy of ZnS. For pristine ZnS, photogenerated electrons tend to recombine which decreases the carrier lifetime thereby decreasing the photocurrent. Hence, the need of MoS$_2$ as transport material arises for not only effective capturing the photogenerated electrons but also helps in generating local electric fields, which prevents the photogenerated electrons from recombination, and ultimately increasing the carrier lifetime. In the case of ZnS-MoS$_2$, since the conduction band (CB) of MoS$_2$ is below the CB of ZnS, it favors the effective separation of photogenerated electron-hole pairs from recombination. The photogenerated electrons and holes in ZnS reach the CB of MoS$_2$, from which the photoelectrons and holes gets transported to the metal contacts. It should be noted that both the contacts are on MoS$_2$ and hence due to the external electric field applied, photogenerated electrons and holes move towards respective electrode, thereby generating current. Due to the work function difference, the local electric fields are generated at the ZnS-MoS$_2$ interface (due to the formation of unipolar junction), favoring the electron-hole separation. Even though both MoS$_2$ and ZnS are n type, ZnS exhibits more n type behavior than MoS$_2$ (fermi level difference is large) and hence the interface is similar to the interface of n-n$^+$ junction thereby forming a unipolar junction [45] which creates barrier at the interface of ZnS-MoS$_2$ whose barrier potential would be the difference in the fermi levels of MoS$_2$ and ZnS. Moreover, there are many such unipolar junctions which cumulatively add up and helps in separation of photogenerated electron-hole pairs. So the

18

contribution of photocurrent is due to the fact that both the contacts are on MoS_2 and not on ZnS. If one of the contact was taken from ZnS, then the holes would have been trapped in MoS2 thereby leading to recombination of photogenerated electrons. For Visible and IR illumination, electrons-hole pairs are generated in MoS2 on light absorption. The presence of excess photoelectrons in the CB of MoS_2 causes a shift in fermi levels, thereby increasing the barrier height between ZnS and MoS_2, which results in the generation of the electric field that facilitates the charge separation. Under visible and IR illumination, the photogenerated electrons from MoS_2 do not tend to recombine due to the local electric fields created between ZnS and MoS_2 interface. The role of ZnS in visible and IR light sensing is the enhancement of charge separation by the electric field produced at the ZnS-MoS_2 interface. The reason for higher sensitivity towards the visible light as compared to UV and IR can be attributed to the larger area MoS_2 compared to ZnS and due to the discrete distribution of ZnS on MoS2, which facilities easy charge separation by creating local electric fields. The lesser sensitivity towards IR is due to the lower absorption of MoS_2 in near IR range (as shown in Figure 4) wherein the number of photogenerated electrons are less as compared to visible light.

There are reports on flexible photodetectors using methods such as Pulsed Laser Deposition (PLD) [46], direct assembly [47], Chemical Vapor Deposition (CVD) [48], and drop casting of materials grown using PVD (Physical Vapor Deposition) [49] etc. on flexible substrates such as polyimide (PI), polyethylene terephthalate (PET), polyethylene naphthalate (PEN). These techniques are often time-consuming and require the use of expensive sophisticated instruments. Despite the advantages offered by plastic substrates, their inability to withstand high processing temperatures, poor recyclability, and non-biodegradability makes them unsuitable for the development of eco-friendly flexible electronics [50]. MoS_2 based composites such as MoS_2-PbS [16] and Gr/MoS_2 [48] for broadband photodetector have been reported but are based on the rigid silicon substrate and involve cleanroom processing respectively. Paper substrate is an excellent alternative for plastic substrates due to its recyclability, excellent biodegradability and low cost. [51] reported a broadband photodetector on the paper substrate using inkjet and aerosol printing wherein expensive polymers were utilized as photoactive layer. In this work, utilization of inexpensive cellulose paper as the substrate, inexpensive precursors for the growth of both ZnS and MoS_2 and hydrothermal procedure for the fabrication of large area flexible photodetectors cuts down the overall cost. Large area fabrication is possible by the use of wide autoclave making it a viable technique for mass production of flexible photodetectors. The broad

range photodetection offered by the as-fabricated device ensues in the development of low-cost flexible broadband photodetectors without the use of sophisticated equipment.

2.3. Conclusion

In summary, we demonstrate for the first time, fabrication of flexible broadband photodetector on paper using ZnS-MoS$_2$ hybrid by a simple and cost effective hydrothermal method. The spectral selectivity of MoS2 has been extended to UV wavelength region, by combining MoS$_2$ with ZnS having high sensitivity towards UV light. The fabricated photodetector displays high sensitivity towards visible spectrum when compared to UV and IR. The photodetector exhibits a responsivity of 4.5 µA/W for IR, 9.4 µA/W for UV light and 17.85 µA/W for visible light. ZnS-MoS$_2$ exhibits increased responsivity due to the reduced electron-hole recombination, which is a result of the straddling type band alignment observed at the interface of ZnS-MoS$_2$. ZnS played the dual role for absorption in UV range as well as in formation of local electric fields, which are responsible for electron-hole separation in visible region. The present work provides a promising route for the development of large scale paper based broadband photodetectors using TMD hybrids at low cost; having diverse applications in the field of wearable electronics, environmental monitoring, and surveillance.

2.4. Experimental Section

Fabrication of paper-based ZnS-MoS$_2$ photodetector was carried out using two-step hydrothermal process. MoS$_2$ was grown on cellulose paper substrate followed by the growth of ZnS on MoS$_2$ grown paper.

Synthesis of MoS$_2$ on paper:

Cellulose paper as the substrate was utilized for the hydrothermal growth of MoS$_2$. The seed solution was prepared by blending 10mM of sodium molybdate (Na$_2$MoO$_4$.2H$_2$O) and 20 mM of thiourea (CH$_4$N$_2$S) in deionized (DI) water. The paper substrate was dipped in as-prepared seed solution for 1 hour followed by drying at 80°C. The nutrient solution comprising of 50 mM sodium molybdate and 100 mM thiourea was stirred in DI water for 30 mins. Thereafter, the seed coated cellulose paper and the nutrient solution was transferred to the hydrothermal reactor and was maintained at 200° for 20 hours. The reactor was allowed to cool down naturally and the resultant black colored paper was dried at 80°.

Growth of ZnS on MoS₂ paper:

In a similar manner, hydrothermal synthesis was performed for the growth of ZnS on MoS_2 paper. Zinc chloride (ZnCl2) and CH4N2S were used as the sources of Zn and S, respectively. The MoS_2 paper was immersed in a seed solution consisting of equimolar concentrations of $ZnCl_2$ and CH_4N_2S in DI water for 60 mins. The seed coated MoS_2 paper was dried in hot air oven at 80°. Subsequently, the MoS_2 paper and the nutrient solution consisting of the precursors was transferred to a Teflon-lined autoclave and was maintained at 200°C for 60 min. The resultant $ZnS\text{-}MoS_2$ obtained was washed with DI water to remove the excess ZnS and dried at 80°C.

Fabrication of photodetector:

The as grown $ZnS\text{-}MoS_2$ paper was cut into 2 cm × 0.5 cm dimension and electrical contacts were established using silver (Ag) paste. The complete schematic for two-step hydrothermal process for $ZnS\text{-}MoS_2$ on paper is as shown in Figure 1.

Materials and characterization

Sodium molybdate, Zinc chloride and Thiourea were purchased from Sigma Aldrich and were used as received for the growth of ZnS-MoS2 hybrids. The structural characteristics of the prepared hybrids were investigated using X'pert PRO X-Ray Diffraction (XRD) with Cu Ká radiation. Raman spectra were obtained from Raman spectrometer (Senterra inVia opus, Bruker) having an excitation wavelength of 532 nm. Field Emission Scanning Electron Microscopy (FESEM) analysis was performed by ZEISS Ultra-55 SEM to study morphology. UV-visible-NIR spectra was obtained using LAMBDA UV/Vis/NIR spectrophotometers (PerkinElmer). The electrical measurements were carried out with Keithley 4200 SCS instrument. The as-fabricated devices were tested for broadband photodetector application on illuminating UV, Visible and IR radiations. The lamp sources utilized for UV, Vis and IR illumination had a wavelength (ë) of 365 nm, 554 nm, and 780 nm respectively.

2.5.   References

1. [1] S. Chen, C. Teng, M. Zhang, Y. Li, D. Xie and G. Shi, A Flexible UV–Vis–NIR Photodetector based on a Perovskite/Conjugated-Polymer Composite, Advanced Materials, 2016, 28(28), 5969-5974.

2. [2] Sahatiya, P. and Badhulika, S., One-step in situ synthesis of single aligned graphene–ZnO nanofiber for UV sensing. RSC Advances, 5(100), pp.82481-82487, (2015).

3. Zhang, W., Chuu, C. P., Huang, J. K., Chen, C. H., Tsai, M. L., Chang, Y. H., ... & Li, L. J. Ultrahigh-gain photodetectors based on atomically thin graphene-MoS2 heterostructures. Scientific Reports, 2014, 4.

4. D.B. Velusamy, M. Haque, M.R. Parida, F. Zhang, T. Wu, O.F. Mohammed and H.N. Alshareef, 2D Organic–Inorganic Hybrid Thin Films for Flexible UV–Visible Photodetectors, Advanced Functional Materials, 2017, 1605554.

5. L. Wang, J. Jie, Z. Shao, Q. Zhang, X. Zhang, Y. Wang, Z. Sun and S.T. Lee, MoS2/Si Heterojunction with Vertically Standing Layered Structure for Ultrafast, High-Detectivity, Self-Driven Visible–Near Infrared Photodetectors, Advanced Functional Materials, 2015, 25(19), 2910-2919.

6. I. Sharma and B.R. Mehta, Enhanced charge separation at 2D MoS2/ZnS heterojunction: KPFM based study of interface photovoltage, Applied Physics Letters, 2017, 110(6), 061602.

7. S.P. Vattikuti, C. Byon and S. Jeon, Enhanced photocatalytic activity of ZnS nanoparticles loaded with MoS2 nanoflakes by self-assembly approach, Physica B: Condensed Matter, 2016, 502, 103-112.

8. X. Fang, Y. Bando, M. Liao, U.K. Gautam, C. Zhi, B. Dierre, B. Liu, T. Zhai, T. Sekiguchi, Y. Koide and D. Golberg, Single-crystalline ZnS nanobelts as ultraviolet-light sensors. Advanced Materials, 2009, 21(20), 2034-2039.

9. Q. Li and C. Wang, Fabrication of wurtzite ZnS nanobelts via simple thermal evaporation, Applied Physics Letters, 2003, 83(2), 359-361.

10. X. Fang, Y. Bando, M. Liao, T. Zhai, U.K. Gautam, L. Li, Y. Koide and D. Golberg, An efficient way to assemble ZnS nanobelts as ultraviolet-light sensors with enhanced photocurrent and stability. Advanced Functional Materials, 2010, 20(3), 500-508.

11. R.M. Clark, B.J. Carey, T. Daeneke, P. Atkin, M. Bhaskaran, K. Latham, I.S. Cole and K. Kalantar-Zadeh, Two-step synthesis of luminescent MoS 2–ZnS hybrid quantum dots. Nanoscale, 2015, 7(40), 16763-16772.

12. K. Pramoda, M. Kaur, U. Gupta and C.N.R. Rao, Nanocomposites of 2D-MoS2 nanosheets with the metal–organic framework, ZIF-8, Dalton Transactions, 2016, 45(35), 13810-13816.

13. J. Liu, H.G. Zhang, J. Wang, J. Cho, J.H. Pikul, E.S. Epstein, X. Huang, J. Liu, W.P. King and P.V. Braun, Hydrothermal Fabrication of Three-Dimensional Secondary Battery Anodes. Advanced Materials, 2014, 26(41), 7096-7101.

14. Sahatiya, P., Gomathi, P.T., Jones, S.S. and Badhulika, S., Flexible substrate based 2D ZnO (n)/graphene (p) rectifying junction as enhanced broadband photodetector using strain modulation. *2D Materials,* 2017, 4 025053.

15. Liu, H., Sun, Q., Xing, J., Zheng, Z., Zhang, Z., Lü, Z. and Zhao, K., Fast and enhanced broadband photoresponse of a ZnO nanowire array/reduced graphene oxide film hybrid photodetector from the visible to the near-infrared range. ACS Applied Materials & Interfaces, 2015, 7(12), pp.6645-6651.

16. Kufer, D., Nikitskiy, I., Lasanta, T., Navickaite, G., Koppens, F.H. and Konstantatos, G., Hybrid 2D–0D MoS2–PbS quantum dot photodetectors. Advanced Materials, 2015, 27(1), pp.176-180.

17. J. Liu, C. Yang, H. Wu, Z. Lin, Z. Zhang, R. Wang, B. Li, F. Kang, L. Shi and C.P. Wong, Future paper based printed circuit boards for green electronics: fabrication and life cycle assessment. Energy & Environmental Science, 2014, 7(11), 3674-3682.

18. A. Manekkathodi, M.Y. Lu, C.W. Wang and L.J. Chen, Direct growth of aligned zinc oxide nanorods on paper substrates for low-cost flexible electronics, Advanced Materials, 2010, 22(36), 4059-4063.

19. Soares, S., Camino, G., & Levchik, S. Comparative study of the thermal decomposition of pure cellulose and pulp paper. Polymer Degradation and Stability, 1995, 49(2), 275-283.

20. Jiang, P., Zhu, C.N., Zhu, D.L., Zhang, Z.L., Zhang, G.J. and Pang, D.W., A room-temperature method for coating a ZnS shell on semiconductor quantum dots. Journal of Materials Chemistry C, 2015, 3(5), pp.964-967.

21. Li, X.L. and Li, Y.D., MoS2 nanostructures: synthesis and electrochemical Mg2+ intercalation. The Journal of Physical Chemistry B, 2004, 108(37), pp.13893-13900.

22. J. Xie, J. Zhang, S. Li, F. Grote, X. Zhang, H. Zhang, R. Wang, Y. Lei, B. Pan and Y. Xie, Controllable disorder engineering in oxygen-incorporated MoS2 ultrathin nanosheets for efficient hydrogen evolution, Journal of the American Chemical Society, 2013, 135(47), 17881-17888.

23. X. Wang, Z. Zhang, Y. Chen, Y. Qu, Y. Lai and J. Li, Morphology-controlled synthesis of MoS2 nanostructures with different lithium storage properties, Journal of Alloys and Compounds, 2014, 600, 84-90.

24. K.D. Rasamani, F. Alimohammadi and Y. Sun, Interlayer-expanded MoS2, Materials Today, 2016.

25. W. Wang, L. Li, K. Wu, G. Zhu, S. Tan, W. Li and Y. Yang, Hydrothermal synthesis of bimodal mesoporous MoS2 nanosheets and their hydrodeoxygenation properties, RSC Advances, 2015, 5(76), 61799-61807.

26. L. Chai, J. Du, S. Xiong, H. Li, Y. Zhu and Y. Qian, Synthesis of wurtzite ZnS nanowire bundles using a solvothermal technique, The Journal of Physical Chemistry C, 2007, 111(34), 12658-12662.

27. S. Egusa, S. Yokota, K. Tanaka, K. Esaki, Y. Okutani, Y. Ogawa, T. Kitaoka, M. Goto and H. Wariishi, Surface modification of a solid-state cellulose matrix with lactose by a surfactant-enveloped enzyme in a nonaqueous medium, Journal of Materials Chemistry, 2009, 19(13), 1836-1842.

28. Q. Xiong, J. Wang, O. Reese, L.C. Lew Yan Voon and P.C. Eklund, Raman scattering from surface phonons in rectangular cross-sectional w-ZnS nanowires, Nano Letters, 2004, 4(10), 1991-1996.

29. G.L. Frey, R. Tenne, M.J. Matthews, M.S. Dresselhaus and G. Dresselhaus, Raman and resonance Raman investigation of MoS2 nanoparticles, Physical Review B, 1999, 60(4), 2883.

30. X. Zhang, W.P. Han, J.B. Wu, S. Milana, Y. Lu, Q.Q. Li, A.C. Ferrari and P.H. Tan, Raman spectroscopy of shear and layer breathing modes in multilayer MoS2, Physical Review B, 2013, 87(11), 115413.

31. K.K. Liu, W. Zhang, Y.H. Lee, Y.C. Lin, M.T. Chang, C.Y. Su, C.S. Chang, H. Li, Y. Shi, H. Zhang and C.S. Lai, Growth of large-area and highly crystalline MoS2 thin layers on insulating substrates, Nano Letters, 2012, 12(3), 1538-1544.

32. H. Li, K. Yu, X. Lei, B. Guo, H. Fu and Z. Zhu, Hydrothermal synthesis of novel MoS2/BiVO4 hetero-nanoflowers with enhanced photocatalytic activity and a mechanism investigation, The Journal of Physical Chemistry C, 2015, 119(39), 22681-22689.

33. X. Zhao, C. Hu and M. Cao, Three-Dimensional MoS2 Hierarchical Nanoarchitectures Anchored into a Carbon Layer as Graphene Analogues with Improved Lithium Ion Storage Performance, Chemistry–An Asian Journal, 2013, 8(11), 2701-2707.

34. L. Hu, Y. Ren, H. Yang and Q. Xu, Fabrication of 3D hierarchical MoS2/polyaniline and MoS2/C architectures for lithium-ion battery applications, ACS Applied Materials & Interfaces, 2014, 6(16), 14644-14652.

35. J. Zhao and R. Liu, Surfactant-free hydrothermal synthesis and optical properties of ZnS solid microspheres, Materials Letters, 2014, 124, 239-241.

36. M. Muruganandham and Y. Kusumoto, Synthesis of N, C codoped hierarchical porous microsphere ZnS as a visible light-responsive photocatalyst, The Journal of Physical Chemistry C, 2009, 113(36), 16144-16150.

37. Chitara, B., Panchakarla, L. S., Krupanidhi, S. B., & Rao, C. N. R. Infrared photodetectors based on reduced graphene oxide and graphene nanoribbons. Advanced Materials, 2011, 23(45), 5419-5424.

38. Lim, Y. R., Song, W., Han, J. K., Lee, Y. B., Kim, S. J., Myung, S., & Lim, J. Wafer-Scale, Homogeneous MoS2 Layers on Plastic Substrates for Flexible Visible-Light Photodetectors. Advanced Materials, 2016, 28(25), 5025-5030.

39. P. Sahatiya, S.K. Puttapati, V.V. Srikanth and S. Badhulika, Graphene-based wearable temperature sensor and infrared photodetector on a flexible polyimide substrate, Flexible and Printed Electronics, 2016, 1(2), 025006.

40. Lopez-Sanchez, O., Lembke, D., Kayci, M., Radenovic, A., & Kis, A. Ultrasensitive photodetectors based on monolayer MoS2. Nature Nanotechnology, 2013, 8(7), 497-501.

41. Lee, K., Kim, H.Y., Lotya, M., Coleman, J.N., Kim, G.T. and Duesberg, G.S., Electrical characteristics of molybdenum disulfide flakes produced by liquid exfoliation. Advanced Materials, 2011, 23(36), pp.4178-4182.

42. Tao, Y., Wu, X., Wang, W., & Wang, J. Flexible photodetector from ultraviolet to near infrared based on a SnS2 nanosheet microsphere film. Journal of Materials Chemistry C, 2015, 3(6), 1347-1353.

43. Lu, M. Y., Song, J., Lu, M. P., Lee, C. Y., Chen, L. J., & Wang, Z. L. ZnO− ZnS heterojunction and ZnS nanowire arrays for electricity generation. ACS Nano, 2009, 3(2), 357-362.

44. Lee, K., Kim, H. Y., Lotya, M., Coleman, J. N., Kim, G. T., & Duesberg, G. S. Electrical characteristics of molybdenum disulfide flakes produced by liquid exfoliation. Advanced Materials, 2011, 23(36), 4178-4182.

45. Nazir, G., Khan, M. F., Akhtar, I., Akbar, K., Gautam, P., Noh, H., & Eom, J. Enhanced photoresponse of ZnO quantum dot-decorated MoS 2 thin films. RSC Advances, 2017, 7(27), 16890-16900.

46. Z. Zheng, T. Zhang, J. Yao, Y. Zhang, J. Xu and G. Yang, Flexible, transparent and ultra-broadband photodetector based on large-area WSe2 film for wearable devices.

Nanotechnology, 2016, 27(22), 225501.

47. K. Heo, H. Lee, Y. Park, J. Park, H.J. Lim, D. Yoon, C. Lee, M. Kim, H. Cheong, J. Park and J. Jian, Aligned networks of cadmium sulfide nanowires for highly flexible photodetectors with improved photoconductive responses. Journal of Materials Chemistry, 2012, 22(5), 2173-2179.

48. De Fazio, D., Goykhman, I., Yoon, D., Bruna, M., Eiden, A., Milana, S., Sassi, U., Barbone, M., Dumcenco, D., Marinov, K. and Kis, A., High Responsivity, Large-Area Graphene/MoS2 Flexible Photodetectors. ACS Nano, 2016, 10(9), pp.8252-8262.

49. Zhou, X., Gan, L., Zhang, Q., Xiong, X., Li, H., Zhong, Z., Han, J. and Zhai, T., High performance near-infrared photodetectors based on ultrathin SnS nanobelts grown via physical vapor deposition. Journal of Materials Chemistry C, 2016, 4(11), pp.2111-2116.

50. Zhu, H., Xiao, Z., Liu, D., Li, Y., Weadock, N.J., Fang, Z., Huang, J. and Hu, L., Biodegradable transparent substrates for flexible organic-light-emitting diodes. Energy & Environmental Science, 2013, 6(7), pp.2105-2111.

51. Aga, R. S., Lombardi, J. P., Bartsch, C. M., & Heckman, E. M. Performance of a printed photodetector on a paper substrate. IEEE Photonics Technology Letters, 2014, 26(3), 305-308.
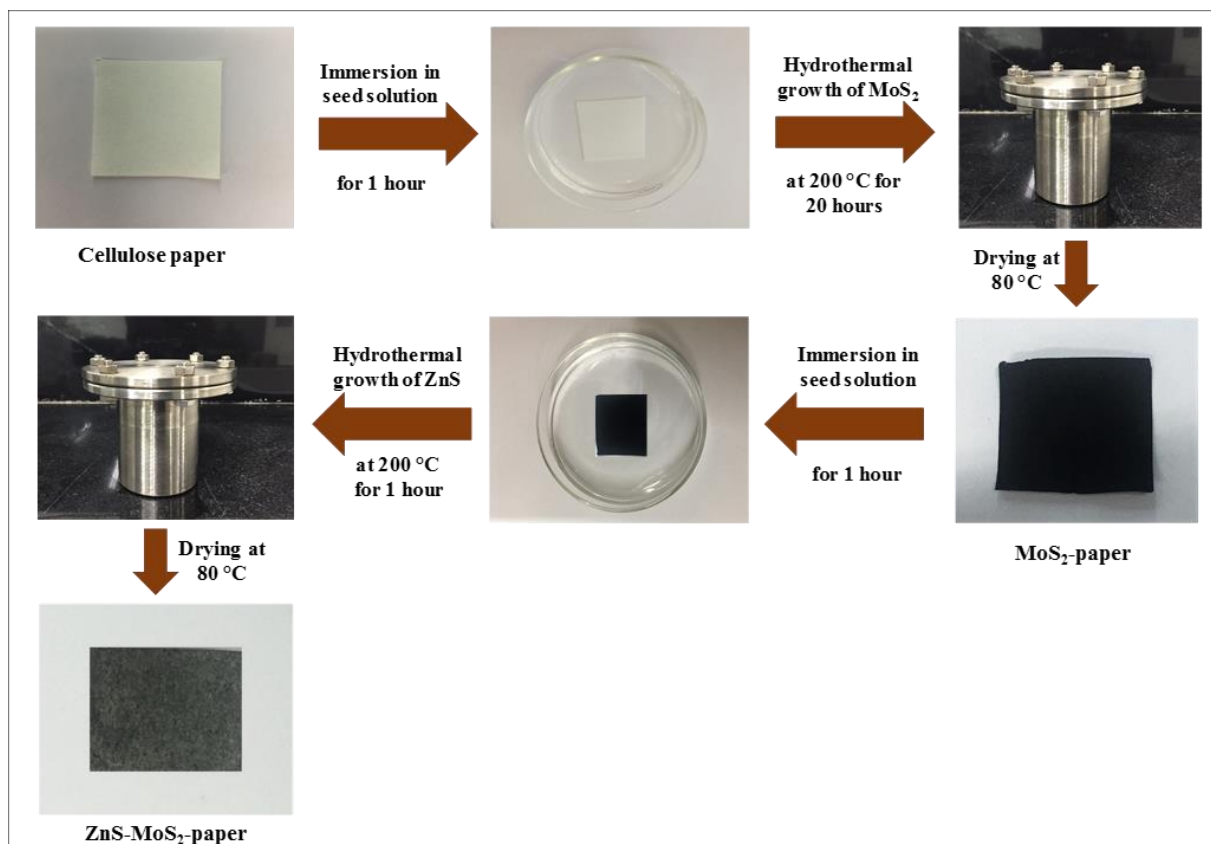
Figure 2.1. Schematic of the two-step hydrothermal process followed for the fabrication of ZnS-MoS$_2$ broadband photodetector.
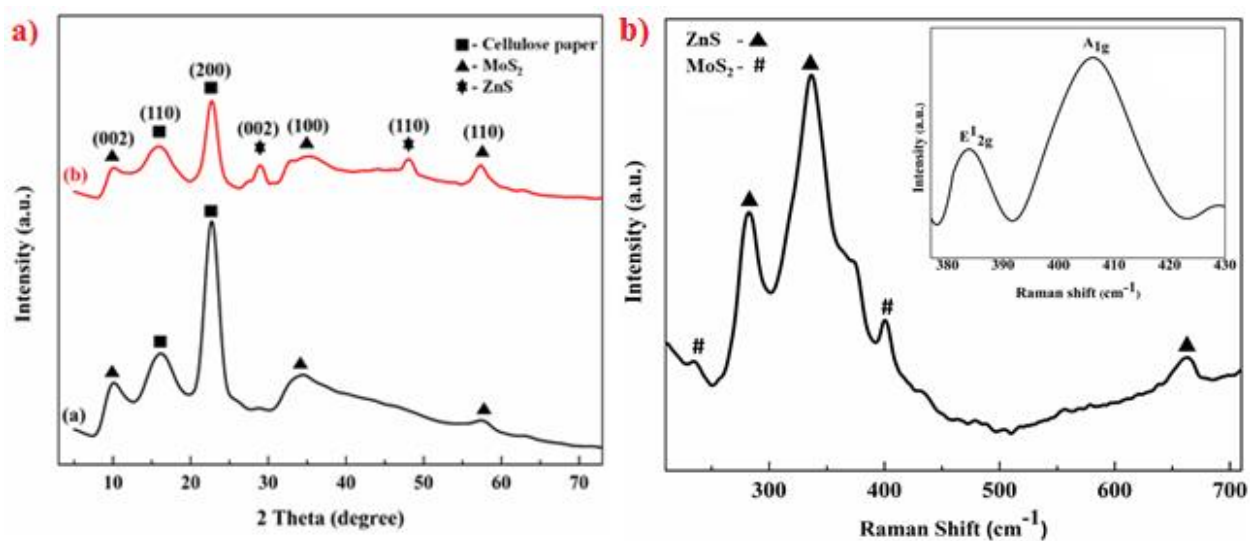
Figure 2.2. a) XRD graph of ZnS-MoS$_2$ hybrids b) Raman spectra of ZnS-MoS$_2$ hybrids (inset is the Raman spectra of pristine MoS$_2$).
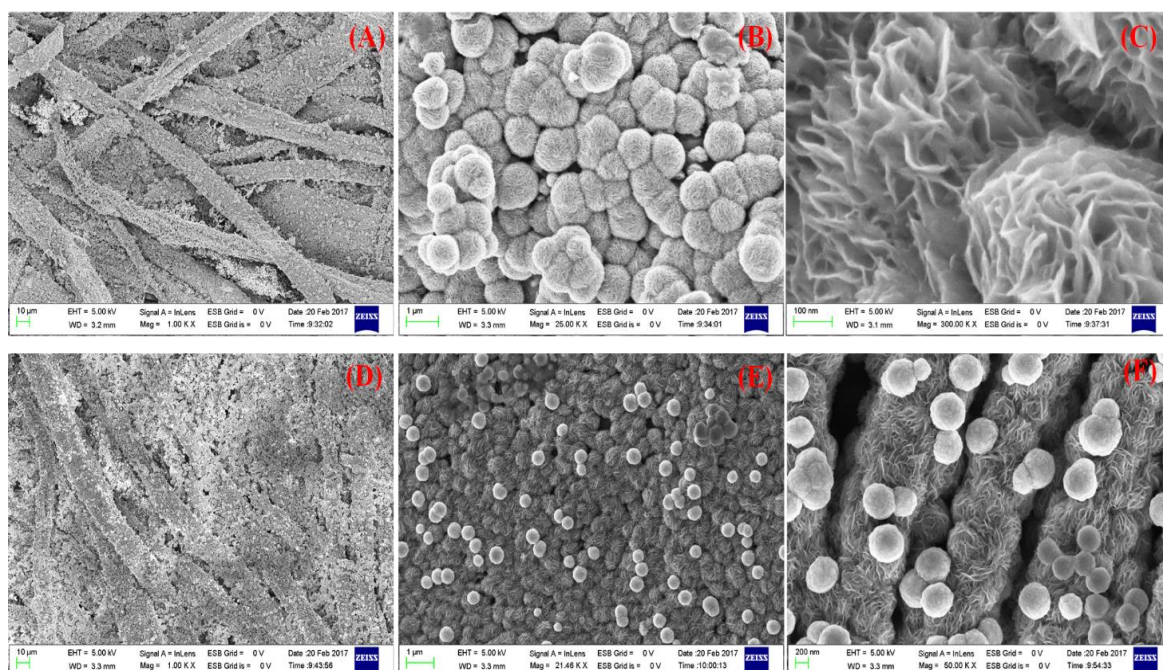
Figure 2.3. FESEM images of a) MoS$_2$ grown on cellulose paper b) MoS$_2$ grown on cellulose paper exhibiting micro flower like structure c) higher magnification MoS$_2$ on cellulose paper d) ZnS on MoS$_2$-cellulose paper e) ZnS on MoS$_2$-cellulose paper exhibiting microspheres like morphology f) higher magnification ZnS on MoS$_2$-cellulose paper.
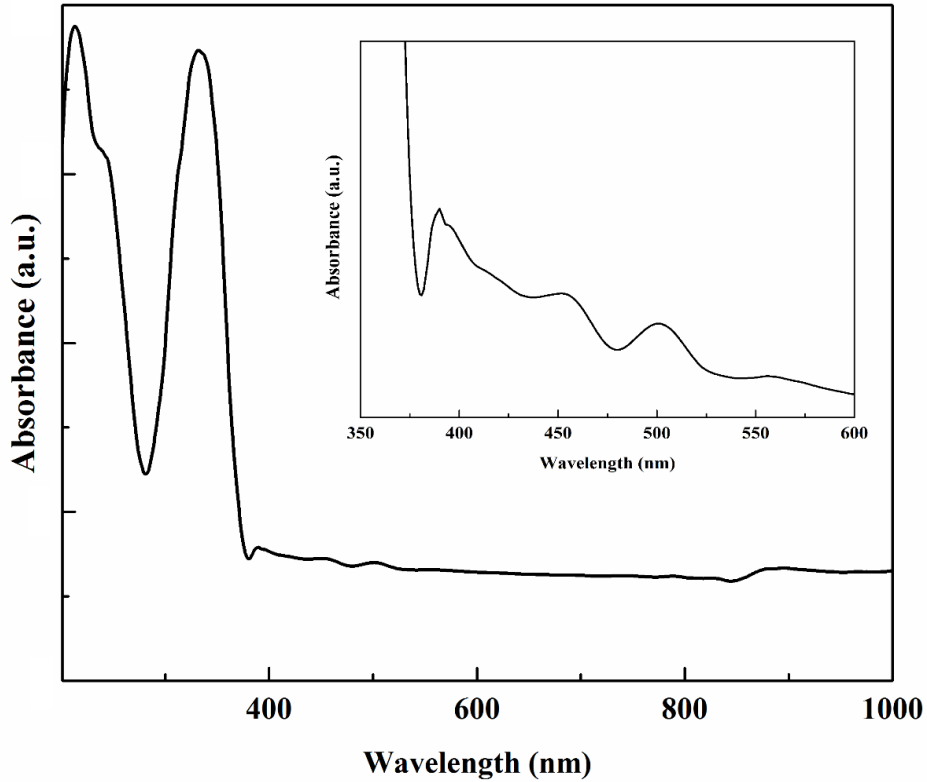

Figure 2.4. UV-visible-NIR spectra of ZnS/MoS$_2$ showing strong absorption in UV range and weak absorption in visible and near NIR range. Inset is the plot showing absorbance in visible and NIR by scaling down the intensity values clearly demonstrating absorbance in visible and NIR range.
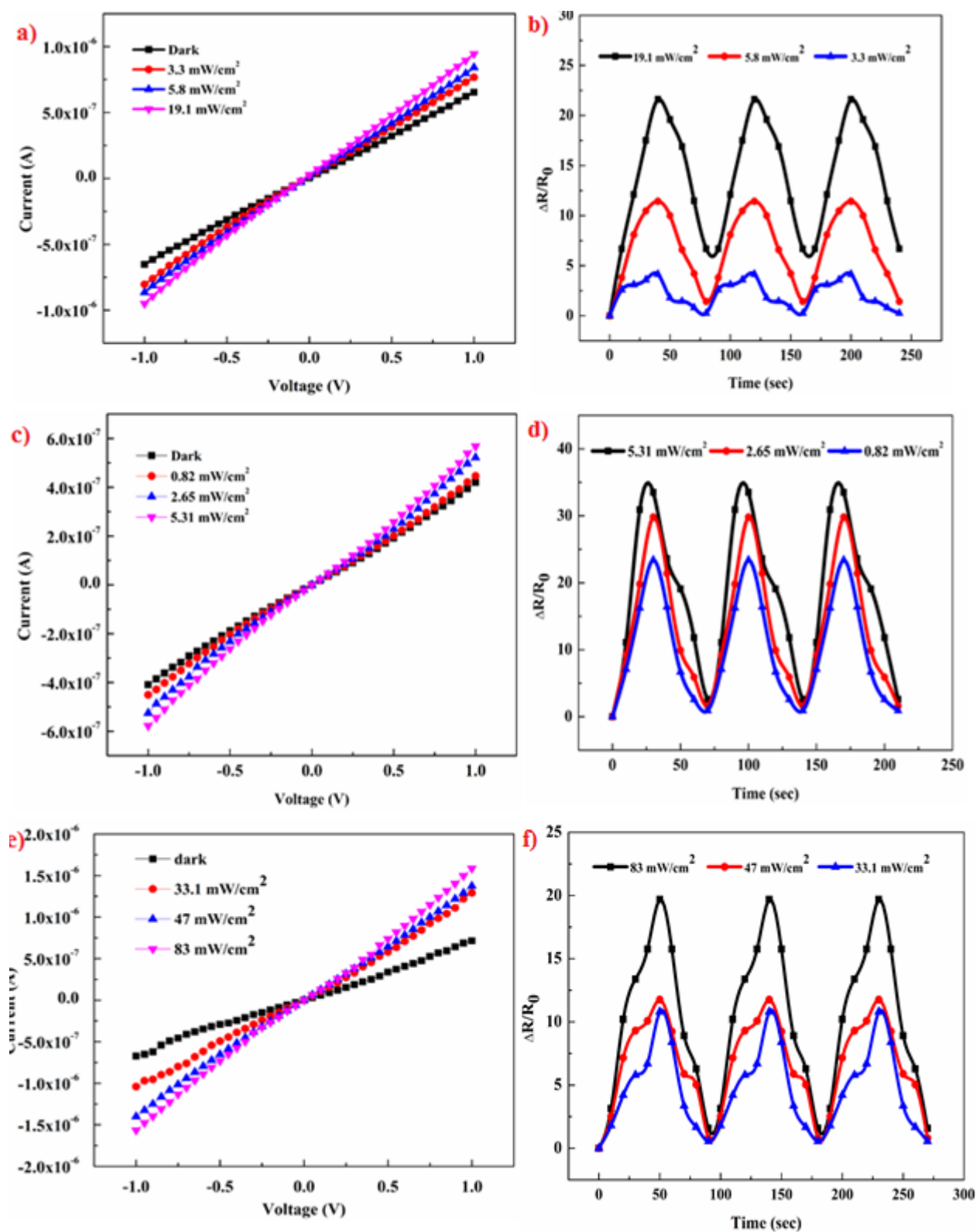
Figure 2.5. a, c and d) I-V characteristics of ZnS-MoS$_2$ for UV, visible and IR respectively showing increasing in photocurrent with increase in intensity b, d and f) temporal response

of ZnS-MoS$_2$ towards UV, visible and IR respectively inferring the sensor is more sensitive towards visible light when compared to UV and IR illumination.
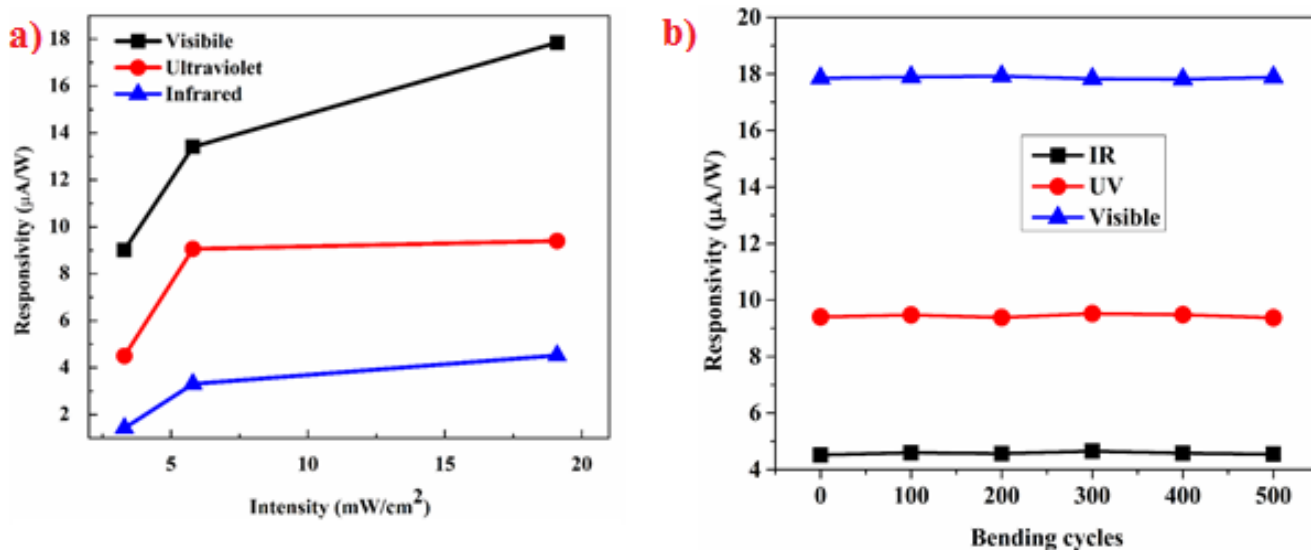

Figure 2.6. Responsivity graph of the fabricated photodetector for UV, Visible and IR illumination suggesting highest responsivity for visible light b) Graph of responsivity v/s bending cycles wherein no notable change was observed in responsivity with bending cycles. Responsivity was measured for 19.1 mW/cm^2 intensity.
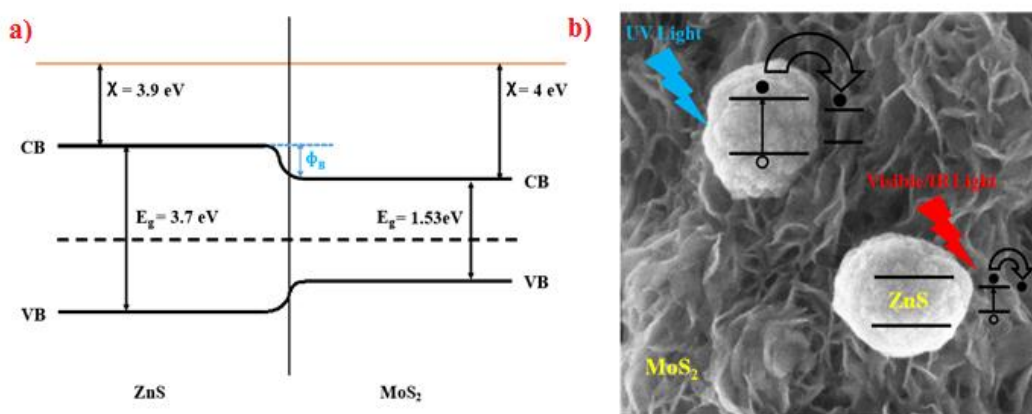

Figure 2.7. a) Energy band diagram of ZnS-MoS$_2$ interface and b) Schematics of charge transfer mechanism occurring in ZnS-MoS$_2$ under photo illumination.

31

Chapter 3

Discretely distributed 1D V$_2$O$_5$ nanowires over 2D MoS$_2$ nanoflakes for enhanced broadband photodetector covering Ultraviolet to Near Infrared region

Abstract

While most reports on photodetectors focus on improving the responsivity in one region of electromagnetic spectrum by fabricating 2D materials hybrids, the main issue still remains unaddressed which is the inability to absorb wide range of electromagnetic spectrum. Most photodetectors comprise of p-n heterojunction, where one of the material is responsible for absorbance, having metal contacts on p and n type allows for effective separation of photogenerated carriers. But for a broadband photodetector, both the materials of the heterojunction should participate in the absorbance. In such a case, metal contacts on p and n type will trap either the photogenerated electrons or hole which leads to the failure of the device. In this work, discrete distribution of 1D V$_2$O$_5$ nanowires over 2D MoS$_2$ and metal contacts on MoS$_2$ combinedly enables the device to absorb from ultraviolet to near Infrared region (365 nm to 780nm) wherein V$_2$O$_5$ is responsible for UV-visible absorbance and MoS$_2$ absorbs in visible-NIR. Further, taking advantage of local heterojunctions of MoS$_2$-V$_2$O$_5$ for effective separation of photogenerated carriers enables for efficient charge transfer, faster electron transfer rate and highly responsive photodetection. Responsivity of the fabricated device was calculated to be 41.5 mA/W, 65.1 mA/W and 29.4 mA/W for UV, visible and NIR illumination suggesting the device to be more responsive in visible region

and was found to be comparable with the photodetectors fabricated using sophisticated cleanroom techniques.. The method provides a new strategy for improving the absorbance range of photodetector by discrete distribution of 1D materials over 2D materials which finds tremendous potential applications in the field of optoelectronics, sensors and photodetectors.

3.1.   Introduction

Flexible photodetectors with a broad spectral range starting from the Ultra violet(UV) to the Near Infrared (NIR) find widespread applications in areas such as optoelectronics, sensors, communication and surveillance [1-2]. However majority of them aim at improving the responsivity in a particular region or wavelength which is achieved by fabricating heterojunctions with different kinds of low dimensional materials (such as 0D, 1D and 2D) [3-5]. The major issue of a photodetector which is the inability to absorb wider region of electromagnetic spectrum still remains a challenge mainly due to the lack of synthesizing suitable hybrids which can absorb from UV to NIR. The other issue is improper device fabrication where the placement of metal electrodes play an important role in collecting the photogenerated carriers. Most photodetectors comprise of p-n heterojunction, where one of the material is responsible for absorbance, having metal contacts on p and n type allows for effective separation of photogenerated carriers. The built in electric field at the potential barrier of the heterojunction is responsible for effective separation of photogenerated carriers. But for a broadband photodetector, both the materials of the heterojunctions should participate in the absorbance. In such a case, metal contacts on p and n type will trap the either photogenerated electrons or hole which leads to the failure of the device. Hence there is an urgent need to synthesize hybrid materials and suitable device fabrication technique which demonstrates both high responsivity and broadband absorbance.

Two-dimensional (2D) layered materials have attracted interest in the area of nanoelectronics due to their remarkable electronic and material properties. [6] Among various Transition metal dichalcogenides (TMDs), Molybdenum disulfide (MoS_2) two has a bandgap of 1.3 to 1.8 eV for bulk and monolayer MoS_2 with a possibility of achieving intermediate bandgap by tuning the layers of MoS_2 thereby possessing better electronic properties when compared to other 2D materials such as graphene. [7] The optical bandgap energy tuned by the thickness modulation of 2D materials have shown excellent photo catalysis applications in the area of broadband photodetector [8]. Various methods of the synthesis of MoS_2 nanostructures have been reported which include Chemical Vapor

Deposition (CVD), [9] exfoliation [10] and hydrothermal method [3]. Among them, hydrothermal method is suitable for large scale deposition of few layered MoS_2 on any arbitrary substrate of choice which can withstand 200°C. Fabricating heterojunctions of MoS_2 with different low dimensional semiconductors results in heterojunction with efficient charge separation, broadband absorption and high electron transfer rate. There are reports on hybrids of MoS_2 with other 2D [3], 1D [4] and 0D [11] materials for photodetector applications. Among all the hybrids, 2D-1D hybrid is suitable for broadband photodetector because of the formation of large area heterojunction when compared to 2D and 0D materials. Large area heterojunction creates potential barriers in majority portion of the photodetector thereby increasing the effective separation of photogenerated carriers.

Transition metal oxides such as vanadium oxides family find wide applications in electronics due to their reversible phase transitions from metals to semiconductors. [12] Particularly, Vanadium Pentaoxide (V_2O_5) from vanadium oxides family has gained a lot of attention because of its direct bandgap of 2.2 to 2.8eV which makes it potential candidate for optoelectronic and photoelectric applications [13] However synthesis of V_2O_5 is a challenging task because of its affinity to exist in different oxidation states. There are several methods available for synthesis of 1D V_2O_5 nanostructures such as CVD, [14] electrochemical deposition [15] and electrospinning. [16] Among these methods, electrospinning is a simple and low cost method for synthesizing 1D V_2O_5 nanowires on a wide variety of substrates on a large scale with easy controllability and precise positioning. Combining 2D MoS_2 with 1D V_2O_5 would be a step forward in the fabrication of novel broadband photodetectors which not only widen the range of absorbance in the electromagnetic spectrum but also increases the responsivity of the photodetector.

Here, we demonstrate for the first time, the fabrication of flexible broadband photodetector (UV-NIR) by using novel 2D MoS_2-1D V_2O_5 heterostructure wherein MoS_2 was grown directly on Al foil using hydrothermal method followed by spin coating of electrospun V_2O_5 nanowires to form heterojunction of 2D MoS_2-1D V_2O_5. Due to absorbance of both V_2O_5 nanowires and 2D MoS_2 in visible regions, the fabricated photodetector displayed higher responsivity in visible region when compared to UV and NIR. Discrete distribution of 1D-V_2O_5 nanowires over 2D-MoS_2 nanoflakes allows for broadband absorbance wherein V_2O_5 is responsible for UV-visible absorbance and MoS2 absorbs in visible-NIR. Further, fabricating contacts on 2D MoS_2 allows for effective collection of photogenerated carriers thereby avoiding recombinations and traps. To the best of our knowledge, this report is a

first demonstration of flexible 2D-1D hybrid structure for broadband photodetector covering UV to NIR region with high responsivity.

3.2.   Results and Discussions

2D MoS2 has been known for its broadband absorption from visible to NIR region. [3] Combining UV absorbing material with MoS_2 would lead to hybrid material which can increase the absorbance from UV to NIR wherein the UV absorbing materials should be discretely placed such that both MoS2 and the hybrid material are exposed to the light illumination. 1D V_2O_5 is an ideal choice as it is known to have broadband absorbance from UV to visible. Moreover 2D-1D structures have inherent advantage compared to 2D-2D and 2D-0D structure in formation of large area potential barriers which increases the responsivity of the photodetector. The key essence of such a hybrid is that both the materials are exposed to illumination such that both participate in the generation of photogenerated carriers. If a hybrid material is deposited uniformly over the base material then the absorbance of the base material would be affected leading to failure of the device working as broadband photodetector. In this work, 2D MoS_2 was grown directly on Al foil using hydrothermal method and 1D V2O5 nanowires, synthesized using electrospinning were spin coated on MoS2-Al foil wherein the parameters were tuned to obtain discrete distribution of V_2O_5 nanowires over 2D MoS_2. Details regarding the synthesis and fabrication of the photodetector can be found in supplementary information (SI). Schematics demonstrating the synthesis and fabrication procedure is as shown in figure 3.1.

To study the crystal structure of the synthesized MoS_2 and V_2O_5, XRD analysis was performed. Figure 3.2a shows the XRD spectrum of MoS_2-V_2O_5 wherein different diffraction peaks corresponding to both MoS_2 and V_2O_5 were observed. Predominant peak of V_2O_5 was observed at 26.3° which corresponds to (110) plane. [17] Furthermore, other reflection peaks were observed at 15.3°, 20.2°, 21.7°, 31.1°, 32.3°, 34.3°, 41.3° and 44.4° corresponds to (200), (001), (101), (301), (011), (310), (002) and (501) respectively corresponds to the orthorhombic phase of V_2O_5 nanowire (JCPDS card No. 00-041-1426). [18] The peaks reveal highly crystalline nature of V_2O_5 nanowires which can be attributed to the calcination temperature of 400°C. Apart from that, diffraction peak at 11.3° was observed which corresponds to (002) plane of MoS_2. [3] The other wide peak of MoS_2 occur at 31°-34° but due to the presence of prominent peaks of V_2O_5, the peaks of MoS_2 are suppressed and hence not visible. The diffraction peaks of MoS_2 matches with JCPDS Card No. 37-1492. Peaks at 45.7°, 52.3° and 62.4° corresponds to reflection peaks of Al

corresponding to (111), (116) and (210) planes. [19] The presence of diffraction peaks of Al foil suggest that the Al foil substrate did not degrade during hydrothermal process.

To further confirm the formation of 2D MoS_2 and 1D V_2O_5, Raman spectroscopy was performed wherein distinct peaks for MoS_2 and V_2O_5 were observed. Figure 3.2b shows the Raman spectra of pristine V_2O_5 and V_2O_5 deposited on MoS_2.The vibrations at 145 and 195cm^{-1} are due to the VO5 - VO5 modes [20]. Peak at 994 cm^{-1} corresponds to the doubly coordinated oxygen bonds (V=O) and 694 cm^{-1} peak can be attributed to triply coordinated oxygen bonds due to the stretching modes at atomic level. The Raman peak at 490 cm^{-1} corresponds to the stretching mode of V-O3-V and the bending vibration of the V=O bonds are observed at 284 and 407 cm^{-1} modes [21] thereby confirming the formation of V_2O_5 nanowires. The Raman spectra of MoS_2-V_2O_5 has two additional peaks at 383 and 405 cm^{-1} which corresponds to E12g and A1g mode respectively wherein E12gmode arises due to the in-plane vibrations of sulfur atoms with respect of molybdenum atoms and A1g mode arises due to the out-of-plane vibrations of sulfur atoms in opposite direction. Further, the frequency separation between the E12g and A1g mode provides information regarding the number of layers of MoS_2. In this case, the frequency separation between the peaks was 22 cm^{-1} which suggest that the as grown MoS_2 comprised of few layer MoS_2 (less than 4 layers) [3]. The extra peaks at 111 cm^{-1} and 244 cm^{-1} can be attributed to the â phase of V_2O_5 which might be induced due to the vigorous stirring of V_2O_5 in DMF [22]. Figure 3.2c shows the Raman spectra of pristine MoS_2 wherein the E12g and A1g are clearly observed with the frequency separation of 22 cm^{-1}. The defects in MoS_2 can be quantified by the Raman spectroscopy wherein the broadening of the E12g and A1g peaks with the respective shifts is an indication of the defects in MoS_2 [23]. In this case, E12g and A1g peak broadening was observed suggesting that the as grown MoS_2 on Al foil possess defects.

To study the morphology of the as grown MoS_2 and the electrospun V_2O_5 nanowires FESEM analysis were performed. Figure 3.3a shows the low magnification FESEM image of MoS_2 grown on Al foil wherein microsphere like morphology was observed. The growth of MoS_2 on Al foil was uniform over large area of 3cm x 3cm. Figure 3.3b,c shows the high magnification FESEM of MoS_2 wherein individual MoS_2 nanoflakes were observed which aggregate to form MoS_2 microspheres. Figure 3.3d shows low magnification FESEM image of 1D V_2O_5 nanowires discretely distributed over 2D MoS_2 nanoflakes wherein both MoS_2 and V_2O_5 are visible. This is necessary for broadband absorbance as both the functional material would be exposed to the illumination. Figure 3.3e,f shows the high magnification FESEM image of 1D V_2O_5 distribution over MoS_2 where 1D V_2O_5 covers majority area of

2D MoS$_2$ which suggests the creation of large area potential barriers which are important for effective separation of photogenerated carriers.

To further utilize the 2D MoS$_2$-1D V$_2$O$_5$ hybrid for broadband photodetector, absorbance spectra for individual materials was obtained using UV-Visible-NIR spectroscopy wherein the UV-vis-NIR spectrum of 1D V$_2$O$_5$ nanowires where its exhibits strong absorbance in UV range (220-360 nm) where as weak absorption at visible region. Strong peak at around 300 nm can be attributed to the charge transfer associated with V^{5+} and O^{2-} which corresponds to the UV absorbance of the V$_2$O$_5$ [24]. There is an absorbance observed at the start of the visible spectrum at ~420 to 500nm which suggest that synthesized V$_2$O$_5$ nanowires can be utilized as broadband photodetector covering UV and visible range. Optical bandgap of synthesized V$_2$O$_5$ was calculated to be 2.4 eV using Tauc's plot which is consistent with previously reported literature [24]. Further, the absorbance spectra of 2D MoS$_2$ was measured wherein two absorptions bands were observed in the range of 400 to 500 nm and weak absorption in NIR range which further suggest that MoS$_2$ can be utilized as broadband photodetector from visible to NIR region. Optical bandgap of synthesized MoS$_2$ was calculated to be 1.53 eV. If both the materials are exposed to illumination and engineered to collect the photogenerated carriers then 2D MoS$_2$-1D V$_2$O$_5$ hybrid can be utilized as a broadband photodetector covering wide range from UV to NIR. Graphs showing the UV-vis-NIR spectra of V$_2$O$_5$ and MoS$_2$ and their corresponding Tauc plots can be found in Appendix A as figure S3.

To study the electronic properties of the fabricated MoS$_2$-V$_2$O$_5$ device, I-V characteristics were obtained in the range of -1V to 1V wherein results revealed ohmic contact. It should be noted that even though V$_2$O$_5$ nanowires are distributed over MoS$_2$, contacts were taken from MoS$_2$. This is important to collect the photogenerated charge carriers from both MoS$_2$ and V$_2$O$_5$. If the contacts were taken from V$_2$O$_5$, photogenerated holes from V$_2$O$_5$ would be trapped in V$_2$O$_5$ leading to the degradation of the device performance. Photographic images of MoS$_2$ grown on Al foil and the masked device for defining metal contact area can be found in Appendix A as figure S4. Prior to the photodetection experiments, devices were kept in dark for 12 hours so as to stabilize them. UV lamp (365 nm), visible (554 nm) and NIR (780 nm) were used for illumination. Figure 3.4a shows the I-V characteristic of MoS$_2$-V$_2$O$_5$ device wherein increment in the current with increasing intensity of UV light was observed. This can be attributed to the increase in the number of photogenerated charge carriers in V$_2$O$_5$ with increase in the intensity. In this case, V$_2$O$_5$ is UV responsive and MoS$_2$ is responsive to visible and NIR. Similar measurements were performed for visible and NIR

region and similar results were obtained wherein increasing the intensity of illumination increases the photocurrent as shown in figure 4c and figure 4e. Figure 3.4b shows the temporal response of fabricated device under different intensities of UV illuminations for 3 cycles wherein the illumination was switched "ON" and "OFF" at repeated intervals.61 % increment in the normalized resistance was observed for the highest intensity (1.1 mW/cm^2). Similar temporal studies were performed for visible and NIR illumination for different intensities as shown in figure 3.4d and figure 4f. 118 % increment was observed for visible illumination (3.1 mW/cm^2) and 31 % increment was observed for NIR illumination (4.4 mW/cm^2) thereby suggesting that the fabricated device was more sensitive to visible illumination as compared to UV and NIR illumination. This can be attributed to the fact that both MoS_2 and V_2O_5 have absorption in visible region thereby generating more photogenerated carriers under visible illumination. It should be noted that the response of the device is slow which can be attributed to the defects introduced in MoS_2 during hydrothermal growth as quantified by Raman spectroscopy.

Responsivity and external quantum efficiency are the important parameters of a photodetector in terms of performance and figure of merit. Responsivity is the measure of the photocurrent generated per unit power of incident light per area and External Quantum efficiency (EQE) which is the number of electrons produced per incident photon and are given by the following equations [26].

$$R_\lambda = \frac{I_\lambda}{P_\lambda \times A}$$

$EQE = hc \, X \, R_\lambda \, /e\lambda$

Figure 3.5a shows the responsivity of the fabricated device under UV, visible and NIR illumination at different intensities wherein highest responsivity was observed for visible light further suggesting the fabricated device was more responsive towards visible light when compared to UV and NIR illumination. Figure 3.5b shows the EQE values of the fabricated device with different intensities. Figure showing the spectral response can be found in Appendix as figure S5. The reason for the higher responsivity towards visible illumination may be attributed to the fact that both MoS_2 and V_2O_5 have absorption in visible region as evident from absorbance spectra. Hence in visible region, both MoS_2 and V_2O_5 participate in the generation of carriers, while in UV region only V_2O_5 and in NIR

38

region only MoS_2 is responsible for generation of electron-hole pairs. It should be noted here that the major contribution of the photogenerated carriers is from V_2O_5 and not from MoS_2 as most of the area of MoS_2 is covered by 1D V_2O_5 nanowires. It is well known fact that MoS_2 absorbs in visible region but in this case, due to the less coverage of MoS_2 towards visible light illumination as evident from FESEM image the contribution of MoS_2 towards visible light was less when compared to V_2O_5. This was further verified by measuring the response of pristine V_2O_5 under UV and visible light illumination wherein responsivity of 29.4mA/W and 32.6 mA/W was observed respectively. Graph showing the response and responsivity of pristine V_2O_5 under both UV and visible illumination can be found in Appendix A as figure S6. Also, V_2O_5, being n type material forms local unipolar heterojunction with n type MoS_2. Hence V_2O_5 plays dual role of absorbing in UV and visible range but also helps in the formation of local electric field due to the potential barrier at the MoS_2-V_2O_5 which helps in effective separation of photogenerated carriers thereby increasing the responsivity of the fabricated photodetector. To compare the performance of MoS_2-V_2O_5 with their pristine counterparts, photodetector measurements were performed in their respective absorbance region and the results revealed that the MoS_2-V_2O_5 photodetector was more responsive than their individual counterparts. This can be attributed to the absence of local electric field in the pristine MoS_2 or V_2O_5 wherein the electric field are only present at the 2D MoS_2-metal and 1D V_2O_5-metal contact and absent in the areas far away from the contact areas. Due to the absence of local electric field at the areas far away from the metal contacts, photogenerated carriers tend to recombine thereby decreasing the responsivity. Figure showing the response of pristine MoS_2 can be found in Appendix A as figure S5. To test the durability of the flexible photodetector under bending conditions, photodetector performance was measured under repeated bending conditions. The device was bent for specific number of cycles and device was tested for its photodetector performance in terms of its responsivity. Figure 3.5c shows the graph of MoS_2-V_2O_5 device under 500 bending cycles showing negligible difference in the responsivity values suggesting that the fabricated device is highly durable and stable under bending conditions.

The transport mechanism of 2D MoS_2-1D V_2O_5 broadband photodetector can be best explained by energy band diagram of MoS_2-V_2O_5 as shown in figure 3.5d. Electron affinity of MoS_2 is 4eV and that of V_2O_5 is 4.3 eV. Optical bandgap calculated from the absorbance spectra for MoS_2 and V_2O_5 is 1.53 eV and 2.4 eV respectively. When V_2O_5 nanowires are drop casted on MoS_2, electrons from V_2O_5 flow towards MoS_2 which results in the alignment of fermi level thereby reaching equilibrium. In case of pristine V_2O_5, under UV

and visible illumination, photogenerated carriers tend to recombine which would hinder the performance of the photodetector. Hence, the need of MoS_2 as a transport layer arises whose energy levels are adjusted such that the recombination in pristine V_2O_5 is avoided and the photogenerated carriers can be easily collected at the metal contacts. Under UV illumination, when the energy of the incident illumination is more than the bandgap of V_2O_5, photogenerated electron-hole pairs are generated and due to the presence of MoS_2 as transport layer whose conduction band lies lower than the conduction band of V_2O_5, the photogenerated electrons transport to MoS_2. Since both the contacts are on MoS_2, photogenerated electrons and holes are captured by metal contacts. Also, V_2O_5 being n type material and $MoS2$ being n type, local electric fields are generated at the MoS_2-V_2O_5 unipolar junction and since there are many such small potential barrier created which cumulatively add up which assist in the effective separation of photogenerated electron hole pairs thereby increasing the photocurrent. Under visible light illumination, electron-hole pairs are generated both in MoS_2 and V_2O_5 as both the materials have absorbance in visible range. Since most of the area of MoS_2 is covered by V_2O_5 nanowires, most of the absorbance process happens in V_2O_5 and hence V_2O_5 is dominant in photogeneration of carriers in visible region. The photogenerated electron hole pairs generated in V_2O_5 follow the same transport mechanism as discussed for UV light illumination. But in case of visible light illumination, photogenerated electron hole pairs are also generated in $MoS2$ which might recombine with the electron hole pairs generated in V_2O_5 and eventually gets transported to MoS_2. Even though there might be some recombination of charge carrier in MoS_2, due to the applied external field and local electric fields generated due to the difference in fermi levels of MoS_2 and V_2O_5, most of the photogenerated electrons and holes gets transported to the metal contact thereby increasing the photocurrent drastically. Hence the responsivity is more in visible light illumination when compared to UV and NIR illumination for the fabricated device. Under NIR illumination, photogenerated electron-hole pairs are generated in $MoS2$ which gets transported to the metal contacts as discussed for UV and visible illumination. The responsivity observed for NIR illumination was very less which can be attributed to the fact that the major portion of the MoS_2 is covered by V_2O_5 nanowires and hence absorbance process occurs in the limited exposed portion of MoS_2.

There are various reports on flexible photodetectors fabricated using various pristine 2D, 1D and 0D functional materials and their hybrids. *Um et al.,* fabricated 2D MoS_2-1D CuO heterojunction based on a wet transfer printing of MoS_2 for enhanced photodetection [27].

Han et al., reported low temperature synthesis of 1D ZnO on 2D graphene for photocatalytic applications [28]. There are reports on various devices based on 2D ZnO over 2D Graphene [4], 2D Graphene-2D MoS_2 [29], ZnS nanospheres over 2D MoS_2 [3] for enhanced optoelectronic performance. *Li et al.,* reported CVD grown 1D Bi_2S_3 nanowire and 2D MoS_2 heterostucture and utilized it for transistor and photodetector applications [30]. *Kim et al.,* fabricated V_2O_5-ZnO hybrid for visible light photodetector. [31] Most of the reports on 2D material hybrids fabricate heterojunctions which can improve the responsivity in particular region of electromagnetic spectrum (UV, visible or NIR), but there are fewer reports which studies the detection over a wide range of electromagnetic spectrum. Further, synthesis of MoS_2 is mostly performed using CVD which involves post transfer process thereby leading to device to device variation. Also, direct growth of MoS_2 on flexible substrates still remains a challenge. Table 1 lists down the comparative performance of flexible broadband photodetector based on 2D material hybrids. Herein, we utilize a simple strategy to synthesize suitable hybrids (1D V_2O_5 over 2D MoS_2) where both the material are exposed to illumination which can absorb over a wide range of electromagnetic spectrum and engineer metal contacts to collect the photogenerated carriers. The use of simple solution processed hydrothermal method for direct large area uniform growth of few layer MoS_2 on Al foil and electrospinning for synthesizing 1D V_2O_5 avoids the use of transfer process involved in CVD process and reduces the overall complexity and cost. The method presented is scalable and can be extended to numerous functional materials of choice. The work presented here is a novel approach for designing and fabricating heterostructure for enhanced broadband photodetectors.

3.3.   Conclusion

In summary, we demonstrate for the first time, electrospun 1D V_2O_5 nanowires on 2D MoS_2 nanosheet grown directly on Al foil by simple solution processed hydrothermal method. Discrete distribution of 1D V_2O_5 nanowires on 2D MoS_2 and metal contacts on 2D MoS_2 enables for broadband absorption from UV to NIR. Since both V_2O_5 and MoS_2 possess absorbance in visible region, the fabricated photodetector was more responsive to visible illumination when compared to UV and NIR. Responsivity in UV, visible and NIR was calculated to 41.5 mA/W, 65.1 mA/W and 29.4 mA/W respectively. This work provides a new approach towards broadband photodetector wherein fabrication of conventional photodiode is replaced by discrete distribution of 1D material over 2D where both the materials participate in absorbance and also forms local heterojunction (p-n junction)

thereby allowing not only broadband photosensing but also increased responsivity of the fabricated photodetector. The presented strategy is a major step ahead in the fabrication of broadband photodetectors which finds potential applications in the field of optoelectronics devices, security and medical healthcare applications.

3.4.   Experimental Section

Synthesis of MoS₂ on Al foil: Aluminum foil as the substrate was utilized for the hydrothermal growth of MoS2. The seed solution was prepared by mixture of 10mM of sodium molybdate ($Na_2MoO_4.2H_2O$) and 20mM of thiourea (CH_4N_2S) in deionized (DI) water. The Al foil substrate was dipped in as-prepared seed solution for 1 h followed by drying at 80 °C. A nutrient solution comprising of 50mM sodium molybdate and 100 mM thiourea was stirred in DI water for 30 min. Thereafter, the seed-coated Al foil paper and the nutrient solution were transferred to the hydrothermal reactor and was maintained at 200 °C for 20 h. The reactor was allowed to cool down naturally and the resultant black colored aluminum foil was dried at 80 °C.

Electrospinning of V₂O₅ nano fibers: 0.4g of polyacrylonitrile (PAN) polymer was dispersed in 5ml of N,N–dimethylformamide (DMF) solution (8 wt. %), followed by the addition of 0.5g of Ammonium metavandate to form a uniform viscous solution ready for electrospinning. The solution was loaded into syringe and electrospinning was performed with direct current voltage of 12KV between the needle tip and the Al foil collector separated by a distance of 10cm. The flow rate of the polymer solution was fixed at 8μL/min. The collected V_2O_5 nanowires over the Al foil were calcined at 400ºC for 2hrs.

Fabrication of Photodetector: The as grown MoS_2 on Al flexible substrate was cut into 7 mm x 7mm dimension. MoS_2-Al foil was then masked with polyimide tape at the end which would serve as the contact area on MoS_2. V_2O_5 nanowires dispersed in DMF solution was then spin coated on MoS_2-Al foil. It should be noted here that the spin coating parameters are tuned to obtain discrete distribution of 1D V_2O_5 nanowires on 2D MoS_2. The mask was then removed followed by defining the contacts with silver (Ag) paste.

Materials and Characterization: Sodium molybdate, Thiourea, Polyacrylonitrile and Ammonium metavandate were purchased from Sigma-Aldrich and were used as received for the growth of MoS2-V2O5 hybrids. The structural characteristics of the prepared hybrids were investigated using X'pert PRO XRD with Cu Kα radiation. Raman spectra were obtained from Raman spectrometer (SenterrainVia opus, Bruker) having an excitation

wavelength of 532 nm. FESEM analysis was performed by ZEISS Ultra-55 SEM to study morphology. UV–visible–NIR spectra were obtained using LAMBDA UV/Vis/NIR spectrophotometers (PerkinElmer). The electrical measurements were carried out with Keithley 4200 SCS instrument. The as-fabricated devices were tested for broadband photodetector application on illuminating UV, visible, and IR radiations. The lamp sources utilized for UV, vis, and IR illumination had a wavelength (λ) of 365, 554, and 780 nm, respectively.

3.5.   References

1. Zheng, Z., Gan, L., Zhang, J., Zhuge, F., & Zhai, T. An Enhanced UV–Vis–NIR and Flexible Photodetector Based on Electrospun ZnO Nanowire Array/PbS Quantum Dots Film Heterostructure. Advanced Science, 2017, 4(3).

2. Zhang, K., Peng, M., Wu, W., Guo, J., Gao, G., Liu, Y., & Zhang, Y. A flexible p-CuO/n-MoS 2 heterojunction photodetector with enhanced photoresponse by the piezo-phototronic effect. Materials Horizons, 2017, 4(2), 274-280.

3. Gomathi, P. T., Sahatiya, P., & Badhulika, S. Large-Area, Flexible Broadband Photodetector Based on ZnS–MoS2 Hybrid on Paper Substrate. Advanced Functional Materials, 2017, 27(31).

4. Sahatiya, P., Jones, S. S., Gomathi, P. T., &Badhulika, S. Flexible substrate based 2D ZnO (n)/graphene (p) rectifying junction as enhanced broadband photodetector using strain modulation. 2D Materials, 2017, 4(2), 025053.

5. Huang, Y., Zhan, X., Xu, K., Yin, L., Cheng, Z., Jiang, C., & He, J. Highly sensitive photodetectors based on hybrid 2D-0D SnS2-copper indium sulfide quantum dots. Applied Physics Letters, 2016, 108(1), 013101.

6. Li, T., & Galli, G. Electronic properties of MoS2 nanoparticles. The Journal of Physical Chemistry C, 2007, 111(44), 16192-16196.

7. Jiang, J. W. Graphene versus MoS2: a short review. Frontiers of Physics, 2015, 10(3), 287-302.

8. Zhou, W., Yin, Z., Du, Y., Huang, X., Zeng, Z., Fan, Z., & Zhang, H. Synthesis of few-layer MoS2 nanosheet-coated TiO2 nanobelt heterostructures for enhanced photocatalytic activities. Small, 2013, 9(1), 140-147.

9. Zhang, W., Huang, J. K., Chen, C. H., Chang, Y. H., Cheng, Y. J., & Li, L. J. High-gain phototransistors based on a CVD MoS2 monolayer. Advanced Materials, 2013, 25(25), 3456-3461.

10. Eda, G., Yamaguchi, H., Voiry, D., Fujita, T., Chen, M., & Chhowalla, M. Photoluminescence from chemically exfoliated MoS2. Nano Letters, 2011, 11(12), 5111-5116.

11. Kufer, D., Nikitskiy, I., Lasanta, T., Navickaite, G., Koppens, F. H., & Konstantatos, G. Hybrid 2D–0D MoS2–PbS quantum dot photodetectors. Advanced Materials, 2015, 27(1), 176-180.

12. Badadhe, S. S., Suryawanshi, S. R., Naphade, R. A., Chaudhary, M. V., More, M. A., Shelke, M. V., & Ogale, S. B. Synthesis, microstructure, optical and field emission studies of iron vanadium oxide nanosheets. Journal of Physics D: Applied Physics, 2016, 49(14), 145301.

13. Fu, W. B., Shang, G. L., Gong, X. X., De Zhang, L., & Fei, G. T. Preparation of large scale and highly ordered vanadium pentoxide (V2O5) nanowire arrays towards high performance photodetectors. Journal of Materials Chemistry C, 2017, 5(6), 1471-1478.

14. Su, Q., Huang, C. K., Wang, Y., Fan, Y. C., Lu, B. A., Lan, W., & Liu, X. Q. Formation of vanadium oxides with various morphologies by chemical vapor deposition. Journal of Alloys and Compounds, 2009, 475(1), 518-523.

15. Asen, P., & Shahrokhian, S. One step electrodeposition of V2O5/polypyrrole/graphene oxide ternary nanocomposite for preparation of a high performance supercapacitor. International Journal of Hydrogen Energy, 2017, 42(33), 21073-21085.

16. Aravindan, V., Cheah, Y. L., Mak, W. F., Wee, G., Chowdari, B. V., & Madhavi, S. Fabrication of High Energy‐Density Hybrid Supercapacitors Using Electrospun V2O5 Nanofibers with a Self-Supported Carbon Nanotube Network. ChemPlusChem, 2012, 77(7), 570-575.

17. Abd-Alghafour, N. M., Ahmed, N. M., Hassan, Z., & Bououdina, M. High-performance p–n heterojunction photodetectors based on V2O5 nanorods by spray pyrolysis. Applied Physics A, 2016, 122(9), 817.

18. Abd-Alghafour, N. M., Ahmed, N. M., & Hassan, Z. Fabrication and characterization of V2O5 nanorods based metal–semiconductor–metal photodetector. Sensors and Actuators A: Physical, 2016, 250, 250-257.

19. Sanwaria, A.R., Nagar, M., Bohra, R., Chaudhary, A., Mobin, S.M., Mathur, P. and Choudhary, B.L., Sol–gel synthesis of highly pure α-Al 2 O 3 nano-rods from a new class of precursors of salicylaldehyde-modified aluminum (iii) isopropoxide. Crystal and molecular structure of [Al (OC 6 H 4 CHO) 3], RSC Advances, 2014, 4(57), 30081-30089

20. Baddour-Hadjean, R., Pereira-Ramos, J. P., Navone, C., & Smirnov, M. Raman microspectrometry study of electrochemical lithium intercalation into sputtered crystalline V2O5 thin films. Chemistry of Materials, 2008, 20(5), 1916-1923.

21. Baddour-Hadjean, R., Raekelboom, E., & Pereira-Ramos, J. P. New Structural Characterization of the Li x V2O5 System Provided by Raman Spectroscopy. Chemistry of Materials, 2006, 18(15), 3548-3556.

22. Baddour - Hadjean, R., Smirnov, M. B., Smirnov, K. S., Kazimirov, V. Y., Gallardo-Amores, J. M., Amador, U.,& Pereira-Ramos, J. P. Lattice dynamics of β-V2O5: Raman spectroscopic insight into the atomistic structure of a high-pressure vanadium pentoxide polymorph. Inorganic chemistry, 2012, 51(5), 3194-3201

23. Mignuzzi, S., Pollard, A. J., Bonini, N., Brennan, B., Gilmore, I. S., Pimenta, M. A., & Roy, D. Effect of disorder on Raman scattering of single-layer MoS2. Physical Review B, 2015, 91(19), 195411

24. Tchenar, Y. N., Choukchou-Braham, A., & Bachir, R. RuO2 supported on V2O5–Al2O3 material as heterogeneous catalyst for cyclohexane oxidation reaction. Bulletin of Materials Science, 2012, 35(4), 673-681.

25. Fu, W. B., Shang, G. L., Gong, X. X., De Zhang, L., & Fei, G. T. Preparation of large scale and highly ordered vanadium pentoxide (V 2 O 5) nanowire arrays towards high performance photodetectors. Journal of Materials Chemistry C, 2017, 5(6), 1471-1478.

26. Sahatiya, P., Puttapati, S. K., Srikanth, V. V., & Badhulika, S. Graphene-based wearable temperature sensor and infrared photodetector on a flexible polyimide substrate. Flexible and Printed Electronics, 2016, 1(2), 025006.

27. Um, D. S., Lee, Y., Lim, S., Park, S., Lee, H., & Ko, H. High-Performance MoS2/CuO Nanosheet-on-One-Dimensional Heterojunction Photodetectors. ACS applied materials & interfaces, 2016, 8(49), 33955-33962.

28. Han, C., Chen, Z., Zhang, N., Colmenares, J. C., & Xu, Y. J. Hierarchically CdS Decorated 1D ZnO Nanorods-2D Graphene Hybrids: Low Temperature Synthesis and Enhanced Photocatalytic Performance. Advanced Functional Materials, 2015, 25(2), 221-229.

29. Sahatiya, P., & Badhulika, S. Strain modulation assisted enhanced broadband photodetector based on large area, flexible, few layered Graphene-MoS2 on cellulose paper. Nanotechnology, 2017. DOI: 10.1088/1361-6528/aa8587

30. Li, Y., Huang, L., Li, B., Wang, X., Zhou, Z., Li, J., & Wei, Z. Co-Nucleus 1D/2D Heterostructures with Bi2S3 Nanowire and MoS2 Monolayer: One-Step Growth and Its Defect-InducedFormation Mechanism, ACS Nano, 2016, 10(9), 8938-8946.

31. Kim, H. S., Chauhan, K. R., Kim, J., & Choi, E. H. Flexible vanadium oxide film for broadband transparent photodetector. Applied Physics Letters, 2017, 110(10), 101907.

32. Lim, Y. R., Song, W., Han, J. K., Lee, Y. B., Kim, S. J., Myung, S., & Lim, J. Wafer-Scale, Homogeneous MoS2 Layers on Plastic Substrates for Flexible Visible-Light Photodetectors. Advanced Materials, 2016, 28(25), 5025-5030

33. Li, Y., Huang, L., Li, B., Wang, X., Zhou, Z., Li, J., & Wei, Z. Co-nucleus 1D/2D heterostructures with Bi2S3 nanowire and MoS2 monolayer: One-step growth and defect-induced formation mechanism, ACS Nano, 2016, 10(9), 8938-8946

34. Lee, Y. B., Kim, S. K., Lim, Y. R., Jeon, I. S., Song, W., Myung, S., & An, K. S. Dimensional Hybrid Structures of 2D Materials with ZnO Nanostructures via pH-Mediated Hydrothermal Growth for Flexible UV Photodetectors. ACS Applied Materials & Interfaces, 2017, 9(17), 15031-15037.
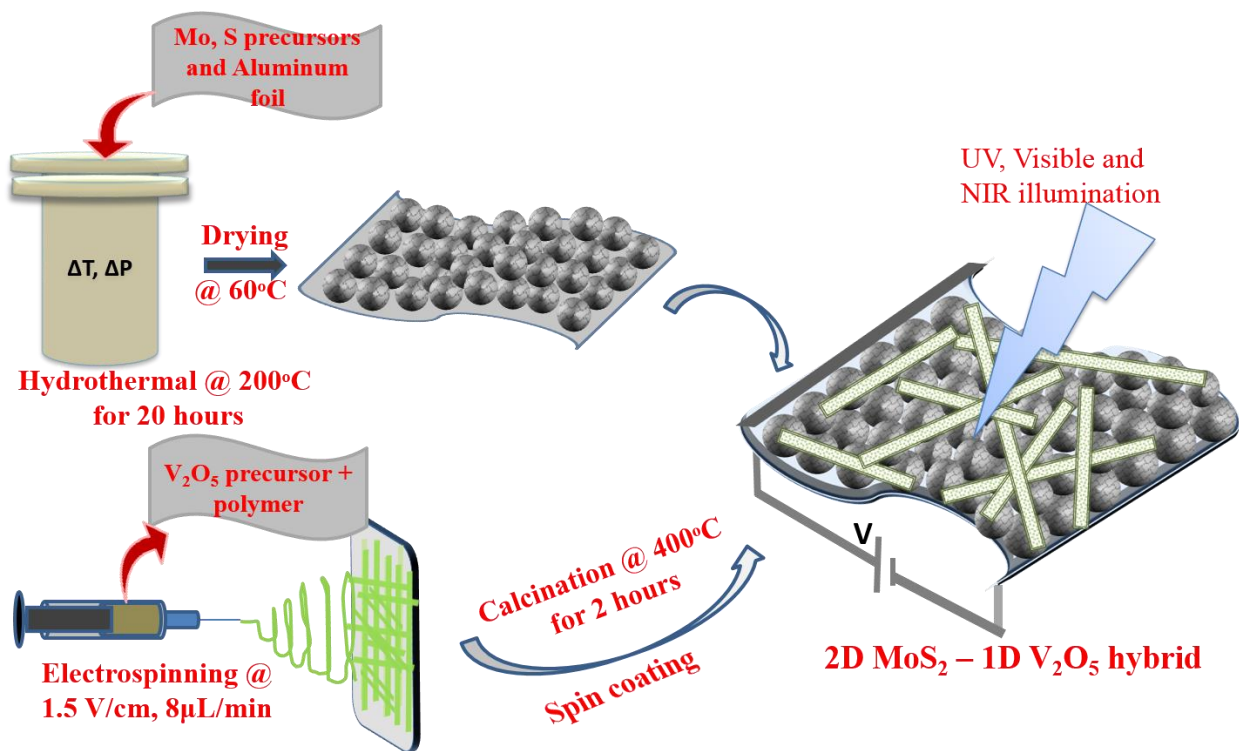
Figure 3.1: Schematic of the fabrication procedure for discretely distributed 1D V_2O_5 nanowires over 2D MoS_2 as a broadband photodetector.
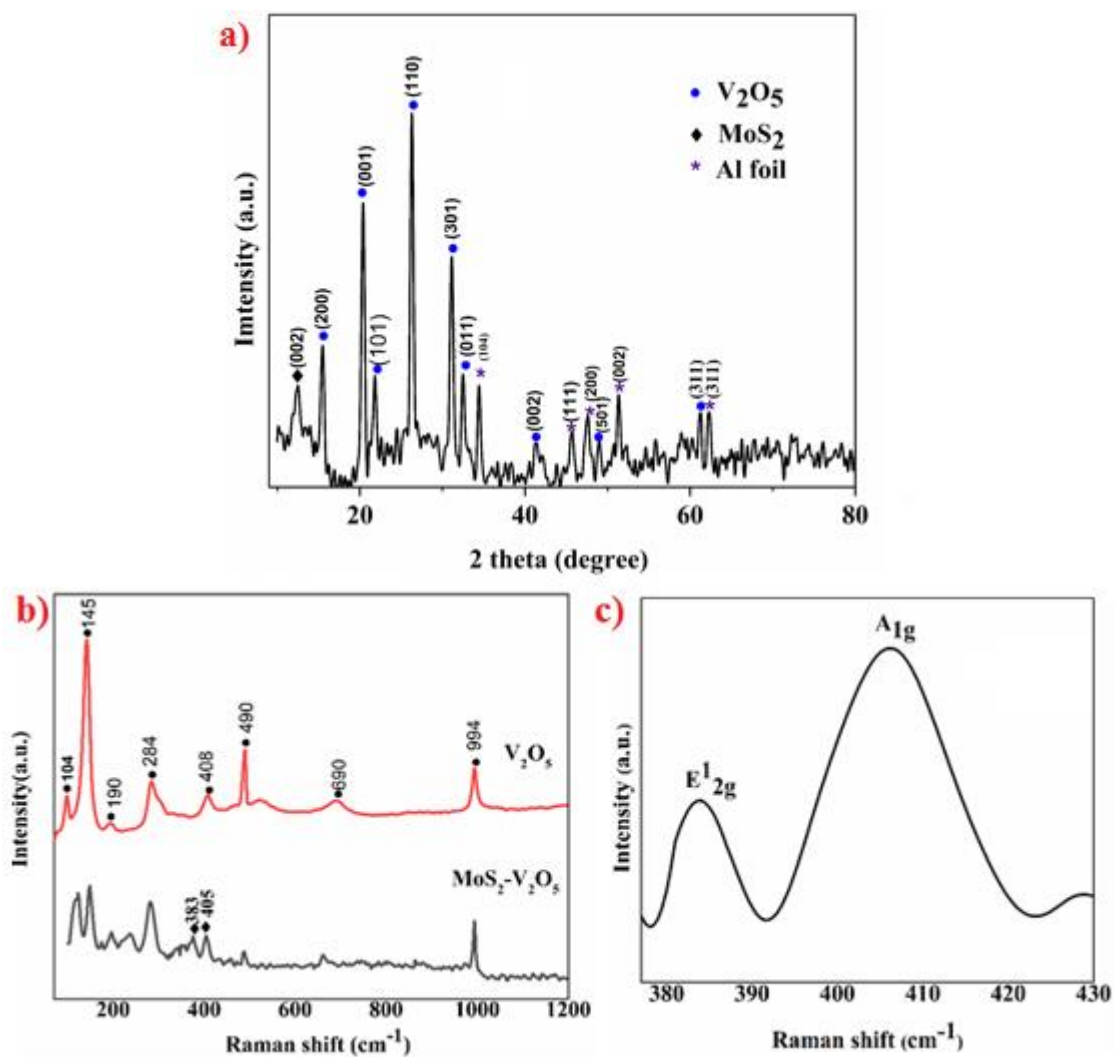
Figure 3.2: a) XRD diffractogram of 1D V_2O_5 nanowires over 2D MoS_2 nanosheets b) Raman spectra of 1D V_2O_5 nanowires over 2D MoS_2 nanosheets c) Raman spectra of MoS_2 showing the frequency separation of 22 cm^{-1}.
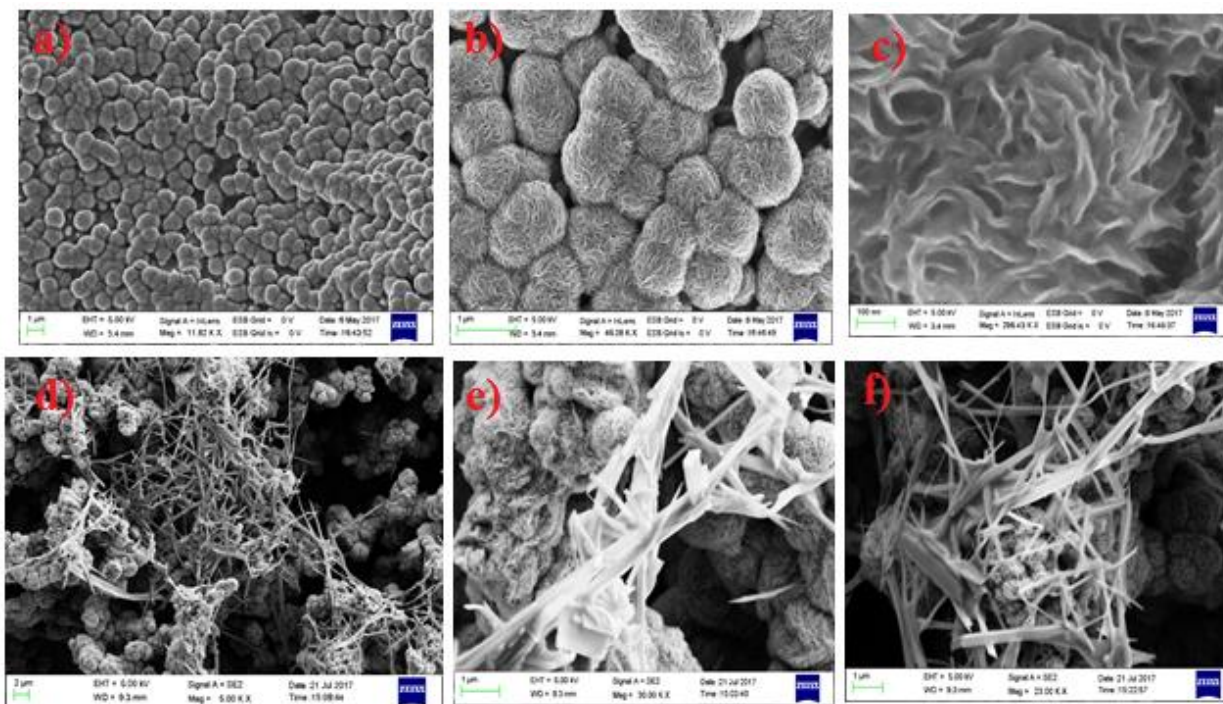
Figure 3.3: a) Low magnification FESEM image of MoS$_2$ grown on Al foil b,c) high magnification FESEM image of MoS$_2$ on Al foil demonstrating microsphere like morphology and individual MoS$_2$ nanoflakes d) Low magnification FESEM image of 1D V$_2$O$_5$ over 2D MoS$_2$ wherein discrete distribution of V$_2$O$_5$ nanowires over MoS$_2$ is clearly observed e,f) high magnification FESEM image of V$_2$O$_5$ over MoS$_2$ showing large area coverage of V$_2$O$_5$
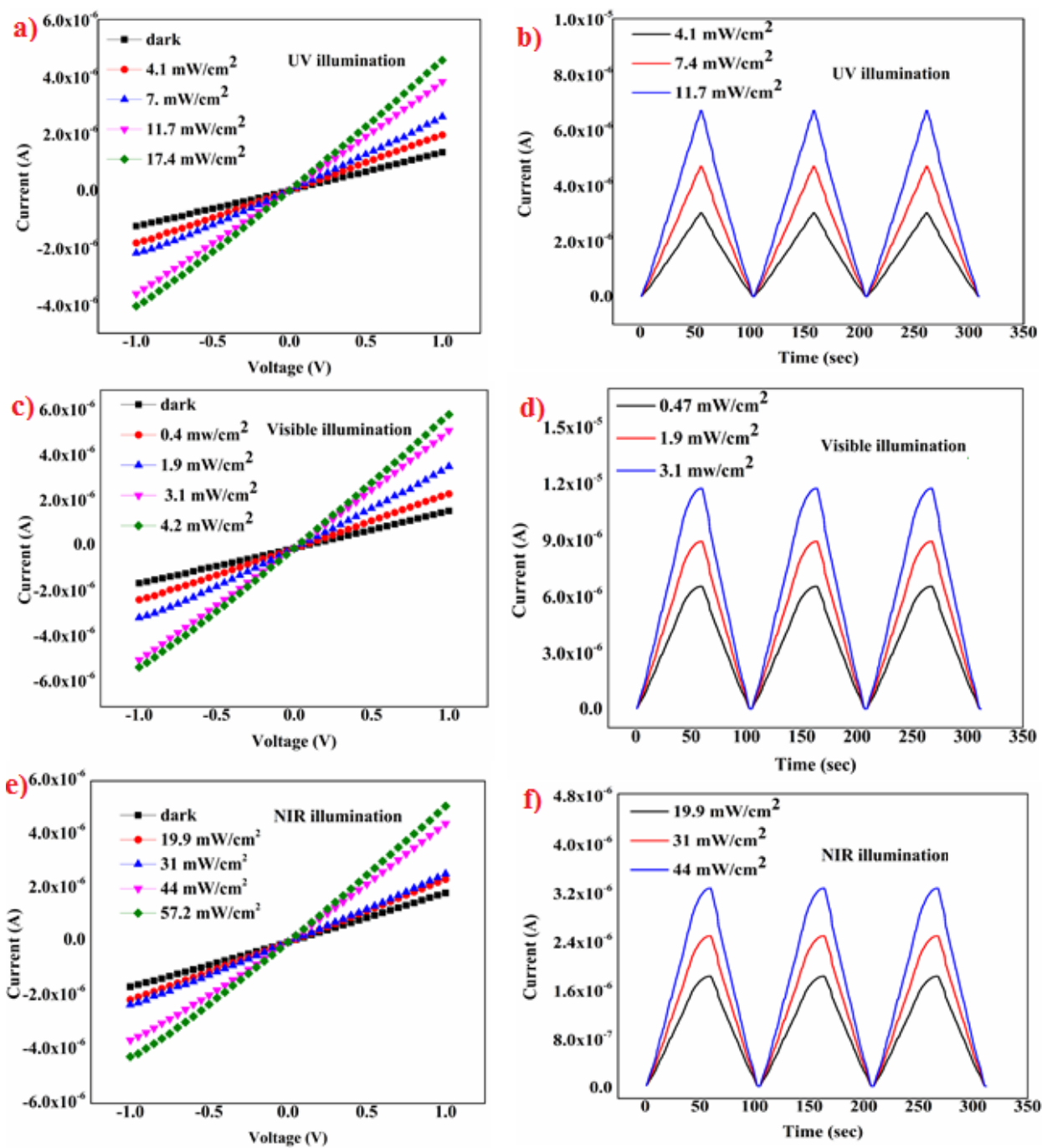
Figure 3.4: a) IV characteristic of MoS$_2$/V$_2$O$_5$ under different intensity of UV illumination b) temporal response of MoS$_2$/V$_2$O$_5$ under different intensities of UV illumination c) IV characteristic of MoS$_2$/V$_2$O$_5$ under different intensity of visible illumination d) temporal response of MoS$_2$/V$_2$O$_5$ under different intensities of visible illumination e) IV characteristic of MoS2/V2O5 under different intensity of NIR illumination f) temporal response of MoS$_2$/V$_2$O$_5$ under different intensities of NIR illumination

Figure 3.5: a) Responsivities v/s different intensities of UV, visible and NIR for MoS_2/V_2O_5 showing highest responsivities for visible illumination b) EQE v/s different intensities of UV, visible and NIR for MoS_2/V_2O_5 showing highest responsivities for visible illumination c) Responsivities v/s bending cycles under UV, vis and NIR showing negligible change d) Energy band diagram showing the charge transport mechanism of MoS_2/V_2O_5 under illumination.

Material/ Hybrid	Substrate	Range of Detection	Responsivity	Reference
MoS_2	Polyimide	UV	2.46 µA/W	32
Bi_2S_3/MoS_2	SiO2/Si substrate	VISIBLE	--	33
MoS_2/ZnS	Cellulose paper	UV to NIR	17.85 µA/W	3
V_2O_5/ZnO	Polyethylene terephthalate(PET)	VISIBLE	20 mA/W	28
Graphene/ZnO	Eraser	UV to Visible	16.5 µA/W	4
MoS_2/ZnO	Polyimide	UV	0.89 mA/W	34
Graphene/MoS_2	Cellulose paper on PDMS	UV to Visible	3.3 mA/W	26
V_2O_5/MoS_2	**Aluminum foil**	**UV VIS NIR**	**65 mA/W**	**This work**

Table 3.1: Comparative table for performance of different flexible broadband photodetectors based on 2D materials and their hybrids

Chapter 4

2D MoS₂-carbon quantum dot hybrid based large area, flexible UV-vis-NIR photodetector on paper substrate

Abstract

While all reports on 2D-0D hybrid photodetectors are on silicon substrate and based on heavy metals quantum dots exhibiting limited range detection, this paper is the first demonstration of 2D MoS$_2$-carbon quantum dot (CQD) based flexible broadband photodetector (PD) wherein MoS$_2$ was grown on cellulose paper using hydrothermal method and CQD was synthesized using a low cost, one step pyrolytic process of chia seeds. The absorbance of CQD in UV region combined with the broadband absorption of MoS$_2$ in visible and NIR region broadens the absorbance range. Structural characterization revealed few layered MoS$_2$ and CQD to be in the range of 2 - 6nm. Responsivity for the fabricated sensor was found to be 8.4, 2.62 and 18.12 mA/W in UV, NIR and visible region respectively which are comparable and even better compared to photodetector fabricated using sophisticated cleanroom techniques. The PD showed negligible variation in photoresponse under repeated (up to 500 cycles) bending conditions. Discrete distribution of CQD over MoS$_2$ creates unipolar junctions which helps in generation of small local electric fields thereby increasing the sensitivity of the sensor. The work presented here is a major step ahead in fabrication of low-cost flexible broadband photodetectors which finds potential applications in the field of flexible and wearable electronics, security and surveillance systems etc.

4.1. Introduction

Flexible broadband photodetectors are highly desirable for various potential applications such as imaging, optical communications and flexible sensors for wearable electronics. Recently, much research on photodetectors has been to

increase the responsivity in a particular region of the electromagnetic spectrum (UV, visible or IR). In view of above, synthesizing hybrid with high carrier mobility material has been the keen focus. But the other issue is the inability of the photodetector to absorb wide range of electromagnetic spectrum. There are reports wherein hybrids have been synthesized to increase the absorbance from UV to visible or from visible to NIR, but there are less reports which discuss the absorbance in the entire range of electromagnetic spectrum. Hence there is need to fabricate photodetectors using hybrid materials which would absorb and sense light in the entire electromagnetic spectrum.

Recently 2D materials are intensely studied due to their remarkable properties which finds potential applications in the field of flexible and wearable electronics [1]. Among them, transition metal dichalcogenides (TMD) has proven to be noteworthy because of their strong excitonic effects, optical transparency, mechanical flexibility, layer dependent bandgap, tuneable optical properties and high breakdown voltages [2-4]. Molybdenum Disulphide (MoS_2) has been the most explored among the TMD family because of its direct bandgap, high electron mobility (up to 480 cm^2 $V^{-1}S^{-1}$) and superior on/off ratio [5] thus making it a better candidate over existing materials such as silicon, organic semiconductors and oxide semiconductors which possess low carrier mobilities in the field of flexible electronics [6].

Carbon dots are zero-dimensional quasi-spherical nanocarbons containing amorphous to a crystalline core with graphitic or turbostratic carbon (sp^2) fused by diamond-like sp^3 carbon insertions [7]. The synthesis of carbon dots can be primarily classified into top down and bottom up approaches. While the top down approach involves the exfoliation of large carbon structures into nanocarbon followed by post treatment, the bottom up approach makes use of carbon-rich molecular precursors which would be subjected to thermal decomposition [8]. Ever since its discovery, the research on carbon dots has been upbeat because of its remarkable properties like excellent solubility, ease of functionalization, chemical inertness, photoluminescence, low cytotoxicity and resistance to photobleaching compared to its 1D counterparts [9-10]. These properties of carbon dots facilitate its usage in numerous applications like optoelectronics, bioimaging, drug delivery,

photovoltaics, biosensing and solar cells [11-14]. To further enhance the scope of applications of pristine CQD, hybrids of CQD have been synthesized with various 2D materials such as MoS_2, metal oxides etc. for applications such as solar cell, supercapacitor, sensors etc. Although, carbon dots possess high photogenerated carrier mobility, tuneable bandgap, a bifunctional electron donor and acceptor capability and high molar extinction coefficient [15, 16], the reports on photodetectors using carbon dots are relatively few [17 - 19].

There are various reports on broadband photodetectors based on different hybrid structures which are fabricated on rigid silicon substrate or flexible plastic substrates, which make use of sophisticated cleanroom techniques that are not only expensive and time consuming but also energy inefficient.[20-21] Moreover, all flexible substrates are not microfabrication compatible. Hence there is a need to develop solution process wherein different substrates properties could be utilized for the development of fabrication of flexible devices. Recently, there have been active research on paper based electronics due to its excellent properties such as highly flexible, low cost and biodegradability which allows them for its use in flexible and wearable electronics [22]. There have been reports which utilizes paper as a substrate for numerous applications such as photodetectors, solar cell, supercapacitor, batteries transistors etc [23-26]. Despite the advantages offered by cellulose paper substrates, direct growth of 2D materials and functionalizing them with CQD on cellulose paper still remains unexplored.

In this work, we report the fabrication of flexible broadband photodetector based on 2D MoS_2-CQD hybrids on cellulose paper. 2D MoS_2 have been grown directly on cellulose paper using simple cost effective solution processed hydrothermal method. Carbon dots has been synthesized by a green, single step, pyrolytic approach to circumvent disadvantages of conventional synthesis procedures such as expensive precursors, complicated post-treatment [27] approaches and low yield, by utilizing an environmentally benign route. The device was fabricated by masking MoS_2-cellulose paper on two ends followed by drop casting of CQD solution. CQD was responsible for absorbance in UV region and 2D MoS_2 was responsible for absorbance in visible and NIR region. Discrete distribution of CQD on MoS_2 helped

in realization of broadband photodetector wherein both CQD and MoS2 could be exposed to incident light. Further, distribution of CQD on MoS_2 forms unipolar junctions which creates small electric field thereby assisting photogenerated electron-hole separation. To best of our knowledge, this is a first demonstration of 2D MoS_2-CQD based flexible broadband photodetector.

4.2.   Results and Discussions

2D MoS_2 has been known for its broadband absorption in visible and NIR region. To extend the absorption region in UV, there have been attempts to synthesize hybrids of UV absorbing materials with MoS_2. CQD absorbs in UV range and the functional groups of CQD assist in forming hybrid with MoS_2, thus facilitating broadband absorption. The reason for less reports on absorption in broad range of electromagnetic spectrum is lack of synthesizing suitable hybrids wherein both the materials should be exposed to the illumination and the device fabrication where the placement of metal contacts plays an important role in capturing the photogenerated electron-hole pairs. In this work, discrete distribution of CQD on MoS_2 and the fabrication of metal contacts on MoS_2 allowed for the broadband absorption. Hydrothermal method was employed for the growth of MoS2 on cellulose paper and one step pyrolytic process was utilized for the synthesizing CQD using chia seeds. The growth of MoS_2 on cellulose paper and the synthesis of CQDs can be found in a recent report from our lab [28-29]. Detailed fabrication procedure of 2D MoS_2-CQD hybrid photodetector can be found in experimental section and schematic of the fabrication procedure is shown in figure 4.1.

To study the crystal structure of as fabricated MoS_2 and CQD, XRD analysis was performed where the diffractogram of carbon dots is showcased in figure 4.2a. The presence of peaks at 25.5°, 43.72° signifies the presence of (002) & (101) facets of the graphitic carbon.[30] The corresponding d spacing value for the peak centered at 25.5° was found to be 0.348 Å which was a little higher than the value of bulk graphite. The increased interplanar spacing observed in carbon dots could have been due to the presence of functional groups at the edges or turbostratic stacking of carbon structures [31]. In the XRD of MoS_2-CQD as shown in figure 2b, the presence of MoS2 in the nanohybrids can be confirmed by the presence of four signature peaks in XRD spectra at 2θ = 12.5 (002), 33 (100), 38 (103), 57(110) respectively [32]. The broadening of peaks was due to the utilization of lower temperature (200°C) for the growth of MoS_2 on paper which has led to a reduction in crystallinity [33]. The synthesis temperature for the growth of MoS_2 was optimized so as to maintain the

flexibility of the substrate. Moreover, there was a consequent reduction and increase in the intensity of (002) and (100) planes of MoS_2 denoting that the synthesized products were few-layered MoS_2 consisting of a large number of edge planes [34, 35].

To further confirm the formation of hybrid, Raman analysis was performed. The Raman spectra of MoS_2 has two peaks centered at 383 and 405 cm^{-1} corresponding to the E12g and A1g mode respectively as shown in figure 4.2c. The in-plane E12g mode arises due to the oscillation of sulphur atoms with respect to the molybdenum atoms in-between them, whereas A2g denotes the out-of-plane vibration of sulphur atoms along in opposite directions [36]. Moreover, the prominence of these peaks indicates that the crystal structure of synthesized MoS_2 was not damaged by the presence of sulphur vacancies [37]. Moreover, it is possible to quantify the number of layers of prepared MoS_2 by calculating the frequency difference between the two modes observed in Raman spectra. From the calculated difference ($\Delta=22$), it can be inferred that the synthesized MoS_2 were comprised of few (<4) layers [38]. Whereas, the Raman spectra of carbon dots exhibits two discernible peaks at 1331 cm^{-1} and 1584 cm^{-1} respectively as shown in figure 2d. The presence of D band is due to the vibrations of carbon atoms with dangling bonds along the termination plane of disordered graphite, whereas, G band is associated with the vibration of sp^2 hybridized carbon atoms along the two-dimensional hexagonal lattice [39]. Also, the existence of both sp^2 and sp^3 hybrids in the prepared material suggests the amorphous nature of the material [40]. The I_D/I_G ratio was calculated to be 1.27 for the prepared sample. In addition, I_D/I_G ratio can be used to quantify the defect density of prepared carbon material. The increase in ratio observed was the consequence of surface oxidation of the synthesized products, which can be further corroborated by the presence of oxygenated functional groups in the presented FTIR spectra [41].

The morphology of synthesized MoS_2/CQD hybrid was studied using FE-SEM and TEM. As evident from figure 4.3a, the growth of few layered MoS_2 nanosheets was conformal on the top of closely packed fibers of cellulose without modifying its inherent morphology. Figure 4.3b shows the high magnification image of MoS_2-cellulose paper wherein the presence of ripples in nanosheets suggests the ultrathin nature of MoS_2. Also, the geometry of sheet edges can be correlated with the crystallinity of MoS_2 and thus the presence of sharp edges, suggests the improved crystallinity of the products [42, 43]. The prepared carbon dots were imaged using TEM to study about its particle size and shape. Figure 3c denotes the uniform distribution of spherical carbon dots with sizes ranging from 2 – 6 nm. These nanosized carbon dots were well-dispersed and distributed evenly without showing

any signs of aggregation as shown in figure 4.3d.The elemental mapping of MoS_2-CQD hybrids was performed to understand the spatial distribution of CQD on the surface of MoS_2 as shown in figure 4.3e. As expected, carbon dots were discretely spread along the surface of MoS_2. The discrete distribution of CQD on MoS_2 is important for broadband absorption as MoS_2 can be exposed to illumination. If the entire MoS_2 would have been covered with CQD would led to the development of UV photodetector with very less response towards visible and NIR illumination.

For photodetector application, it is important to study the absorption spectra of individual materials. The UV-Vis spectra consist of two absorption peaks which are typically observed for carbon dots as shown in figure 4.4a. The absorption at 280 nm can be attributed to the π-π* transition of the conjugated C=C structure. Whereas, the broad shoulder peak at 345 nm was due to n- π* transition of the surface functional groups [44]. The Full width half maximum (FWHM) was calculated to be 126 nm. The high value of FWHM could attributed to the presence of multiple emissive sites arising from the emission induced by graphitic core and its surface functionalities [45]. The UV spectra of MoS_2 comprise of two absorption bands wherein the optical transitions between the higher densities of state regions gives rise to the peaks from 400 to 450 nm as shown in figure 4.4b. There was also a weak absorption at 600 – 700 nm which was due to the interband excitonic transitions at K point of the 2D Brillouin zone of MoS_2. [46]

The surface potential of synthesized carbon dots was analysed using Zeta potential analyzer at neutral pH and room temperature. The zeta potential of the prepared carbon dots was found to be -26.6 mV. The net surface charge is negative due to the presence of abundant oxygenated functional groups on the surface of prepared carbon dots which is also reflected in the FTIR spectra [47].

The growth of layered MoS_2 was initiated by the aggregation of MoS_2 nanoparticles formed during the seeding process of hydrothermal. At elevated temperatures, these agglomerated nanoparticles transform into petals. These petals form flower-like architectures due to van der Waals attraction between individual sheets [48, 49]. However, irrespective of the synthesis strategy for MoS_2, sulfur vacancy is the predominant type of point defect found in MoS_2 [25]. Such point defects can be utilized for synthesizing composites with CQD having surface functional groups which can be linked to the sulfur vacancy sites.[50] Figure 4.4c shows the FTIR spectra of pristine CQD wherein the peaks at 1680, 1368, 3250, 1640, 1529 and 1236 cm^{-1} corresponds to C=O, COOH, O-H, H-O-H, C=C, C-O-C molecular

vibrations.[51-56] These results suggests that the surface of carbon dots consists of various functional groups. These functional groups gets linked to the sulfur vacancy thereby forming MoS_2-CQD hybrid.

To study the behavior of fabricated MoS_2-CQD device under different light illumination, I-V studies were performed using Ag paste as contacts. It should be noted that the masking process allows the contacts to be on MoS_2 and not on CQD thereby creating ohmic contacts. Prior to the illumination studies, the devices were kept in dark for 12 hours to stabilize the device. Illumination wavelength of 365nm, 554nm and 780 nm were used to study the photodetection performance. Figure 4.5a shows the I-V characteristic of MoS_2-CQD hybrid with different intensities of UV light wherein increase in the current was observed with increasing intensity. This could be attributed to the more number of photogenerated electron-hole pair upon increasing of intensity. The same was repeated for visible and NIR illumination and similar increase in the current was observed upon increase of intensity as shown in figure 4.5c and figure 4.5e respectively.

To check the repeatability of the photodetector, temporal response was measured under repeated UV, visible and NIR illuminations. Figure 5b shows the temporal response of the MoS_2-CQD device under UV illumination for 3 cycles wherein the illumination were turned "on" and "off" at repeated intervals. Further, the photodetector was subjected to different intensities where increase in the current levels were observed. The results indicate excellent repeatability of the sensor where the photodetector regained its initial resistance value upon turning "off" the illumination. Experiments were performed for visible and NIR illumination wherein similar results were observed as shown in figure 4.5d and figure 5f. 28, 61 and 52 % increase in normalized resistance was observed for UV, visible and NIR region, further suggesting that the photodetector is more sensitive towards visible light compared to UV and NIR illumination. It should be noted that even though different intensities were used for measurements, responsivity was calculated for similar intensities, highest responsivity was calculated for visible, thereby confirming the sensor to be more responsive towards visible light.

The important parameters for evaluating the photodetector performance are Responsivity which is the measure of the photocurrent generated per unit power of incident light per area and External Quantum efficiency (EQE) which is the number of electrons produced per incident photon. The responsivity and EQE are given by following equations

$$R_\lambda = \frac{I_\lambda}{P_\lambda \times A}$$

$EQE = hc \: X \: R_\lambda \: /e\lambda$

Figure 6a shows the graph of responsivity with different illumination intensity wherein increase in the value of responsivity was observed with increasing intensity. Responsivity values observed were respectively inferring that photodetector was more responsive to visible light followed by UV and NIR illumination. Figure 4.6b shows the graph of EQE with different intensities. The responsivity and EQE values calculated are comparable and even better to some of the reports on flexible photodetectors fabricated using sophisticated cleanroom techniques. It should be noted that even though CQD are deposited on MoS_2, responsivity and EQE values are found to be larger for visible light illumination due to the discrete distribution of the CQD on MoS_2. This allows for more exposed area of MoS_2 towards illumination. This is in agreement with UV-vis-NIR spectroscopy data wherein more absorbance was observed in visible region compared to NIR region. The discrete distribution of CQD not only allows MoS_2 to be exposed to illumination but also helps in creating local unipolar junctions with MoS_2 which generated local electric fields, thereby assisting for effective separation of photogenerated charge carriers. In case of pristine MoS_2, electric fields are generated only at the metal-MoS_2 contacts and there is no electric field generated in the areas far away from the metal contacts. When light is illumination on pristine MoS_2, the photogenerated electrons near the metal-MoS_2 interface will be collected by the metal contact and the photogenerated electrons away from the metal-MoS_2 are likely to be recombined due to the low mobility of MoS_2 caused by the cellulose paper substrate. Therefore, in case of pristine MoS_2, the response is due to the photogenerated electrons near the metal-MoS_2 interface which exhibits low responsivity and sensitivity when compared to MoS_2-CQD hybrid photoresponse. Figure showing the response of pristine MoS_2 on illumination of visible and NIR illumination can be found in Appendix A as figure S8.

The performance of broadband photodetector was evaluated in terms of response time wherein the step input of the visible light was illuminated and the time taken to reach from 10% to 90% of the maximum value was calculated. The as fabricated photodetector was found to have a response time of 0.57 sec as shown in figure 4.6c. The measured value of response time is comparable and even better to some of the photodetectors fabricated on different flexible substrates. It should be noted that the response time values are less

compared to the reports.[57] The reason for low response time can be attributed to the paper substrate which being a dielectric material decreases the mobility of the charge carriers. Further, discrete distribution of CQD on MoS_2 leads to improper band alignment which further increases the scattering thereby decreasing the mobility of the photogenerated charge carriers. It should be noted that the discrete distribution is necessary for broadband detection as it's required for MoS_2 to be exposed to visible light which would have not been possible if CQD are uniformly distributed. Uniform distribution of CQD on MoS_2 would hinder the absorbance of MoS_2 in visible and NIR region. Further the performance of the device was evaluated under several bending cycles. The fabricated device was attached to another paper substrate and bending was performed manually. After specific bending cycles, the device performance was measured for UV, visible and NIR illumination. Figure 4.6d shows the graph of responsivity with bending cycles wherein negligible performance in the MoS_2-CQD broadband photodetector was observed demonstrating the robust nature of the fabricated flexible photodetector.

The transport mechanism of MoS_2-CQD in UV-vis and NIR region can be well understood by energy band diagram and the charge transport schematic as shown in figure 4.7. The electron affinity of CQD and MoS_2 is respectively. When CQD was drop casted and dried on MoS_2 thereby reaching equilibrium conditions, electrons from CQD flow towards MoS_2 which results in alignment of fermi level. Under UV light illumination, absorption of photons by localized π electrons results in electron-hole pairs. Radiative recombination of these photogenerated electrons results in the blue emission. In case of pristine CQD in solution, under UV illumination, shows blue emission inferring that radiative recombination occurs as shown in figure. Hence in case of pristine CQD, the photogenerated electron-hole pair would tend to radiatively recombine which would hinder the performance for photodetector performance. Hence there is a need for MoS_2 as transport material whose energy levels are well adjusted such that the radiative recombination is avoided and the photogenerated electron-hole pair can be easily captured. In this case, due to the presence of MoS_2, whose conduction band lies lower than the LUMO of CQD and VB lies above the HUMO, the photogenerated electron-hole pair transports to MoS_2. Since both the contacts are on MoS_2, due to external applied electric field and the electric field generated due to the unipolar junction created between MoS_2 and CQD, electron-hole pairs get separated. Even though CQD are found to be electron donor by zeta potential measurements, the fermi level difference between MoS_2 and CQD favours the formation of unipolar junctions whose barrier potential would be the difference between the fermi levels of MoS_2 and CQD.

Moreover, there are many such unipolar junctions which cumulatively add up and helps in creating effective electric field thereby assisting for electron-hole separation and increasing the photocurrent. It should be noted that if one of the contacts would have been taken from CQD, then photogenerated holes would have been trapped in MoS_2 which might have led to recombination of photogenerated electrons. For visible and NIR illumination, electron-hole pair are generated in MoS_2 wherein the presence of extra electrons causes a change in fermi level which further increases the barrier height of MoS_2-CQD. The increase in barrier height helps in avoiding the recombination of photogenerated electron-hole pair. Because the CB of MoS_2 is less than LUMO of CQD and also VB of MoS_2 is higher than HUMO of CQD, the photogenerated electrons remains in MoS_2 and gets transported to metal contacts due to the applied external electric field and local electric field generated due to the barrier potential created between MoS_2 and CQD. Even though CQD is discretely distributed on MoS_2, there is larger portion of MoS_2 exposed to illumination which leads to higher responsivity values under visible illumination. So the role of CQD is two-fold: to absorb in UV range and creation of local electric fields which helps in efficient charge separation under visible and NIR illumination.

There has been recent reports on the fabrication of 2D-0D photodetectors featuring hybrids of MoS_2-PbS, MoS_2-HgTe, MoS_2-CdSe, WSe_2-PbS, and graphene-PbS [58- 62]. But, the quantum dots used for sensitization in all these cases are heavy-metal based limiting their usage in many applications because of their inherent toxicity even at low concentrations [7]. Furthermore, all the above report's usage of inorganic rigid substrates such as SiO_2 makes it difficult for its integration into flexible and wearable electronic applications. Table 1 displays a comparative reports on 2D-0D hybrid broadband photodetectors based on toxicity, substrate and the range of detection of electromagnetic spectrum wherein it is observed that most of the reported literature has limited range detection. Although MoS_2 with tailored size and thickness could be realized using CVD, the processing conditions like high temperature and limited choice of substrates imposes challenges for its large-scale production and practical applications [63]. Moreover, CVD growth is followed by transfer process and defining the metal contacts using electron beam lithography which not only leads to device to device variation in performance but also is expensive and time consuming. Herein, we utilize low cost cellulose paper as a substrate for device fabrication and simple solution processed hydrothermal method for direct growth of MoS_2 on cellulose paper. Further, hybrid of MoS_2-CQD was fabricated by drop casting CQD solution synthesized by natural chia seeds. The growth process can be extended to large area as well

as other functional materials of choice. Thus the work presented here is a major step ahead in fabrication of low cost flexible 2D-0D broadband photodetectors.

4.3.   Conclusion

In summary, we demonstrate for the first time fabrication of 2D MoS_2-CQD based flexible broadband photodetector wherein MoS_2 was grown on cellulose paper using simple and cost effective solution processed hydrothermal method and CQD were synthesized using one step pyrolytic process of natural chia seeds. Response under UV illumination was due to CQD and under visible and NIR illumination was due to MoS_2. Due to the discrete distribution of CQD and metal contacts on MoS_2 led to increase in the spectral selectivity of the fabricated MoS_2-CQD photodetector. Also, due to the difference in the fermi levels of CQD and MoS_2 led to the formation of unipolar junctions thereby creating local electric fields which assisted in effective charge separation under visible and NIR illumination. Responsivity calculated was for UV, visible and NIR respectively suggesting that the as fabricated photodetector was more responsive towards visible light when compared to UV and NIR illumination. The work presented is a major step ahead in fabrication of low cost cellulose paper based 2D-0D flexible broadband photodetector covering entire range of electromagnetic spectrum which finds numerous applications in the field of flexible and wearable electronics, security and optoelectronics.

4.4.   Experimental Section

Growth of MoS$_2$ on cellulose paper:

The growth of few-layered MoS_2 nanosheets was performed by a one-step hydrothermal method recently reported from our lab [22]. Briefly, a seed solution containing sodium molybdate ($Na_2MoO_4.2H_2O$) and thiourea (CH_4N_2S) in 1:2 ratio was prepared and the paper substrate was immersed in it. After 30 minutes, the paper substrate was dried in a convection oven at 80°C for an hour. The seed layer coated substrate was then subjected to hydrothermal treatment in a nutrient solution comprising of sodium molybdate and thiourea in a similar proportion as discussed earlier. The nutrient solution with the substrate was a loaded into a Teflon-lined autoclave followed by which the temperature was maintained at 200°C for 20 hours. The autoclave was then let to cool down naturally to room temperature after which the MoS_2 grown substrate was dried and stored for further usage.

Synthesis of carbon quantum dots:

The synthesis of carbon dots was performed by a one-step pyrolytic treatment of chia seeds. Edible, food-grade chia seeds were procured and used without further purification. Briefly, 500 mg of chia seeds was loaded in a ceramic crucible and carbonized at 350°C for 6 hours. The heating rate was maintained at 30°C/min. The end product was broken down into fragments by grinding and it was suspended in dichloromethane. This dispersion was centrifuged at 12,000 rpm for 20 minutes to remove the unreacted organic moieties and larger carbon agglomerates. The supernatant was separated and diluted for further usage. Schematic of the complete fabrication procedure is as shown in figure 1.

Fabrication of MoS$_2$-CQD flexible photodetector

MoS$_2$-cellulose paper was masked on two ends using Al foil and polyimide tape for defining the active and metal contact area. CQD solution was drop casted on MoS$_2$-cellulose paper followed by drying at 70°C for 30 minutes. The masking was removed to fabricate contacts using Ag paste.

Materials and characterization

Sodium molybdate and Thiourea were purchased from Sigma Aldrich and were used as received for the growth MoS2on cellulose paper. Chia seeds were purchased from local supermarket. The structural characteristics of the prepared hybrids were investigated using X'pert PRO X-Ray Diffraction (XRD) with Cu Ká radiation. Raman spectra were obtained from Raman spectrometer (Senterra inVia opus, Bruker) having an excitation wavelength of 532 nm. Field Emission Scanning Electron Microscopy (FESEM) analysis was performed by ZEISS Ultra-55 SEM to study morphology. UV-visible-NIR spectra was obtained using LAMBDA UV/Vis/NIR spectrophotometers (PerkinElmer). The electrical measurements were carried out with Keithley 4200 SCS instrument. The as-fabricated devices were tested for broadband photodetector application on illuminating UV, Visible and IR radiations. The lamp sources utilized for UV, Vis and IR illumination had a wavelength (ë) of 365 nm, 554 nm, and 780 nm respectively.

4.5. References

1. Zhang, X., Lai, Z., Tan, C., & Zhang, H. Solution-Processed Two-Dimensional MoS2 Nanosheets: Preparation, Hybridization, and Applications. *Angewandte Chemie International Edition*, **2016**, 55(31), 8816-8838.
2. Mak, K.F. Shan, J,Nat. Photonics.2016, 10,216.

3. Koppens, F. H. L., Mueller, T., Avouris, P., Ferrari, A. C., Vitiello, M. S., & Polini, M. Photodetectors based on graphene, other two-dimensional materials and hybrid systems. *Nature Nanotechnology*, **2014**, 9(10), 780-793.

4. Allain, A., Kang, J., Banerjee, K., & Kis, A. Electrical contacts to two-dimensional semiconductors. *Nature Materials*, **2015**, 14(12), 1195-1205.

5. Zhu, W. Low, T. Lee, Y.H. Wang, H. Farmer, D.B. Kong, J. Xia, F.Avouris, P,Nat.Commun.2014, 5.

6. Cheng, R., Jiang, S., Chen, Y., Liu, Y., Weiss, N., Cheng, H. C., & Duan, X. Few-layer molybdenum disulfide transistors and circuits for high-speed flexible electronics. *Nature communications,* **2014**, 5.

7. Lim, S. Y., Shen, W., & Gao, Z. Carbon quantum dots and their applications. *Chemical Society Reviews,* **2015**, 44(1), 362-381.

8. Wang, F., Xie, Z., Zhang, H., Liu, C. Y., & Zhang, Y. G. Highly luminescent organosilane-functionalized carbon dots. *Advanced Functional Materials*, **2011**, 21(6), 1027-1031.

9. Xu, X., Ray, R., Gu, Y., Ploehn, H. J., Gearheart, L., Raker, K., & Scrivens, W. A. Electrophoretic analysis and purification of fluorescent single-walled carbon nanotube fragments. *Journal of the American Chemical Society*, **2004**, 126(40), 12736-12737.

10. Cremar, L. D., Acosta-Martinez, J., Villarreal, A., Salinas, A., & Lozano, K. Mechanical and electrical characterization of carbon nanofibers produced from water soluble precursors. *Materials Today Communications*, **2016**, 7, 134-139.

11. Himaja, A. L., Karthik, P. S., & Singh, S. P. Carbon dots: the newest member of the carbon nanomaterials family. *The Chemical Record*, **2015**, 15(3), 595-615.

12. Valappil, M. O., Pillai, V. K., & Alwarappan, S. *Applied Materials Today*, **2017**

13. Bourlinos, A. B., Rathi, A. K., Gawande, M. B., Hola, K., Goswami, A., Kalytchuk, S.,& Giannelis, E. P. Fe (III)-functionalized carbon dots—Highly efficient photoluminescence redox catalyst for hydrogenations of olefins and decomposition of hydrogen peroxide. *Applied Materials Today*, **2017**, 7, 179-184.

14. Bailón-Ruiz, S., & Perales-Pérez, O. J. Generation of singlet oxygen by water-stable CdSe (S) and ZnSe (S) quantum dots. *Applied Materials Today*, **2017**, 9, 161-166.

15. Tang, Q., Zhu, W., He, B., & Yang, P. Rapid Conversion from Carbohydrates to Large-Scale Carbon Quantum Dots for All-Weather Solar Cells. *ACS Nano*, **2017**, 11(2), 1540-1547.

16. Wang, Y., & Hu, A. Carbon quantum dots: synthesis, properties and applications. *Journal of Materials Chemistry C*, **2014**, 2(34), 6921-6939.

17. Xie, C., Nie, B., Zeng, L., Liang, F. X., Wang, M. Z., Luo, L., & Yu, S. H. Core–shell heterojunction of silicon nanowire arrays and carbon quantum dots for photovoltaic devices and self-driven photodetectors. *ACS Nano*, **2014**, 8(4), 4015-4022.

18. Guo, D.Y. Shan, C.X. Qu, S.N.Shen, D.Z,Sci. Rep.2014, 4.

19. Lee, S. W., Choi, K. J., Kang, B. H., Lee, J. S., Kim, S. W., Kwon, J. B., & Kang, S. W. Low dark current and improved detectivity of hybrid ultraviolet photodetector based on carbon-quantum-dots/zinc-oxide-nanorod composites. *Organic Electronics*, **2016**, 39, 250-257.

20. Lopez-Sanchez, O., Lembke, D., Kayci, M., Radenovic, A., & Kis, A. Ultrasensitive photodetectors based on monolayer MoS2. *Nature nanotechnology*, **2013**, 8(7), 497-501.

21. Sahatiya, P., & Badhulika, S. One-step in situ synthesis of single aligned graphene–ZnO nanofiber for UV sensing. *RSC Advances*, **2015**, 5(100), 82481-82487.

22. Tobjörk, D., & Österbacka, R. Paper electronics. *Advanced Materials*, **2011**, 23(17), 1935-1961.

23. Guo, H., Yeh, M. H., Zi, Y., Wen, Z., Chen, J., Liu, G., & Wang, Z. L. Ultralight Cut-Paper-Based Self-Charging Power Unit for Self-Powered Portable Electronic and Medical Systems. *ACS Nano*, **2017**, 11(5), 4475-4482.

24. Down, M. P., Foster, C. W., Ji, X., & Banks, C. E. Pencil drawn paper based supercapacitors. *RSC Advances*, **2016**, 6(84), 81130-81141.

25. Sahatiya, P., & Badhulika, S. Fabrication of a solution-processed, highly flexible few layer MoS 2 (n)–CuO (p) piezotronic diode on a paper substrate for an active analog frequency modulator and enhanced broadband photodetector. *Journal of Materials Chemistry C*, **2017**, 5(44), 11436-11447.

26. Sahatiya, P., & Badhulika, S. Discretely distributed 1D V2O5 nanowires over 2D MoS2 nanoflakes for an enhanced broadband flexible photodetector covering the ultraviolet to near infrared region. *Journal of Materials Chemistry C*, **2017**, 5(48), 12728-12736.

27. Park, S. Y., Lee, H. U., Park, E. S., Lee, S. C., Lee, J. W., Jeong, S. W., & Lee, J. Photoluminescent green carbon nanodots from food-waste-derived sources: large-scale synthesis, properties, and biomedical applications. *ACS Applied Materials & Interfaces*, **2014**, 6(5), 3365-3370.

28. Gomathi, P. T., Sahatiya, P., & Badhulika, S. Large-Area, Flexible Broadband Photodetector Based on ZnS–MoS2 Hybrid on Paper Substrate. *Advanced Functional Materials*, **2017**, 27(31).

29. Jones, S. S., Sahatiya, P., & Badhulika, S. One step, high yield synthesis of amphiphilic carbon quantum dots derived from chia seeds: a solvatochromic study. *New Journal of Chemistry*, **2017**, 41(21), 13130-13139.

30. Wickramaratne, N. P., Perera, V. S., Park, B. W., Gao, M., McGimpsey, G. W., Huang, S. D., & Jaroniec, M. Graphitic mesoporous carbons with embedded prussian blue-derived iron oxide nanoparticles synthesized by soft templating and low-temperature graphitization. *Chemistry of Materials*, 2013, 25(14), 2803-2811.

31. Oza, G. Ravichandran, M. Merupo, V.I. Shinde, S. Mewada, A. Ramirez, J.T. Velumani, S. Sharon, M.Sharon, M,Sci.Rep.2013,6.

32. Xiao, J., Choi, D., Cosimbescu, L., Koech, P., Liu, J., & Lemmon, J. P. Exfoliated MoS2 nanocomposite as an anode material for lithium ion batteries. *Chemistry of Materials*, 2010, 22(16), 4522-4524.

33. Xie, J., Zhang, J., Li, S., Grote, F., Zhang, X., Zhang, H., & Xie, Y. Controllable disorder engineering in oxygen-incorporated MoS2 ultrathin nanosheets for efficient hydrogen evolution. *Journal of the American Chemical Society*, **2013**, 135(47), 17881-17888.

34. Yan, Y., Xia, B., Ge, X., Liu, Z., Wang, J. Y., & Wang, X. Ultrathin MoS2 nanoplates with rich active sites as highly efficient catalyst for hydrogen evolution. *ACS Applied Materials & Interfaces*, **2013**, 5(24), 12794-12798.

35. Lei, B., Li, G. R., & Gao, X. P. Morphology dependence of molybdenum disulfide transparent counter electrode in dye-sensitized solar cells. *Journal of Materials Chemistry A*, **2014**, 2(11), 3919-3925.

36. Ganatra, R., & Zhang, Q. Few-layer MoS2: a promising layered semiconductor. *ACS Nano*, **2014**, 8(5), 4074-4099.

37. Li, H., Tsai, C., Koh, A. L., Cai, L., Contryman, A. W., Fragapane, A. H., & Nørskov, J. K. Activating and optimizing MoS2 basal planes for hydrogen evolution through the formation of strained sulphur vacancies. *Nature Materials*, **2016**, 15(1), 48-53.

38. Liu, K. K., Zhang, W., Lee, Y. H., Lin, Y. C., Chang, M. T., Su, C. Y., & Lai, C. S. Growth of large-area and highly crystalline MoS2 thin layers on insulating substrates. *Nano Letters*, **2012**, 12(3), 1538-1544.

39. Qu, S., Wang, X., Lu, Q., Liu, X., & Wang, L. A Biocompatible Fluorescent Ink Based on Water-Soluble Luminescent Carbon Nanodots. *Angewandte Chemie*, **2012**, 124(49), 12381-12384.

40. Liu, R., Wu, D., Liu, S., Koynov, K., Knoll, W., & Li, Q. An aqueous route to multicolor photoluminescent carbon dots using silica spheres as carriers. *Angewandte Chemie*, **2009**, 121(25), 4668-4671.

41. Bao, L., Liu, C., Zhang, Z. L., & Pang, D. W. Photoluminescence-Tunable Carbon Nanodots: Surface-State Energy-Gap Tuning. *Advanced Materials*, **2015**, 27(10), 1663-1667.

42. Xie, J., Zhang, J., Li, S., Grote, F., Zhang, X., Zhang, H., & Xie, Y. Controllable disorder engineering in oxygen-incorporated MoS2 ultrathin nanosheets for efficient hydrogen evolution. *Journal of the American Chemical Society*, **2013**, 135(47), 17881-17888.

43. Choi, Y. H., Lee, J., Parija, A., Cho, J., Verkhoturov, S. V., Al-Hashimi, M., & Banerjee, S. An in Situ Sulfidation Approach for the Integration of MoS2 Nanosheets on Carbon Fiber Paper and the Modulation of Its Electrocatalytic Activity by Interfacing with n C60. *ACS Catalysis*, **2016**, 6(9), 6246-6254.

44. Dhenadhayalan, N., Lin, K. C., Suresh, R., & Ramamurthy, P. Unravelling the multiple emissive states in citric-acid-derived carbon dots. *The Journal of Physical Chemistry C*, **2016**, 120(2), 1252-1261.

45. Lim, Y. R., Song, W., Han, J. K., Lee, Y. B., Kim, S. J., Myung, S., & Lim, J. Wafer-Scale, Homogeneous MoS2 Layers on Plastic Substrates for Flexible Visible-Light Photodetectors. *Advanced Materials*, **2016**, 28(25), 5025-5030.

46. Ganiga, M., & Cyriac, J. FRET based ammonia sensor using carbon dots. *Sensors and Actuators B: Chemical*, **2016**, 225, 522-528.

47. Wang, K., Wang, J., Fan, J., Lotya, M., O'Neill, A., Fox, D., & Zhang, H. Ultrafast saturable absorption of two-dimensional MoS2 nanosheets. *ACS nano*, **2013**, 7(10), 9260-9267.

48. Li, N., Than, A., Wang, X., Xu, S., Sun, L., Duan, H., & Chen, P. Ultrasensitive profiling of metabolites using tyramine-functionalized graphene quantum dots. *ACS nano*, **2016**, 10(3), 3622-3629.

49. Li, H., Yu, K., Lei, X., Guo, B., Fu, H., & Zhu, Z. Hydrothermal synthesis of novel MoS2/BiVO4 hetero-nanoflowers with enhanced photocatalytic activity and a mechanism investigation. *The Journal of Physical Chemistry C*, **2015**, 119(39), 22681-22689.

50. Salehi, S., & Saffarzadeh, A. Atomic defect states in monolayers of MoS2 and WS2. *Surface Science*, **2016**, 651, 215-221.

51. Kufer, D., Lasanta, T., Bernechea, M., Koppens, F. H., & Konstantatos, G. Interface engineering in hybrid quantum dot–2D phototransistors. *ACS Photonics*, **2016**, 3(7), 1324-1330.

52. Borse, V., Thakur, M., Sengupta, S., & Srivastava, R. N-doped multi-fluorescent carbon dots for 'turn off-on'silver-biothiol dual sensing and mammalian cell imaging application. *Sensors and Actuators B: Chemical*, **2017**, 248, 481-492.

53. Hao, Y., Gan, Z., Zhu, X., Li, T., Wu, X., & Chu, P. K. Emission from trions in carbon quantum dots. *The Journal of Physical Chemistry C*, **2015**, 119(6), 2956-2962.

54. Wang, W., Cheng, L., & Liu, W. Biological applications of carbon dots. *Science China Chemistry*, **2014**, 57(4), 522-539.

55. Stach, R., Krebs, P., Jones, F., & Mizaikoff, B. Observing non-classical crystallisation processes in gypsum via infrared attenuated total reflectance spectroscopy. *CrystEngComm*, **2017**, 19(1), 14-17.

56. Chen, H. C., Yang, H. W., Yang, K. H., Chen, C. H., Hou, C. C., & Tu, Y. M. Facile preparation of electroactive graphene derivative and its potential application in electrochemical detection. *Sensors and Actuators B: Chemical*, **2017**, 240, 1153-1159.

57. Ryu, J., Lee, E., Lee, K., & Jang, J. A graphene quantum dots based fluorescent sensor for anthrax biomarker detection and its size dependence. *Journal of Materials Chemistry B*, **2015**, 3(24), 2015, 4865-4870.

58. Kufer, D., Nikitskiy, I., Lasanta, T., Navickaite, G., Koppens, F. H., & Konstantatos, G. Hybrid 2D–0D MoS2–PbS quantum dot photodetectors. *Advanced Materials*, **2015**, 27(1), 176-180.

59. Huo, N. Gupta, S. Konstantatos, G, Adv. Mater.2017, 29.

60. Ra, H. S., Kwak, D. H., & Lee, J. S. A hybrid MoS2 nanosheet–CdSe nanocrystal phototransistor with a fast photoresponse. *Nanoscale*, **2016**, 8(39), 17223-17230.

61. Hu, C. Dong, D. Yang, X.Qiao, K. Yang, D. Deng, H. Yuan, S. Khan, J. Lan, Y. Song, H. Tang, J, Adv. Funct. Mater.2016, 27, 2, 1603605.

62. Konstantatos, G., Badioli, M., Gaudreau, L., Osmond, J., Bernechea, M., De Arquer, F. P. G., & Koppens, F. H. Hybrid graphene-quantum dot phototransistors with ultrahigh gain. *Nature nanotechnology*, **2012**, 7(6), 363-368.

63. Zhang, X., Lai, Z., Tan, C., & Zhang, H. Solution-Processed Two-Dimensional MoS2 Nanosheets: Preparation, Hybridization, and Applications. *Angewandte Chemie International Edition*, **2016**, 55(31), 8816-8838.

Chia seeds

Carbon soot

CQD solution

Cellulose paper

MoS$_2$-Cellulose paper

(a) Pyrolysis of chia seeds 350⁰ C for 6 hours
(b) Separation and purification
(c) Hydrothermal synthesis of MoS$_2$
(d) Drying of MoS$_2$ grown on Cellulose Paper
(e) Masking and drop casting of CQD
(f) Drying of MoS$_2$-CQD and establishment of contacts using Silver paste
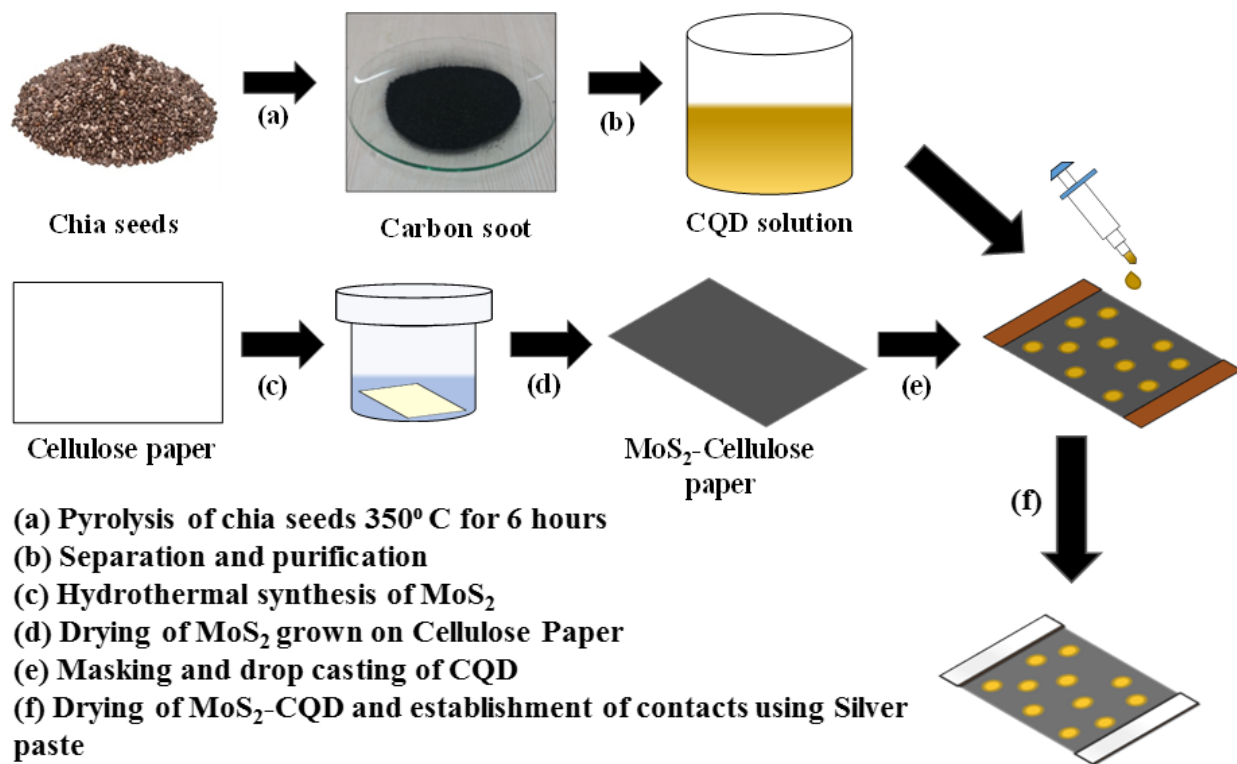
Figure 4.1. Schematic of the fabrication step of flexible MoS$_2$/CQD broadband photodetector
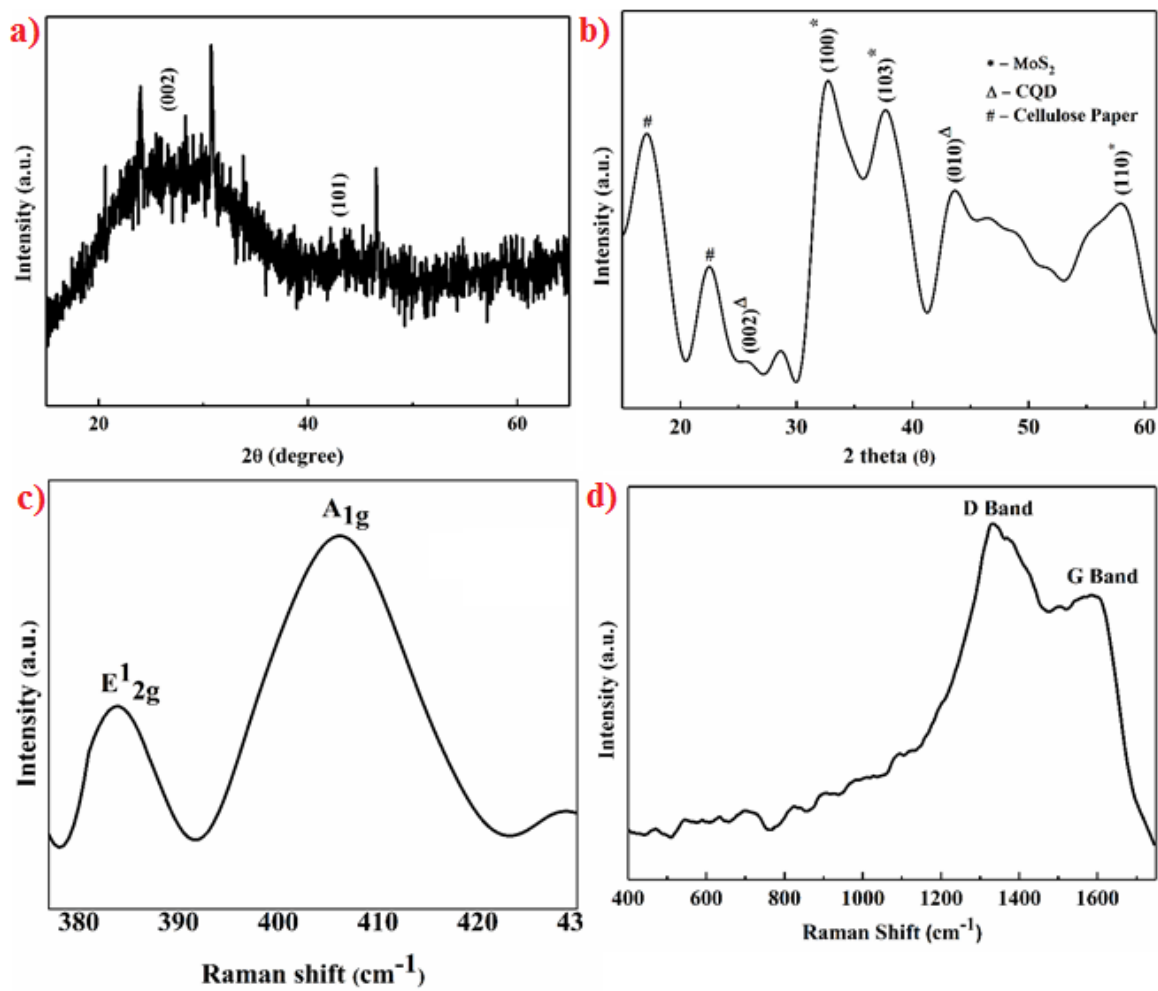
Figure 4.2. XRD of a) pristine CQD b) MoS_2/CQD hybrid c) Raman spectra for MoS_2/CQD demonstrating the peaks for MoS_2 d) showing the peaks of CQD
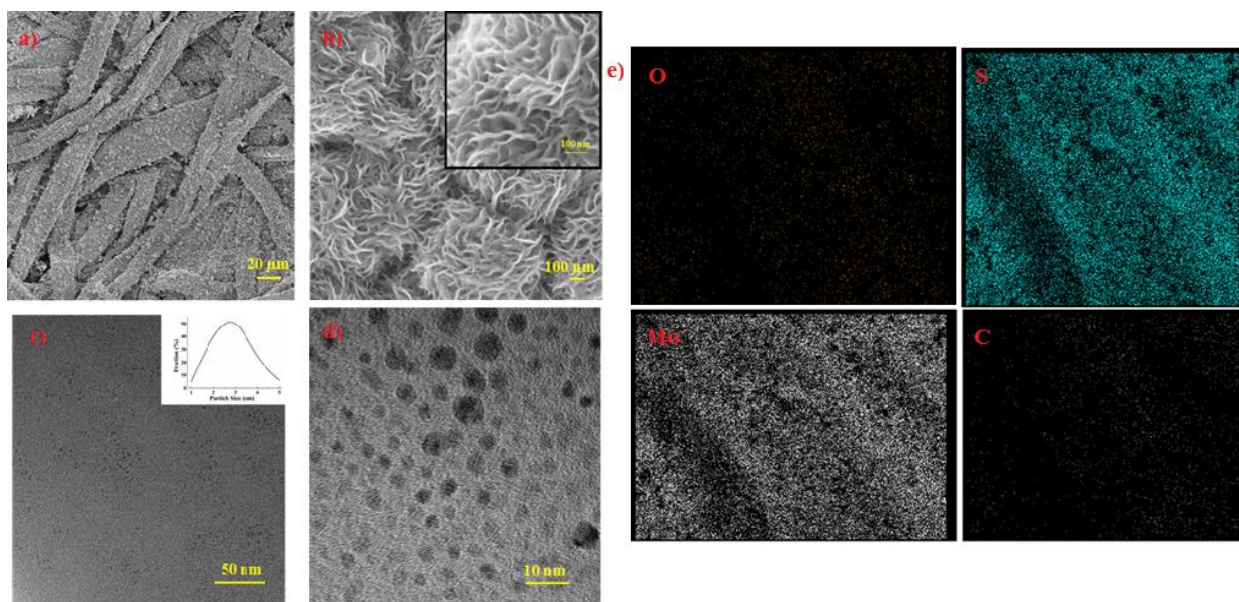
Figure 4.3. FESEM of a) MoS_2 on cellulose paper wherein microfiber morphology of cellulose paper is clearly visible b) High magnification image of MoS_2 on cellulose paper showing nanosheets morphology of MoS_2 c) TEM image of CQD showing the spherical morphology. Inset shows the distribution of diameter d) High magnification TEM image of CQD e) Elemental mapping of MoS_2/CQD wherein discrete distribution of CQD on MoS_2
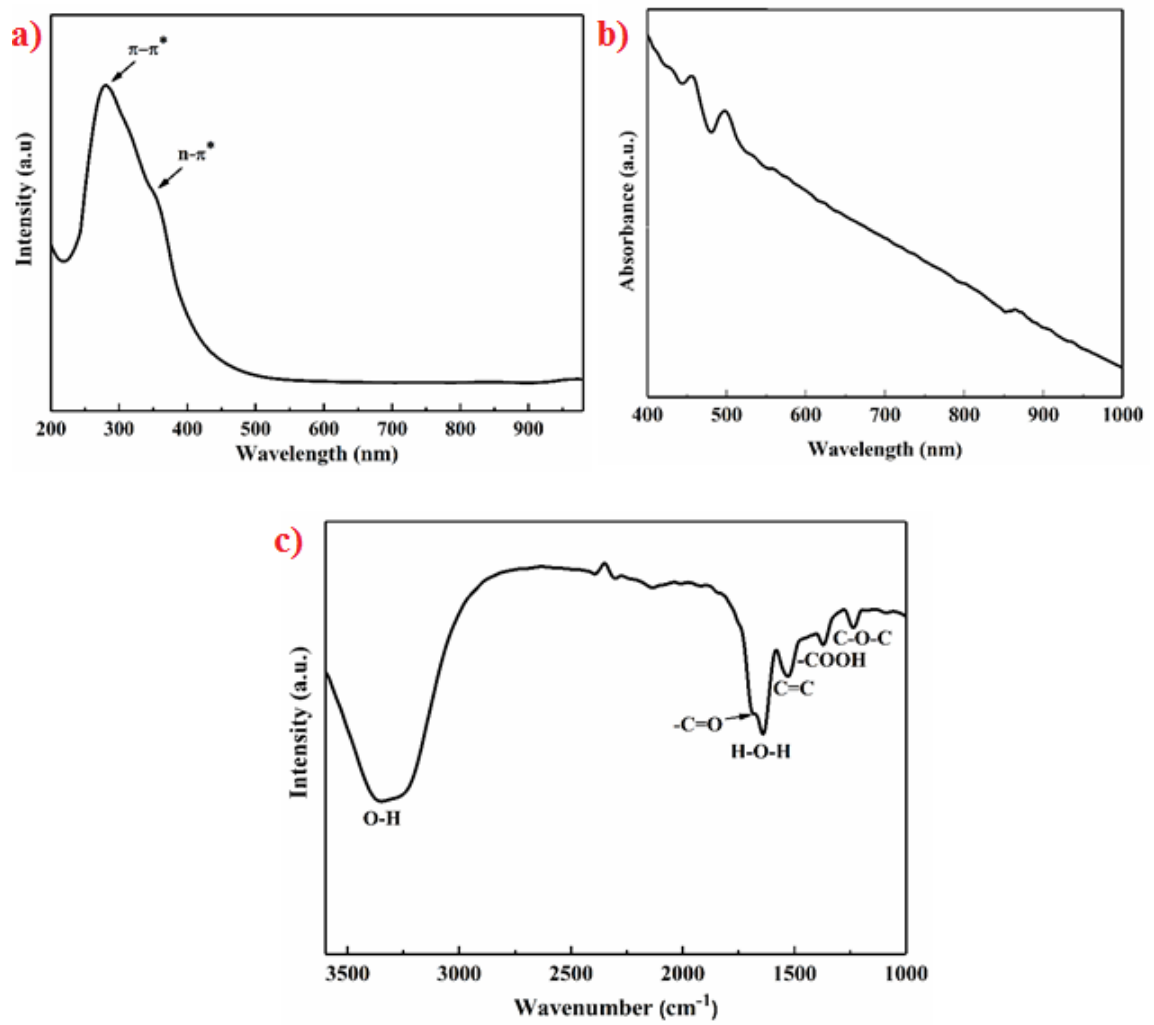
Figure 4.4. UV-vis-NIR spectra of a) pristine CQD b) pristine MoS2 c) FTIR spectra of MoS$_2$/CQD.
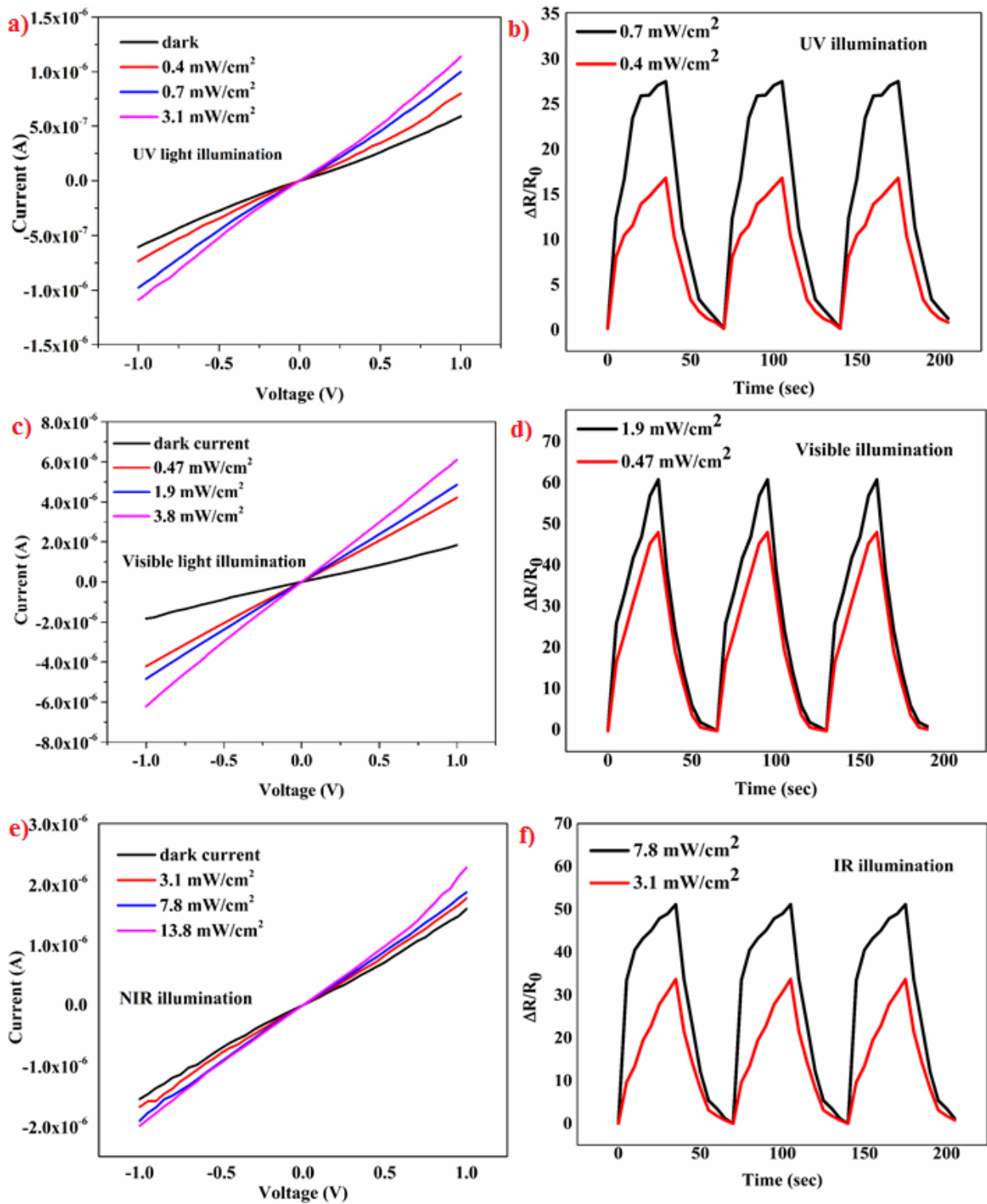
Figure 4.5. a) IV characteristic of MoS_2/CQD under different intensity of UV illumination b) temporal response of MoS_2/CQD under different intensities of UV illumination c) IV characteristic of MoS_2/CQD under different intensity of visible illumination d) temporal response of MoS_2/CQD under different intensities of visible illumination e) IV characteristic

of MoS$_2$/CQD under different intensity of NIR illumination f) temporal response of MoS$_2$/CQD under different intensities of NIR illumination
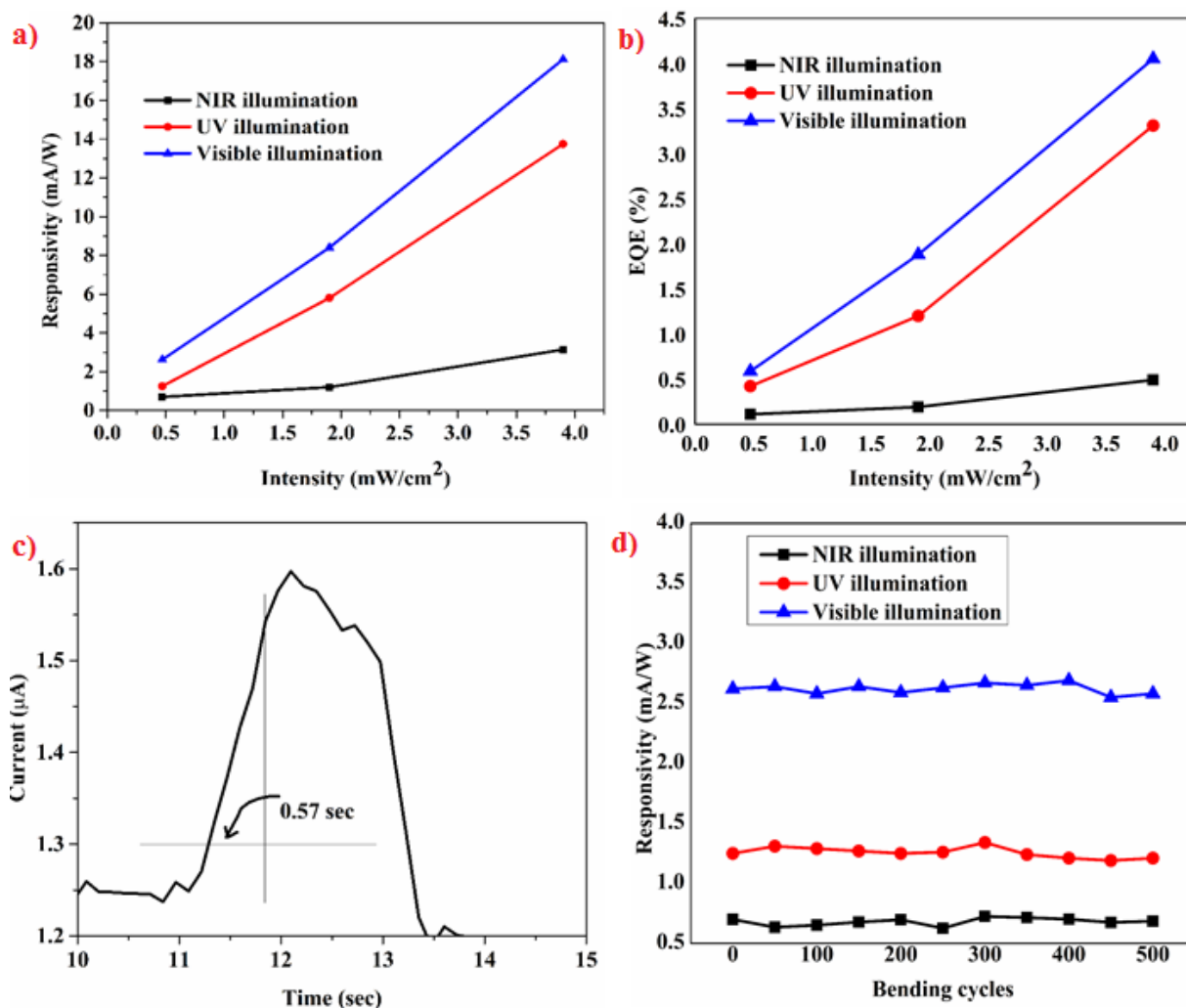
Figure 4.6. a) Responsivities v/s different intensities of UV, visible and NIR showing highest responsivities for visible illumination b) EQE v/s different intensities of UV, visible and NIR showing highest responsivities for visible illumination c) Graph showing the calculation for response time for visible light illumination d) Responsivities v/s bending cycles under UV, vis and NIR showing negligible change
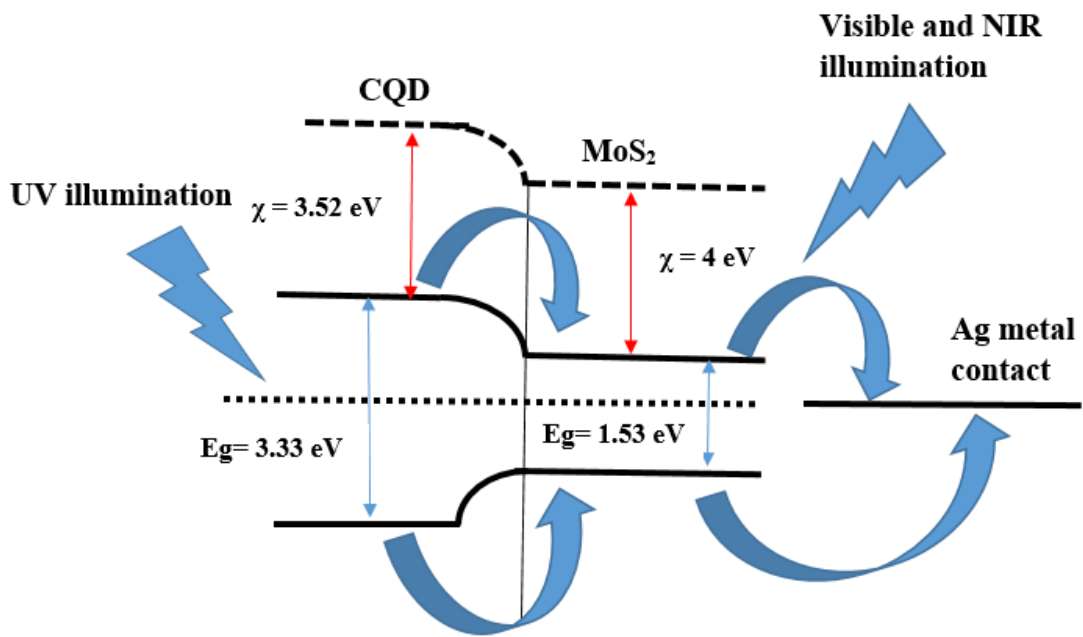
Figure 4.7. Schematic showing the energy band diagram of MoS$_2$/CQD and charge transport under UV, visible and NIR illumination

Material composition (2D/0D)	Substrate	Toxic/Non-Toxic	Range of detection	Ref
MoS$_2$-PbS	Silicon	Toxic	Visible-NIR	[50]
MoS$_2$-HgTe	Silicon	Toxic	Short and mid-range IR	[51]
MoS$_2$-CdSe	Silicon	Toxic	Visible	[52]
WSe$_2$-PbS	Silicon	Toxic	Visible-NIR	[53]
Graphene-PbS	Silicon	Toxic	Visible	[54]
MoS$_2$-CQD	Cellulose paper	Non-toxic	UV-visible-NIR	**This work**

Table 4.1: Comparative table for different 2D-0D hybrids for broadband photodetectors

Chapter 5

Flexible substrate based 2D ZnO (n)/ Graphene (p) rectifying junction as enhanced broadband photodetector using strain modulation

Abstract

Strain modulation is considered to be an effective way to modulate the electronic structure and carrier behavior in flexible semiconductors heterojunctions. In this work, 2D Graphene (Gr)/ZnO junction was successfully fabricated on flexible eraser substrate using simple, low-cost solution processed hydrothermal method and has been utilized for broadband photodetection in the UV to visible range at room temperature. Optimization in terms of process parameters were done to obtain 2D ZnO over 2D graphene which shows decrease in bandgap and broad absorption range from UV to visible. Under compressive strain piezopotential induced by the atoms displacements in 2D ZnO, 87% enhanced photosensing for UV light was observed under 30% strain. This excellent performance improvement can be attributed to piezopotential induced under compressive strain in 2D ZnO which results in lowering of conduction band energy and raising the schottky barrier height

thereby facilitating electron-hole pair separation in 2D Gr/ZnO junction. Detailed mechanism studies in terms of density of surface states and energy band diagram is presented to understand the proposed phenomena. Results provide an excellent approach for improving the optoelectronic performance of 2D Gr/ZnO interface which can also be applied to similar semiconductor heterojunctions.

5.1. Introduction

Semiconductor interfaces are vital components for fabricating electronic and optoelectronic devices. Properties of interfaces between two hetero-structured semiconductors play an important role in modulating the electronic structure and carrier behavior in modern nanoelectronics devices [1]. Thus ability to precisely tailor the properties of the semiconductor interfaces provides lot of possibilities to enhance performance or add new functionalities altogether in devices. Semiconductor interface engineering is gaining interest in recent years to rationally design and fabricate novel nanoelectronics devices. There are different ways to modulate the electronic structure and carrier behavior in semiconductors which include structure design [2], surface treatment [3], chemical doping [4] etc. Strain modulation is considered as an effective means of tuning the electronic structure and carrier behavior in semiconductors. Moreover, at nanoscale, materials possess higher toughness and hence strain modulation effect could be more significant [5]. There are reports on properties enhancement in nanostructures via strain modulation which include bandgap opening in graphene and ZnO [6], light emission properties in ZnO and Si nanowires [7], GaAs [8] and CdS microwires [9] etc. However, all the literature are on rigid silicon substrates wherein the strain is induced due to the process which makes it difficult to understand the physical mechanism. To overcome this drawback, mechanical tensile strain like wafer bending method was employed. But due to the rigid nature of silicon, high strain cannot be applied. Hence there is a need to develop flexible p-n junctions where the interface properties could be modulated by applying external mechanical strain.

Unique properties of graphene such as high conductivity, mechanical flexibility, high carrier mobility, optical transparency and linear energy band dispersion have established it as a superior material for electronic and optoelectronic applications [10]. ZnO has been one of the metal oxide semiconductors that continues to gain researchers attention over decades due to its excellent properties like wide bandgap (3.37 eV), high exciton binding energy (60meV), and transparent conductivity. Such novel electrical and optical properties of nanostructured ZnO has led to its use in electronics, optoelectronics and photonics [11].

Various morphologies of ZnO nanostructures [11] have been synthesized using methods such as sol-gel, Chemical Vapor Deposition (CVD), electrodeposition, aqueous solution precipitation, micro-emulsions and hydrothermal method [12]. Of all, hydrothermal method is found to be effective because of its enhanced reactivity of reactants, low energy consumption and versatility in synthesis of different morphologies by controlling the hydrothermal parameters such as temperature, growth time, pH, and concentration. Also hydrothermal method provides the ability to control the interface reactions occurring in the solution, by which one can tune the size and crystallinity of the materials being synthesized [13]. Recently, 2D ZnO nanostructures have instilled great interest due to their exceptional properties such as high anisotropy, large surface area, high surface charge density, smaller charge transfer resistance and better electron-hole separation [14-15].

Gr/ZnO hybrids are found to be better than their individual counterparts due to the combination of properties like the large surface area of Gr and ZnO nanostructures, high charge carrier mobility of Gr and superior wavelength selectivity of nanostructured ZnO [16-17]. Although there are numerous reports on the synthesis of 1D ZnO, its low internal surface area and complexity in establishing electrical contacts restricts its widespread use in CMOS devices unlike 2D ZnO [14]. Moreover, due to the coupled piezoelectronic and semiconducting properties, when a 2D ZnO crystal is subjected to strain, piezopotential is generated due to the polarization of ions [18]. By taking advantage of this phenomena, the charge carrier transport behavior can be effectively tuned across a p-n junction.

In this work, we have fabricated 2D ZnO/Gr heterojunction on polyvinyl chloride (PVC) eraser substrate for broadband photodetection in the UV to visible range at room temperature. Most of the commercially available eraser contains PVC which makes the eraser non-biodegradable. Recently, new class of PVC free eraser are commercially available which are not only bio-degradable but also softer than PVC free containing erasers. Softer erasers are easily bendable which helps in ease of inducing strain as compared to PVC containing erasers. Gr was deposited on PVC free eraser substrate using rolling pin method wherein Teflon cylinder was rolled over Gr on eraser. Low-temperature hydrothermal synthesis was performed for the growth of 2D ZnO over Gr. Strain induced piezo-polarization charges in 2D ZnO were utilized to effectively modulate the optoelectronic process such as charge separation in 2D Gr/ZnO p-n junction. As per our knowledge this is first report on fabrication of p-n junction using 2D ZnO (n)/ graphene (p) on flexible eraser substrate. The results of the electrical characterizations suggest that as

fabricated device holds promise for future flexible electronic device applications such as photodetectors, energy harvesters and rectifiers.

5.2.　　　　Results and Discussions

Compared to the electronic devices that are fabricated on conventional rigid substrates, flexible and wearable electronic devices are gaining interest because of potential applications such as photodetectors energy harvesters, energy storage and rectifiers.

To fabricate electronic devices such as junctions and schottky barriers, complicated clean room processes such as lithography and evaporation are employed on both rigid and flexible substrates. These processes are not only expensive but also energy inefficient. Moreover, not all flexible substrate are microfabrication compatible thereby limiting their scope in the choice of materials for fabrication. Eraser despite providing high external mechanical stress is not microfabrication compatible. Hence there is a need to develop fabrication processes for substrates that are not microfabrication compatible to fabricate electronic devices. Recently, a novel rolling pin method for deposition of MWCNTs on polyimide and eraser substrate was demonstrated by our group [19-20]. Details regarding the fabrication procedure and the parameters of rolling pin on eraser substrate can be found in a recent report by our group [20]. In brief, rolling pin was performed manually and to reduce the variation caused due to the manual operation pre-compaction press was performed with pressure of $5Kg/cm^2$. Increasing the rolling pin cycles deforms the eraser and increasing the pre-compaction pressure stiffens the eraser which then loses the flexibility property. Using similar method, we deposited Gr on PVC free eraser which acted as a substrate for growing 2D ZnO. Variations in thickness and resistance with rolling pin cycles was observed and it was found that as rolling pin cycles increases there is increase in resistance and decrease in thickness of Gr film. To study the effect of rolling pin on Gr film, raman spectroscopy was performed. Typical raman peaks were observed for both pristine and rolled pin Gr with later introducing more defects. For pristine Gr I_D/I_G ratio was found to be 0.201 while I_D/I_G ratio for rolled pin Gr film was found to be 0.405. Rolling pin is a manual process where pressure variations are difficult to control. To reduce the variations caused in rolling pin press, Gr/eraser substrate was compressed using pre-compaction mechanical press with pressure of $5Kg/cm^2$. Details regarding rolling pin and pre-compaction press can be found in [20]. Graphs illustrating variation in thickness and variations of Gr film with rolling pin cycles and details of raman spectra of pristine and rolled pin Gr film can be found in supplementary information (SI) as fig S1 and fig S2

respectively. It is important to note that the Gr used in this work is not monolayer but few layer Gr. The current response would definitely depend on the number of Gr layers and it would be rather good for monolayer Gr due to its high mobility and ballistic transport. Also pre-compaction press would not induce defect on monolayer Gr. But growing large area monolayer Gr using CVD is still a challenge and it involves complicated transfer process which leads to device to device variation.

Gr deposited eraser was utilized for growing 2D ZnO nanostructures. 2D ZnO can be synthesized in alkaline medium with OH- ions suppressing the growth in polar plane (0001) [21]. The morphology of as-prepared Gr/ZnO films were analyzed using FESEM. Fig 5.2 depicts the different types of ZnO nanostructures obtained on varying the concentration of precursors, pH and temperature of synthesis. An insight into the crystal structure of ZnO would enable a better understanding of the growth mechanism. ZnO consists of three basal planes namely (0001), (20) and (010). The (0001) plane is polar whereas the other two basal planes are non-polar. Although there exist three planes for the growth of ZnO, the growth along the polar plane i.e. (0001) is more viable thermodynamically because of their higher surface energy than the other non-polar planes [22]. The (0001) plane is terminated by $Zn2+$ ions and O2- ions and because of their difference in ionic nature, the effective charge would vary along the two ends of these planes [23]. The Zn^{2+} terminated (0001) plane has higher surface charge and thus growth propagates along the c-axis [24]. Moreover, in this study, nanorods of ZnO were synthesized by using equimolar concentration of precursors without addition of buffers. This suggests that the growth along c-axis might have been due to the lower concentration of OH- ions in precursor solution which has facilitated the preferential growth along (0001) plane rather than (20) plane. These factors make nanorods as the intrinsic growth habit of ZnO along (0001) plane [21]. Fig 5.2a) displays the growth of such nanorods lying perpendicular to the substrate. By increasing the precursor concentration it was observed that nucleation rate of ZnO increases thereby attaining supersaturation. Under these conditions, ZnO nuclei aggregates and nanorods would continue to grow along c-axis which leads to the formation of flower-like structures [24] as shown in fig 5.2b and fig 5.2c. Meanwhile, when the pH of the precursor solution was increased to 8, the concentration of OH- ions increases. OH- ions, in this case, serves the dual role of acting as a capping agent and providing hydroxyl ions for the formation of ZnO nanobelts as shown in fig 5.2d,e . Increasing the pH to 10 generated excess of OH- ions which were attracted to the positively charged (0001) plane thereby limiting the growth of crystal along c-axis. [23]. Hence, on increasing the concentration of OH- ions in solution, the growth direction was controlled to

an extent to be along the a-axis (<2$\bar{1}\bar{1}$0> direction) [21] which leads to the formation of 2D ZnO as shown in fig 5.2 f,g,h. Fig 2f) shows uniform growth of 2D ZnO over the entire surface of Gr and figs 2g,h) show higher magnification images wherein 2D ZnO nanoflakes are clearly visible.

UV-visible spectrum of 2D ZnO (pH = 10) is as shown in fig 5.3 wherein strong absorbance is observed in UV range (300-370 nm) whereas weak and constant absorption is observed in visible region. The absorbance in visible region is attributed to the quantum confinement effect of 2D ZnO. It is well reported theoretically that bandgap in 2D ZnO decreases as compared to its bulk counterparts [25]. The inset of fig 5.3 shows tauc's plot wherein the optical bandgap of 2D ZnO was calculated to be 2.8 eV. The decrease in the bandgap is an indication that there is a blue shift in the absorbance spectra and hence 2D ZnO can be utilized as a broadband photodetector which absorbs in both UV and visible region.

I-V characteristic of Gr/ZnO under dark is as shown in fig 5.4a) which clearly demonstrates well defined rectifying junction formation with turn on voltage of 0.6V. To test the rectifying behavior was not due to Ag/Gr or Ag/ZnO, experiment were performed on individual Ag/Gr and Ag/ZnO and I-V characteristics were plotted which demonstrated ohmic behavior. To further analyze the transport mechanism of Gr/ZnO p-n junction, thermionic emission theory was employed and can be expressed as

$$I = Io \exp\left(\frac{q(V-IR)}{\eta KT}\right) \tag{1}$$

$$Io = AA^* T^2 exp\left(\frac{-q\Phi_B}{KT}\right), \quad A^* = \frac{4\pi q m^* K^2}{h^3} \tag{2}$$

$$\eta = \frac{q}{KT}\frac{dV}{d(lnI)} \tag{3}$$

where K is Boltzmann constant, q is electronic charge, R is series resistance, η is ideality factor, which is the measure of how much the diode deviates from ideal diode, T is absolute temperature, A is junction area, A* is Richardson constant which is theoretically estimated to be 32 for ZnO considering m* = 0.27 mo. Φ is the barrier height at zero bias, Io is reverse saturation current and h is Planck's constant

The ideality factor η and schottky barrier height Φ were found to be 1.65 and 0.335 eV respectively by linear fit of natural log plot of voltage versus current. The ideality factor deviates from ideal value of 1 which can be attributed to the defects introduced in 2D ZnO

during hydrothermal process, disordered structure, barrier inhomogeneity and presence of surface states which provides multiple current pathways in the interface [26]. The calculated Φ value of 0.335 eV was higher than difference between the work function of graphene (4.5 eV) and electron affinity of ZnO (4.3 eV). This could be possibly due to the oxidation of graphene under atmospheric conditions making it p-type and as a result raises the schottky barrier height. In order to investigate the Gr/ZnO interface quality, voltage dependence of η was studied and utilized to calculate the density of interface states. Density of interface state can be estimated by following equation assuming the surface states to be in equilibrium:

$$Nss = \frac{\varepsilon_i}{t_i q^2}(\eta - 1) - \frac{\varepsilon_{sc}}{Wq^2} \tag{4}$$

where ε_i and t_i are relative dielectric constant and thickness of interfacial layer respectively. Since the 2D Gr/ZnO interface is exposed to air, the value of ε_i was assumed to be permittivity of free space and thickness to be 5A° [27]. ε_{sc} and W are the relative dielectric constant and depletion width respectively. The value of ε_{sc} is considered to be 114 ε_o [28] and width of the depletion region to be 160 nm [29]. Using equation 5 and the bias voltage dependence of Nss, Nss (V) can be obtained by following equation

$$Ec - E = \Phi_B - qV \tag{5}$$

Fig 5.4b) shows the plot of Nss (V) as a function of Ec-E wherein a peak at 0.14 indicates that deep level traps are located at 0.14eV below the conduction band energy. High surface states are attributed to disordered junction which is linked to high dislocation density which is commonly observed in ZnO composites [30]. The interface play an important role in charge transfer to or from conduction band and are responsible for η value greater than unity. It acts as an interfacial layer through which carrier can be easily transport through metal or inter transition band and are responsible for photogenerated carriers in visible range.

Fig 5.4c) represents the performance of 2D graphene/ZnO photodetector under 365 nm UV illumination at a reverse bias of -1V for various intensities wherein it was observed that as intensity increases there is an increase in the photogenerated current. The same was repeated for visible light which demonstrated similar response as shown in fig 5.4d). It should be noted that intensities used for visible photodetector are 10 fold more than UV light intensities due to the fact that at lower intensities of visible light, weak response was observed. Even though the intensities of visible light are high compared to UV light, it is in

range for defense/security related applications. The response time for the UV and visible photodetector was found to be 0.6 sec and 0.84 sec respectively and was calculated by time difference taken by the sensor to reach from 10% to 90 % of the maximum value. The exceptional performance of as fabricated device can be attributed to broad absorption spectra of 2D ZnO from UV to visible light, deep level travels below the conduction ban, effective electron-hole pair separation by built-in electric field due to reverse biasing and lastly fast carrier transport in graphene as evident from the reported literature in other graphene based heterojunctions photodetectors.

To further study the performance of the 2D Gr/ZnO PD under strain, different strains were applied on the fabricated device and was systematically analyzed as shown in fig 5.5. It was observed that length of the eraser had significant impact on the amount of maximum strain that it can induce due to bending. Derivation of relationship between strain and the bend angle can be found in SI. The IV characteristics of 2D Gr/ZnO junction under various strains were investigated wherein strain was applied by bending the eraser substrate by the clip holder. As seen in fig 5.5a), on application of strain, current value decreases and turn on voltage of 2D Gr/ZnO junction increases which was due to the variation in the schottky barrier height at the 2D Gr/ZnO interface. Under compressive strain, negative polarization charges are developed in 2D Gr/ZnO due to relative displacement of Zn and O atoms in ZnO which generates piezoelectric field and can lower the conduction band thereby increasing the schottky barrier height. It should be noted that change in current, under strain, is not due to contact area change of Gr and 2D ZnO. This is because as fabricated device shows non symmetrical change between forward and reverse current which should be symmetrical if it was from contact area change. Variations in the schottky barrier height can be calculated from IV characteristics using above mentioned thermionic emission theory. Assuming the Richardson coefficient, junction area and the ideality factor are constant under different strain, $\Delta\Phi$ can be expressed as

$$\ln\left(\frac{I\varepsilon}{Io}\right) = -\frac{q}{KT}\Delta\emptyset \qquad (6)$$

Where $I\varepsilon$ and Io are the currents measured at fixed bias with and without strain. As seen from the fig 5.5b), $\Delta\Phi$ shows linear increase with increase in strain confirming the interface properties of 2D Gr/ZnO can be modulated by application of external strain.

Temporal response of the strained 2D Gr/ZnO device under fixed illumination (both UV and visible) was studied and is as shown in fig 5.5c and fig 5.5d respectively. As shown in figure different strains ranging from 5% to 30 % were applied to the 2D Gr/ZnO PD and significant enhancement in the current was observed. Current enhancement was observed more for UV light compared to visible light which can be attributed to the fact that absorption is more in UV range rather than visible range. 87% current enhancement was observed for UV light under 30 % strain. As can be seen from UV-Vis spectra of 2D ZnO (fig 5.3), absorbance is more in UV range compared to visible. Higher the absorbance greater is the photo-current enhancement. The experiment was repeated for 3 devices and similar response was observed. Graph demonstrating the variation in the current levels with varying strain for 3 devices can be found in SI as fig S3. Responsivity of the photodetector was calculated as a function of strain for both UV and visible light and is as shown in fig 5.5f. Responsivity can be defined as photocurrent generated per unit power of the incident light on the photodetector and is given by

$$R = I_\lambda /(P_\lambda S) \qquad\qquad (7)$$

Where I_λ is the photocurrent and is given by (Iillumination - Idark), P_λ is the incident light intensity and S is the effective illuminated area. As can be seen from fig 5.5f), responsivity increases on application of strain which can be attributed to the effective separation of photogenerated charge carriers. High responsivity for UV light as compared to visible light was observed which is due to the fact that absorbance of 2D Gr/ZnO PD is more in UV range than visible range.

The mechanism of excellent broadband photosensing property of the 2D Gr/ZnO PD and enhancement in the performance due to strain modulation can be understood and explained by a schematic diagram of electronic band structure at the interface of 2D Gr/ZnO. As shown in fig 5.6 when contact is formed between Gr and ZnO, electrons from ZnO diffuses to Gr until fermi level is aligned thereby forming a depletion region and built-in electric field. Under UV illumination and reverse bias, photogenerated electrons are separated by built-in electric field, resulting in photocurrent generation. Out of the two materials, Gr and ZnO, absorption happens in ZnO and hence most of the optoelectronic process mostly happens in ZnO necessary for piezopotential modulation. Under compressive strain, ZnO generates negative piezopotential wherein the charges starts accumulating near the conduction band, thereby lowering the conduction band energy. Lowering of the conduction band energy causes the schottky barrier to raise which increases the width of depletion

region favorable for separation of photo-generated electron-hole pairs and thus improve the sensitivity of the Gr/ZnO PD. Moreover, negative piezopotential mainly distributes on the surface of 2D ZnO which is favorable for effective charge separation at the Gr/ZnO interface [31].

Various methods have been reported for the synthesis of ZnO/Gr hybrids. [32] reported the growth of ZnO nanostructures on Gr using thermal CVD process. [33] demonstrated the growth of ZnO by thermal oxidation of Zn followed by CVD growth of Gr. Electrospinning method was used for the in-situ synthesis of Gr/ZnO nanofibers [34]. ZnO was grown hydrothermally on Gr, obtained by Low-Pressure CVD (LPCVD) [35]. Most of the procedures reported for the synthesis of Gr/ZnO hybrids involve the use of sophisticated equipments, transfer of Gr to arbitrary substrates which is not only tedious but lacks controllability in terms of variation in device performance. Of all the reported methods, hydrothermal method is found to be effective because of its enhanced reactivity of reactants, low energy consumption and possibility to obtain different morphologies by controlling process parameters such as temperature, growth time, pH, and concentration. Furthermore, hydrothermal method provides the ability to control the interface reactions occurring in the solution, by which one can tune the size and crystallinity of the materials being synthesized [36-37]. In this work, we demonstrated a simple, low-cost solution processed fabrication of 2D Gr/ZnO rectifying junction for enhanced broadband photodetection under strain modulation. The results give an insight into the functionality of 2D Gr/ZnO for broadband photodetection ranging from UV to visible region. Such a versatile, reproducible technique for fabrication of flexible 2D Gr/ZnO on unconventional substrates is a major step ahead in research related to Gr/ZnO interfaces and their applications in analog, optoelectronics devices and sensors.

5.3.   Conclusion

In summary, 2D Gr/ZnO rectifying junction is fabricated on PVC free pencil eraser using simple, low-cost solution processed hydrothermal method and has been utilized for broadband photodetection. Ideality factor and schottky barrier height of the as fabricated Gr/ZnO junction was calculated to be 1.65 and 0.335 eV. Barrier inhomogeneities at the Gr/ZnO interface are the cause for high η and Nss. Decrease in the bandgap (2.8 eV) was observed for 2D ZnO which was responsible for broadband photodetection in UV and visible region. 87% enhanced photosensing for UV light was observed under 30% strain. The performance improvement is due to

piezopotential induced under compressive strain in 2D ZnO which results in lowering of conduction band energy and raising the schottky barrier height thereby facilitating electron-hole pairs separation in 2D Gr/ZnO junction. The work demonstrated here paves way for developing highly scalable flexible semiconductor heterojunctions on unconventional substrates for use in optoelectronics, analog electronics and sensors.

5.4. Experimental Section

Substrate preparation

PVC free pencil eraser (10mm x 5mm x 3mm) was used as the substrate for the growth of ZnO on Gr. The substrate was cleaned using ultrasonication with Deionized (DI) water followed by propanol. The substrate was then dried in ambient atmosphere. The as-cleaned PVC free pencil eraser substrate was used for further process of device fabrication.

Deposition of Gr on pencil eraser

Deposition of Gr on eraser substrate was carried out by a novel solvent free rolling pin method recently reported from our lab [19-20]. In brief, different weights of Gr were deposited using rolling pin to form Gr film on eraser. Optimization in terms of Gr weight, thickness (t) and resistance (R) of the Gr film was done to ensure uniform deposition with desired thickness. 200 cycles of rolling pin were found to be optimal for producing the desired resistance and thickness of the Gr film. To remove the unattached Gr from the eraser substrate, it was gently washed with DI water and was dried at 70°C for 30 minutes. As prepared Gr deposited PVC free eraser was then utilized for 2D ZnO growth.

The Growth of 2D ZnO on Gr-pencil eraser.

Hydrothermal synthesis route was followed for the selective growth of 2D ZnO on Gr-pencil eraser substrate. In brief, a portion of Gr-pencil eraser was masked using aluminum foil and polyimide (PI) tape. Gr-pencil eraser was soaked in seed solution consisting of 1mM zinc acetate dihydrate $[Zn(CCH_3O_2)_2.(H_2O)_2]$ and 10 mL of propanol for 30 minutes. The Gr-pencil eraser substrate was then dried at 70°C for 2 hours. Hydrothermal process was optimized in terms of concentrations, pH and temperature for growth of 2D ZnO on 2D Gr wherein masked Gr-pencil eraser was placed in a nutrient solution made of different

concentrations (1:1, 1:2 and 1:3) of [Zn(CCH$_3$O$_2$)$_2$.(H$_2$O)$_2$] and hexamethylenetetramine (HMTA) in 20mL of DI water with different pH (8 & 10), for 5 hours at different temperatures (70-90°C). The obtained samples were washed with DI water and dried at 70°C, thus resulting in the growth of ZnO on Gr-pencil eraser. Schematic of the complete fabrication procedure is as shown in fig 1.

5.5. References

1. Sahatiya, P., & Badhulika, S. UV/ozone assisted local graphene (p)/ZnO (n) heterojunctions as a nanodiode rectifier. Journal of Physics D: Applied Physics, 2016, 49(26), 265101.

2. Yang, C., Zhong, Z., & Lieber, C. M. Encoding electronic properties by synthesis of axial modulation-doped silicon nanowires. Science, 2005, 310(5752), 1304-1307.

3. Li, C., Zhang, D., Lei, B., Han, S., Liu, X., & Zhou, C. Surface treatment and doping dependence of In2O3 nanowires as ammonia sensors. The Journal of Physical Chemistry B, 2003, 107(45), 12451-12455.

4. Zhou, C., Kong, J., Yenilmez, E., & Dai, H. Modulated chemical doping of individual carbon nanotubes. Science, 2000, 290(5496), 1552-1555.

5. Stolyarov, V. V., Valiev, R. Z., & Zhu, Y. T. Enhanced low-temperature impact toughness of nanostructured Ti. Applied physics letters, 2006, 88(4), 041905.

6. Fu, X., Jacopin, G., Shahmohammadi, M., Liu, R., Benameur, M., Ganiere, J. D. & Yu, D. Exciton drift in semiconductors under uniform strain gradients: application to bent ZnO microwires. ACS nano, 2014, 8(4), 3412-3420.

7. Hong, K. H., Kim, J., Lee, S. H., & Shin, J. K. Strain-driven electronic band structure modulation of Si nanowires. Nano letters, 2008, 8(5), 1335-1340.

8. Signorello, G., Karg, S., Björk, M. T., Gotsmann, B., & Riel, H. Tuning the light emission from GaAs nanowires over 290 meV with uniaxial strain. Nano letters, 2013, 13(3), 917-924.

9. Fu, Q., Zhang, Z. Y., Kou, L., Wu, P., Han, X., Zhu, X., & Yu, D. Linear strain-gradient effect on the energy bandgap in bent CdS nanowires. Nano Research, 2011, 4(3), 308-314.

10. Liu, R., You, X. C., Fu, X. W., Lin, F., Meng, J., Yu, D. P., & Liao, Z. M. Gate modulation of graphene-ZnO nanowire Schottky diode. Scientific reports, 2015, 5.

11. Baruah, S., & Dutta, J. Hydrothermal growth of ZnO nanostructures. Science and Technology of Advanced Materials, 2008, 013001.

12. Li, X., He, G., Xiao, G., Liu, H., & Wang, M. Synthesis and morphology control of ZnO nanostructures in microemulsions. Journal of colloid and interface science, 2009, 333(2), 465-473.

13. Feng, S., & Xu, R. New materials in hydrothermal synthesis. Accounts of chemical research, 2001, 34(3), 239-247.

14. Vabbina, P. K., Kaushik, A., Pokhrel, N., Bhansali, S., & Pala, N. Electrochemical cortisol immunosensors based on sonochemically synthesized zinc oxide 1D nanorods and 2D nanoflakes. Biosensors and Bioelectronics, 2015, 63, 124-130.

15. Liu, J., Hu, Z. Y., Peng, Y., Huang, H. W., Li, Y., Wu, M.,& Su, B. L. 2D ZnO mesoporous single-crystal nanosheets with exposed {0001} polar facets for the depollution of cationic dye molecules by highly selective adsorption and photocatalytic decomposition. Applied Catalysis B: Environmental, 2016, 181, 138-145.

16. Liu, J., Lu, R., Xu, G., Wu, J., Thapa, P., & Moore, D. Development of a Seedless Floating Growth Process in Solution for Synthesis of Crystalline ZnO Micro/Nanowire Arrays on Graphene: Towards High-Performance Nanohybrid Ultraviolet Photodetectors. Advanced Functional Materials, 2013, 23(39), 4941-4948.

17. Lin, J. C., Huang, B. R., & Lin, T. C. Hybrid structure of graphene sheets/ZnO nanorods for enhancing electron field emission properties. Applied Surface Science, 2014, 289, 384-387.

18. Zhang, Y., Yan, X., Yang, Y., Huang, Y., Liao, Q., & Qi, J. Scanning probe study on the piezotronic effect in ZnO nanomaterials and nanodevices. Advanced Materials, 2012, 24(34), 4647-4655

19. Sahatiya, P., & Badhulika, S. Solvent-free fabrication of multi-walled carbon nanotube based flexible pressure sensors for ultra-sensitive touch pad and electronic skin applications. RSC Advances, 2016, 6(98), 95836-95845.

20. Sahatiya, P., & Badhulika, S. Eraser-based eco-friendly fabrication of a skin-like large-area matrix of flexible carbon nanotube strain and pressure sensors. Nanotechnology, 2017, 28(9), 095501.

21. Cao, B., & Cai, W. From ZnO nanorods to nanoplates: chemical bath deposition growth and surface-related emissions. The Journal of Physical Chemistry C, 2008, 112(3), 680-685.

22. Kong, X. Y., & Wang, Z. L. Polar-surface dominated ZnO nanobelts and the electrostatic energy induced nanohelixes, nanosprings, and nanospirals. Applied physics letters, 2004, 84(6), 975-977.

23. Alenezi, M. R., Henley, S. J., Emerson, N. G., & Silva, S. R. P. From 1D and 2D ZnO nanostructures to 3D hierarchical structures with enhanced gas sensing properties. Nanoscale, 2014, 6(1), 235-247.

24. Peng, W., Qu, S., Cong, G., & Wang, Z. Synthesis and structures of morphology-controlled ZnO nano-and microcrystals. Crystal growth & design, 2006, 6(6), 1518-1522.

25. Topsakal, M., Cahangirov, S., Bekaroglu, E., & Ciraci, S. First-principles study of zinc oxide honeycomb structures. Physical Review B, 2009, 80(23), 235119.

26. Zhou, J., Gu, Y., Fei, P., Mai, W., Gao, Y., Yang, R.,& Wang, Z. L. Flexible piezotronic strain sensor. Nano letters, 2008, 8(9), 3035-3040.

27. Jung, S., Lee, S. N., & Kim, H. Surface states and carrier transport properties at semipolar (11–22) n-type GaN planes. Applied Physics Letters, 2013, 102(15), 151603.

28. Jammula, R. K., Pittala, S., Srinath, S., & Srikanth, V. V. Strong interfacial polarization in ZnO decorated reduced-graphene oxide synthesized by molecular level mixing. Physical Chemistry Chemical Physics, 2015, 17(26), 17237-17245.

29. Saw, K. G., Tneh, S. S., Yam, F. K., Ng, S. S., & Hassan, Z. Determination of Acceptor Concentration, Depletion Width, Donor Level Movement and Sensitivity Factor of ZnO on Diamond Heterojunction under UV Illumination. PloS one, 2014, 9(2), e89348.

30. Faraz, S. M., Willander, M., & Wahab, Q. Interface state density distribution in Au/n-ZnO nanorods Schottky diodes. In IOP Conference Series: Materials Science and Engineering, 2012, 34(1), 012006.

31. Zhao, M. H., Wang, Z. L., & Mao, S. X. Piezoelectric characterization of individual zinc oxide nanobelt probed by piezoresponse force microscope. Nano Letters, 2004, 4(4), 587-590.

32. Lin, J., Penchev, M., Wang, G., Paul, R. K., Zhong, J., Jing, X., & Ozkan, C. S. Heterogeneous Graphene Nanostructures: ZnO Nanostructures Grown on Large-Area Graphene Layers. Small, 2010, 6(21), 2448-2452.

33. Boruah, B. D., Ferry, D. B., Mukherjee, A., & Misra, A. Few-layer graphene/ZnO nanowires based high performance UV photodetector. Nanotechnology, 2015, 26(23), 235703.

34. Sahatiya, P., & Badhulika, S. One-step in situ synthesis of single aligned graphene–ZnO nanofiber for UV sensing. RSC Advances, 2015, 5(100), 82481-82487.

35. Liu, J., Zhang, Z., Lv, Y., Yan, J., Yun, J., Zhao, W., & Zhai, C. Synthesis and characterization of ZnO NWAs/graphene composites for enhanced optical and field emission performances. Composites Part B: Engineering, 2016, 99, 366-372.

36. Lu, C. H., & Yeh, C. H. Influence of hydrothermal conditions on the morphology and particle size of zinc oxide powder. Ceramics International, 2000, 26(4), 351-357.

37. Feng, S., & Xu, R. New materials in hydrothermal synthesis. Accounts of chemical research, 2001, 34(3), 239-247.

(a) Rolling pin (b) Masking (c) Dipping into seed solution (d) Drying (e) Hydrothermal growth (f) Drying
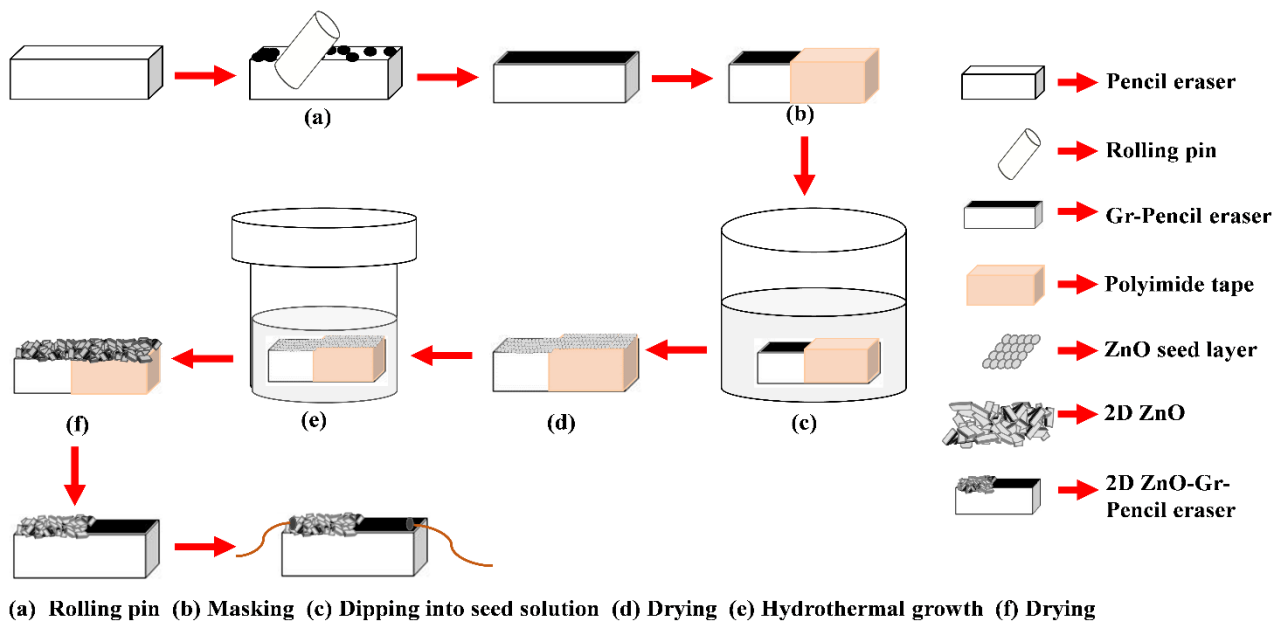
Figure 5.1: Schematic of the fabrication process of 2D ZnO/Gr p-n junction on PVC free eraser substrate
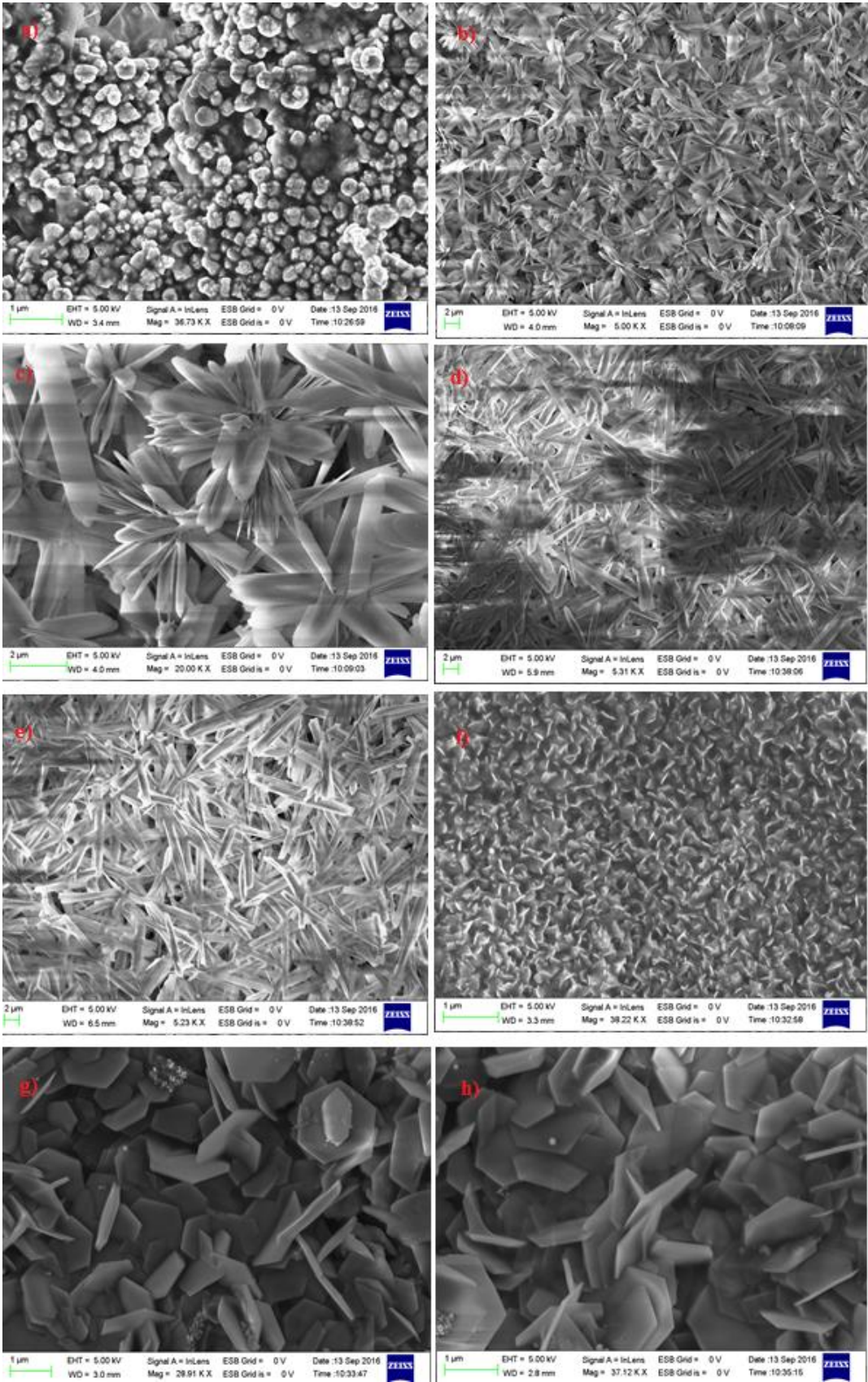
Figure 5.2: FESEM images of ZnO showing different morphologies a) ZnO nanorods (equimolar concentrations) b,c) flowerlike ZnO (1:3 concentrations) d,e) ZnO nanobelts (pH = 8) and f,g,h) 2D ZnO (pH = 10).
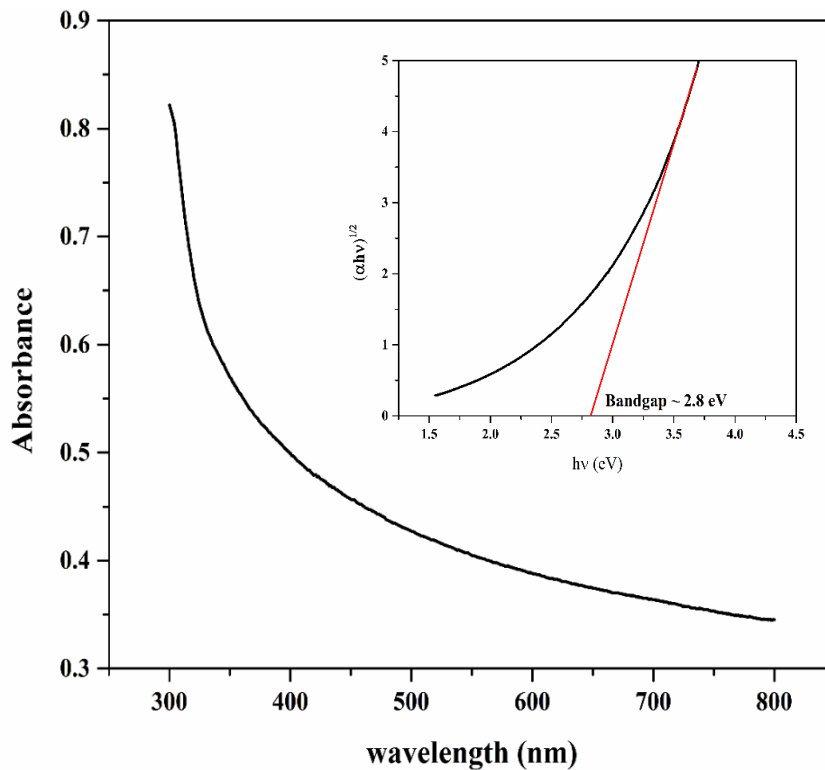
Figure 5.3: UV-vis spectra of 2D ZnO (pH = 10) showing strong absorption in UV range whereas weak and constant absorption in visible range. Inset is the tauc's plot of 2D ZnO wherein optical bandgap of 2D ZnO was calculated to be 2.8 eV.
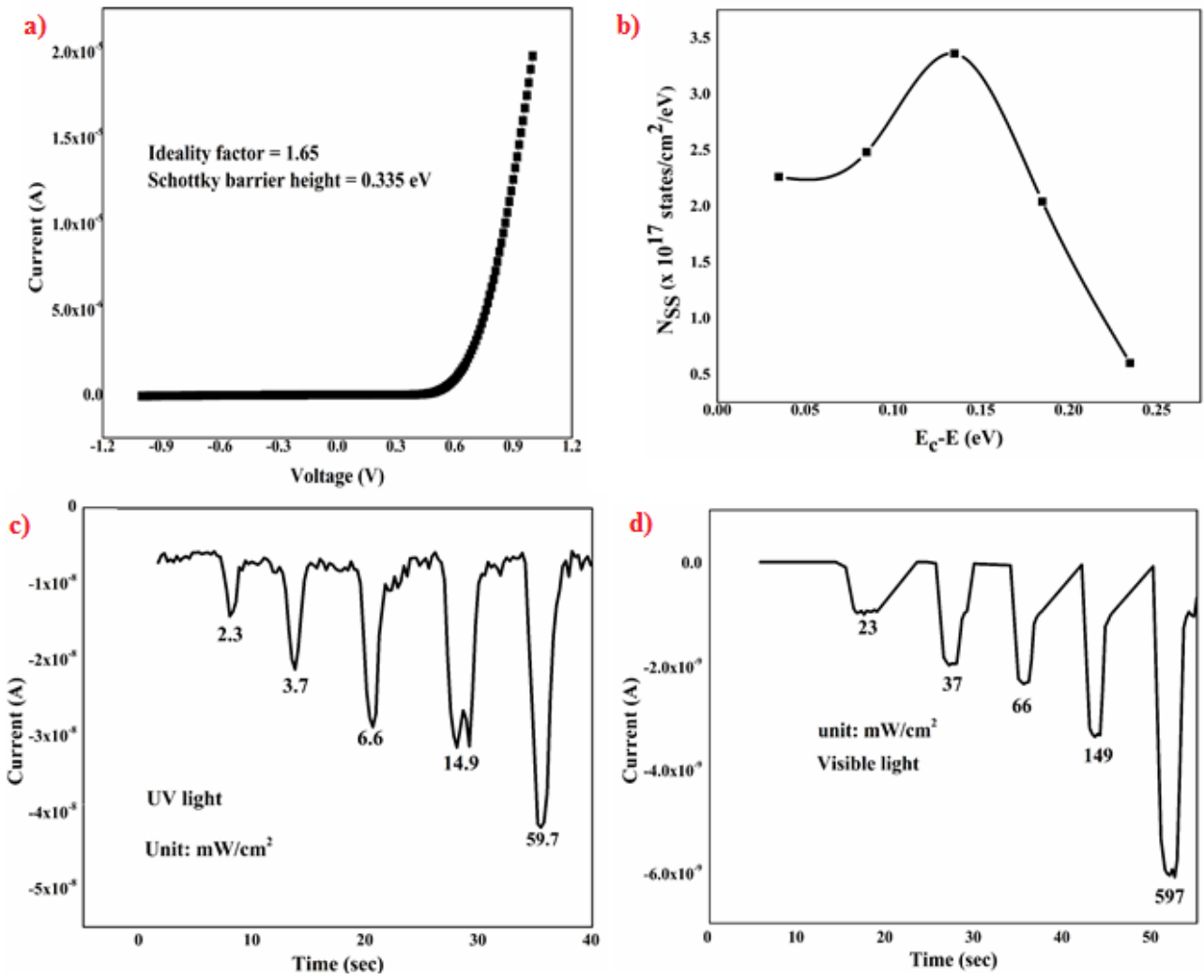
Figure 5.4: a) I-V characteristic of 2D Gr/ZnO p-n junction demonstrating rectifying behavior b) Plot of Nss vs Ec-E c) temporal response of 2D gr/ZnO PD for different intensities of UV light and d) temporal response of 2D Gr/ZnO PD for different intensities of visible light.

95
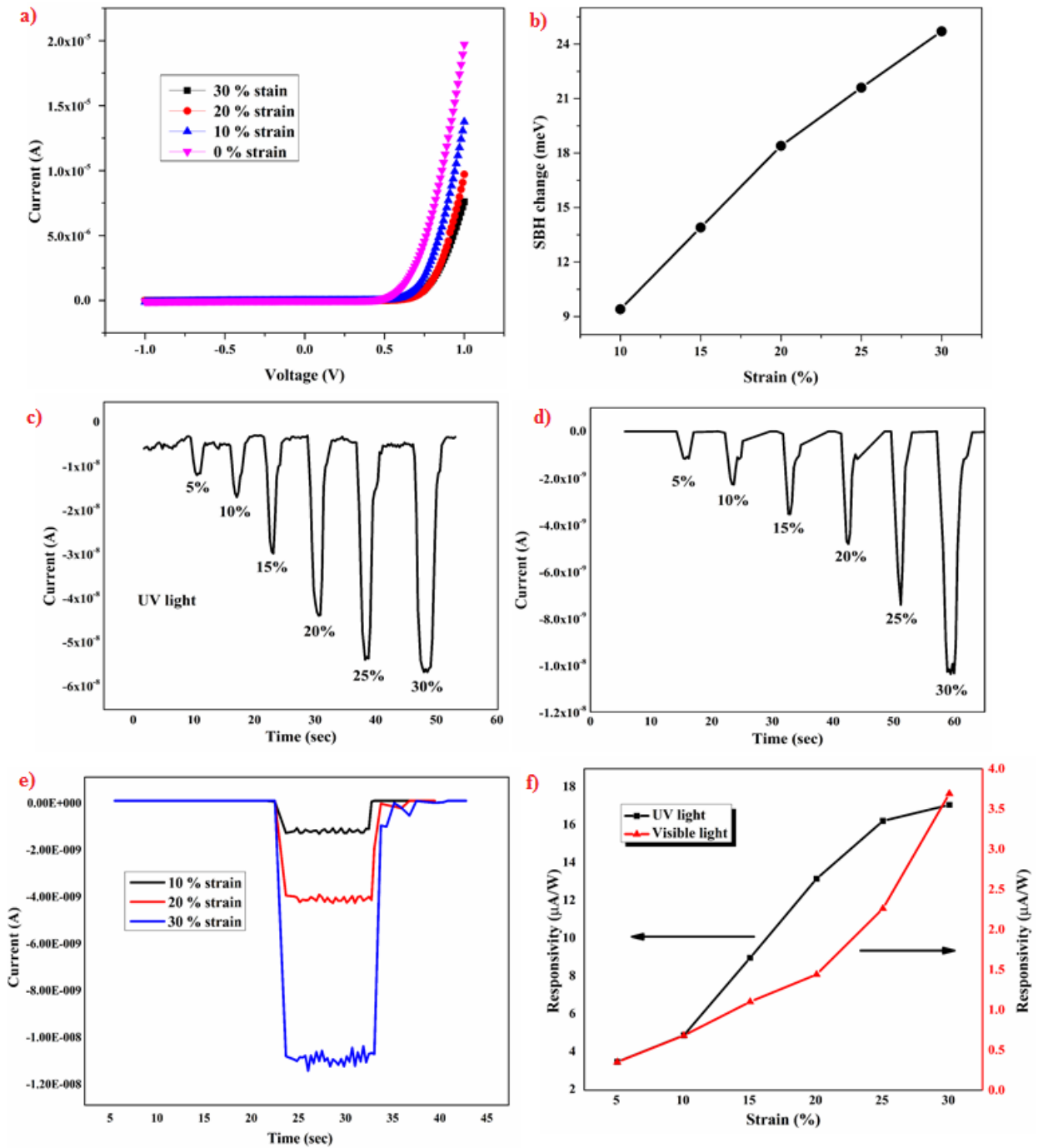
Figure 5.5: a) I-V characteristic of 2D Gr/ZnO under compressive strain b) graph of SBH change vs strain c) temporal response of 2D Gr/ZnO at fixed illumination of 66mW/cm2 UV light under various strains d) temporal response of 2D Gr/ZnO at fixed illumination of 66mW/cm2 visible light under various strains e) temporal response showing change in current levels at various strains at fixed intensity of 66 mW/cm^2 f) graph of responsivity vs strain for fixed illumination of 66 mW/cm^2 UV and visible light.

96
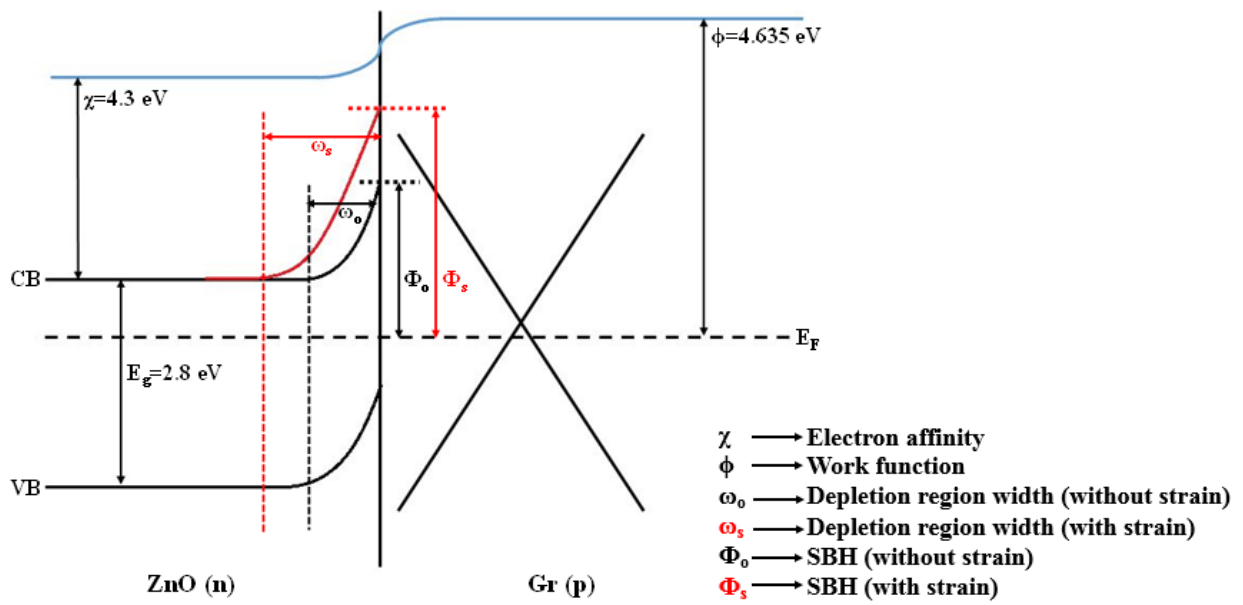
Figure 5.6: Energy band diagram of 2D Gr/ZnO p-n junction

Chapter 6

Fabrication of solution processed, highly flexible few layer MoS2 (n)-CuO (p) piezotronic diode on paper substrate for active analog frequency modulator and enhanced broadband photodetector

Abstract

In this work, we demonstrate for the first time, solution processed MoS_2 (n)-CuO (p) piezotronic diode on flexible paper substrate for enhanced broadband photodetector and active analog frequency modulator by application of external mechanical strain. There are no reports on solution processed large area fabrication of MoS_2 based heterojunctions wherein the external mechanical strain modulates the transport properties at the device level which can be further utilized at circuit level for frequency modulation. When external strain is applied, because of the non-centrosymmetric structure of MoS_2, the piezopotential induced adjusts the band structure at the junction and broadens the depletion region which decreases the depletion capacitance of the diode. The widening of the depletion region improves the separation of photo-generated carriers and enhances the performance of diode under both visible and NIR illumination. The fabricated piezotronic diode exhibited higher responsivity towards visible light illumination when compared to NIR illumination. The

Responsivity of the fabricated piezotronic diode increased by 69.7% under 2% strain. Such a versatile technique for fabrication of diode and its utilization at both device and circuit levels is a major step ahead in flexible and wearable electronics with applications ranging from digital, analog and optoelectronics.

6.1.　Introduction

Interactive intelligent electronic devices wherein the transport properties can be modulated by external stimuli have been of great interest due to their applications in smart wearable, personal health monitoring and sensor networks [1-2]. Modulation of the transport properties and analog signal of the electronic devices by the use of external stimuli plays a vital role in development of human machine interfaces and flexible electronics. There have been reports to tune the electronic properties of the junction for enhancement of photoresponse by means of external strain wherein one of the materials is a piezoelectric material [3-4]. But the use of such junctions for enhancement of both transport properties at device level and active analog signal at circuit level has not been studied yet.

Transistion metal dichalcogenides (TMDs) are promising 2D semiconductors materials for future electronic and optoelectronic devices. Among them, MoS_2 has a bandgap of 1.8eV to 1.3 eV for monolayer and bulk MoS_2 respectively with a possibility of achieving intermediate bandgap by tuning the layers of MoS_2 thereby possessing better stability and electronic properties when compared to other 2D materials such as graphene [5-6]. Such tunable layer dependent behavior of MoS_2 makes it suitable for optoelectronic applications such as photodetectors [7]. Coupling MoS_2 with different semiconductors results in formation of heterojunction with efficient charge separation, high electron transfer rate and broadband absorption. There are reports on hybrids of MoS_2 with various metal oxides such as ZnO, CuO, NiO, SnO for applications ranging from electronics to energy storage [8-9]. Out of all the metal oxides, p type copper oxide (CuO) forms hybrid p-n junction with n type MoS_2 thereby expanding the scope of electronic applications of pristine MoS_2.

Recently, odd layers of MoS_2 have shown piezoelectric effect which would be utilized for modulation of transport properties of MoS_2 based heterojunctions under external strain [10]. External application of strain not only changes the transport properties at the interface of junction but also modulates the depletion capacitance offered by the junction in reverse bias which could be utilized for frequency modulation at circuit level. Hence piezoelectric effect in MoS_2 could be utilized for modulating the performance of electronic device and also utilizing the device at circuit level for various analog applications. Although there are

reports on piezotronic effects in ZnO and GaN based devices [11-12], reports on modulation of electronic properties of 2D materials based heterojunctions are limited.

There are various methods to synthesize MoS_2 such as chemical vapor deposition, mechanical exfoliation etc [13-14]. Most of the reports of synthesis of MoS_2 are performed in vacuum or by thermolysis [15]. There are no reports on solution phase synthesis of large area MoS_2 directly on flexible substrates. Hydrothermal solution phase synthesis is a versatile technique as it provides the ability to synthesize 2D materials at very low cost with distinct morphologies and high phase purity [16]. Despite the advantages offered by hydrothermal method, direct deposition of MoS_2 on flexible substrates using hydrothermal method remains unexplored.

In this work, we demonstrate the solution processed fabrication of MoS_2/CuO piezotronic diode for enhanced photodetection and active analog frequency modulator using external mechanical strain. The external applied strain not only modulates the transport properties at the junction which not only enhances the broadband photoresponse but also changes the depletion capacitance of junction under reverse bias thereby utilizing it for frequency modulation at circuit level. Under illumination, 48.4% and 23.7% increase in normalized resistance was observed for visible and IR illumination respectively suggesting that the fabricated device is more sensitive towards visible light. Under 2% strain, 69.7% enhancement in responsivity was observed for visible light illumination. On application of strain, the capacitance of the junction decreased from 15pF to 6pF. The work paves way for future flexible piezotronic devices wherein the external stimuli can modulate the properties of the device which have tremendous applications in the field of communications, signal processing, human machine interface etc.

6.2. Results and Discussions

Flexible electronics have gained significant momentum because of the wide range of applications it offers in the field of electronics, energy harvesters, sensors etc [17-18]. However, fabrication of the flexible devices utilize sophisticated cleanroom techniques which are not only expensive but also time consuming and energy inefficient. Moreover, all flexible substrates are not microfabrication compatible and hence there is an urgent need to develop lithography free solution phase processes for the fabrication of devices on flexible substrates. Also, recently much focus is on growing monolayer MoS_2 by CVD process involving tedious transfer process which is followed by complicated electron beam

lithography process thereby leading to device to device variation in performance. There are reports wherein there is no change in the performance of the monolayer MoS_2 device under strain/bend which is excellent for applications wherein the external bend or integrating the device on curved surface does not affect the performance of the device [19-20]. But there are reports wherein the external stimuli enhances the performance of the device and opens up new avenues of applications [3]. Hence there is a need to develop process for growing few layered MoS_2 on flexible substrates whose behavior can be modulated on application of external strain. Hydrothermal method was employed for the growth of MoS_2 on cellulose paper followed by spin coating of hydrothermally grown CuO nanoparticles on masked MoS_2-cellulose paper thereby forming MoS_2/CuO junction. The temperature was optimized for the hydrothermal method based on the substrate. Experiments were performed for hydrothermal growth of MoS_2 on cellulose paper for temperature less than 200°C which results in no formation of MoS_2. Increasing the temperature above 220°C makes the substrate fragile while then cannot be utilized for flexible electronic applications. Schematic of the complete fabrication process is as shown in Figure 6.1. Detailed procedure for synthesis and fabrication process is explained in experimental section.

XRD analysis of CuO deposited MoS_2-paper was performed to study the crystal structure of the prepared CuO-MoS_2 hybrids on cellulose paper as shown in Figure 6.2a. The characteristic peaks of cellulose paper are noticed at $2\theta \sim 14°$ (110) and 22° (200) [21]. The diffraction peaks of CuO marked with an * symbol, matches well with the JCPDS card number. 05-0661 and reveals the formation of monoclinic CuO [22]. The prominent peaks found between 35°-38° (002) and (200) arises from the phase pure crystallites of CuO. The presence of MoS_2 can be confirmed by four signature peaks in XRD spectra at $2\theta = 12.5°$ (002), 33° (100), 57° (110) respectively. The diffraction peaks of MoS2 are marked with * symbol corresponds to that of hexagonal MoS_2 (JCPDS card number. 37-1492) [23]. It can be observed from the XRD pattern that the presence of CuO on MoS_2 suppresses the diffraction peaks of MoS_2 thereby reducing the peak intensities.

To further confirm the formation of the MoS_2 on cellulose paper and to investigate the details of the number of MoS_2, Raman analysis was performed for pristine MoS_2 on cellulose paper as shown in Figure 6.2b which exhibits strong Longitudinal optic (LO), transverse optic (TO) and surface optic (SO) phonon modes [24].Two characteristic peaks of MoS_2 were noticed at 383 cm^{-1} and 405 cm^{-1}, which are assigned to E12g and A1g phonon modes, respectively. E12g mode involves the in-plane vibrations of Mo atoms whereas A1g mode is due to the out of plane vibrations of the S atoms [25]. The peak

position difference between the two modes was calculated to be ~22, corresponding to trilayer MoS_2 [26].

To study the morphology of as grown MoS_2 on cellulose paper and CuO nanoparticles FESEM studies were performed. Figure 6.2c shows low magnification FESEM image of MoS_2 hydrothermally grown on cellulose paper. MoS_2 growth was clearly observed with microfiber porous morphology of cellulose paper retained which suggest that cellulose paper did not degrade with the growth of MoS_2. Figure 6.2d shows the high magnification image wherein several nanoflakes of MoS_2 have self-assembled to form microsphere like morphology. Each nanoflakes was found to be of 2nm which further confirms the formation of trilayer MoS_2 as shown in figure 6.2e. Figure 6.2f shows the low magnification image wherein the uniform deposition of CuO on MoS_2-cellulose paper was clearly evident thereby demonstrating the formation of well-defined heterojunction. This is important to study the interface quality of MoS_2 and CuO which is crucial for the p-n junction performance. Figure 6.2i shows the FESEM of CuO nanoparticles spin coated over MoS_2 wherein uniform deposition of CuO is observed thereby forming an ordered junction. Figure 6.2g,h shows the high magnification image of CuO nanoparticles wherein hollow irregular shaped hollow nanorods like structure are observed.

To further explore the behavior of MoS_2/CuO junction as broadband photodetector, optical absorption spectra was measured using (ultraviolet) UV-visible-(Near Infrared) NIR spectroscopy. Figure 6.2i shows the absorption spectra of MoS_2 wherein strong absorption peaks were observed in visible region and absorption decreases in NIR region suggesting that MoS_2 would be more sensitive towards visible light compared to NIR light. This clearly suggests that as fabricated MoS_2 offers broad range of absorption in both visible and NIR region which can potentially be utilized as broadband photodetector. The peak intensity observed was less which might be due to the low concentration of MoS_2. It should be noted that the UV-visible-NIR spectroscopy was measured following the same synthesis condition with MoS_2 in solution form and hence there is no response of cellulose paper in the absorbance plot. The optical bandgap calculate from Tauc's plot was 1.53 eV which is consistent with the reports for trilayer MoS_2 [27]. Similarly, UV-visible-NIR spectroscopy was performed for hollow CuO nanorods as shown in figure 6.2j wherein the bandgap calculated was 2.9 eV which is consistent with the reports of CuO nanorods [28]. The corresponding Tauc plot for calculating the optical bandgap for both MoS_2 and CuO can be found in Appendix A as figure S9.

The as fabricated MoS_2 (n)/CuO (p) junction with Ag contacts was utilized for broadband photodetector covering visible and near infrared (NIR) regions and active analog frequency modulator in reverser bias configuration. Visible light with 554nm wavelength and IR lamp of 780 nm wavelength were used to perform photodetector measurements. Prior to photodetector experiments, the devices were kept in dark for more than 12 hours to stabilize them. Figure 6.3a shows the IV characteristic of MoS_2/CuO device which displays excellent rectifying characteristics. The ideality factor and the schottky barrier height for the device was calculated to be 1.89 and 0.243 eV respectively. Deviation from the ideal value of ideality factor might be attributed to defects introduced during the hydrothermal synthesis of MoS_2 and CuO, barrier inhomogeneity and presence of surface states which are responsible for providing multiple pathways at the interface for current conduction [29]. In order to further investigate the MoS_2/CuO interface quality, voltage dependent of η was studied and was used to calculate the density of interface states which can be estimated by following expression

$$Nss = \frac{\varepsilon_i}{t_i q^2}(\eta - 1) - \frac{\varepsilon_{sc}}{W q^2}$$

Where ε_i and t_i are relative dielectric constant and thickness of the interface respectively. Since the junction of MoS_2/CuO is exposed to air the value of ε_i was assumed to be equivalent to the permittivity of free space and thickness to be 5A°. ε_{sc} and W are the relative dielectric constant of the semiconductor and depletion region width respectively whose values were considered to be $4\varepsilon_0$ [30] and 160 nm respectively [31]. Using equation and the bias voltage dependence Nss (V) can be obtained by following equation

$$Ec - E = \Phi_B - qV$$

Figure 6.3b shows the plot of Nss as a function of Ec-E wherein the peak is observed at which indicates that deep level traps are located at 0.11 eV below the conduction band. Such high surface states can be attributed to the high dislocation density and disordered junction. Also, these surface states play an important role in charge transfer to and from the conduction band wherein it acts as an interfacial layer through metal and interband transition thereby leading to high value of η.

Figure 6.3c shows the IV characteristic of MoS_2/CuO junction under various illumination intensities of visible light under reverse bias of -1V wherein increment in the current was

observed as illumination intensity increases which can be attributed to the increased number of photogenerated carriers and the effective separation of the same under reverse bias condition. The same was repeated for IR illumination and similar response was observed as shown in figure 6.3d. It should be noted that the intensities used for IR illumination were greater when compared to visible light intensity as less response was observed for lower intensities value for IR illumination. Even though the intensities for IR are higher they are in the range for defense and security applications. Figure 6.3e shows the temporal response for different visible light illumination intensities wherein increment in the normalized resistance was observed with increasing visible light intensity. Temporal response was measured for 6 cycles by regularly switching the illumination suggesting that sensor exhibited excellent repeatability towards visible light illumination as shown in figure 6.3e. Similar experiments were repeated for IR illumination of intensity wherein similar response was observed as shown in figure 6.3f. Temporal response was measured for 6 cycles by regularly switching the IR illumination suggesting that sensor exhibited repeatability with variation in the response. The irregularity in the temporal response can be attributed to the defects in the heterojunctions which might trap the photogenerated carriers thereby leading to minor variations in the performance. The same experiment for performed for 3 different devices and similar response was observed. Figure 6.3g shows the temporal response of the MoS_2/CuO junction under same intensity repeated for 3 cycles wherein 48.4 and 23.7 % increment in the normalized resistance was observed for visible and IR illumination respectively suggesting the sensor to be more responsive towards visible light illumination when compared to IR light illumination. The observed response is in agreement with the UV-vis-NIR spectroscopy wherein more absorbance was observed in visible region when compared to NIR region. The exceptional behavior of the MoS_2/CuO can be attributed to broad absorption spectra for MoS_2 from visible to NIR region, deep level traps below the conduction band and effective separation of photogenerated carrier due to the built in electric field and reverse bias.

The important figures of merit for photodetector performance are Responsivity (R_λ) which is the measure of photocurrent generated per unit power of incident light per unit area and External Quantum Efficiency (EQE) which is number of electrons produced per incident photon. The responsivity and EQE are given by the following equations [32].

$$R_\lambda = \frac{I_\lambda}{P_\lambda \times A}$$

$$EQE = hc \, \frac{R_\lambda}{\lambda \times e}$$

Where I_λ is the photocurrent, P_λ is the power and A is the active sensing area of photodetector. Figure 6.3h shows the graph of responsivity of the as fabricated device under different illuminations of visible and IR light. Higher responsivity was observed for visible light illumination when compared to IR light illumination further confirming that sensor is more responsive towards visible light. EQE calculated was 5.8 % and 0.95% for visible and IR light respectively which is comparable and even better to some of the flexible substrate based photodetector fabricated using sophisticated fabrication techniques [33-34]. It should also be noted that the responsivity and EQE is low compared to some of the reports on single layer MoS_2 photodetectors which is due to the low crystallinity of MoS_2 and also due to the fact that carrier mobility of MoS_2 decreases due to the cellulose paper substrate.

To further study the effect of strain on the performance of MoS_2/CuO junction, different strains were applied on MoS_2/CuO device and was systematically analyzed as shown in Figure 6.4. It was observed that length of the device had significant impact on the amount of strain induced in MoS_2/CuO under bend. Explanation and derivation for the relationship between the strain produced and the length of the device can be found in recently report from our lab [3]. Under strain, piezopotential induced in MoS_2 was responsible for the variation in the schottky barrier height. To verify this, pristine large area MoS_2 (3 cm x 3 cm) was investigated for voltage generation under strain. Figure 6.4a shows the voltage generation for pristine MoS_2 wherein 2V p-p was observed under bend. Copper tape was used as contact covering the entire area of pristine MoS_2-cellulose paper and was used for further voltage generation measurements. Odd number of MoS2 layers have been reported for piezoelectricity [10]. MoS_2 exhibits covalent bond in the sequence of atomic planes of molybdenum (Mo) between two atomic planes of Sulphur (S) with adjacent Mo-S-Mo bonded by weak Van der Waals forces. Because of the opposite orientation of alternating layer of MoS_2, odd layers of MoS_2 forms non-centrosymmetric structure which is not seen in even layers of MoS_2 [35]. Hence due to the non-centrosymmetric structure of the as grown MoS_2 (trilayer) on cellulose paper the strain induced charges can easily bring variation of carrier transport of 2D MoS_2. Here, due to the formation of p-n junction, transport behavior is due to piezotronic effect wherein the strain induced charge modulates the schottky barrier height. The potential generated due to the bending of MoS_2 was responsible for the change in the effective potential at the MoS_2/CuO interface which

increases the schottky barrier height and depletion region width and experiences more reverse bias voltage at the interface thereby assisting in effective separation of photogenerated carriers. Figure 6.4b shows the temporal response of MoS_2/CuO under visible light illumination at 2% strain. 69.7% increment in the current was observed when compared to the response without strain. Same was repeated for IR illumination and similar response of increment in current was observed as shown in figure 6.4c. Figure 6.4d shows the graph of responsivity of the sensor as a function of applied strain wherein it was observed that as applied strain increases, responsivity of the sensor increases for both visible and IR light illumination. Under external mechanical strain to the flexible MoS_2/CuO device, MoS_2 generates piezopotential charges at the interface which enhances conduction and valence band energy bending at the interface which raises the schottky barrier height and depletion width. The raising of schottky barrier height and widening of the depletion region provides extra reverse bias potential which assist in effective separation of photogenerated electron-hole pairs thereby reducing the recombination rate. Similar experiments were performed on pristine MoS_2 to compare the photodetector performance of pristine MoS_2 with and without strain. The results demonstrated less responsivity when compared to responsivity of MoS_2-CuO diode. The reason for the same can be attributed to the absence of electric field in pristine MoS_2 device. The electric field for the pristine MoS_2 device is distributed only at the MoS_2-Ag contacts and is absent in the areas far away from the metal contacts. Hence the photogenerated electrons generated away from the metal contacts tends to recombine and does not participate in the photocurrent thereby leading to low responsivity in case of pristine MoS_2. Pristine MoS_2 device was further tested for photodetector at different strains. The results displayed increment in the photocurrent as the applied strain increases which can be attributed to the local electric fields created due to the stretching of the individual nanoflakes. Since each MoS_2 can be considered as a metal plate and the separation between them is air it forms a potential barrier. Under strain, individual MoS_2 nanoflakes separate from each other thereby increasing the potential barrier which helps in effective separation of charge carriers. But since these are local heterojunctions, the responsivity in case of pristine MoS_2 was found to be very less when compared to MoS_2-CuO. Graphs showing the I-V characteristics under strain and responsivity of strained pristine MoS_2 under UV illumination can be found in Appendix A as figure S10.

To further study the behavior of the as-fabricated piezotronic diode in developing circuits it was utilized for analog signal modulation. The schematic of the frequency modulator using

piezotronic diode is as shown in Figure 6.5a which consists of feedback LC resonant circuit and an amplifier circuit wherein the frequency of oscillation was given by the expression

The piezotronic diode under reverse bias would behave like a capacitor whose capacitance can be varied upon strain thereby modulating the frequency of oscillation. Figure 6.5b shows the graph of capacitance measured with respect to strain wherein decrease in the capacitance was observed with increase in strain. As discussed, upon strain, piezopotential induced in MoS_2 alters the band bending at the MoS_2/CuO interface which raises the schottky barrier height and widens the depletion region width. Widening of the depletion region width alters the depletion capacitance associated with the diode under reverse bias. The change in the depletion capacitance of the piezotronic diode under strain was further utilized in oscillator circuit to modulate the frequency of oscillation. Figure 6.5b shows the change in frequency of the signal generated upon external strain. Figure 6.5c shows the sinusoidal signal generated from the oscillator and its corresponding change in frequency upon external strain. It was observed that as applied strain increases frequency of oscillation increases. This could be attributed to the fact that the depletion capacitance associated with the diode decreases upon external strain which increases the frequency of oscillation. To further demonstrate the stability of the as fabricated MoS_2-CuO piezotronic diode, bending cycles test was performed wherein the devices were bend for 500 cycles and was tested for photodetector performance. The device was bend for specific number of cycles and then photodetector measurements were performed. Minimum variation in the responsivity values were observed after 500 cycles demonstrating excellent stability of the fabricated diode. Such small variations can be attributed to the defects and the change in the deep level traps due to bending. It should be noted that even though there are small variations in the responsivity values, repeated bending did not affect the working of the diode. Graph showing the responsivity values after 500 cycles can be found in Appendix A as figure S11.

The enhancement in the photocurrent and change in the depletion capacitance of the piezotronic diode can be well understood by energy band diagram of MoS_2/CuO as shown in Figure 6.6. The electron affinity of the CuO is 4.07[36] and the bandgap for CuO is 2.9 eV while for MoS_2, the electron affinity of 4 eV [37] and the bandgap of 1.53 eV. The reason for the calculated value of schottky barrier height to be higher than the difference between the electron affinity of MoS_2 and CuO could be due to possible oxidation of MoS_2 making it less n type and as a result raises the schottky barrier height. Another reason might be disordered junction which in turn raises the schottky barrier height. The offset in the conduction and valence band creates heterostructure interface. Upon illumination, electron-

hole pairs are generated in MoS_2 and due to the local electric field at the interface effective separation of carriers occurs which results in the enhancement of photocurrent. Upon external strain, due to the piezopotential induced in the MoS_2 there is a rise in schottky barrier height and widening of the depletion region which can be confirmed by the fact that upon strain the current decreases. The widening of the depletion region increases the effective reverse bias potential at the junction which helps in the effective separation of photogenerated carriers. Also, upon strain, due to the widening of the depletion region, depletion capacitance of the diode under reverse bias decreases.

There are few reports on fabricating flexible broadband photodetectors based on MoS_2 [38-39] but the utilization of the MoS_2 junction at the circuit level has not yet been demonstrated. *Zhang et al.,* fabricated flexible MoS_2/CuO heterojunction photodetector and reported its enhancement using strain modulation [40]. But the fabrication procedure involved the use of CVD for MoS_2 growth and sputtering for CuO deposition which are not only expensive but also energy inefficient and time consuming techniques. Also, the process required transfer of CVD grown MoS_2 which further leads to device to device variation in performance. Moreover, monolayer MoS_2 was utilized for strain modulated photodetector whose behavior remains unaffected by strain [19]. *Liu et al.,* reported transfer free printable Graphene/ZnO for high performance photodetector with responsivity of 5000A/W [41]. *Zhang et al.,* demonstrated lead free organic-inorganic hybrid materials for photovoltaic applications [42]. *Zheng et al.,* reported MoS_2/ TiO_2 hybrid enhanced photo electrochemical performance which uses simple anodization and hydrothermal method [43]. *Zhou et al.,* reported the tribotronic tuning of silicon based diode for active analog signal modulation [44]. However, the above photodetectors being fabricated on rigid silicon substrate which restricts their usage in flexible electronics applications. There are reports on photodetectors fabricated on various flexible substrates based on different functional materials and the comparison of the same in terms of photodetection parameters and the range of detection with the current work can be found in Table 6.1. In this work, we demonstrate the fabrication of piezotronic p-n junction by the growth of few layer MoS_2 on flexible cellulose paper followed by deposition of hollow CuO nanorods. The fabricated piezotronic diode was utilized for enhanced broadband photodetector and used at circuit level for design of variable frequency oscillator upon application of external mechanical strain. Furthermore, the method can be extended to different flexible substrates of choice which can withstand 200°C. The entire fabrication procedure is scalable and can easily be extended for large area fabrication.

6.3.   Conclusion

In summary, we demonstrate the solution processed MoS_2-CuO flexible piezotronic diode using simple yet cost effective hydrothermal method which was utilized for active analog frequency modulator and enhanced broadband photodetector upon external strain. The ideality factor and schottky barrier height were calculated to be 1.89 and 0.243 eV respectively. The fabricated piezotronic diode high sensitivity towards visible light when compared to IR light illumination. Under 2% strain, 69.7% increment in normalized resistance was observed for visible illumination. Further, the as fabricated piezotronic diode was utilized at circuit level for designing an oscillator wherein the frequency of oscillator was controlled by applied external strain. The work demonstrated here is the step ahead in utilizing the fabricated flexible devices at circuit level designing which holds tremendous potential in the field of flexible and wearable sensors, analog and digital electronics applications.

6.4.   Experimental Section

Synthesis of MoS₂ on cellulose paper

Hydrothermal process was used for the growth of large area MoS_2 on cellulose paper which involves two steps namely seed coating process followed by hydrothermal. The seed solution was prepared by mixture of sodium molybdate (10mM) and Thiourea (20mM) in deionized (DI) water. The paper substrate was dipped in seed solution for 1 hour followed by drying at 80°C for 30 minutes. The nutrient solution was prepared by mixing sodium molybdate (50mM) and Thiourea (100mM) in DI water. The seed coated cellulose paper and nutrient solution were then transferred to Teflon line autoclave and was maintained at 200°C for 20 hours. The autoclave was allowed to naturally cool down and the MoS_2 deposited cellulose paper was dried at 70°C for 15 minutes.

Synthesis of Copper oxide nanoparticles

Copper oxide nanoparticles were synthesized using hydrothermal method wherein nutrient solution consisting of 20 mM copper acetate and 0.2 M of Hexamethylenetetramine (HMTA) was mixed with 20 ml of water. The as prepared nutrient solution was transferred to Teflon lined autoclave and hydrothermal was performed at 80°C for 5 hours. The

resultant solution was washed, centrifuged and dried to obtain hollow CuO irregular nanorods.

Fabrication of MoS$_2$/CuO diode

The as synthesized MoS$_2$ on cellulose paper was masked using Al foil and polyimide (PI) tape. Thereafter CuO nanoparticles solution was spin coated on the remaining exposed area. Spin coating was performed several times to ensure uniform coating of CuO nanoparticles over MoS$_2$. The device was then kept for drying at 70°C for 15 minutes. The mask was then removed which was followed by defining contact on MoS$_2$ (n) and CuO (p) type using silver paste. The silver paste contacts were fabricated using custom built stencil mask wherein the sensing area of the photodetector remained same for different fabricated device. The active area for photodetector was 5mm x 5mm.

Materials and characterization

Analytical grade chemicals (Sodium molybdate, Thiourea and copper acetate) were purchased from Sigma Aldrich and used without further purification for the fabrication of MoS$_2$-CuO piezotronic diode. The structural characteristics of the prepared materials were investigated using X'pert PRO X-Ray Diffraction (XRD) with Cu Ká radiation. Raman spectra were obtained from Raman spectrometer (SenterrainVia opus, Bruker) having an excitation wavelength of 532 nm. Field Emission Scanning Electron Microscopy (FESEM) analysis was performed by ZEISS Ultra-55 SEM to study morphology. The electrical measurements were carried out with Keithley 4200 SCS instrument. Agilent digital storage oscilloscope (DSO 3062A) was utilized for the measurement of frequency of oscillation of oscillator circuit. The as-fabricated devices were tested for broadband photodetector application on illuminating visible and IR radiations. The lamp sources used for Vis and IR source had a wavelength (ë) of 554 nm and 780 nm respectively.

6.5.   References

1. Rautaray, S. S., & Agrawal, A. Vision based hand gesture recognition for human computer interaction: a survey. Artificial Intelligence Review, 2015, 43(1), 1-54.
2. Rus, D., & Tolley, M. T. Design, fabrication and control of soft robots. Nature, 2015, 521(7553), 467-475.

3. Sahatiya, P., Jones, S. S., Gomathi, P. T., & Badhulika, S. Flexible substrate based 2D ZnO (n)/graphene (p) rectifying junction as enhanced broadband photodetector using strain modulation. 2D Materials, 2017, 4(2), 025053.

4. Zhang, F., Ding, Y., Zhang, Y., Zhang, X., & Wang, Z. L. Piezo-phototronic effect enhanced visible and ultraviolet photodetection using a ZnO–CdS core–shell micro/nanowire. ACS Nano, 2012, 6(10), 9229-9236.

5. Lee, H. S., Min, S. W., Chang, Y. G., Park, M. K., Nam, T., Kim, H., & Im, S. MoS2 nanosheet phototransistors with thickness-modulated optical energy gap. Nano Letters, 2012, 12(7), 3695-3700.

6. Conley, H. J., Wang, B., Ziegler, J. I., Haglund Jr, R. F., Pantelides, S. T., & Bolotin, K. I. Bandgap engineering of strained monolayer and bilayer MoS2. Nano Letters, 2013, 13(8), 3626-3630.

7. Tsai, D. S., Liu, K. K., Lien, D. H., Tsai, M. L., Kang, C. F., Lin, C. A., & He, J. H. Few-layer MoS2 with high broadband photogain and fast optical switching for use in harsh environments. ACS Nano, 2013, 7(5), 3905-3911.

8. Guo, S., Li, X., Zhu, J., Tong, T., & Wei, B. Au NPs@ MoS2 Sub-Micrometer Sphere-ZnO Nanorod Hybrid Structures for Efficient Photocatalytic Hydrogen Evolution with Excellent Stability. Small, 2016, 12(41), 5692-5701.

9. Um, D. S., Lee, Y., Lim, S., Park, S., Lee, H., & Ko, H. High-Performance MoS2/CuO Nanosheet-on-One-Dimensional Heterojunction Photodetectors. ACS Applied Materials & Interfaces, 2016, 8(49), 33955-33962.

10. Wu, W., Wang, L., Li, Y., Zhang, F., Lin, L., Niu, S., & Hone, J. Piezoelectricity of single-atomic-layer MoS2 for energy conversion and piezotronics. Nature, 2014, 514(7523), 470-474.

11. Zhang, Y., Yan, X., Yang, Y., Huang, Y., Liao, Q., & Qi, J. Scanning probe study on the piezotronic effect in ZnO nanomaterials and nanodevices. Advanced Materials, 2012, 24(34), 4647-4655.

12. Yu, R., Dong, L., Pan, C., Niu, S., Liu, H., Liu, W., & Wang, Z. L. Piezotronic effect on the transport properties of GaN nanobelts for active flexible electronics. Advanced Materials, 2012, 24(26), 3532-3537.

13. Perea-López, N., Lin, Z., Pradhan, N. R., Iñiguez-Rábago, A., Elías, A. L., McCreary, A., & Terrones, M. CVD-grown monolayered MoS2 as an effective photosensor operating at low-voltage. 2D Materials, 2014, 1(1), 011004.

14. Wu, J., Li, H., Yin, Z., Li, H., Liu, J., Cao, X., & Zhang, H. Layer thinning and etching of mechanically exfoliated MoS2 nanosheets by thermal annealing in air. Small, 2013, 9(19), 3314-3319.

15. Zhao, Y., Zhang, Y., Yang, Z., Yan, Y., & Sun, K. Synthesis of MoS2 and MoO2 for their applications in H2 generation and lithium ion batteries: a review. Science and Technology of Advanced Materials, 2013, 14(4), 043501.

16. Peng, Y., Meng, Z., Zhong, C., Lu, J., Yu, W., Jia, Y., & Qian, Y. Hydrothermal synthesis and characterization of single-molecular-layer MoS2 and MoSe2. Chemistry Letters, 2001, 30(8), 772-773.

17. Nathan, A., Ahnood, A., Cole, M. T., Lee, S., Suzuki, Y., Hiralal, P., & Haque, S. Flexible electronics: the next ubiquitous platform. Proceedings of the IEEE, 100(Special Centennial Issue), 2012, 1486-1517.

18. Forrest, S. R. The path to ubiquitous and low-cost organic electronic appliances on plastic. Nature, 2004, 428(6986), 911-918.

19. Lopez-Sanchez, O., Lembke, D., Kayci, M., Radenovic, A., & Kis, A. Ultrasensitive photodetectors based on monolayer MoS2. Nature Nanotechnology, 2013, 8(7), 497-501.

20. De Fazio, D., Goykhman, I., Yoon, D., Bruna, M., Eiden, A., Milana, S., & Kis, A. High Responsivity, Large-Area Graphene/MoS2 Flexible Photodetectors. ACS Nano, 2016, 10(9), 8252-8262.

21. Egusa, S., Yokota, S., Tanaka, K., Esaki, K., Okutani, Y., Ogawa, Y.,& Wariishi, H. Surface modification of a solid-state cellulose matrix with lactose by a surfactant-enveloped enzyme in a nonaqueous medium. Journal of Materials Chemistry, 2009, 19(13), 1836-1842.

22. Yang, W., Wang, J., Ma, W., Dong, C., Cheng, G., & Zhang, Z. Free-standing CuO nanoflake arrays coated Cu foam for advanced lithium ion battery anodes. Journal of Power Sources, 2016, 333, 88-98.

23. Wang, X., Zhang, Z., Chen, Y., Qu, Y., Lai, Y., & Li, J. Morphology-controlled synthesis of MoS2 nanostructures with different lithium storage properties. Journal of Alloys and Compounds, 2014, 600, 84-90.

24. Parkin, W. M., Balan, A., Liang, L., Das, P. M., Lamparski, M., Naylor, C. H., & Drndic, M. Raman shifts in electron-irradiated monolayer MoS2. ACS Nano, 2016, 10(4), 4134-4142.

25. Zhang, X., Han, W. P., Wu, J. B., Milana, S., Lu, Y., Li, Q. Q., & Tan, P. H. Raman spectroscopy of shear and layer breathing modes in multilayer MoS2. Physical Review B, 2013, 87(11), 115413.

26. Liu, K. K., Zhang, W., Lee, Y. H., Lin, Y. C., Chang, M. T., Su, C. Y., & Lai, C. S. Growth of large-area and highly crystalline MoS2 thin layers on insulating substrates. Nano Letters, 2012, 12(3), 1538-1544.

27. Ganatra, R., & Zhang, Q. Few-layer MoS2: a promising layered semiconductor. ACS Nano, 2014, 8(5), 4074-4099.

28. Sathishkumar, P., Sweena, R., Wu, J. J., & Anandan, S. Synthesis of CuO-ZnO nanophotocatalyst for visible light assisted degradation of a textile dye in aqueous solution. Chemical Engineering Journal, 2011, 171(1), 136-140.

29. Chen, X., & Fan, R. Low-temperature hydrothermal synthesis of transition metal dichalcogenides. Chemistry of Materials, 2001, 13(3), 802-805.

30. Santos, E. J., & Kaxiras, E. Electrically driven tuning of the dielectric constant in MoS2 layers. ACS Nano, 2013, 7(12), 10741-10746.

31. Saw, K. G., Tneh, S. S., Yam, F. K., Ng, S. S., & Hassan, Z. Determination of Acceptor Concentration, Depletion Width, Donor Level Movement and Sensitivity Factor of ZnO on Diamond Heterojunction under UV Illumination. PloS One, 2014, 9(2), e89348.

32. Sahatiya, P., Puttapati, S. K., Srikanth, V. V., & Badhulika, S. Graphene-based wearable temperature sensor and infrared photodetector on a flexible polyimide substrate. Flexible and Printed Electronics, 2016, 1(2), 025006.

33. Lee, Y. B., Kim, S. K., Lim, Y. R., Jeon, I. S., Song, W., Myung, S., & An, K. S. Dimensional Hybrid Structures of 2D Materials with ZnO Nanostructures via pH-Mediated Hydrothermal Growth for Flexible UV Photodetectors. ACS Applied Materials & Interfaces, 2017, 9(17), 15031-15037

34. Tao, Y., Wu, X., Wang, W., & Wang, J. Flexible photodetector from ultraviolet to near infrared based on a SnS2 nanosheet microsphere film. Journal of Materials Chemistry C, 2015, 3(6), 1347-1353.

35. Wu, W., Wang, L., Li, Y., Zhang, F., Lin, L., Niu, S., & Hone, J. Piezoelectricity of single-atomic-layer MoS2 for energy conversion and piezotronics. Nature, 2014, 514(7523), 470-474.

36. Zainelabdin, A., Zaman, S., Amin, G., Nur, O., & Willander, M. Optical and current transport properties of CuO/ZnO nanocoral p–n heterostructure hydrothermally synthesized at low temperature. Applied Physics A, 2012, 108(4), 921-928.

37. Lee, K., Kim, H. Y., Lotya, M., Coleman, J. N., Kim, G. T., & Duesberg, G. S. Electrical characteristics of molybdenum disulfide flakes produced by liquid exfoliation. Advanced Materials, 2011, 23(36), 4178-4182.

38. Chen, H., Liu, H., Zhang, Z., Hu, K., & Fang, X. Nanostructured photodetectors: from ultraviolet to terahertz. Advanced Materials, 2016, 28(3), 403-433.

39. Gomathi, P. T., Sahatiya, P., & Badhulika, S. Large-Area, Flexible Broadband Photodetector Based on ZnS–MoS2 Hybrid on Paper Substrate. Advanced Functional Materials, 2017, 1701611.

40. Zhang, K., Peng, M., Wu, W., Guo, J., Gao, G., Liu, Y., & Zhang, Y. A flexible p-CuO/n-MoS2 heterojunction photodetector with enhanced photoresponse by the piezo-phototronic effect. Materials Horizons, 2017, 4(2), 274-280.

41. Liu, Q., Gong, M., Cook, B., Ewing, D., Casper, M., Stramel, A., & Wu, J. Transfer-free and printable graphene/ZnO-nanoparticle nanohybrid photodetectors with high performance. Journal of Materials Chemistry C, 2017, 5, 6427-6432.

42. Zhang, X., Yin, J., Nie, Z., Zhang, Q., Sui, N., Chen, B., & Zhou, H. Lead-free and amorphous organic–inorganic hybrid materials for photovoltaic applications: mesoscopic CH3NH3 MnI3/TiO2 heterojunction. RSC Advances, 2017, 7(59), 37419-37425.

43. Zheng, L., Han, S., Liu, H., Yu, P., & Fang, X. Hierarchical MoS2 nanosheet@ TiO2 nanotube array composites with enhanced photocatalytic and photocurrent performances. Small, 2016, 12(11), 1527-1536.

44. Zhou, T., Yang, Z. W., Pang, Y., Xu, L., Zhang, C., & Wang, Z. L. Tribotronic Tuning Diode for Active Analog Signals Modulation. ACS Nano, 2016, 11(1), 882-888

45. Lim, Y. R., Song, W., Han, J. K., Lee, Y. B., Kim, S. J., Myung, S., & Lim, J. Wafer-Scale, Homogeneous MoS2 Layers on Plastic Substrates for Flexible Visible-Light Photodetectors. Advanced Materials, 2016, 28(25), 5025-5030.

46. Sahatiya, P., & Badhulika, S. Strain modulation assisted enhanced broadband photodetector based on large area, flexible, few layered graphene-MoS2 on cellulose paper. Nanotechnology, 2017. DOI: 10.1088/1361-6528/aa8587
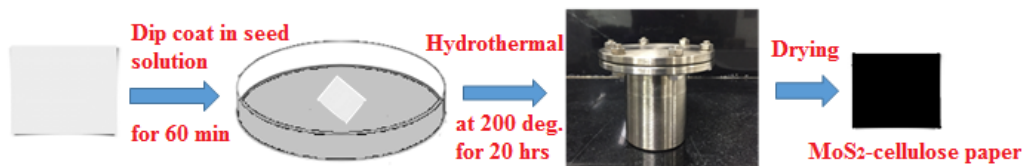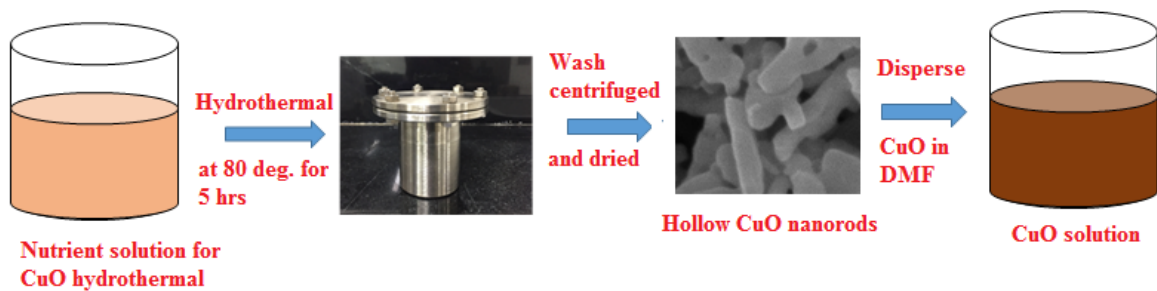
Figure 6.1: Schematic of the synthesis of MoS$_2$ on cellulose paper, hollow CuO nanorods and fabrication of MoS$_2$-CuO piezotronic diode
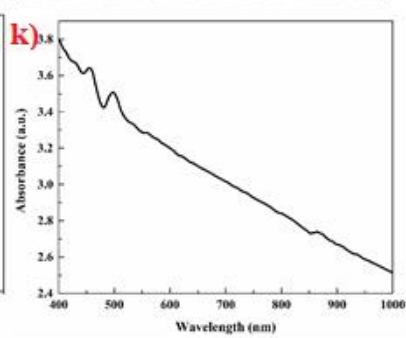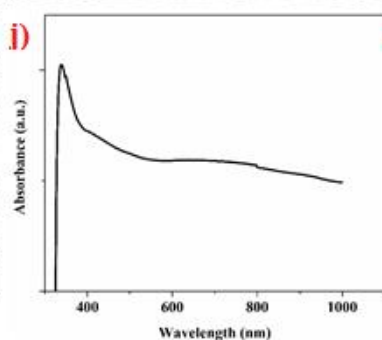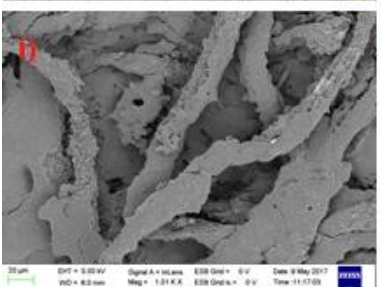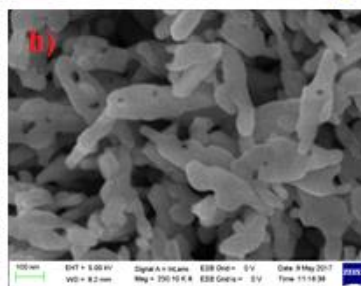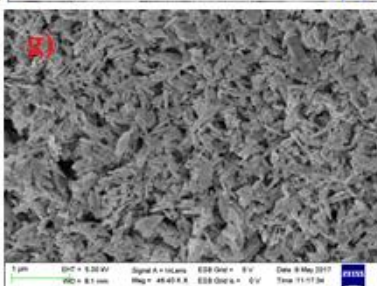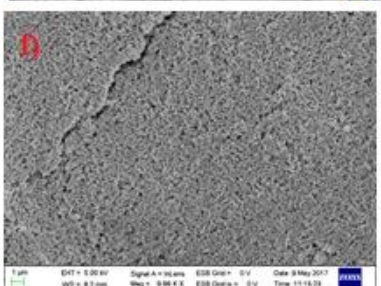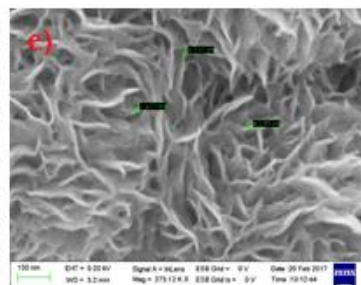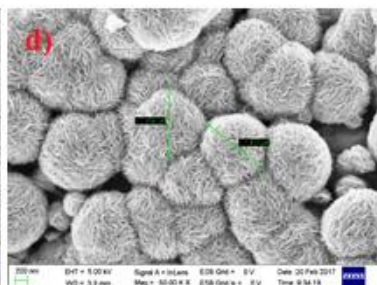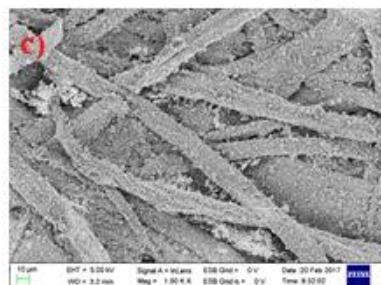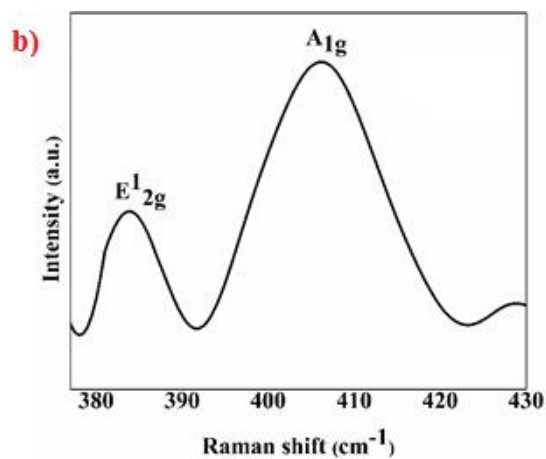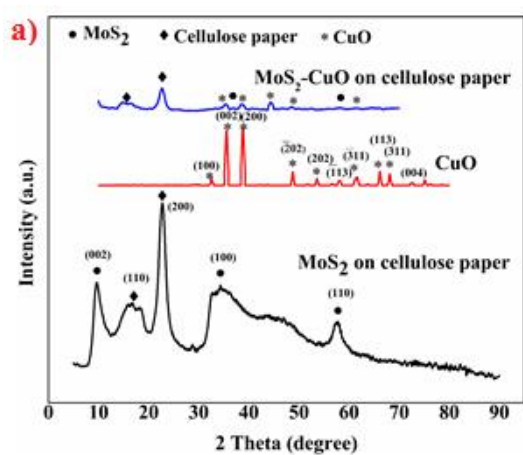
Figure 6.2: a) XRD graph of pristine MoS_2/CuO b) Raman spectra of pristine MoS_2 suggesting trilayer MoS2 c) FESEM image of MoS_2 grown on cellulose paper wherein the morphology of cellulose paper is retained d) High magnification FESEM image of MoS_2 on cellulose paper showing microflower like morphology e) High magnification image of MoS_2 showing single MoS_2 nanoflake diameter of 2nm further suggesting trilayer MoS_2 f,i) Low magnification image of CuO solution after spin coating over MoS2-cellulose paper indicating uniform deposition of CuO on MoS_2 thereby forming uniform heterojunction g,h) High magnification image of CuO showing hollow irregular nanorod like morphology j, k) UV-visible-NIR spectra of CuO and pristine MoS_2 respectively wherein broadband absorbance is observed for pristine MoS_2.
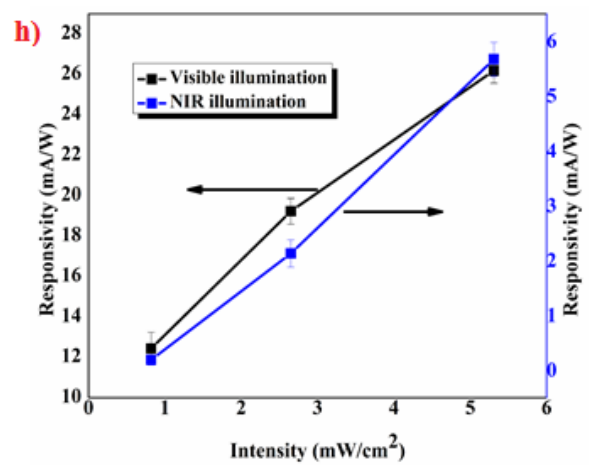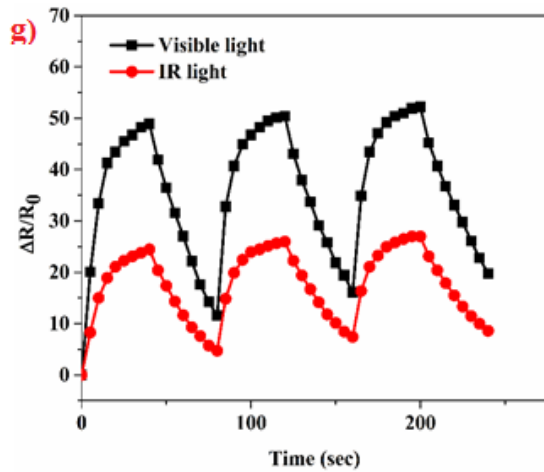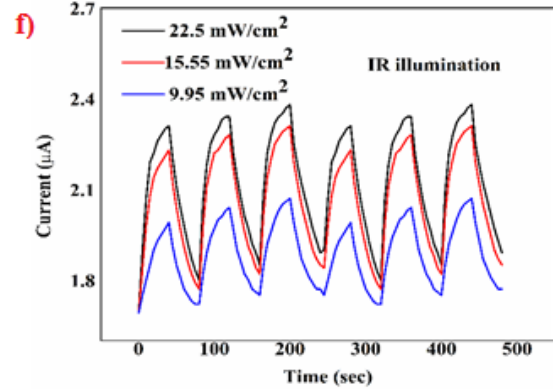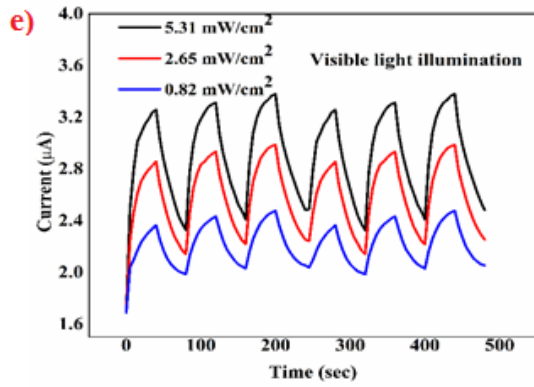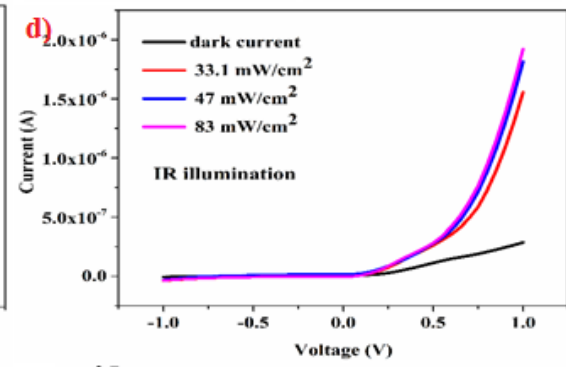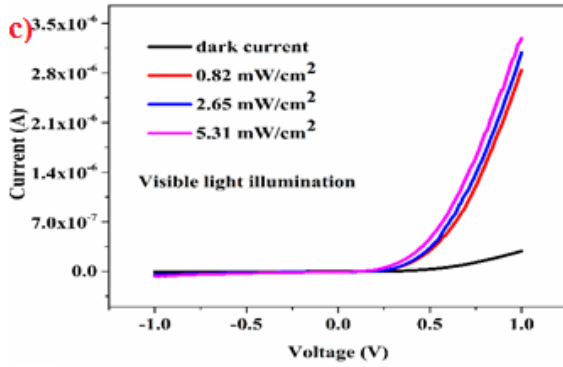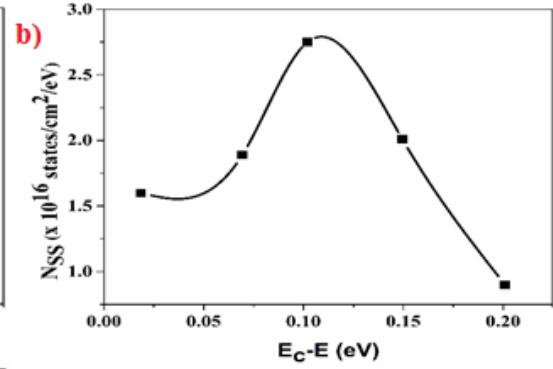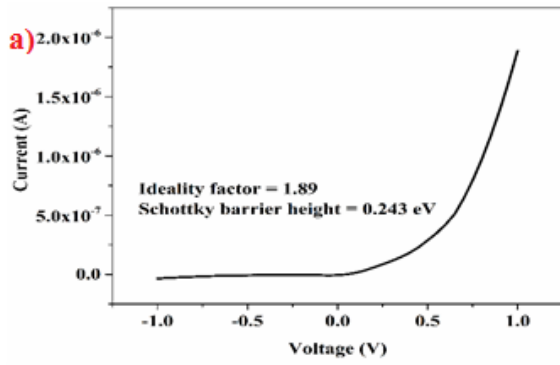
Figure 6.3: a) IV characteristics of MoS_2-CuO piezotronic diode showing excellent rectifying characteristics b) Plot of Nss v/s Ec-E c) IV characteristic of MoS_2-CuO diode for different intensities of visible light illumination d) IV characteristic of MoS_2-CuO diode for different intensities of IR light illumination e) Temporal response of the MoS_2-CuO diode for different intensities of visible light illumination f) Temporal response of the MoS_2-CuO diode for different intensities of IR light illumination g) Temporal response of MoS_2-CuO for fixed intensity of both visible and IR illumination showing higher response for visible light h) Responsivity v/s intensity graph for both visible and IR illumination (N=3).
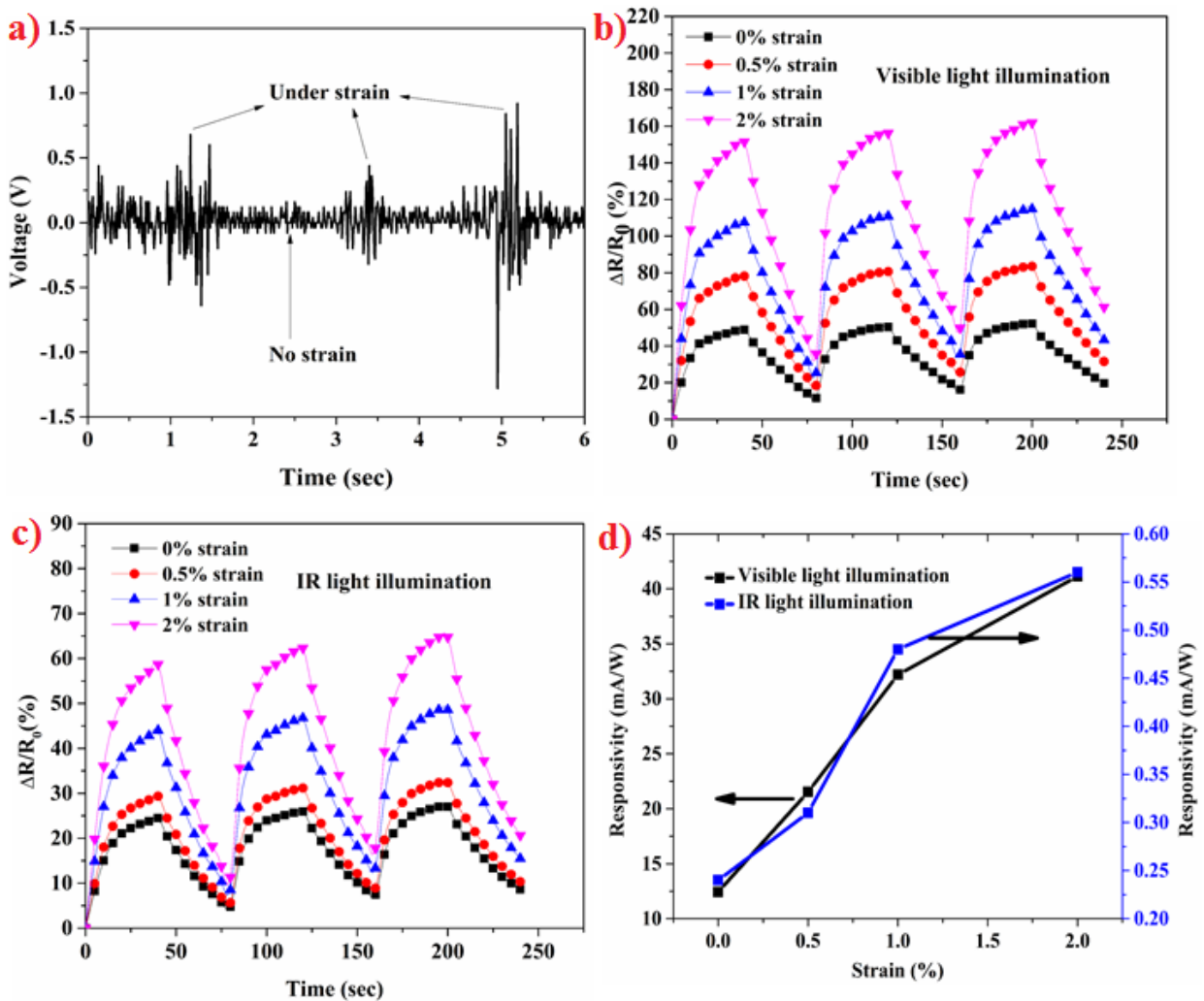
Figure 6.4: a) Voltage output for pristine MoS_2-cellulose paper showing a peak to peak voltage of 2V b) Temporal response of MoS_2-CuO diode for fixed visible illumination under varying strains c) Temporal response of MoS_2-CuO diode for fixed IR illumination under varying strains d) Responsivity of the as fabricated device for fixed visible and IR light illumination under varying strain.
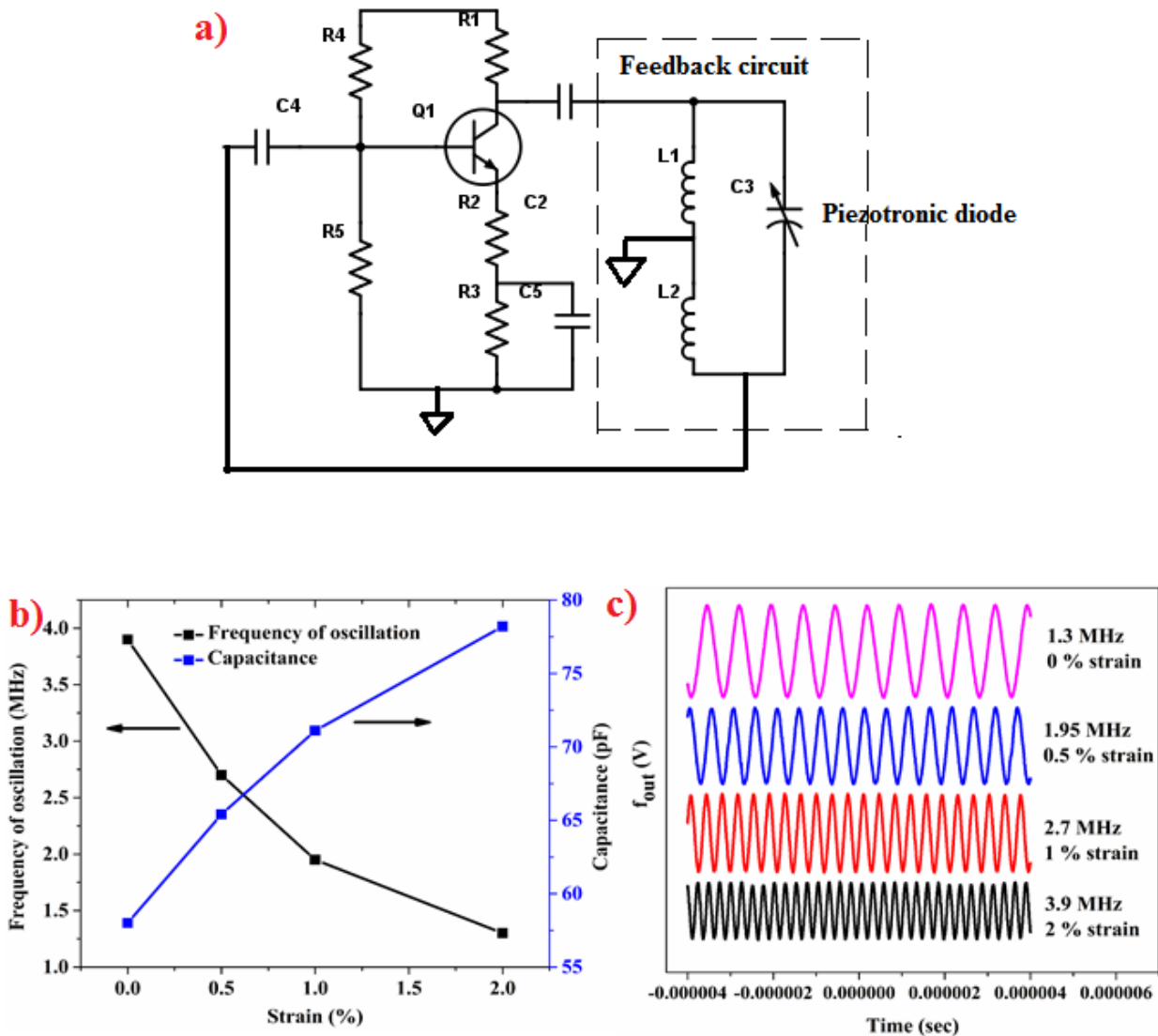
Figure 6.5: a) Circuit diagram for the oscillator with LC resonant feedback circuit b) Graph of frequency of oscillation and capacitance variation with strain c) Graph showing different frequency of oscillation under varying external mechanical strain. As applied strain increases frequency of oscillation increases.
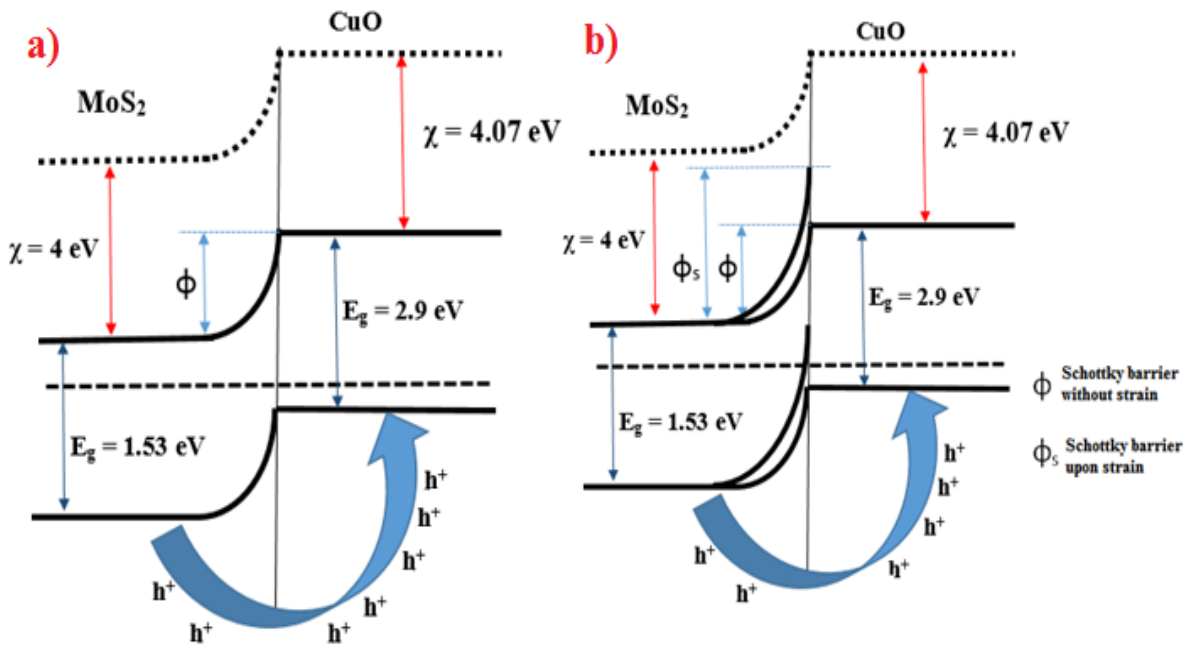
Figure 6.6: a) Energy band diagram of MoS_2-CuO piezotronic diode under illumination b) Energy band diagram of MoS_2-CuO piezotronic diode under external mechanical strain showing increase in the depletion region width and schottky barrier height.

Material/ Hybrid	Substrate	Range of detection	Responsivity	Ref
MoS_2/ZnS	Cellulose paper	UV to NIR	17.85 µA/W	39
MoS_2/ZnO	Polyimide	UV	0.89 mA/W	33
SnS_2	Polypropylene	UV to NIR	9.36 nA/W	34
MoS_2	Polyimide	UV	2.46 µA/W	45
Graphene/ZnO	Eraser	UV to Visible	16.5 µA/W	3
Graphene/MoS_2	Cellulose paper on PDMS	UV to Visible	3.3 mA/W	46
MoS_2/CuO	**Cellulose paper**	**Visible to NIR**	**42 mA/W**	**This work**

Table 6.1: Comparison of the Range of detection and responsivity for various flexible photodetectors

Chapter 7

Carbon nanotube on eraser based eco-friendly fabrication of skin-like large area matrix of flexible strain and pressure sensor

Abstract

This paper reports a new type of electronic, recoverable skin-like pressure and strain sensor on flexible, bio-degradable pencil eraser substrate and has been fabricated by a solvent-free, low-cost and energy efficient process. Multi-walled carbon nanotube (MWCNTs) film as strain sensing element was patterned on pencil eraser by rolling pin and pre-compaction mechanical press which induces high interfacial bonding between the MWCNTs and eraser substrate which enables the sensor to achieve recoverability under ambient conditions. Eraser, serves as a substrate for strain sensing as well as acts as a dielectric for capacitive pressure sensing, thereby eliminating the steps of dielectric deposition which is crucial in capacitive based pressure sensors. Strain sensing transduction mechanism is attributed to the tunneling effect caused due to the elastic behavior of MWCNTs and strong mechanical interlock between MWCNTs and eraser substrate which restricts slippage of MWCNTs on eraser thereby minimizing hysteresis. The gauge factor of the strain sensor was calculated to be 2.4 which is comparable to and even better than most of the strain and pressure sensors fabricated with subtle design and architecture. The sensitivity of the capacitive pressure

sensor was found to be 0.135MPa^{-1}.To demonstrate the applicability of the sensor as artificial electronic skin the sensor was assembled on various parts of human body and their corresponding movement and the touch sensation were monitored. The entire fabrication process is scalable and can be integrated to large area for mapping spatial pressure distribution. This low cost, easily scalable MWCNT rolled pin eraser based pressure and strain sensor has huge potential applications as artificial e-skin in flexible electronics and medical diagnostics especially in surgeries as it provides high spatial resolution without complex nanostructure architecture.

7.1.   Introduction

Conventional electronic devices fabricated on rigid crystalline semiconductors wafers have evolved with the motivation to miniaturize thereby realizing faster, smaller and densely integrated devices [1]. A parallel research that is rapidly evolving for future electronics is to integrate the property of flexibility and stretchablity to develop user friendly devices. There have been number of reports on strain and pressure sensors on stretchable, bendable and soft materials like polyimide, polyurethane sponge, natural rubber, cellulose paper, tissue paper etc. using various nanomaterials such as metal oxides, carbon nanomaterials and metal nanowires [2-11]. Even though these devices are low cost, environmental friendly and involve low energy fabrication processes, they lack the multi-functionality of both pressure and strain sensing, which is essential for artificial electronic skin applications. PU sponge is highly flexible but possess less stretchablity which limits its use as strain sensor. Moreover, making the sponge conductive for pressure sensing applications involves processes like spin coating, dip coating and freeze drying which use toxic solvents and subsequently degrade the performance of the device. Fabricating devices on cellulose paper has the advantage of being eco-friendly and low-cost, but low tear resistance and poor stretchablity of cellulose paper restricts its use in robust applications. Natural rubber is an ideal choice for fabricating pressure and strain sensors as it possesses high tear resistance, stretchablity and is also bio-degradable. Most of the commercially available erasers contain polyvinyl chloride (PVC) which are not biodegradable. PVC free eraser was chosen due to two main reason, first being, it is softer compared to other commercial PVC containing erasers and second, it is biodegradable. Softer eraser helps in easily bendable and induces more strain. Various stretchable devices have been fabricated on rubber using different materials and their composites [12-15]. There has been a recent trend of synthesizing composites of natural rubber with conductive CNTs filler to obtain electrically conductive and reinforced rubber materials [16-17]. But to obtain a proper dispersion of CNTs in rubber matrix it is

functionalized with carboxylic group (COOH), hydroxyl group (OH) for which CNTs are treated with acids thereby degrading the properties of CNTs. Also, most of the reports either deal with pressure or strain sensing using natural rubber which does not fit the scope of artificial skin applications. For e-skin applications, devices should be able to monitor human motion as well as sense touch with functionalities of both pressure and strain sensing. [18] demonstrated skin like transparent pressure and strain sensor using PDMS, CNT and ecoflex for resistive strain sensing and capacitive pressure sensing. Even though the results are very encouraging the fabrication process includes photolithography and metal evaporation which makes it costly and energy inefficient.

The transduction mechanism for most of the reported strain sensors is based on geometrical changes of the sensing material which does not allow the sensor to recover its original state which induces high hysteresis thereby not only degrading the performance but also reducing the lifetime of the sensor. Therefore, in addition to stretchable and bendability of the device introducing properties to these soft electronic devices that can repeatedly recover electrical and mechanical performance under stretchable and bendable conditions, is of high importance to avoid the degradation of device performance under deformation. There are reports on self-healing flexible strain sensors by use of various nanoparticles in elastomer matrix but the performance of these sensors is moderate and the process is non-ecofriendly [19-21]. Hence, it of interest to fabricate strain sensors by combining the advantage of solvent free process for applications in artificial skin, robotics and medical monitoring.

In this work, we introduce a new type of piezoresistive polyvinyl chloride (PVC) free pencil eraser based pressure and strain sensing sensor which could be utilized as an artificial e-skin using MWCNTs as sensing element. PVC free eraser not only act as a highly stretchable material for strain sensing but also act as a dielectric for capacitive pressure sensing eliminating the use of time consuming and energy inefficient dielectric deposition techniques such as RF sputtering, evaporation and atomic layer deposition (ALD).The fabrication process outlined in this work is solvent free where the deposition of MWCNTs on both sides of PVC free eraser was performed using simple rolling pin and pre-compaction mechanical press which ensures excellent interfacial bonding between MWCNTs and eraser substrate. This excellent interfacial bonding between MWCNTs and eraser substrate is the key for recoverability of the sensor under deformation. Deposited MWCNTs not only act as strain sensing element but also act as metal electrodes for capacitive pressure sensing with eraser as dielectric which again eliminates the need for depositing metals using sophisticated sputtering and evaporation techniques. The results

indicate that the as fabricated sensor can be utilized for development of artificial skin which has numerous applications in the field of healthcare for acid and burn victims, robotics etc. Moreover, this being fully a solvent free technique enables the device to be used in developing disposable sensor applications where cost is a limitation. To the best of our knowledge this is first report of MWCNTs deposited using solvent free technique on biodegradable eraser as both flexible substrate as well as dielectric for capacitive pressure sensor and its application in artificial electronic skin.

7.2.   Results and Discussions

To achieve flexibility and stretchablity of the devices two common strategies have been used. First is to directly bond thin conductive materials having low young's moduli to rubber/elastic substrate [22-23]. Second method is to fabricate the device using intrinsically stretchable conductors that are assembled by mixing conductive material into elastomeric matrix [24]. But above methods make use of toxic solvents and acids for achieving proper dispersion which not only makes the whole process eco-unfriendly but also degrades the performance of the device. Moreover, conductive filler is functionalized for proper adhesion of conductive materials onto rubber/elastic substrate which not only reduces the conductivity of the materials but also induces defects [25].In a recent report from our lab we demonstrated a novel solvent free fabrication process using simple rolling pin and pre-compaction mechanical press for fabrication of ultrasensitive pressure sensor and its use in artificial electronic skin [26]. But the use of polyimide as substrate restricted its use in pressure sensor as polyimide is not stretchable. For artificial electronic skin applications device should not only be flexible but also stretchable and allow to monitor both movement and touch. In this work, to fabricate a large area eraser based strain and pressure sensor, we adopted solvent free method as recently reported by our lab [26] to deposit MWCNTs as conductive coating on commercial PVC free eraser. MWCNTs being 1-D material we fabricate large area, flexible, solvent free strain sensor on eraser substrate as it conforms well to 1-D nanofibers like porous nature of eraser thereby developing strong mechanical interlock between MWCNTs and eraser substrate. 200 rolling pin cycles followed by pre-compaction press of 5Kg/cm^2 was optimized to form a uniform MWCNTs film.

Variation in thickness and resistance with rolling pin cycles were observed and it was found that as rolling pin cycles increase there is decrease in thickness and increase in the resistance of film of MWCNTs. Figure 7.2a shows the variation of thickness of MWCNTs with rolling pin cycles. As rolling pin cycles increases from 50 to 300, 24.3 % decrease in the thickness

was observed. This is due to the fact that as rolling pin cycles increases, MWCNTs film tend to stretch which decreases the thickness of the film. As the rolling pin pressure is increased there is increase in length to thickness ratio of MWCNTs film. Decrease in thickness decreases the overall area of the MWCNTs film which further increases the pressure applied by rolling pin thereby further reducing the thickness. Increasing the rolling pin cycles above 300 deforms the eraser substrate. Figure 7.2a shows the variation of resistance with rolling pin cycles and 83 % increase in the resistance was observed. For resistance measurements silver paste was used as contacts. Due to decrease in thickness of the film, MWCNTs penetrate more in eraser substrate thereby increasing the insulating nature of the film and hence resistance of the film increases. The increase in resistance may also be attributed to the defects induced during rolling pin and pre-compaction mechanical press. To study the effect of rolling pin and pre-compaction press on MWCNTs film Raman spectroscopy was performed. Typical signatures for MWCNTs were observed for both pristine and rolled pin pre-compaction press of 5Kg/cm^2 MWCNTs as shown in figure 7.2b. D band at 1342 cm^{-1} represents defect band, G band at 1576 cm^{-1} represents graphitic band and peak at 2708 cm-1 represents G' band. It was found that on pre-compaction press MWCNT retained sp^2 hybridized structure with some defects induced. This was verified by taking ID/IG ratio of both pristine and pre-compaction pressed MWCNTs. For pristine MWCNTs I_D/I_G ratio was found to be 0.315 while I_D/I_G ratio for pre-compaction pressed MWCNTs was found to be 0.385. Each wall of CNT are bonded to each other by weak van der Waals forces. On application of pressure, due to the weak nature of van der Waals forces, the nanotubes merge together giving rise to sp3 hybridized bonds. This sp3 hybridized bonds contribute to the D band of the raman spectra. Here on application of pressure of 5 Kg/cm^2 some of the nanotube merge together which increases defects and thereby increasing the I_D/I_G ratio. It should be noted that even though pre-compaction press induced few defects in MWCNTs it does not totally modify the structure from sp2 to sp3 hybridization and hence 5Kg/cm^2 pre-compaction pressure was optimized for the process. The shift in Raman peaks after rolling pin cycles could be attributed to the residual strain developed on MWCNTs after rolling pin process followed by pre-compaction mechanical press [27]. Increase in the resistance observed in figure 2a can also be attributed to the defects induced due to the pressure applied. Increasing the pre-compaction pressure not only induces more defects but also stiffens the eraser which does not serve the purpose of flexible substrate.

Owing to the stretchable and bendable nature of the eraser substrate, flexible strain sensor was conveniently fabricated for different lengths of eraser. Length of the eraser had significant impact on the amount of maximum strain that it can induce due to bending. Derivation and plot for relationship between the bend angle of the eraser and the corresponding strain produced can be found in Appendix B. It was observed that as length of the eraser increases there is a decrease in the maximum strain that can be produced at 360° bend. As length of the eraser increases, change in length (ΔL) decreases which decreases the overall strain produced in the MWCNTs film. Figure 7.3a shows the hysteresis curve for the resistance against strain for different lengths of the eraser. The sensor regained its initial value of resistance thus demonstrating negligible hysteresis which can be attributed to the strong interfacial binding between the MWCNTs and the eraser substrate and is superior to many other flexible strain sensors[18].Hysteresis is primarily caused due to friction between the slippage of filler elements under stretching and delay time associated with the re-establishment of the elements network upon release [28].In this case, due to the strong bonding between the MWCNTs film and eraser substrate, no slipping or detachment of MWCNTs occurs giving rise to the excellent recoverability of MWCNTs-eraser device. Moreover, MWCNTs conforms well to nanofiber porous like structure which develops strong mechanical interlock between MWCNTs and eraser. The as fabricated sensor was easily able to distinguish between compressive and tensile strains. Figure 7.3b shows the change in current against tensile strain i.e. when the sensor was bend outwards. When the sensor is bend outwards tensile stress is developed in the eraser substrate and is then transferred to MWCNTs film which causes the re-arrangement and re-orientation of MWCNTs and forms cracks in the MWCNTs film thereby increasing the electrical resistance of the MWCNTs film. It should be noted that the re-arrangement and re-orientation of MWCNTs is due to the tensile strain developed in eraser and not in MWCNTs itself. Moreover MWCNTs have excellent elastic properties with tensile strain upto 40% [29] enabling MWCNTs to stretch and bend with the elongation and bending of eraser substrate. Under applied tensile strain, MWCNTs tend to form cracks which are occupied either by eraser substrate or by air. Electron can tunnel through eraser or air when the distance between the adjacent MWCNTs is below threshold distance. The tunneling resistance depends on the distance between the adjacent CNTs. On tensile strain, due to the stretching of MWCNTs film there is an increase in the interspace at CNT-CNT junction which consequently increases the tunneling resistance. Hence, being conventionally different from metal strain sensors, the resistance strain dependency of the MWCNTs on eraser substrate is not mainly due to the geometrical changes but also due to the tunneling

effect between the MWCNTs and the geometrical deformations itself. When the tensile strain is removed, eraser releases the tensile strain and hence MWCNTs retain its initial position thereby again occupying cracks. Figure 7.3c shows the change in the current when the sensor was subjected to compressive strain i.e. bending the eraser inwards. It was found that current increases due to the compressive strain. This can be attributed to the decrease in the tunneling resistance due to the overlapping of CNTs. When the eraser is bend inwards, this interspace between the adjacent MWCNTs are occupied and hence there is an overall decrease in the tunnel resistance of the MWCNTs film thereby increasing the current. It should be noted here that compressive strain was manually applied and hence there was variation in the current levels observed. This was done to ensure that sensor operates in real time situations where the strain variations are non-uniform. To demonstrate the response of sensor under constant compressive strain, same experiment was repeated for constant compressive strain of 10% and the sensor response was uniform and can be found in Appendix as fig S13. There are reports which identify the mechanism for piezoresistivity is due to the disconnection of CNTs because of the application of strain [18] [30]. This disconnection can be attributed to the weak interfacial adhesion between CNTs and the substrate which not only reduces the sensitivity, reversibility but also reduces the lifetime of the sensor. However, dominant reason for the piezoresistivity in MWCNTs-eraser film is the tunneling effect due to the elastic behavior of CNTs and strong interfacial binding and mechanical interlock between MWCNTs and eraser substrate, rather than disconnection of the adjacent CNTs which is the primary reason for excellent recoverability of MWCNTs and negligible hysteresis in the performance of the sensor. Figure 7.3d shows the graph of resistance change with both compressive and tensile strain. The positive values of strain in the graph corresponds to tensile strain and the negative values corresponds to the compressive strain. The graph shows the similarity in the values of the normalized resistance when the sensor is under compression and tensile strain.

Gauge factor (GF) was used for quantitative analysis and to calculate the sensitivity of the strain sensor which is defined as ratio of relative change in resistance to strain and is given by GF = $\Delta R/\Delta\varepsilon$, where ε represents strain. The GF calculated for the as fabricated sensor is 2.4 which is better than some of the reports on MWCNTs based strain sensors [15][10][31]on different substrates with subtle design architectures.

The technological goal is to integrate these sensors as artificial electronic skin (e-skin) which requires the sensors to detect motion and sense touch. Most of the papers in literature report either human motion monitoring sensor or touch sensor with very few reports

demonstrating both [18]. Even though there are reports on both human motion monitoring and touch, the fabrication procedures outlined are time consuming and energy inefficient. To fulfill this gap, the as fabricated sensor was further applied as capacitive based pressure sensor. To do so, the eraser not only acts as a substrate for strain sensing but also acts as a dielectric for capacitive based pressure sensor. This greatly reduces the efforts in integrating dielectrics which requires cleanroom environment involving sophisticated processes like evaporation and sputtering. In this case, MWCNTs film was deposited on back side of the eraser with the above mentioned rolling pin and pre-compaction method. The MWCNTs film on top as well as bottom side of eraser behaved as metal plates for parallel plate capacitor with contacts taken from silver paste and copper tape. This greatly reduces the efforts in deposition of metal plates for parallel plate capacitor. Finally the as-fabricated capacitive pressure sensor was laminated by polyimide tape as MWCNTs are known to respond to temperature and humidity [32]. The cross sectional view of the capacitive pressure sensor in relaxed and pressed condition can be found in Appendix A as fig S14.

The capacitance C of a parallel plate capacitor is proportional to $1/d$, where d is the spacing between the plates. On applying pressure, the spacing d changes thus changing the capacitance. First, the dielectric constant (ε) of eraser was evaluated by plotting capacitance value with different A/d, where A is area. The plot was linearly fitted and the ε value was calculated to be 3.94. Figure 7.4a shows the variation of capacitance with A/d. Dielectric constant was extracted as reported in [33]. Figure 7.4b shows the response of the sensor to different pressures. The pressure was applied using an air compressor whose pressure can be varied. The compressed air with fixed pressure was pointed towards the sensor and corresponding change in the capacitance was observed. As pressure of compressed air was increased, increase in the capacitance was observed. Sensitivity of the sensor was calculated by $S = (\Delta C/C0)/\Delta P$, where ΔC is the relative change in capacitance and C0 is the initial capacitance of the sensor under no load or press and ΔP is the change in the applied pressure. As shown in figure 7.4b, with linear fit of the graph between ($\Delta C/C0$) and ΔP, the sensitivity of the sensor was calculated to be 0.135MPa^{-1}. It is worth noting that even though the sensitivity is not significant with some of the reported literatures which make use of complex fabrication techniques[18][34], the focus of our approach is solvent free, simple fabrication and low cost while still maintaining a fairly good sensitivity suitable for touch sensing applications. The sensing mechanism is the change in the distance don applying pressure, which is nothing but width of the eraser. As the pressure is applied, distance d between the plates decreases which increases the capacitance. Figure 7.4c shows the

temporal response of the sensor wherein the pressure was applied several times showing excellent repeatability. The sensor was further tested for soft and hard touch wherein the pressure was applied by human hand with different pressures as shown in figure 7.4d. It was clearly observed that sensor demonstrates repeatable performance for distinct pressure touches of human hand.

To demonstrate the potential application of the eraser based sensor in artificial electronic skin the as fabricated sensor was integrated onto various parts of the body such as fingers, wrist, elbow, neck etc. where the bodily movement is significantly high. Different types of bodily movements either produce tensile or compressive strain in the sensor and hence the sensor (capable of detecting both compressive and tensile strain) was able to detect the motion of almost every part of human body. Figure 5 shows photographic images of integration of the sensor on different human body parts and their corresponding temporal response showing excellent repeatability. Figure 7.5a shows the temporal response of the sensor when it was integrated with forefinger wherein it was bend and released several times and the corresponding response was measured. It was observed that finger movements induces tensile strain and hence there was decrease in current when finger was bend. The same was repeated for 10 times and similar response was observed. Figure 7.5b shows response of the sensor when the finger was bend and held in the bent position for few seconds and then released. It was observed that when the sensor was in bent position the sensor retains the response of the bent position with a slight increment in the current levels. This could possibly be due to the eraser substrate trying to regain its lowest energy state i.e. relaxed state. When the sensor is perturbed by bending it always tries to regain its original state by opposing the tensile strain and inducing small amount of compressive strain which slightly increases the current levels. The same was repeated 5 times with sensor showing similar response. Figure 7.5c shows response of the sensor when integrated onto wrist of human hand where the movement induces compressive strain thereby increasing the current levels. Lastly, it was integrated onto human neck and elbow wherein the upside down movement of both induces tensile strain as shown in Figure 7.5d and 7.5e respectively.

The process developed for the development of facile pressure and strain sensors for e-skin applications can easily be scaled up to allow for production of large area flexible e-skin. Entire pencil eraser (30mm x 15mm x 5mm) was directly used to fabricate artificial e-skin

with 8 pixels x 6 pixels. Detailed fabrication procedure is explained in Appendix A. The obtained scaled up artificial e-skin is as shown in figure 7.6b. Due to soft and porous nature of the pencil eraser used, the touch feeling of the as-obtained as fabricated artificial skin is elastic as that of real skin. The pressure sensing mechanism of artificial e-skin is related to capacitive variations of the eraser with MWCNT deposited on both top and bottom side. Mapping out the capacitive variation of each pixel on applying load clearly showed the two dimensional pressure distribution on the e-skin. For this alphabets "I" "T" and "H" were placed on e-skin separately and corresponding capacitive variations were recorded and plotted in figure 7.6a. The measured spatial distribution is highly consistent with the shape and weight distribution of the object demonstrating excellent response of artificial skin to external pressures.

There have been numerous reports of flexible substrates for both pressure and strain sensing which includes using metal nanoparticles on PDMS substrate [35], cotton based pressure sensors [36], pencil on paper [37], graphene-rubber composite for human motion monitoring [38], CNT, graphene-polyimide foam, Si nanowire and graphene nanocellulose nanopaper based flexible strain sensors [39-42]. CNT and graphitic films based strain sensor on natural rubber was reported wherein the CNT film was sandwiched in natural rubber [43]. Even though the fabrication is simple and the results are encouraging the process of depositing CNT on natural rubber is not well defined and optimized which may vary the performance from device to device making it unsuitable for large scale fabrication. Moreover, the process of passivating the device is by liquid natural rubber whose effect on the properties of CNTs is still unknown. Other substrates such as PU sponge, cellulose paper, tissue paper etc. are promising for flexible pressure and strain sensing but they lack multi-functionality of both pressure and strain sensing which is crucial for e-skin applications. Each of the substrate offers excellent response for either pressure or strain sensing, not both. In this case, we fabricate multi-functional pressure and strain sensor by depositing MWCNT on PVC free eraser by a novel rolling pin and pre-compaction pressing which not only gives uniformity in the film but is also a repeatable process with minimum error. It should be noted that even though in this case the deposition was performed manually, it can be automated by integrating the roll pin to electric motor thereby minimizing variation and ensuring repeatability suitable for commercialization. The total estimated cost of the sensor (6 x 8 array) was less than $0.15

7.3. Conclusion

In summary, a facile fabrication method for multi-functional skin like pressure and strain sensor was developed using MWCNTs on PVC free eraser with solvent free, low cost and low energy technique. A novel rolling pin and pre-compaction mechanical press technique for deposition of MWCNTs on eraser was developed, optimized and tested. Thickness and resistance variation with rolling pin cycles were studied in order to quantify the deposition technique. Eraser not only acts as a substrate for strain sensing but also acts as a dielectric for capacitive pressure sensor. Also, deposited MWCNTs acts a metal plates for capacitive pressure sensor. Both these process eliminates the need for depositing dielectric and metal which are crucial step in capacitive based pressure sensor. Gauge factor of strain sensor was calculated to be 2.4 which is comparable to the strain sensor fabricated with complex fabrication steps. The sensitivity of the capacitive pressure sensor was found to be 0.135MPa^{-1}. Sensing mechanism of MWCNTs eraser based strain sensor was attributed to the tunneling effect rather than geometrical deformations. The as fabricated sensor was then integrated to various parts of human body such as hand, neck, wrist and elbow wherein excellent responses to the corresponding movements were observed. The process was scaled for large area fabrication of flexible artificial skin and spatial pressure mapping results reveals excellent consistency in recognizing the shape and location of the object. This novel and low-cost fabrication process could be used in future to design and develop organic skin like devices and abilities to sense moisture, temperature, pH, light and chemical and biological species.

7.4.   Experimental Section

Fabrication of eraser based strain sensor

MWCNTs was deposited on PVC free eraser by pre compaction mechanical pressing and rolling pin. Eraser was pre-stretched and bend several times to relax the strain and open gaps for easy deposition of MWCNTs. Before deposition, eraser was cleaned with DI water and sonicated in isopropanol (IPA) for 3 minutes. It was then dried at 70°C for 20 minutes. MWCNTs (different weights) was then applied on the eraser and MWCNTs film was formed using rolling pin. Optimization in terms of process, MWCNTs weight and rolling pin cycles was done to ensure uniform film with desired initial resistance. For accurate fabrication of the device rolling was performed for different rolling cycles to ensure uniformity in the film. To remove the unattached MWCNTs on eraser, it was washed with copious amount of DI water. The eraser was then dried at 70°C for 30 minutes. The eraser was then cut into desired lengths and widths. Rolling pin was performed manually wherein

pressure variations are difficult to control. To ensure uniform pressure, MWCNTs rolled pin eraser was then compressed using pre-compaction mechanical press with pressure of $5Kg/cm^2$ for 15 seconds. Pre-compaction compression press decreases non-uniformity caused due to pressure variations during rolling pin. Contacts were then made using silver conductive paste. Finally the eraser was passivated by the use of polyimide (PI) tape. The resistance of the eraser based sensor varied with the width and length of the MWCNTs deposited on the eraser and can be found in supplementary information (SI) as fig S1. The schematic of the complete fabrication process is as shown in figure 1. Information regarding the materials and characterization tools can be found in SI.

7.5. References

1. Iwai, H. I. R. O. S. H. I. Roadmap for 22nm and beyond. Microelectronic Engineering, 2009, 86(7), 1520-1528.

2. Yao, H. B., Ge, J., Wang, C. F., Wang, X., Hu, W., Zheng, Z. J., & Yu, S. H. A flexible and highly pressure-sensitive graphene–polyurethane sponge based on fractured microstructure design. Advanced Materials, 2013, 25(46), 6692-6698.

3. Sahatiya, P., Puttapati, S. K., Srikanth, V. V., & Badhulika, S. Graphene-based wearable temperature sensor and infrared photodetector on a flexible polyimide substrate. Flexible and Printed Electronics, 2016, 1(2), 025006.

4. Gullapalli, H., Vemuru, V. S., Kumar, A., Botello-Mendez, A., Vajtai, R., Terrones, M., & Ajayan, P. M. Flexible piezoelectric ZnO–paper nanocomposite strain sensor. Small, 2010, 6(15), 1641-1646.

5. Gong, S., Schwalb, W., Wang, Y., Chen, Y., Tang, Y., Si, J., & Cheng, W. A wearable and highly sensitive pressure sensor with ultrathin gold nanowires. Nature communications, 2014, 5.

6. Li, Y., Cheng, X. Y., Leung, M. Y., Tsang, J., Tao, X. M., & Yuen, M. C. W. A flexible strain sensor from polypyrrole-coated fabrics. Synthetic Metals, 2005, 155(1), 89-94.

7. Li, X., Wang, Y. H., Zhao, C., & Liu, X. Paper-based piezoelectric touch pads with hydrothermally grown zinc oxide nanowires. ACS applied materials & interfaces, 2014, 6(24), 22004-22012.

8. Dharap, P., Li, Z., Nagarajaiah, S., & Barrera, E. V. Nanotube film based on single-wall carbon nanotubes for strain sensing. Nanotechnology, 2004, 15(3), 379.

9. Jing, Z., Guang-Yu, Z., & Dong-Xia, S. Review of graphene-based strain sensors. Chinese Physics B, 2013, 22(5), 057701.

10. Amjadi, M., Pichitpajongkit, A., Lee, S., Ryu, S., & Park, I. Highly stretchable and sensitive strain sensor based on silver nanowire–elastomer nanocomposite. ACS nano, 2014, 8(5), 5154-5163.

11. Radha, B., Sagade, A. A., & Kulkarni, G. U. Flexible and semitransparent strain sensors based on micromolded Pd nanoparticle–carbon μ-stripes. ACS applied materials & interfaces, 2011, 3(7), 2173-2178.

12. Shimojo, M., Namiki, A., Ishikawa, M., Makino, R., & Mabuchi, K. A tactile sensor sheet using pressure conductive rubber with electrical-wires stitched method. IEEE Sensors journal, 2004, 4(5), 589-596.

13. Tjahyono, A. P., Aw, K. C., & Travas-Sejdic, J. A novel polypyrrole and natural rubber based flexible large strain sensor. Sensors and Actuators B: Chemical, 2012, 166, 426-437.

14. Kang, I., Khaleque, M. A., Yoo, Y., Yoon, P. J., Kim, S. Y., & Lim, K. T. Preparation and properties of ethylene propylene diene rubber/multi walled carbon nanotube composites for strain sensitive materials. Composites Part A: Applied Science and Manufacturing, 2011, 42(6), 623-630.

15. Yamada, T., Hayamizu, Y., Yamamoto, Y., Yomogida, Y., Izadi-Najafabadi, A., Futaba, D. N., & Hata, K. A stretchable carbon nanotube strain sensor for human-motion detection. Nature nanotechnology, 2011, 6(5), 296-301.

16. Peng, Z., Feng, C., Luo, Y., Li, Y., & Kong, L. X. Self-assembled natural rubber/multi-walled carbon nanotube composites using latex compounding techniques. Carbon, 2010, 48(15), 4497-4503.

17. Bhattacharyya, S., Sinturel, C., Bahloul, O., Saboungi, M. L., Thomas, S., & Salvetat, J. P. Improving reinforcement of natural rubber by networking of activated carbon nanotubes. Carbon, 2008, 46(7), 1037-1045.

18. Lipomi, D. J., Vosgueritchian, M., Tee, B. C., Hellstrom, S. L., Lee, J. A., Fox, C. H., & Bao, Z. Skin-like pressure and strain sensors based on transparent elastic films of carbon nanotubes. Nature nanotechnology, 2011, 6(12), 788-792.

19. Huynh, T. P., & Haick, H. Self-Healing, Fully Functional, and Multiparametric Flexible Sensing Platform. Advanced Materials, 2016, 28(1), 138-143.

20. Tee, B. C., Wang, C., Allen, R., & Bao, Z. An electrically and mechanically self-healing composite with pressure-and flexion-sensitive properties for electronic skin applications. Nature nanotechnology, 2012, 7(12), 825-832.

21. Hur, J., Im, K., Kim, S. W., Kim, J., Chung, D. Y., Kim, T. H.,& Park, N. Polypyrrole/agarose-based electronically conductive and reversibly restorable hydrogel. ACS nano, 2014, 8(10), 10066-10076.

22. Brosteaux, D., Axisa, F., Gonzalez, M., & Vanfleteren, J. Design and fabrication of elastic interconnections for stretchable electronic circuits. IEEE Electron Device Letters, 2007, 28(7), 552-554.

23. Kim, D. H., Song, J., Choi, W. M., Kim, H. S., Kim, R. H., Liu, Z.,& Rogers, J. A. Materials and noncoplanar mesh designs for integrated circuits with linear elastic responses to extreme mechanical deformations. Proceedings of the National Academy of Sciences, 2008, 105(48), 18675-18680.

24. Sekitani, T., Noguchi, Y., Hata, K., Fukushima, T., Aida, T., & Someya, T. A rubberlike stretchable active matrix using elastic conductors. Science, 2008, 321(5895), 1468-1472.

25. Shanmugharaj, A. M., Bae, J. H., Lee, K. Y., Noh, W. H., Lee, S. H., & Ryu, S. H. Physical and chemical characteristics of multiwalled carbon nanotubes functionalized with aminosilane and its influence on the properties of natural rubber composites. Composites Science and Technology, 2007, 67(9), 1813-1822.

26. Sahatiya, P., & Badhulika, S. Solvent-free fabrication of multi-walled carbon nanotube based flexible pressure sensors for ultra-sensitive touch pad and electronic skin applications. RSC Advances, 2016, 6(98), 95836-95845.

27. Proctor, J. E., Gregoryanz, E., Novoselov, K. S., Lotya, M., Coleman, J. N., & Halsall, M. P. High-pressure Raman spectroscopy of graphene. Physical Review B, 2009, 80(7), 073408.

28. Amjadi, M., Pichitpajongkit, A., Lee, S., Ryu, S., & Park, I. Highly stretchable and sensitive strain sensor based on silver nanowire–elastomer nanocomposite. ACS nano, 2014, 8(5), 5154-5163.

29. Obitayo, W., & Liu, T. A review: carbon nanotube-based piezoresistive strain sensors. Journal of Sensors, 2012.

30. Thostenson, E. T., & Chou, T. W. Real-time in situ sensing of damage evolution in advanced fiber composites using carbon nanotube networks. Nanotechnology, 2008, 19(21), 215713.

31. Park, J. J., Hyun, W. J., Mun, S. C., Park, Y. T., & Park, O. O. Highly stretchable and wearable graphene strain sensors with controllable sensitivity for human motion monitoring. ACS applied materials & interfaces, 2015, 7(11), 6317-6324.

32. Han, J. W., Kim, B., Li, J., & Meyyappan, M. Carbon nanotube based humidity sensor on cellulose paper. The Journal of Physical Chemistry C, 2012, 116(41), 22094-22097.

33. Grove, T. T., Masters, M. F., & Miers, R. E. Determining dielectric constants using a parallel plate capacitor. American Journal of Physics, 2005, 73(1), 52-56.

34. Wu, W., Wen, X., & Wang, Z. L. Taxel-addressable matrix of vertical-nanowire piezotronic transistors for active and adaptive tactile imaging. Science, 2013, 340(6135), 952-957.

35. Lee, J., Kim, S., Lee, J., Yang, D., Park, B. C., Ryu, S., & Park, I. A stretchable strain sensor based on a metal nanoparticle thin film for human motion detection. Nanoscale, 2014, 6(20), 11932-11939.

36. Li, Y., Samad, Y. A., & Liao, K. From cotton to wearable pressure sensor. Journal of Materials Chemistry A, 2015, 3(5), 2181-2187.

37. Liao, X., Liao, Q., Yan, X., Liang, Q., Si, H., Li, M., & Zhang, Y. Flexible and highly sensitive strain sensors fabricated by pencil drawn for wearable monitor. Advanced Functional Materials, 2015, 25(16), 2395-2401.

38. Boland, C. S., Khan, U., Backes, C., O'Neill, A., McCauley, J., Duane, S., & Coleman, J. N. Sensitive, high-strain, high-rate bodily motion sensors based on graphene–rubber composites. ACS nano, 2014, 8(9), 8819-8830.

39. Cai, L., Song, L., Luan, P., Zhang, Q., Zhang, N., Gao, Q., & Zhou, W. Super-stretchable, transparent carbon nanotube-based capacitive strain sensors for human motion detection. Scientific reports, 2013, 3.

40. Qin, Y., Peng, Q., Ding, Y., Lin, Z., Wang, C., Li, Y., & Li, Y. Lightweight, superelastic, and mechanically flexible graphene/polyimide nanocomposite foam for strain sensor application. ACS nano, 2015, 9(9), 8933-8941.

41. Zhang, B. C., Wang, H., Zhao, Y., Li, F., Ou, X. M., Sun, B. Q., & Zhang, X. H. Large-scale assembly of highly sensitive Si-based flexible strain sensors for human motion monitoring. Nanoscale, 2016, 8(4), 2123-2128.

42. Yan, C., Wang, J., Kang, W., Cui, M., Wang, X., Foo, C. Y., & Lee, P. S. Highly stretchable piezoresistive graphene–nanocellulose nanopaper for strain sensors. Advanced materials, 2014, 26(13), 2022-2027.

43. Tadakaluru, S., Thongsuwan, W., & Singjai, P. Stretchable and flexible high-strain sensors made using carbon nanotubes and graphite films on natural rubber. Sensors, 2014, 14(1), 868-876.
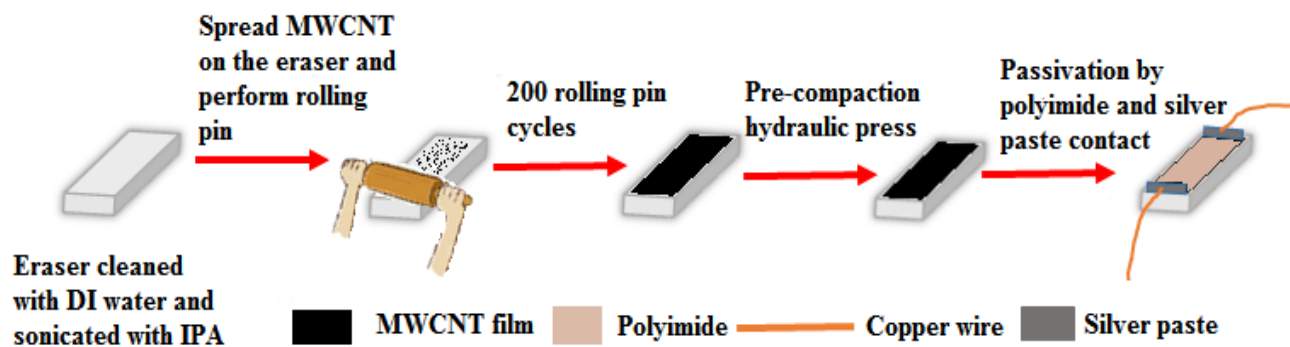
Figure 7.1: Schematic representation of fabrication procedure for solvent free MWCNTs film based strain sensor on biodegradable eraser substrate.
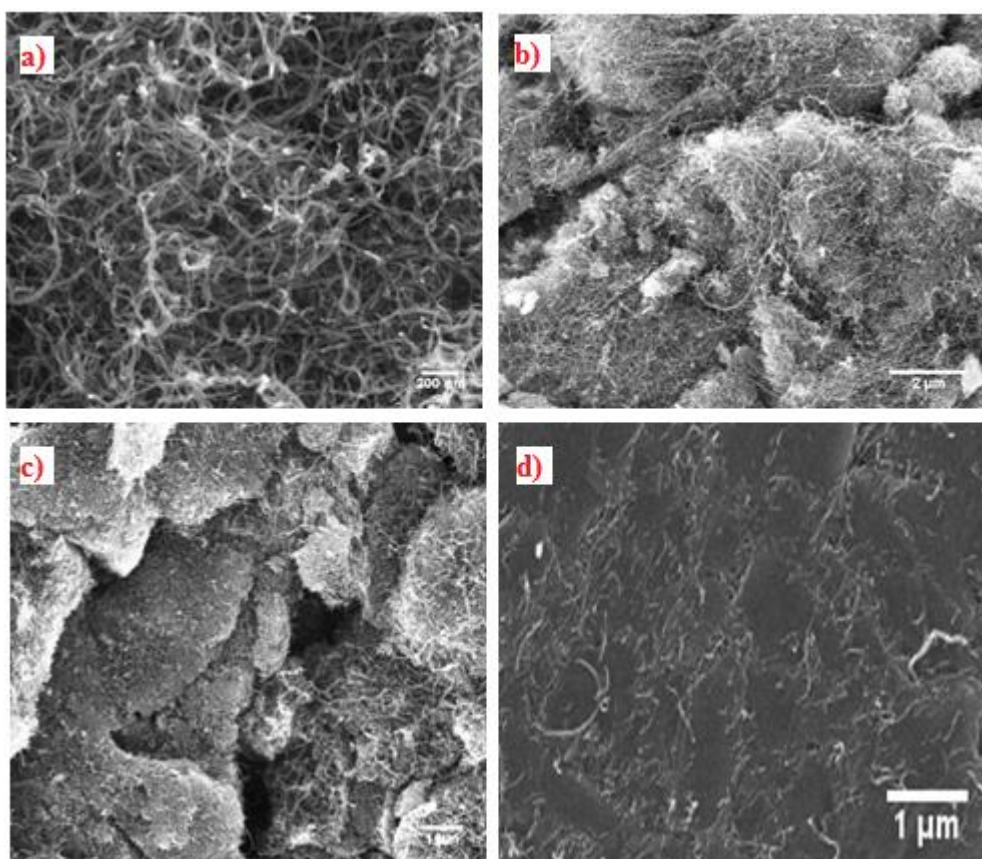
Figure 7.2: FESEM images of a) MWCNTs powder b) MWCNTs deposited on eraser by mechanical pressing without rolling pin c) MWCNTs deposited on eraser with mechanical

pressing performed before rolling pin d) MWCNTs film on eraser with rolling pin for 200 cycles followed by mechanical pressing.
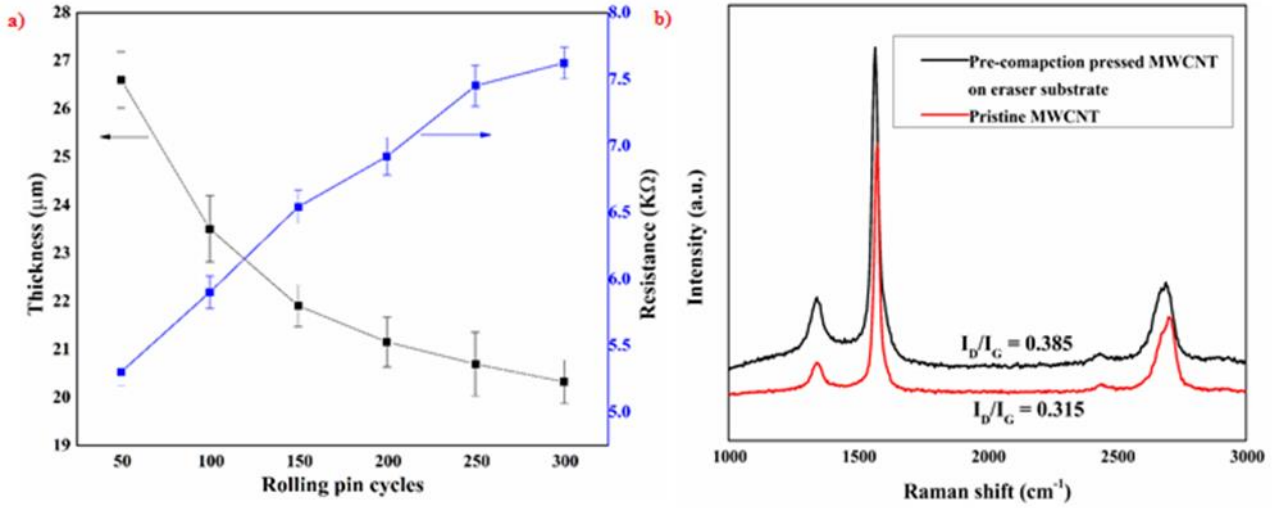
Figure 7.3: Graph showing a) variation of thickness and resistance with rolling pin cycles with average thickness of MWCNTs found to be 23-28 µm (N = 3) b) Raman spectra of MWCNT for pristine and pre-compaction pressed MWCNT which indicates that pre-compaction mechanical press induces defects thereby increasing the I_D/I_G ratio.
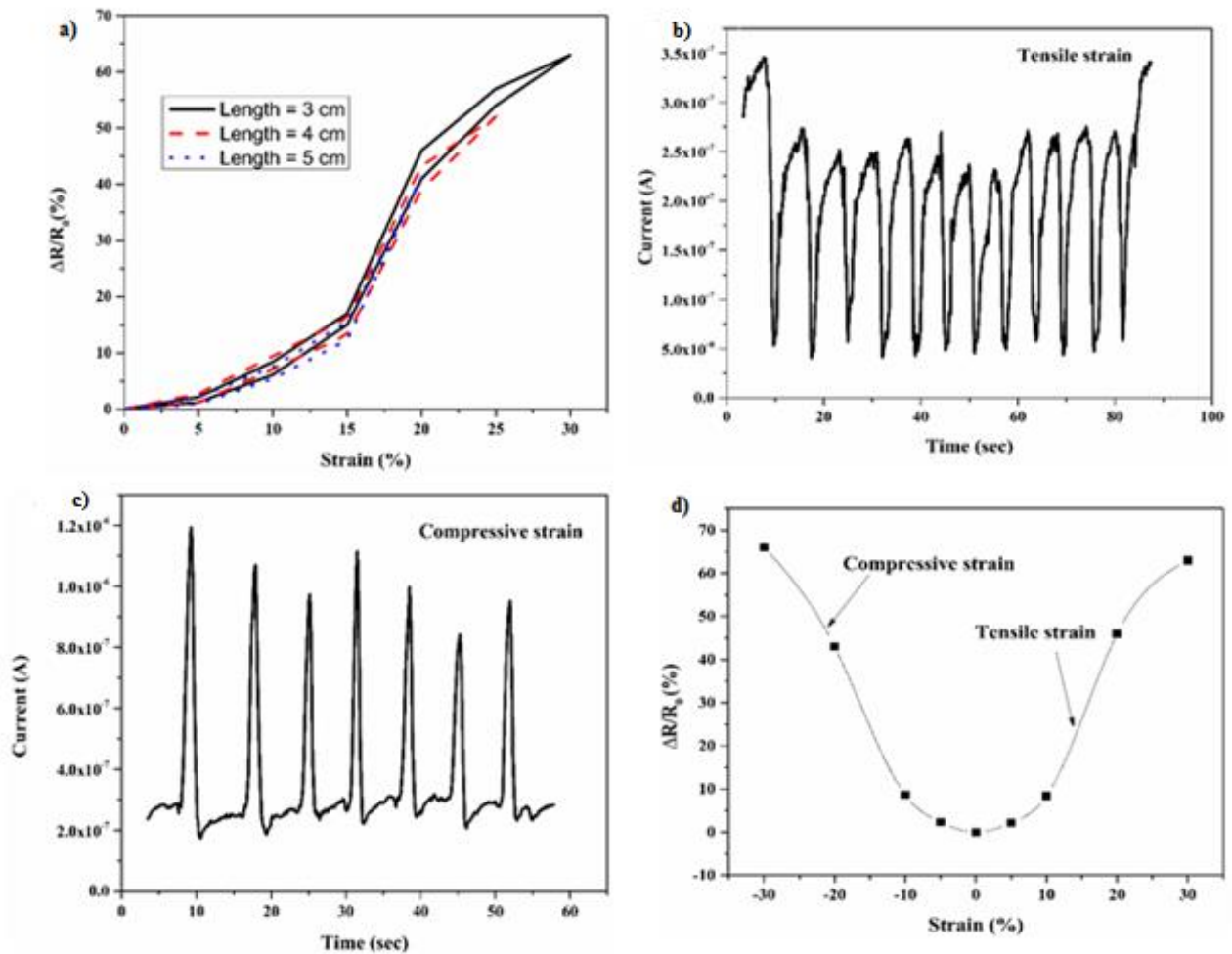
Figure 7.4: a) Hysteresis curve for the resistance against strain for different lengths of the eraser b) temporal response of sensor under compressive strain c) temporal response of the sensor under tensile strain d) graph of resistance change showing near similar response for both compressive and tensile strain
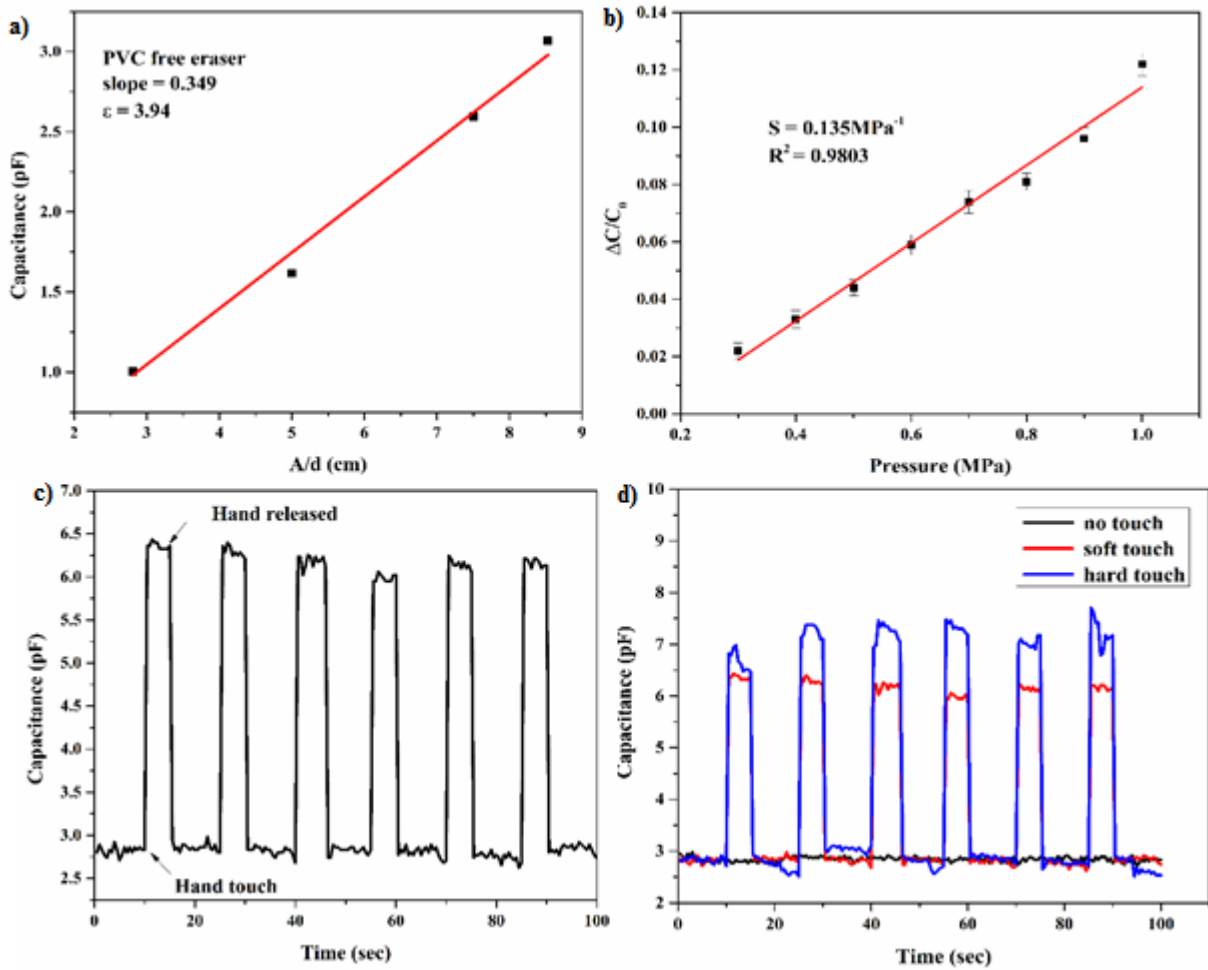
Figure 7.5: a) Graph showing the variation of eraser capacitance with A/d which on linear fit gives dielectric constant of 3.94 b) Graph of normalized eraser capacitance variation with different pressures which on linear fit gives sensitivity of 0.135MPa^{-1} (N = 3) c) Graph showing the temporal response of capacitance variation on human hand touch for 6 cycles showing excellent repeatability d) Graph showing the temporal response of capacitance variation on different human hand (soft and hard) touch for 6 cycles showing excellent repeatability.
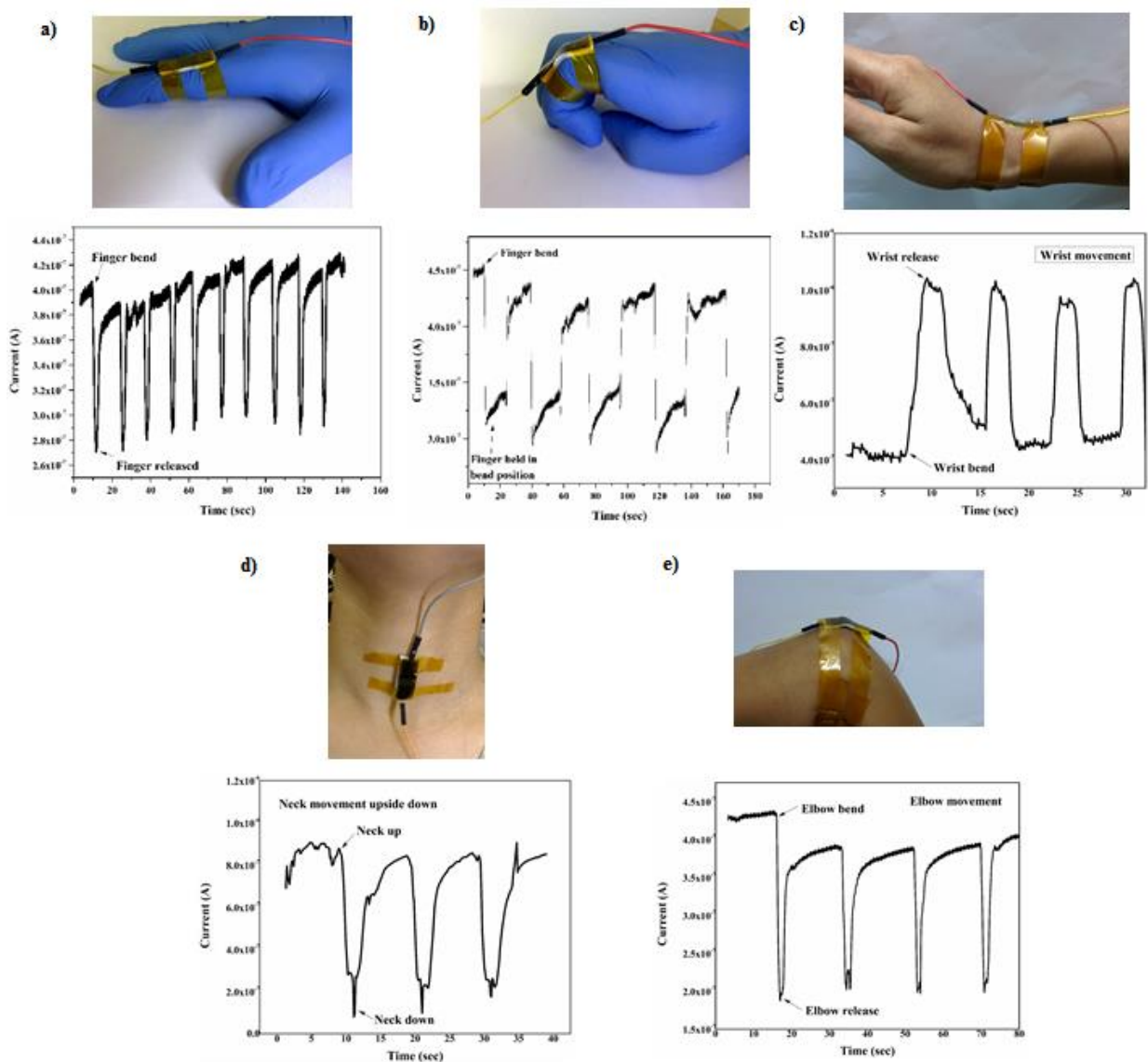
Figure 7.6: Graphs showing different bodily movements and their corresponding temporal response showing excellent repeatability. Insets are photographic images of integration of sensor to different human body parts such as (starting from leftmost corner and coming clockwise) fingers, bent finger, wrist, neck and elbow.
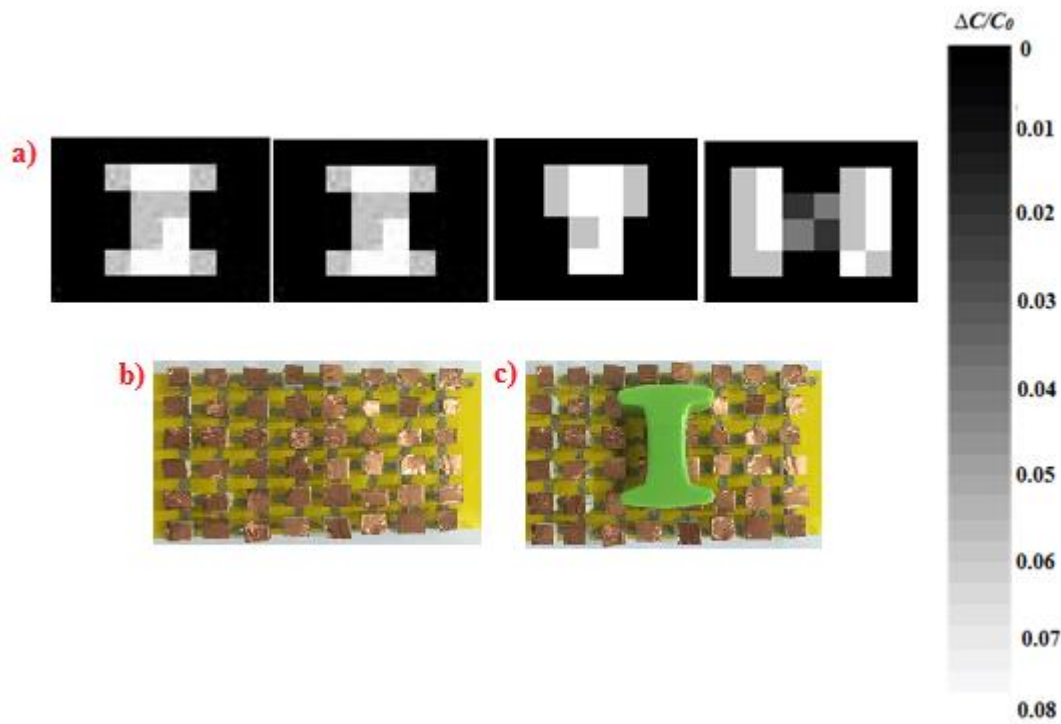
Figure 7.7: a) Mapping profile of pixels for different alphabets "I", "T" and "H" for the letter "IITH" b) Photograph of as fabricated large area artificial e-skin on MWCNT deposited eraser substrate c) Photograph of alphabet "I" (6 g) on the surface of as fabricated artificial e-skin to test pressure sensing capability.

Chapter 8
Conclusion

8.1. Conclusion

In summary, Chapter 2, 3 and 4 demonstrates fabrication of flexible broadband photodetector on flexible substrates using different MoS_2 hybrids by a simple and cost effective hydrothermal method. The selection of the hybrid material was made with two special criteria, one being, it should be high bandgap material and other that it should be n type material which makes the hybrid to possess straddling type of bandgap, thereby enabling broadband photodetection. The spectral selectivity of MoS_2 has been extended to UV wavelength region, by combining MoS_2 with ZnS, 1D V_2O_5 nanowires and 0D carbon dot having high sensitivity towards UV light. The fabricated photodetector displays high sensitivity towards visible spectrum when compared to UV and IR with higher responsivity for $MoS2$-V_2O_5 nanowire hybrid. The work presented in Chapter 2, 3 and 4 provides a promising route for the development of large scale flexible broadband photodetectors using TMD hybrids at low cost; having diverse applications in the field of wearable electronics, environmental monitoring, and surveillance.

Chapter 5 describes the fabrication of 2D Gr/ZnO rectifying junction on PVC free pencil eraser using simple, low-cost solution processed hydrothermal method and has been utilized for increment in the responsivity of broadband photodetection using external strain modulation. Decrease in the bandgap (2.8 eV) was observed for 2D ZnO which was responsible for broadband photodetection in UV and visible region. 87% enhanced photosensing for UV light was observed under 30% strain. The performance improvement is due to piezopotential induced under compressive strain in 2D ZnO which results in lowering of conduction band energy and raising the schottky barrier height thereby facilitating electron-hole pair separation in 2D Gr/ZnO junction. The work demonstrated in chapter 5 paves way for developing highly scalable flexible semiconductor heterojunctions on unconventional substrates for use in optoelectronics, analog electronics and sensors.

Chapter 6 describes the solution processed MoS_2-CuO flexible piezotronic diode using simple yet cost effective hydrothermal method which was utilized for active analog

frequency modulator and enhanced broadband photodetector upon external strain. Under 2% strain, 69.7% increment in normalized resistance was observed for visible illumination. Further, the as fabricated piezotronic diode was utilized at circuit level for designing an oscillator wherein the frequency of oscillator was controlled by applied external strain. The work demonstrated in Chapter 6 is the step ahead in utilizing the fabricated flexible devices at circuit level designing which holds tremendous potential in the field of flexible and wearable sensors, analog and digital electronics applications.

Chapter 7 describes a facile fabrication method for multi-functional skin like pressure and strain sensor was developed using MWCNTs on PVC free eraser with solvent free, low cost and low energy technique. A novel rolling pin and pre-compaction mechanical press technique for deposition of MWCNTs on eraser was developed, optimized and tested. Thickness and resistance variation with rolling pin cycles were studied in order to quantify the deposition technique. Eraser not only acts as a substrate for strain sensing but also acts as a dielectric for capacitive pressure sensor. Also, deposited MWCNTs acts a metal plates for capacitive pressure sensor. Both these process eliminates the need for depositing dielectric and metal which are crucial step in capacitive based pressure sensor. The as fabricated sensor was then integrated to various parts of human body such as hand, neck, wrist and elbow wherein excellent responses to the corresponding movements were observed. The process was scaled for large area fabrication of flexible artificial skin and spatial pressure mapping results reveals excellent consistency in recognizing the shape and location of the object. The novel and low-cost fabrication process described in Chapter 7 could be used in future to design and develop organic skin like devices and abilities to sense moisture, temperature, pH, light and chemical and biological species.

8.2. Future Directions

The future scope of the thesis deals with integrating the multifunctional sensors with a wireless module (Bluetooth) so that data can be acquired wirelessly on the smart phone thereby enabling the development of smart sensors for IoT applications. Multifunctional sensors responding to different chemical stimuli fabricated using functional nanomaterials still remains a challenge due to the usage of same sensor multiple times for different sensing and unreliable frontend processing of the sensing data. This challenge is intensified by the lack of suitable techniques for fabricating disposable sensors which are integrated to smartphone with a dedicated application developed for each sensing. The sensor can be

utilized for particular sensing and then can be disposed avoiding the need for utilizing the same sensor for different sensing thereby increasing accuracy of the sensing data. The fabricated sensor can be further utilized for real time diagnosis of hydration level of human body using breath. Development of such unique hybrid materials for wireless disposable multifunctional sensor would be a great step ahead in flexible and wearable electronics having potential applications in medical, security, Internet of things etc.

Appendix A
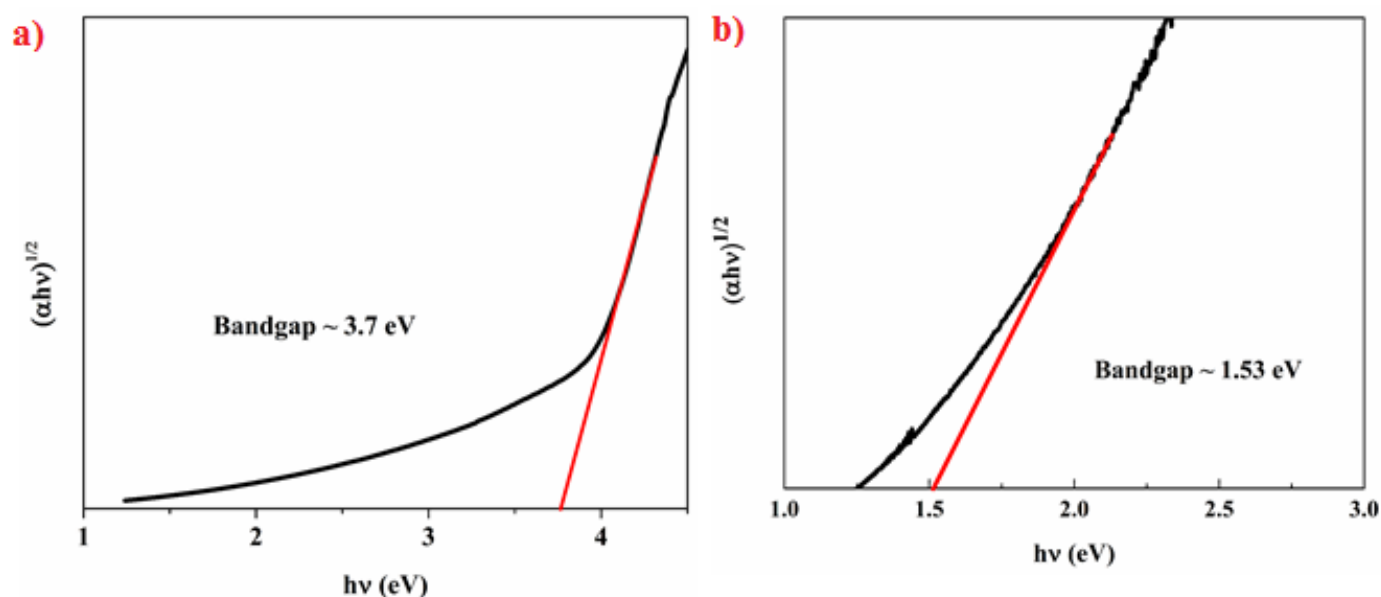
Fig S1: a) Tauc plot for ZnS wherein the bandgap calculated was 3.7 eV b) Tauc plot for MoS$_2$ wherein the bandgap calculated was 1.53 eV.
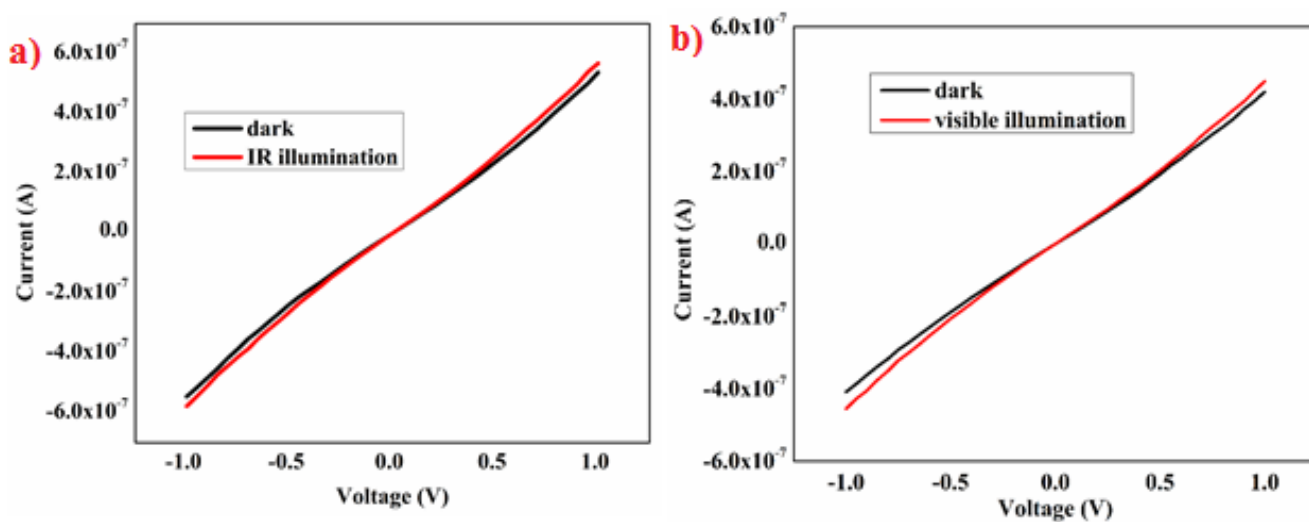
Fig S2: I-V characteristic of pristine MoS$_2$ a) under IR illumination b) visible illumination
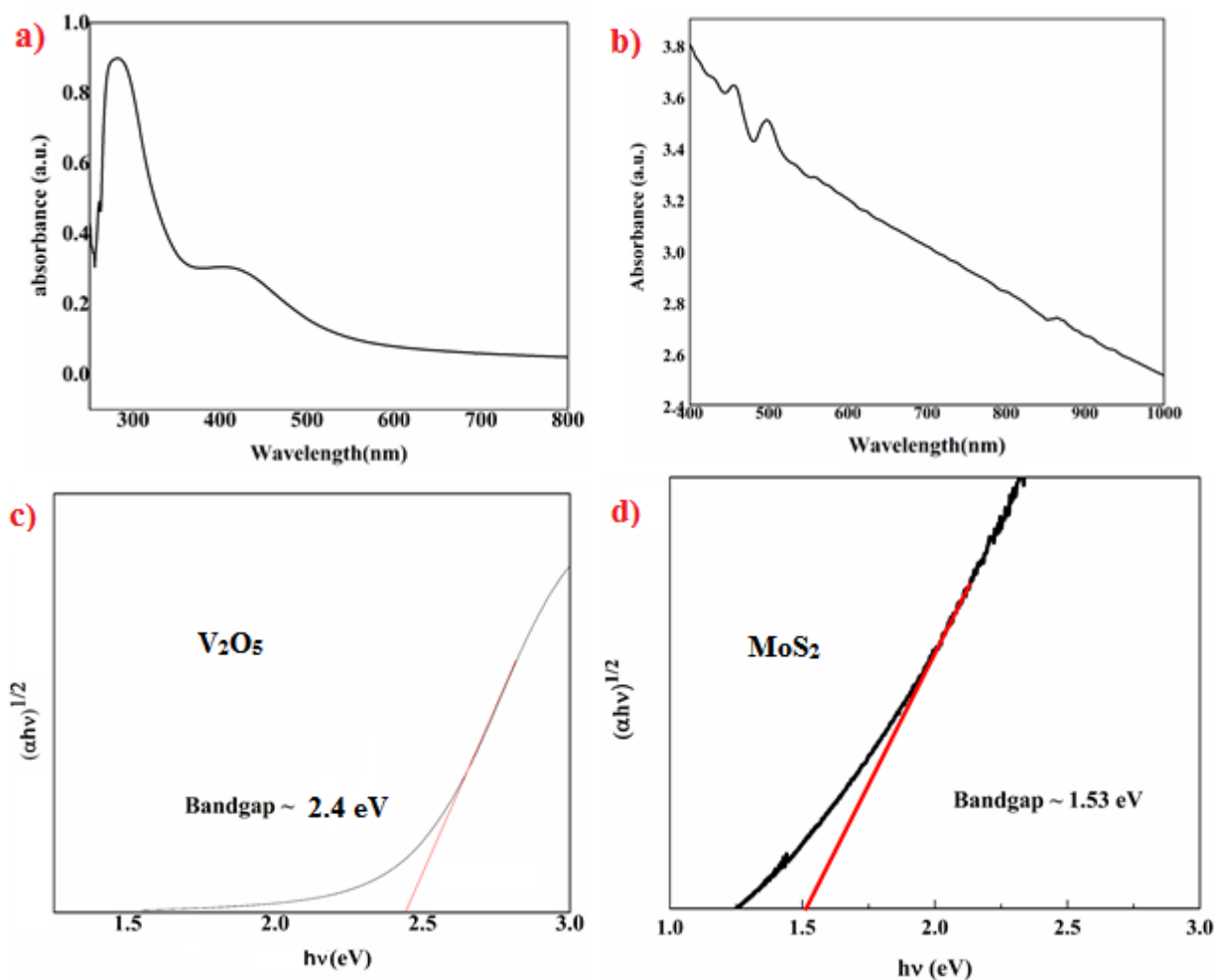
Figure S3: UV-VIS spectra of a) V_2O_5 nanowire showing absorbance in UV to visible region b) MoS_2 showing absorbance in visible to NIR region c) Tauc plot of V2O5 demonstrating a bandgap of 2.4 eV and d) Tauc plot of MoS2 demonstrating a bandgap of 1.53 eV.
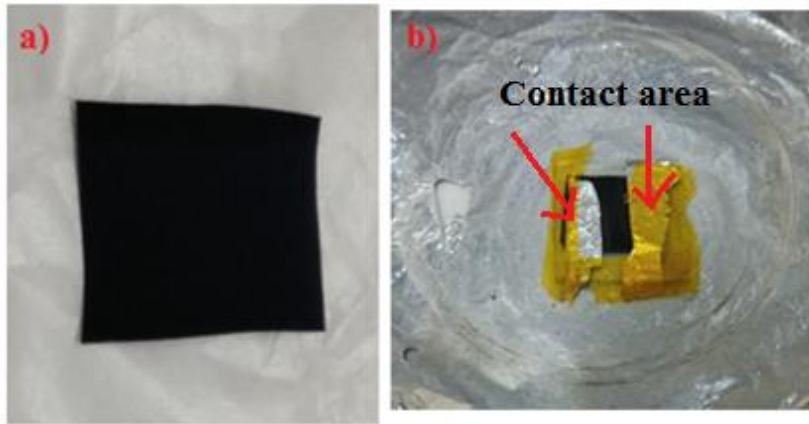
Figure S4: Photographic images of a) MoS2 grown on Al foil b) Masking the side areas of the device for defining metal contact area
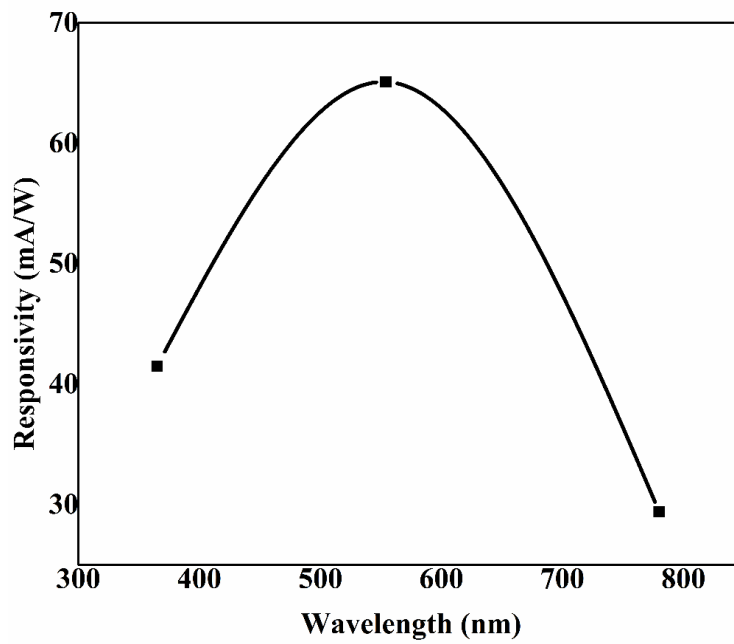
Figure S5: Graph showing the spectral response of the MoS_2/V_2O_5 photodetector from 365 nm to 780 nm
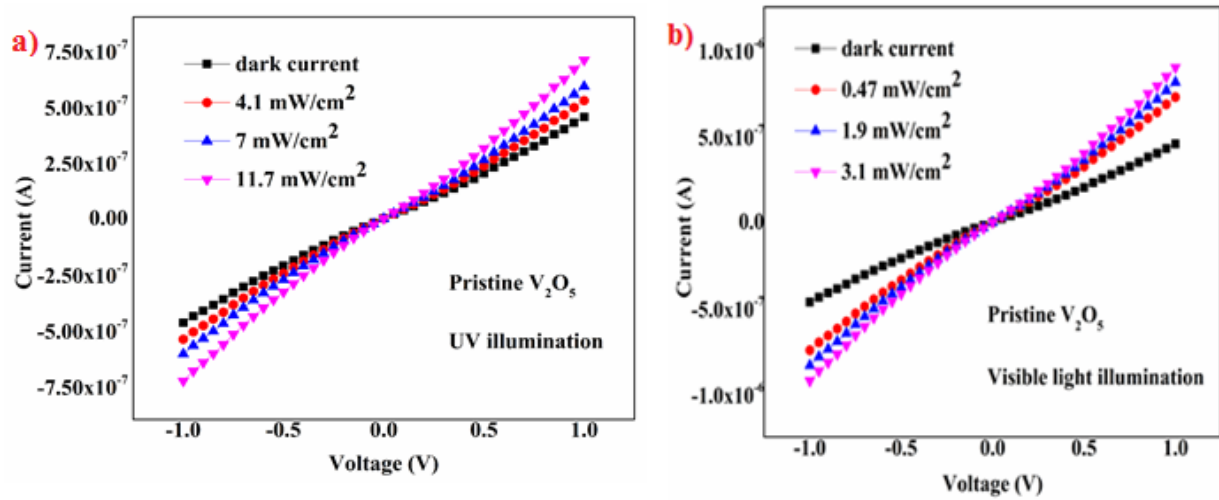
Figure S6: I-V characteristic of pristine V_2O_5 for different a) UV light intensities b) visible light intensities
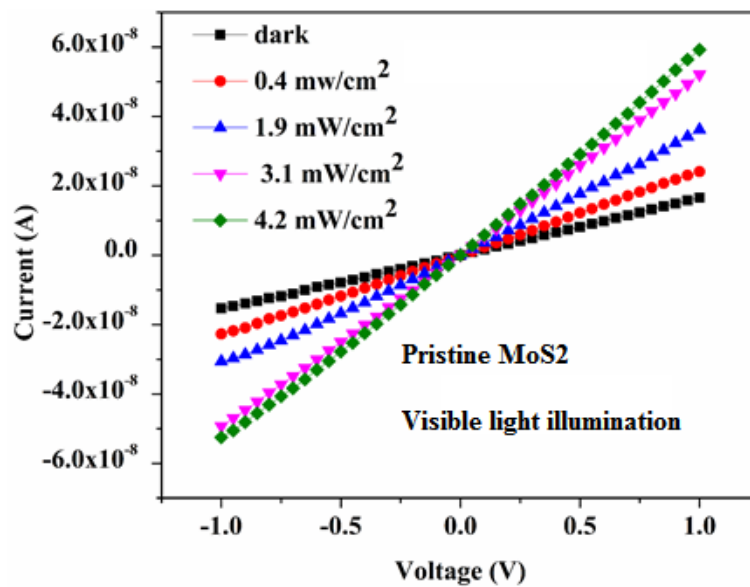
Figure S7: I-V characteristic of pristine MoS_2 for different visible light intensities.
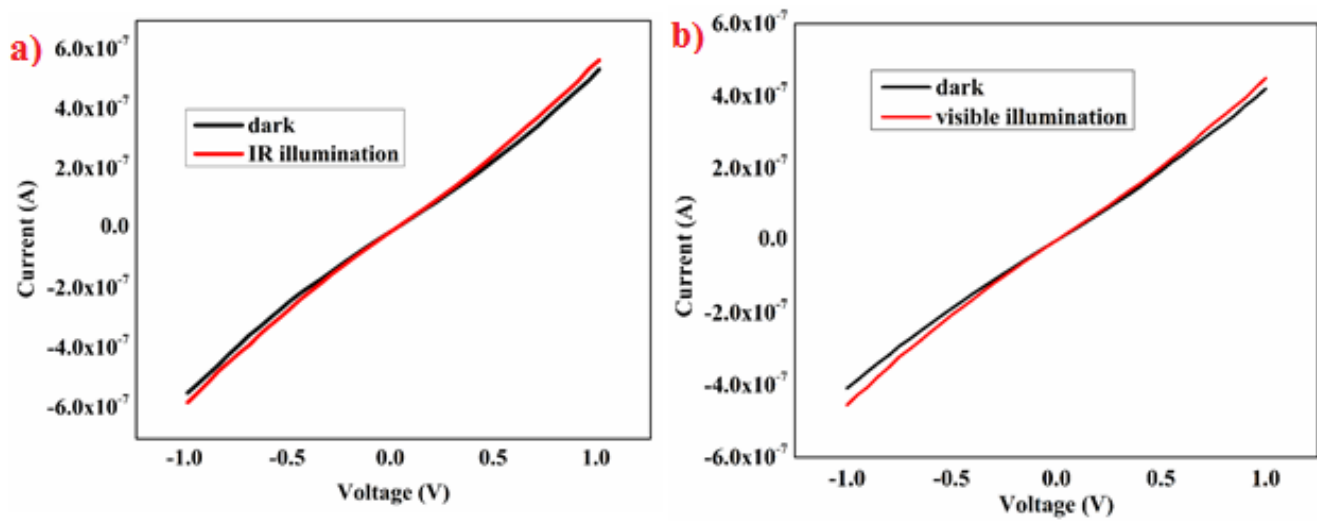
Fig S8: I-V characteristic of pristine MoS2 a) under IR illumination b) visible illumination
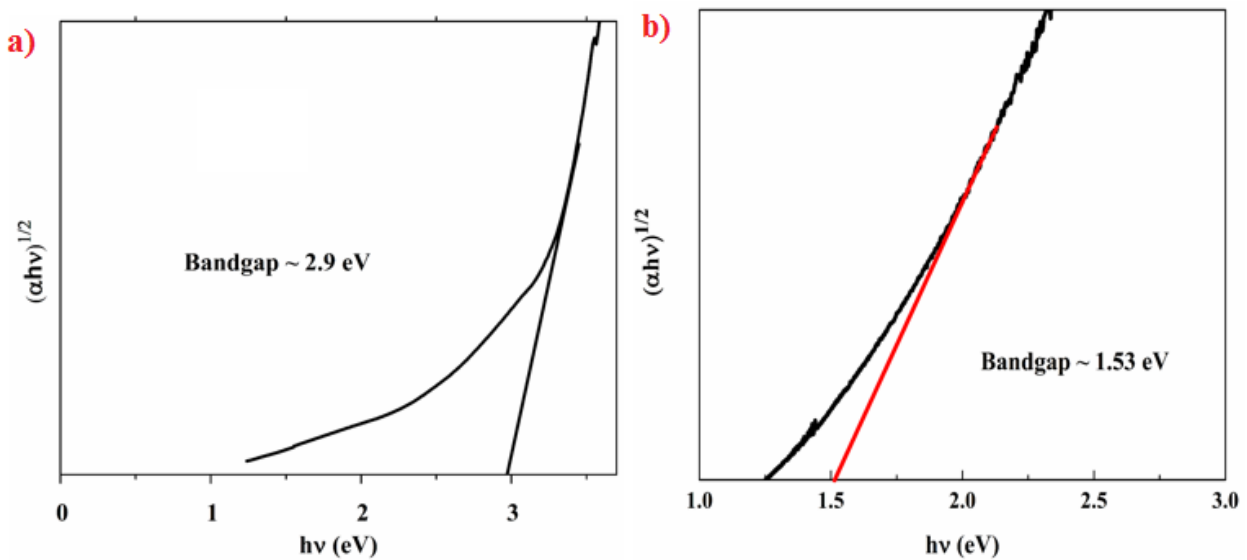
Fig S9: Tauc plot of a) CuO showing optical bandgap value of 2.9 eV b) MoS$_2$ showing optical bandgap value to be 1.53 eV
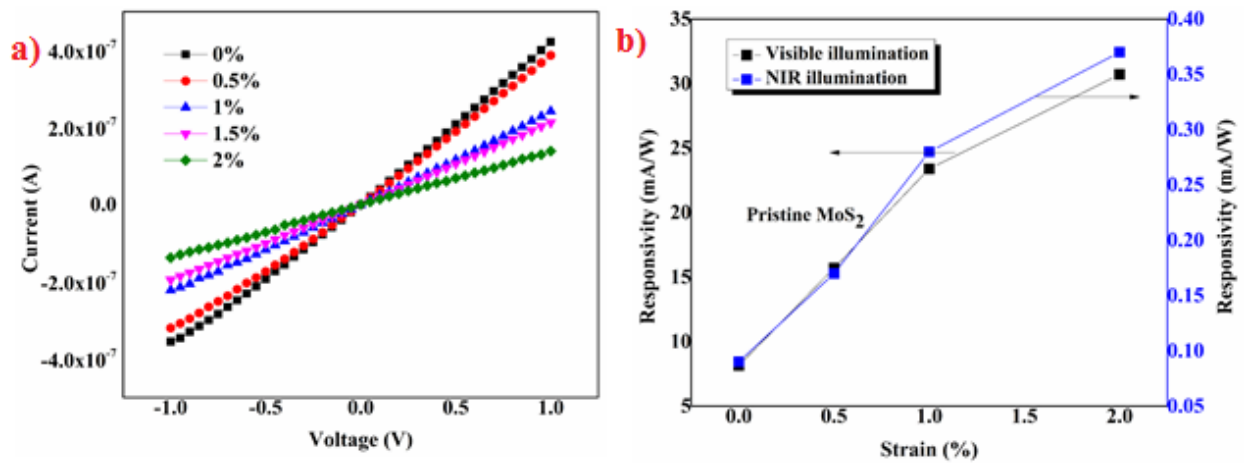
Figure S10: a) I-V characteristic of pristine MoS$_2$ under strain b) Responsivity of pristine MoS$_2$ device under visible and NIR illumination
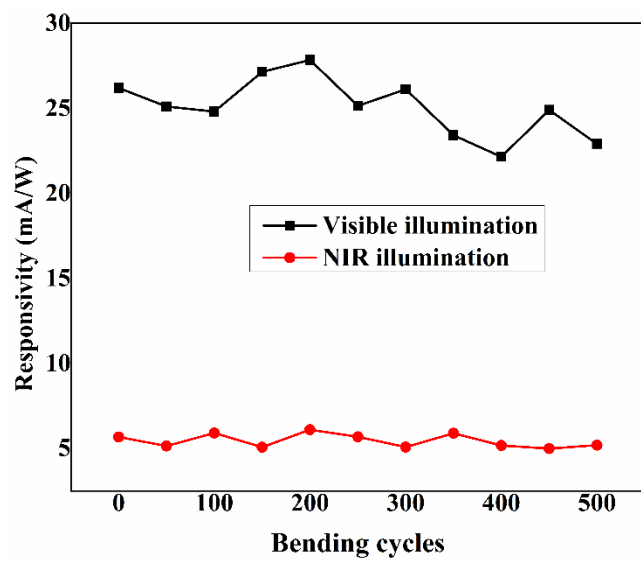
Figure S11: Graph showing the bending cycle test for MoS$_2$/CuO piezotronic diode demonstrating negligible change in the responsivity values under both visible and NIR illumination
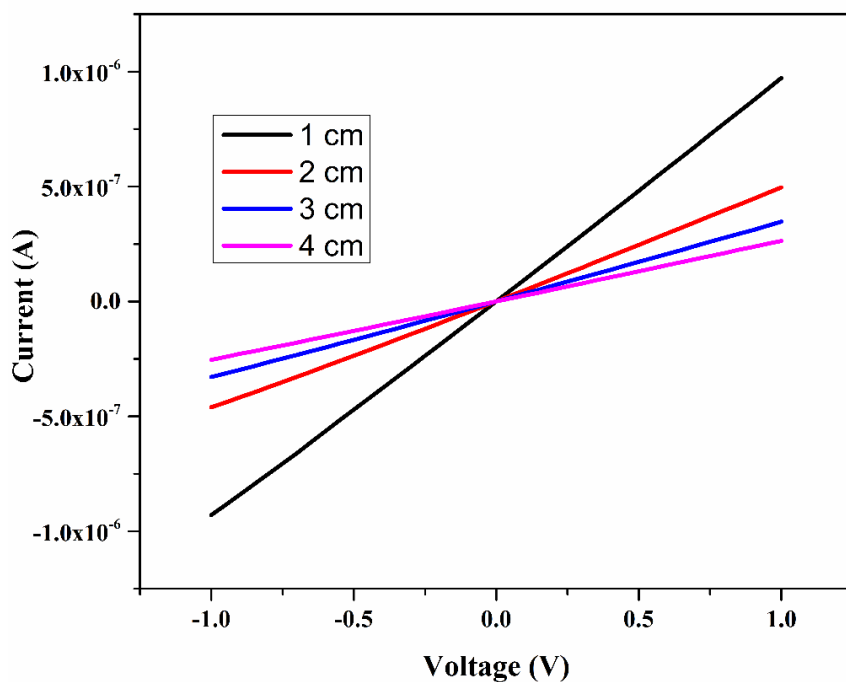
Fig S12: IV characteristic of different lengths of MWCNT film. As length increases there is decrease in current explaining the increase in resistance
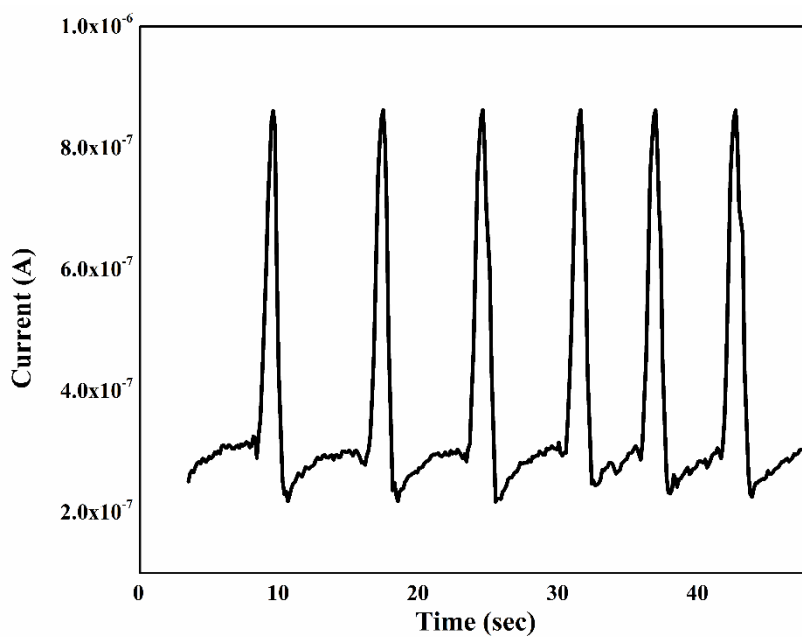
Fig S13: Temporal response of sensor under compressive strain of 10 %.

153
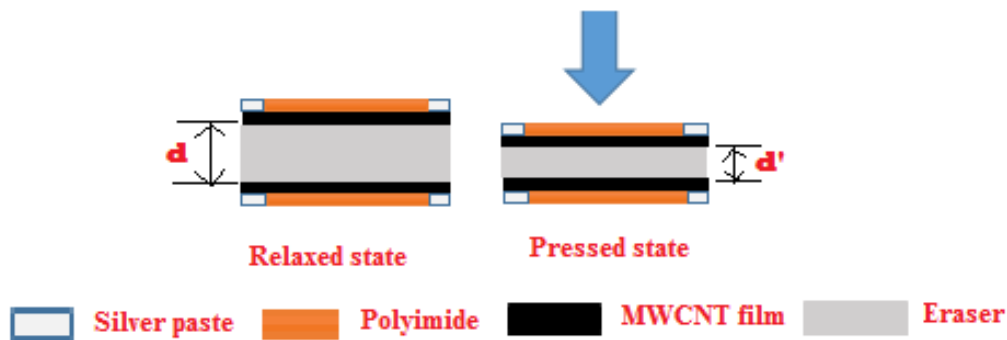
Figure S14: Schematic showing the side view of the capacitive based pressure sensor in relaxed and pressed state where MWCNTs film acts as metal plates and eraser acts as a dielectric thus forming a capacitor

Fabrication of large area flexible e-skin

A commercial PVC free eraser was cleaned with DI water and sonicated in IPA for 3 minutes and then dried at 70°C for 10 minutes. MWCNT was coated on both bottom and tope side of eraser by rolling pin method. To remove the unattached MWCNT it was sonicated in DI water for 3 minutes and dried at 70°C for 30 minutes. The MWCNT rolled pin eraser was then compressed using pre-compaction mechanical press with a pressure of 5Kg/cm^2 for 15 seconds. The eraser was then cut into 5mm^2 x 5mm^2 dimension. Each 5mm^2 x 5mm^2 MWCNT coated eraser acted as a single pixel. Polyimide was used as a supporting substrate for large scale flexible e-skin fabrication. Each pixel was attached to polyimide by the use of silver paste which acted not only as adhesive but also as a bottom electrode. Array of 6 x 8 (each of 5mm^2 x 5mm^2) such pixels were fabricated on polyimide substrate. Each pixel was connected to other on the bottom side by the use of silver paste so as to get a common ground for all the pixels. Finally on top of the eraser, Cu tape was attached which served as a connection for external circuitry

Appendix B

Derivation of the relation between bend angle and strain produced
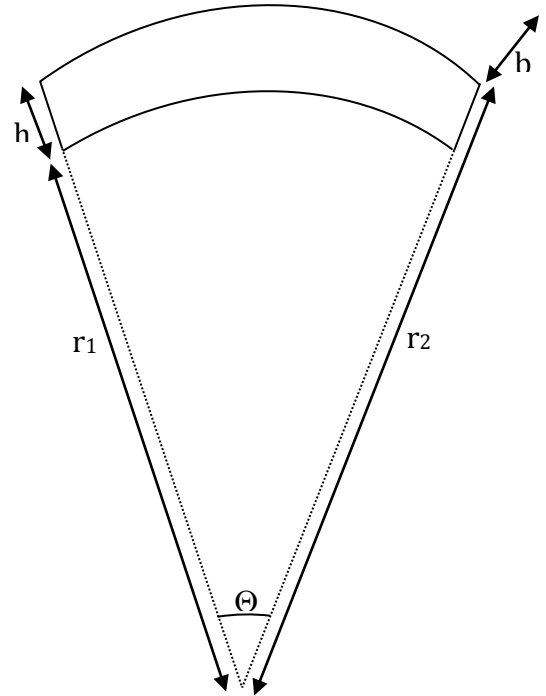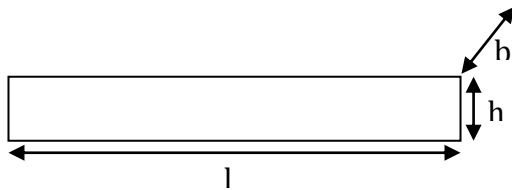
l = length of the eraser

b = breadth of the eraser

h = height of the eraser

r_1 = inner radius of the eraser after bending

r_2 = outer radius of the eraser after bending

Θ = angle of bending

The volume of the eraser will remain constant before & after bending.

So equating the volume before and after bending, we get,

l*b*h = [Θ/360]*π*b*($r_2^2 - r_1^2$)

(Dividing by b on both sides),

l*h = [Θ/360]*π*($r_2^2 - r_2^2$ - h^2+2r_1h)

(Dividing by h on both sides),

l = [Θ/360]*π*(2r_2 - h)

$\Rightarrow$ (360*l)/ (Θ* π) = (2r_2 - h)

$\Rightarrow r_2$ = [(180*l)/ (Θ* π)] + h/2

$\therefore r_1$ = [(180*l)/ (Θ* π)] - h/2

l' = length of the outer arc of the eraser after bending

ε = strain

Δl = change in length of the outer arc of the eraser

l' = [Θ/360]*2π*r$_2$

⇒l' = [Θ/360]*2π*[{(180*l)/ (Θ* π)} + h/2]

⇒l' = l + [Θ/360]*π*h

∴Δl = [Θ/360]*π*h

ε = Δl/l

⇒ε = [Θ/360]*π*h/l

⇒ε% = [[Θ/360]*π*h/l] *100

∴ε% = [Θ/3.6]*π*h/l